Transition to turbulence in linearly stable shear flows

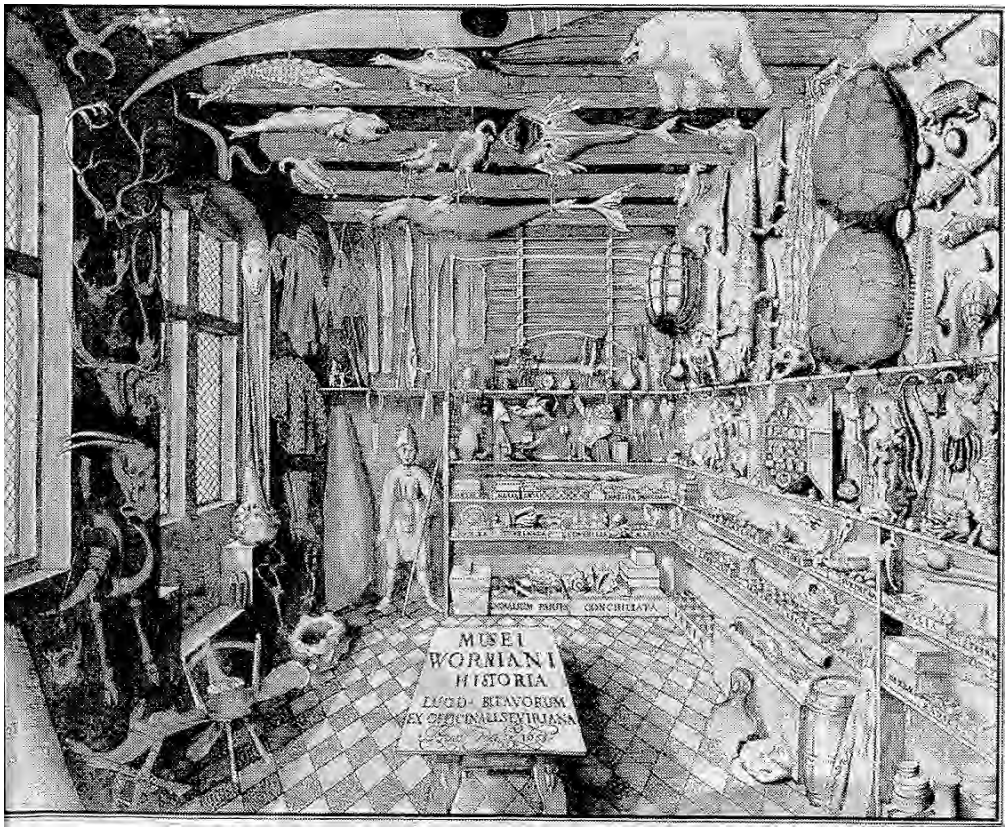

DISSERTATION

zur Erlangung des Doktorgrades

der Naturwissenschaften (Dr. rer. nat.)

dem Fachbereich Physik der Philipps-Universität Marburg

vorgelegt von

Armin Schmiegel

aus Bremerhaven

Marburg/Lahn 1999

Vom Fachbereich der Physik
der Philipps-Universität
als Dissertation angenommen am 1.12.1999

Erstgutachter Prof. Dr. Bruno Eckhardt

Zweitgutachter Prof. Dr. Florian Gebhard

Tag der mündlichen Prüfung: 9.12.1999

Weil vor soviel Wunder,
ich nur Armut bin.

Thomas von Aquino

Contents

1 Turbulenzübergang in linear stabilen Scherströmungen

Man soll öfters dasjenige untersuchen,
was von den Menschen meist vergessen wird,
wo sie nicht hinsehen, und was so sehr
als bekannt angenommen wird,
daß es keiner Untersuchung
mehr wert geachtet wird.

G. C. Lichtenberg, KA 13[60]

1.1 Einleitung

Die Entstehung der Turbulenz bei den in der Praxis häufig auftretenden Scherströmungen gilt als eines der großen noch ungelösten Probleme der klassischen Physik. Obgleich die Bewegungsgleichung eines inkompressiblen Fluids bereits seit mehr als hundertfünfzig Jahren bekannt ist, ist eine vollständige analytische Lösung dieser Gleichung bisher nur in wenigen Fällen gelungen. Man versucht in der Regel mit Hilfe experimenteller oder numerischer Untersuchungen die wesentlichen Elemente der untersuchten Dynamik zu ermitteln, um die Bewegungsgleichung entsprechend vereinfachen zu können. Das Phänomen des Turbulenzübergangs ist jedoch so komplex, daß nicht klar ist, wie die Dynamik vereinfacht werden kann. Wird eine Scherströmung turbulent, findet eine chaotische, zeitabhängige Dynamik statt. Selten ist die turbulente Strömung zweidimensional. In der Regel ist sie dreidimensional, und sehr viele unterschiedliche Längen- und Zeitskalen sind an ihr beteiligt. Nur in wenigen Fällen war man bisher in der Lage, die wesentlichen Elemente dieses Turbulenzübergangs zu identifizieren. Dabei wäre ein tiefergehendes Verständnis dieses Übergangs von großem praktischen Interesse, könnte es doch neue Wege zur Kontrolle des Übergangs aufzeigen.

Einer der Mechanismen, die einen Übergang hervorrufen, ist das Auftreten einer linearen Instabilität des laminaren Strömungsprofils [20, 35, 61]. Tritt diese auf, entstehen neue, häufig stabile Strömungsstrukturen, die wiederum instabil werden und unter Umständen einen chaotischen Attraktor generieren können [73]. In der Rayleigh-Bénard Konvektion, bei der eine Flüssigkeitsschicht durch einen Temperaturgradienten getrieben wird, oder in der

Ebenen Poiseuille-Strömung, der druckgetriebenen Strömung zwischen zwei unendlich ausgedehnten, parallelen Platten, treten solche Instabilitäten auf. So wird die Ebene Poiseuille-Strömung linear instabil, wenn die Reynoldszahl einen Wert von 5772.4 überschreitet [56, 73, 74].[1] Eine solche Analyse ist erfolgreich, wenn die relevanten Phasenraumstrukturen aus dem laminaren Profil hervorgehen. Doch bereits die Ebene Poiseuille-Strömung zeigt die Grenzen dieser Untersuchung auf. Ein Turbulenzübergang ist bereits bei einer Reynoldszahl von 1500 zu beobachten, wenn die Störung eine endliche Amplitude besitzt [51]. Zudem gibt es eine Reihe von Systemen, die nicht linear instabil werden und die dennoch einen Übergang zur Turbulenz zeigen [9, 31, 80]. Hierzu gehört die Hagen-Poiseuille-Strömung, bei der das Fluid mit einem konstanten Druckgradienten durch ein Rohr getrieben wird [14, 35, 61, 102, 110], wie auch die Ebene Couette-Strömung, bei der ein Fluid zwischen zwei unendlich ausgedehnten, parallelen Platten geschert wird. Aufgrund ihrer einfachen Geometrie ist die Ebene Couette-Strömung der Hauptgegenstand der vorliegenden Arbeit.

Ausgangspunkt dieser Arbeit ist die Beobachtung, daß es in diesen beiden Systemen im Gegensatz zu linear instabilen Systemen keine scharfe Grenze zwischen jenen Bereichen gibt, in denen alle Störungen des laminaren Profils zerfallen, und denjenigen, in denen ein Übergang zu beobachten ist [9, 15, 31, 96]. Vielmehr erscheint diese Grenze diffus und stark von der eingebrachten Störung und ihrer Amplitude abzuhängen. In der Ebenen Couette-Strömung zeigen numerische Untersuchungen, daß die nicht zerfallenden Störungen in ein bestimmtes Phasenraumgebiet relaxieren. In diesem Gebiet laufen nahe beieinanderliegende Zustände exponentiell auseinander [95]. Es handelt sich jedoch nicht um einen chaotischen Attraktor, denn die Störungen haben fast alle eine endliche Lebensdauer. Es liegt nahe, diese langlebigen, turbulenten Zustände als chaotische Transienten zu interpretieren, die durch einen chaotischen Repellor erzeugt werden. Ein chaotischer Repellor oder chaotischer Sattel [15, 28, 36, 54, 59, 98, 99] unterscheidet sich von einem chaotischen Attraktor darin, daß er über eine instabile Mannigfaltigkeit verfügt. Über diese Mannigfaltigkeit verläßt jeder Zustand den Repellor. Solange sich der Zustand auf dem Repellor befindet, weist seine Dynamik allerdings dieselben Eigenschaften auf, wie sie bei einem chaotischen Attraktor zu beobachten sind. Die Lebensdauern der auftauchenden chaotischen Transienten können dabei unter Umständen bedeutend größer sein, als die zur Verfügung stehende Beobach-

[1] Die dimensionslose Reynoldszahl definiert sich aus einer charakteristischen Geschwindigkeit U, einer charakteristischen Länge L und der kinematischen Viskosität ν gemäß

$$\mathrm{Re} = \frac{U\,L}{\nu}$$

Die kritische Reynoldszahl von 5772.4 bei der Ebenen Poiseuille-Strömung bezieht sich auf die mittlere Strömungsgeschwindigkeit als charakteristische Geschwindigkeit und den Plattenabstand als charakteristische Länge.

tungszeit. Brosa machte ähnliche Beobachtungen, als er die Evolution von Störungen der Hagen-Poiseuille-Strömung über einen längeren Zeitraum hinweg verfolgte [15]. Bereits Crutchfield und Kaneko konnten zeigen [28], daß in nichtlinearen Systemen mit sehr vielen Freiheitsgraden chaotische Transienten auftauchen können. Die von Crutchfield und Kaneko beobachteten Lebensdauern wuchsen dabei schneller als exponentiell mit der Zahl der Freiheitsgrade an.

Der Ursprung dieses Repellors in der Ebenen Couette-Strömung konnte bisher noch nicht geklärt werden. Hierzu ist es notwendig, nach Phasenraumstrukturen zu suchen, die nicht mit dem laminaren Profil verbunden sind. In der Ebenen Couette-Strömung gelang es Nagata [68, 69], Busse und Clever [27] ein Paar von stationären Zuständen zu identifizieren, die durch eine Sattel-Knoten Bifurkation entstehen. Die lineare Stabilitätsanalyse des Knotens zeigt, daß dieser mehrere Hopf-Bifurkationen durchläuft. In der Umgebung dieses Zustandes wird daher ein ähnlicher Übergang wie in linear instabilen Systemen beobachtet: Ein vormals stabiler Zustand verliert seine Stabilität und ein neuer, stabiler Zustand geht aus ihm hervor, der weitere Bifurkationen durchläuft. Die Existenz des von Nagata, Busse und Clever gefundenen Paares von Zuständen erklärt jedoch nicht den Übergang zur Turbulenz. Dieses Sattel-Knoten Paar liegt in Gebieten des Phasenraums, die nur von entsprechend präparierten Störungen erreicht werden können. Außerdem findet die turbulente Dynamik zufällig eingebrachter Störungen erst bei deutlich höheren Reynoldszahlen und in anderen Gebieten des Phasenraums statt.

Die Untersuchungen dieser Arbeit zeigen jedoch, daß noch weitere stationäre Zustände existieren, die allerdings alle linear instabil sind. Einige von ihnen liegen jedoch in Gebieten des Phasenraums, in denen auch die turbulente Dynamik beobachtet wird. Das Studium der heteroklinen und homoklinen Flüsse in der Umgebung dieser Zustände deutet an, wie der Turbulenzübergang in der Ebenen Couette-Strömung erfolgen könnte: Mit wachsender Reynoldszahl entstehen immer neue stationäre Zustände und neue Verbindungen. Eine Störung des laminaren Profils wird von der stabilen Mannigfaltigkeit eines Zustandes angezogen und gelangt so in das Netzwerk aus instabilen heteroklinen und homoklinen Verbindungen. Diesem Netzwerk kann die Störung folgen, bis sie letztlich auf das laminare Profil zurückfällt.

Die Situation ist vergleichbar mit dem Besucher des Raritätenkabinetts, dem Titelbild dieser Arbeit: Keines der Ausstellungsstücke ist für sich allein in der Lage, einen Besucher ewig zu fesseln. Letztlich wird jeder Gast irgendwann das Kabinett verlassen. Doch je mehr interessante Objekte vorhanden sind, und je mehr der Besucher in der Lage ist, Verknüpfungen, Gemeinsamkeiten und Beziehungen zwischen den einzelnen Gegenständen zu erkennen, desto länger wird er verweilen.

Diese Arbeit gliedert sich in fünf Abschnitte: Nach einer Vorstellung der Ebenen Couette-Strömung untersuche ich zunächst das Verhalten endlicher Störungen. Diese Experimente dienen der Charakterisierung des Übergangs und dem Studium der Eigenschaften der turbulenten Dynamik. Dann werden die Eigenschaften verschiedener stationärer Zustände untersucht. Ihre unterschiedlichen Topologien werden diskutiert und die einzelnen Zustände klassifiziert. Es werden zwei lineare Mechanismen vorgestellt, die an der Entstehung der stationären Zustände beteiligt sind.

Die heteroklinen und homoklinen Flüsse in der Umgebung der Zustände werden untersucht, die Bedeutung dieser Flüsse für die Entstehung von Turbulenz dargestellt und mit dem Einfluß der von Nagata, Busse und Clever gefundenen Zustände verglichen.

Die Arbeit wird mit der Untersuchung des Turbulenzübergangs in einem niedrigdimensionalen Modell einer linear stabilen Scherströmung abgeschlossen. In diesem Modell, das ein ähnliches Übergangsverhalten wie die Ebene Couette-Strömung aufweist, wird der Repellor durch periodische Bahnen aufgespannt. Mit Hilfe dieser periodischen Bahnen wird versucht, die Entweichrate und der größte Lyapunov-Exponent des Repellors quantitativ zu bestimmen.

1.2 Untersuchungen zum Turbulenzübergang

Experimentelle Untersuchungen zum Turbulenzübergang in der Ebenen Couette-Strömung zeigen, daß der Übergang nicht mit einer bestimmten kritischen Reynoldszahl in Verbindung gebracht werden kann. Die kritischen Reynoldszahlen, ab denen erste Übergänge beobachtet wurden, hängen von der Art der verwendeten Störung ab und reichen von 280 bis 370 [1, 11, 13, 32, 34, 63, 101].[2]

Um das Auftreten dieser unterschiedlichen Werte genauer zu untersuchen, bestimmte ich in Kapitel 4 die Lebensdauern unterschiedlicher finiter Störungen in Abhängigkeit ihrer Amplitude und der Reynoldszahl. Dabei definiert sich die Lebensdauer einer Störung als jene Zeit, bis zu der die Geschwindigkeitskomponente des Fluids in wandnormaler Richtung nicht unter einen Schwell-Wert gefallen ist. Da diese Geschwindigkeitskomponente die einzige ist, die dem laminaren Grundprofil Energie entnehmen kann, zerfallen dann auch die anderen beiden Geschwindigkeitskomponenten und die Störung verschwindet. Diese Untersuchungen zeigen, daß es drei verschiedene Arten von Zuständen gibt: lineare Transienten, nichtlineare Transienten und turbulente Zustände. Während die transienten Zustände innerhalb der Beobachtungszeit zerfallen, bleiben die turbulenten Zustände bis zum Ende der numerischen

[2] Im Gegensatz zur Ebenen Poiseuille-Strömung bezieht sich hier die Reynoldszahl auf die halbe Relativgeschwindigkeit der Platten und den halben Plattenabstand.

Integration bestehen.

Darüberhinaus weisen die Lebensdauern eine extreme Abhängigkeit von der Art der Anfangsbedingung auf. Selbst eine hohe Auflösung in der Amplitude oder der Reynoldszahl zeigt keine Glättung der funktionalen Abhängigkeit. Angesichts dieser sensitiven Abhängigkeit von den Parametern ist es praktisch unmöglich eine Grenze zu bestimmen, bei der diese langlebigen Zustände erstmals (als Funktion der Reynoldszahl) auftreten. Daher erscheint es sinnvoller, den Turbulenzübergang mit einer statistisch definierten *Transitions-Reynoldszahl* $\mathrm{Re}_{\mathrm{tr}}$ in Verbindung zu bringen. $\mathrm{Re}_{\mathrm{tr}}$ definiert sich als jene Reynoldszahl, ab der die Hälfte der beobachteten Störungen für eine bestimmte Beobachtungszeit turbulent bleibt. Eine solche statistische Definition schlugen bereits Darbyshire und Mullin für die Untersuchung des Übergangs innerhalb einer Rohrströmung vor [31]. Bottin und Chaté griffen diese Definition auf und bestimmten für die Ebene Couette-Strömung eine Transitions-Reynoldszahl von $\mathrm{Re}_{\mathrm{tr}} = 328$ [11]. In dieser Arbeit wurde ein Wert von 315 ± 10 bestimmt, dabei lag die Beobachtungszeit bei 3000 Zeiteinheiten. In ihrem Experiment konnten Bottin und Chaté das System über einen Zeitraum von 20000 Zeiteinheiten beobachten. Die Verlängerung der Beobachtungszeit um einen Faktor 7 liefert lediglich eine vierprozentige Verschiebung zu höheren Reynoldszahlen. Reduziert man die Beobachtungszeit auf 1000 Zeiteinheiten, erhält man eine Transitions-Reynoldszahl, die zwischen 275 und 305 liegt und die in noch stärkerem Maße von der Art der Anfangsbedingung abhängt.

Die nichtlinearen Transienten und die turbulenten Zustände unterscheiden sich nur in ihren Lebensdauern voneinander. Sie gleichen sich in ihren statistischen Eigenschaften, die unabhängig von der Art der induzierten Störung sind. Dies läßt vermuten, daß der Übergang zur Turbulenz in der Ebenen Couette-Strömung durch die Entstehung eines Repellors verursacht wird. Dieser zieht endliche Störungen an, entläßt sie aber letztlich. Die Zeitskalen, auf denen dieses geschieht, die Relaxationsrate und die Entweichrate, lassen sich numerisch bestimmen.

Um zu bestimmen, wann erste turbulente Zustände bzw. nichtlineare Transienten auftreten können, versuchte ich mit Hilfe von Kühl-Experimenten turbulente Zustände zu kleineren Reynoldszahlen hin zu verfolgen. Bei diesen Experimenten wird zunächst ein turbulenter Zustand bei einer Reynoldszahl oberhalb der Transitions-Reynoldszahl erzeugt. Danach wird die Reynoldszahl langsam reduziert, was einer zeitabhängigen Änderung der Viskosität entspricht. Im Gegensatz zu den Quench-Experimenten von Bottin und Chaté [11], bei denen die Reynoldszahl instantan reduziert wird, berücksichtigen die Kühl-Experimente, daß der turbulente Zustand bei verschiedenen Reynoldszahlen in unterschiedlichen Bereichen des Phasenraums zu beobachten ist. Die Störung kann auf den verschobenen Zustand relaxieren und folgt seiner Bewegung. So läßt sich die turbulente Dynamik zu deutlich niedrigeren

Reynoldszahlen verfolgen, als dies bei Quench-Experimenten der Fall ist. Mit Hilfe dieser Experimente gelingt es, die turbulente Dynamik bis zu einer *Kühl Reynoldszahl* $\mathrm{Re}_{\mathrm{anneal}}$ von 240 zu verfolgen.

1.3 Stationäre Zustände in der Ebenen Couette-Strömung

Um den Ursprung des turbulenten Zustands zu klären, suchte ich nach zeitunabhängigen Lösungen der Navier-Stokes Gleichung. Ein erstes Paar von Zuständen fanden bereits Nagata [68, 69], sowie Busse und Clever [27]. Dieses entsteht bei einer Reynoldszahl von 129 durch eine Sattel-Knoten Bifurkation. Bei Reynoldszahlen oberhalb 1000 fanden Cherhabili und Ehrenstein [21] sowie Balakumar [5] weitere Paare von Zuständen. Es handelt sich dabei um räumlich lokalisierte, zweidimensionale Strukturen, aus denen bei höherer Reynoldszahl ein dreidimensionaler Zustand herausbifurkiert [22].

Diese Zustände gingen aus bekannten stationären Zuständen linear instabiler Scherströmungen hervor. Indem man die linear instabilen Scherströmungen stetig in die Ebene Couette-Strömung überführte und den stationären Zustand verfolgte, gelang es den Autoren, diese Zustände in der Ebenen Couette-Strömung zu realisieren. Nagata untersuchte dabei den Übergang vom Couette-Taylor System zur Ebenen Couette-Strömung. Busse und Clever brachten einen Temperaturgradienten in die Ebene Couette-Strömung ein und führten so einen Übergang vom Rayleigh-Bénard System zur Ebenen Couette-Strömung durch. Cherhabili und Ehrenstein sowie Balakumar führten einen Druckgradienten ein und verfolgten so den Übergang von der Ebenen Poiseuille-Strömung zur Ebenen Couette-Strömung.

Die Untersuchungen dieser Arbeit erfolgten nicht durch eine solche Modifikation. Stattdessen wurde zur Bestimmung von Lösungen der zeitunabhängigen Navier-Stokes Gleichung ein Newton-Raphson Verfahren verwendet [83]. Die Anfangsbedingungen wurden einem turbulenten Zeitsignal entnommen. Die Lösungszweige der gefundenen stationären Lösungen wurden mit Hilfe des Pfadverfolgungsprogramms PITCON ermittelt [88, 89]. Dabei suchte ich nach Zuständen, die bestimmten Symmetriegruppen zugeordnet werden konnten. Ich untersuchte zum einen jene Symmetriegruppe, der das von Nagata, Busse und Clever gefundene Paar angehörte, sowie eine weitere Symmetriegruppe. Beide Gruppen setzten sich aus Punkt- und Flächenspiegelungen zusammen.

Weitere Zustände konnten gefunden werden. Diese Zustände haben alle eine ähnliche Topologie: Sie bestehen aus in Scherrichtung modulierten schlauchartigen Regionen, die einen hohen Fluid-Transport entgegen der Scherrichtung aufweisen. Diese Regionen werden von Wirbeln durchdrungen, deren Achse in Strömungsrichtung weist. Die Wirbel transportieren schnell fließendes Fluid von den scherenden Wänden in diese Regionen hinein.

Dieser sogenannte *lift-up* Effekt ist bereits seit langem beim Blasius-Profil bekannt. Es ist eine direkte Konsequenz der Nichtnormalität der Evolutionsgleichung [43, 65, 81, 103].

Die stationären Zustände lassen sich in vier Klassen einteilen. Dabei dient die Form der schlauchartigen Regionen – man bezeichnet sie als *streamwise streaks* – zur Charakterisierung. Die einfachsten Formen stellen die S- und I-Schläuche dar. Diese Zustände bestehen aus einzelnen Schläuche, die nicht miteinander verbunden sind. S- und I-Schläuche unterscheiden sich in ihrer Modulation in Strömungsrichtung voneinander. Sie ist bei S-streaks deutlicher ausgeprägt als bei den I-streaks.

Bei den H-Schläuchen verschmelzen zwei Schläuche in einem gewissen Raumgebiet und trennen sich wieder. Sie ähneln den Φ-Schläuchen, bei denen sich ein einzelner Schlauch zu zwei Schläuchen aufspaltet, die sich wieder vereinigen.

In der von Nagata, Busse und Clever untersuchten Symmetriegruppe bifurkiert der von ihnen gefundene Zustand bei der niedrigsten Reynoldszahl. Variationen der Breite des Periodizitätsvolumens[3] zeigen, daß dieser ein optimales Seitenverhältnis von $d : 2\pi\, d : \pi\, d$ (Plattenabstand: Länge: Breite) besitzt und bei $Re = 125$ aus einer Sattel-Knoten Bifurkation entsteht.

Neben Zuständen dieser Symmetriegruppe untersuchte ich noch eine weitere Symmetriegruppe. Hier bifurkierte ein Zustand bereits bei einer Reynoldszahl von $\mathrm{Re} = 117.4$, wenn man ein Seitenverhältnis von $d : 2\pi\, d : 1.39\pi\, d$ wählt. Dieser Zustand besteht aus zwei übereinanderliegenden Strömungsschläuchen. Das von Nagata, Busse und Clever gefundene Paar besteht aus zwei nebeneinanderliegenden Strömungsschläuchen.

Elementare Überlegungen bezüglich der Entstehung dieser Strukturen erklären qualitativ, welche physikalischen Mechanismen für die Wahl der optimalen Längenverhältnisse verantwortlich sind. Diese Überlegungen folgen im Wesentlichen den Ideen von Waleffe, der das dynamisch beobachtete Auftreten von Schläuchen und Wirbeln untersuchte [105] und das Entstehen dieser Strukturen zusammen mit Hamilton und Kim studierte [41].

Mit Hilfe des *lift-up* Effektes gewinnen die Schläuche ihre Energie aus den Wirbeln, deren Achse in Strömungsrichtung weist. Die Breite dieser Wirbel gibt die Breite der Schläuche vor. Diese wird durch den Plattenabstand festgelegt. Läßt man nur jeweils eine Mode für die Modulation der Wirbel in wandnormaler Richtung und der Geschwindigkeitskomponente in Scherrichtung zu, erhält man eine optimale Wirbelbreite von $\tilde{L}_y = 1.8889\, d$.

Die in die Schläuche *gepumpte* Energie muß wieder in die Wirbel zurückgeführt werden. Da der Schlauch einer Scherinstabilität unterliegt, kann angenommen werden, daß der Ener-

[3] Das Geschwindigkeitfeld wurde entlang der Scherrichtung und quer dazu als periodisch angenommen.

gieaustausch über die instabilste Mode erfolgt. Betrachtet man den Fall einer zweidimensionalen Scherinstabilität mit einer Scheramplitude von 1 und geht von einer Schlauchbreite von $\tilde{L}_y$ aus, liegt die Wellenlänge der optimalen Scherinstabiliät bei $\tilde{L}_x = 2.935\,d$ im nichtviskosen Fall und $\tilde{L}_x = 3.035\,d$ im viskosen Fall. Dabei wurde eine Reynoldszahl von 100 betrachtet. Diese Ergebnisse legen ein optimales Verhältnis von $d : 1.65\tilde{L}_y : \tilde{L}_y$ nahe.

1.4 Untersuchungen zur Vernetzung der stationären Zustände

Vergleiche der Energien und Scherraten von turbulenten Zeitsignalen mit den Energien und Scherraten der stationären Zustände zeigen, daß nicht alle stationären Zustände in Gebieten des Phasenraums liegen, in denen der turbulente Zustand beobachtet wird. Ähnliche Ergebnisse erhielten auch Ehrenstein und Koch bei ihren Untersuchungen von stationären Lösungen der Ebenen Poiseuille-Strömung [104].[4]

Bei Reynoldszahlen oberhalb der Transitions-Reynoldszahl liegt der beobachtete turbulente Zustand in der Umgebung einer großen Zahl von stationären Zuständen. Extrapoliert man die Verschiebung des turbulenten Zustands zu kleineren Reynoldszahlen, zeigt sich, daß er bei $\mathrm{Re} \approx 240$ jenen Bereich verläßt, in dem stationäre Zustände existieren. Dieser Wert entspricht ungefähr der Kühl-Reynoldszahl. Dies deutet darauf hin, daß nichtlineare Transienten und turbulente Zustände nur in der Umgebung der stationären Zustände auftreten können.

Um den Einfluß der stationären Zustände auf die Struktur des Phasenraums zu untersuchen, betrachtete ich den Fluß, der in der Umgebung der stationären Zustände herrscht. Dabei verfolgte ich die Evolution von 20 Störungen eines stationären Zustands und projizierte sie auf die Energie/Schermaß-Ebene.[5] Es handelt sich dabei um eine Projektion eines hochdimensionalen Systems auf einen zweidimensionalen Unterraum. Dabei können Überschneidungen auftreten, die im vollen System nicht existieren. Die Untersuchungen der stationären Zustände zeigte jedoch keine zufälligen Überlagerungen. Die Betrachtung der Evolution eines Ensembles reduziert zusätzlich die Wahrscheinlichkeit, solche Überlagerungen

[4] Im Fall der Ebenen Poiseuille-Strömung bezieht sich dabei der Begriff *stationär* auf ein mitbewegtes Koordinatensystem, welches dem mittleren Fluß folgt.

[5] Bei dem hier verwandten Schermaß handelt es sich um das Integral der Quadrate der Scherraten in wandnormaler Richtung:

$$M = \frac{1}{A}\int_{-1}^{1} \mathrm{d}z \left(\int_A \frac{\partial}{\partial\, z}\,(u+z) \right)^2 .$$

u ist die Geschwindigkeitskomponente der Störung in Scherrichtung, z entspricht dem laminaren Profil in Einheiten der Plattengeschwindigkeit. Dieses Maß berücksichtigt nicht nur die Scherung an den Wänden, sondern auch die Scherung innerhalb des Fluids.

mehrmals zu treffen. Bekannte Flüsse zwischen Zuständen desselben Lösungszweiges konnten außerdem reproduziert werden.

Ein Vorteil dieser Projektion ist der Umstand, daß alle Zustände, die durch Anwendung der Punkt- oder Flächenspiegelung oder einer Translation eines stationären Zustands hervorgehen, als derselbe Zustand identifiziert werden.

Zwei Typen von lokalen Bifurkationen, die eine Auswirkung auf den globalen Fluß haben, konnten identifiziert werden: Gabelverzweigungen und rückwärtsgerichtete Sattel-Knoten Bifurkationen. Der Begriff der *rückwärtsgerichteten Sattel-Knoten Bifurkation* bezieht sich hier auf das Bifurkationsverhalten in Abhängigkeit von der Reynoldszahl.

Bei der Gabelverzweigung bifurkiert aus einem bereits existierenden Zustand ein weiteres Paar von stationären Zuständen heraus. Dieses bricht eine Symmetrie des vorherigen Zustands. Die erste Bifurkation eines solchen Typs findet sich bei einer Reynoldszahl von 151.

Bei der rückwärtsgerichteten Sattel-Knoten Bifurkation verschmelzen zwei Zustände miteinander und löschen sich aus. Vor dieser Verschmelzung sind sie über eine heterokline Verbindung verbunden. Ist einer der beiden Zustände bereits aus einer anderen Sattel-Knoten Bifurkation hervorgegangen, existiert ein Fluß zwischen dem dritten Zustand und den anderen beiden. Die erste Bifurkation diesen Typs tritt bei einer Reynoldszahl von 157 auf.

Bereits Busse und Clever konnten zeigen, daß der Knoten des ersten Paares von stationären Zuständen in der Ebenen Couette-Strömung mehrere Hopf-Bifurkationen durchläuft [27]. Dabei entsteht am Knoten zunächst ein stabiler Grenzzyklus. Weitere Hopf Bifurkationen des Knotens sorgen dafür, daß der Zyklus zu einem instabilen Torus aufbricht. Dieser befindet sich in einem Gebiet des Phasenraums, in dem eine turbulente Dynamik nur beobachtet wird, wenn eine Störung entsprechend präpariert wird. Er kann daher nicht mit den turbulenten Zuständen in Verbindung gebracht werden. Erst bei Reynoldszahlen oberhalb 320 erreicht der Torus jene Gebiete des Phasenraums, in denen der turbulente Zustand beobachtet wird.

Da die heteroklinen Verbindungen, die durch Gabelverzweigungen und rückwärtsgerichtete Sattel-Knoten Bifurkationen einzelner Zweige entstehen, keinen geschlossenen Orbit generieren, ist eine weitere Vernetzung notwendig, damit langlebige chaotische Transienten möglich werden. Bei wachsender Reynoldszahl nimmt die Zahl der beobachteten heteroklinen Verbindungen zu. Während bei einer Reynoldszahl von 200 nur sechs Verbindungen ermittelt werden konnten, wurden bei einer Reynoldszahl von 240 elf gefunden. Der Großteil dieser Verbindungen liegt in jenem Bereich des Phasenraums, in dem sich auch zeitliche Mittelwerte des turbulenten Zustands befinden.

1.5 Der Übergang zur Turbulenz in einem niedrigdimensionalen Modell einer Scherströmung

Es zeigt sich, daß die Vernetzung von stationären Zuständen nicht die einzigen Phasenraumstrukturen sind, die langlebige chaotische Transienten erzeugen können. Auch instabile periodische Bahnen, die nicht aus heteroklinen oder homoklinen Verbindungen stationärer Zustände hervorgehen, können langlebige chaotische Transienten erzeugen. Da die Bestimmung instabiler periodischer Bahnen in einem hochdimensionalen System extrem schwierig und zeitaufwendig ist, studierte ich einen solchen Übergang in einem niedrigdimensionalen Modell einer linear stabilen Scherströmung.

Das Modell – eine weitere Vereinfachung des 19-Moden Modells von Eckhardt und Mersmann [38] – zeigt ein ähnliches Transitionsverhalten wie die Ebene Couette-Strömung. Obwohl das System linear stabil ist, treten langlebige chaotische Transienten auf. Die Verteilung der Lebensdauern dieser Zustände hängt auch hier empfindlich von der Art der Startbedingung ab. Stationäre Zustände entstehen in diesem Modell erst bei Reynoldszahlen, die deutlich oberhalb der Transitions-Reynoldszahl liegen. In diesem System sind es instabile periodische Bahnen, die den Repellor bilden.

Bei einer Reynoldszahl von 133.08 entsteht ein erstes Paar von Periode-1 Orbits in einer Sattel-Knoten Bifurkation. Der Sattel durchläuft weitere vor- und rückwärtsgerichtete Bifurkationen. Bei einer Reynoldszahl von 223.4 bifurkiert ein neues Paar von Periode-1 Orbits. Dieses Paar generiert durch vor- und rückwärtsgerichtete Bifurkationen bis zu acht verschiedene Orbits. Von diesen bleiben oberhalb von $\mathrm{Re} = 280$ nur zwei Orbits bestehen.

Erste Periode-2 Orbits entstehen bei Reynoldszahlen oberhalb 248. Dabei existieren zwei Typen von Periode-2 Orbits. Bei dem ersten Typ oszillieren zwei Komponenten gegenphasig, so daß das Zeitverhalten der Gesamtamplitude des Zustandsvektors der eines Periode-1 Orbits entspricht. Der zweite Typ entspricht einer Oszillation mit zwei unterschiedlichen Frequenzen.

Diese periodischen Zustände besitzen eine ähnliche Topologie wie die stationären Zustände in der Ebenen Couette-Strömung: Es handelt sich um schlauchförmige Regionen, die einen hohen Fluidtransport in Scherrichtung aufweisen und von Wirbeln durchzogen sind, deren Achse in Scherrichtung weist. Aufgrund der Symmetrie des Systems liegen stets zwei Schläuche mit unterschiedlicher Strömungsrichtung übereinander. Diese Schläuche treiben durch das Periodizitätsvolumen in entgegengesetzten Richtungen und ändern dabei ihre Form. Es handelt sich um advektierte, *atmende* Schläuche.

1.6 Ausblick

Die Ergebnisse dieser Arbeit zeigen, daß der Turbulenzübergang in der Ebenen Couette-Strömung – und vermutlich auch in anderen linear stabilen Strömungen – durch die Entstehung von ausgezeichneten Phasenraumstrukturen erzeugt wird. Bei diesen Strukturen handelt es sich um instabile stationäre Zustände oder instabile periodische Bahnen, die aus Sattel-Knoten-Bifurkationen hervorgehen und die den globalen Fluß innerhalb des Phasenraums ändern.

In Strömungssystemen, die sowohl einen Übergang durch eine Instabilität als auch einen Übergang ohne Instabilität aufweisen, wie zum Beispiel dem Blasius-Profil oder der Ebenen Poiseuille-Strömung, existiert der turbulente Zustand bereits bevor ein chaotischer Attraktor entstanden ist. Es stellt sich die Frage, inwieweit die Phasenraumstrukturen, die den Repellor bilden, mit dem Attraktor wechselwirken, und inwieweit diese beiden Phasenraumstrukturen ineinander übergehen.

Die Identifizierung der verantwortlichen Phasenraumstrukturen erlaubt neue Konzepte der aktiven und passiven Kontrolle des Turbulenzübergangs. Die Strömungsgeometrie kann so modifiziert werden, daß die Entstehung der verantwortlichen Strömungsstrukturen unterstützt oder gehemmt wird. Das Experiment von Bottin et al. [12] kann als ein solcher Versuch interpretiert werden. Indem ein Draht in der neutralen Fläche quer zur Scherrichtung aufgespannt wurde, war man in der Lage, Strömungsschläuche zu fixieren und ihre Eigenschaften zu kontrollieren. Dabei wurde durch Variation der Drahtdicke die Störung des laminaren Profils graduell geändert.

Die Techniken zur aktiven Kontrolle sind noch nicht sehr weit entwickelt. In Experimenten am Blasius-Profil konnte Boikov im linear stabilen Bereich einen Turbulenzübergang hervorrufen [10]. Dabei wurde ein Wirbel, dessen Achse in Strömungsrichtung wies, in das System eingebracht. Weitere Konzepte, die die Kontrolle der Grenzschicht zum Ziel haben, werden unter anderem von Kozlov entwickelt [57]. Noch konzentrieren sich diese Techniken auf die Kontrolle der amplifizierenden Strukturen. Ein tiefergehendes Studium der repellorbildenden Phasenraumstrukturen und ihrer Kontrolle eröffnet neue Möglichkeiten einer differenzierteren und effektiveren Kontrolle und kann von großem praktischen Interesse sein.

2 Introduction

The transition to turbulence in linearly stable flows is one of the unsolved problems in hydrodynamics. While big advances have been made in understanding linearly unstable flows like the Rayleigh-Bénard problem, i.e. the flow of a fluid layer heated from below, less is known about the transition in linearly stable flows, such as the Hagen-Poiseuille pipe flow and the plane Couette flow, where a fluid is sheared between two infinite parallel plates. In case of the plane Couette flow Romanov [93] has proven that the laminar flow is linearly stable for all Reynolds numbers. Similar results have been obtained by linear stability analysis of the Hagen-Poiseuille pipe flow [14, 35, 61, 102, 110]. However, both systems undergo a transition to turbulence if finite perturbations are introduced at sufficient high Reynolds numbers. Furthermore, even in linearly unstable flows, like the plane Poiseuille flow, the flow between two infinite parallel plates driven by constant pressure, and the Blasius boundary layer, i.e. the flow over a flat plate, a transition to turbulence can be observed at Reynolds numbers where both flows are linearly stable [67, 72].

It is the aim of this work to shed some light on this transition. I restrict my investigations to the plane Couette flow, which undergoes a transition to turbulence if finite perturbations are imposed. After I have introduced the system and the results obtained by other authors, I start with an investigation of the transition to turbulence of this flow. The lifetime of finite perturbations show a strong dependence on their shape and the Reynolds number, and all long living perturbations relax to the same turbulent state independent of their original shape. Some of them escape from this state and decays. This suggests that the turbulent state is a chaotic repellor, which attracts perturbations but repels them after some time.

In chapter 5, I investigate the bifurcation of stationary states. The different types of topologies of the stationary states are discussed and the states are classified by their symmetries. Since these stationary states might be responsible for the transition to turbulence, I study the heteroclinic and homoclinic flow in the vicinity of these states. The obtained results suggest that the turbulent state might be build up by the growing network of heteroclinic connections and homoclinic orbits.

In order to get a deeper insight of the formation of a chaotic repellor in a linearly stable shear flow, I study a low dimensional model consisting of 9 degrees of freedom, which show a

similar transitional behavior like the plane Couette flow. Finally the results are summarized and an outlook to further investigations is given.

3 The plane Couette flow

3.1 The plane Couette flow

One of the simplest shear flows is the plane Couette flow (Fig. 3.1), where a fluid is sheared between two infinite parallel plates. The gap width is d and the relative velocity of these plates equals $2\,U_0$. Measuring lengths in units of half the gap width $d/2$ and velocities in units of the velocity of one plate U_0, the laminar flow equals $\mathbf{U}_0 = z\,\mathbf{e}_x$. In these units the Reynolds number becomes

$$\mathrm{Re} = \frac{U_0 d}{2\nu}\,,$$

where ν is the kinematic viscosity. Throughout this work the advective timescale is used which is defined as $\frac{d}{2\,U_0}$.

3.2 Experimental realization

In order to realize the plane Couette flow experimentalists have to deal with two different problems: to exclude growing perturbations generated at the edges of the moving plates which travel into the system, the gap width must be significantly smaller than the spanwise and streamwise extension of the system. Furthermore, both plates should move because a mean flow decreases the accessible observation time. On the other hand, the assembly of a measuring device at one plate is only possible for a non moving plate. In case of two moving plates only laser-doppler anemometry and particle-image velocimetry are applicable. Furthermore, the preparation of a distinct disturbance is difficult if both plates move.

Different realizations are shown in figure 3.2. The first setup realized by Reichardt [86] (Fig. 3.2a) had only a small aspect ratio but used a counter moving belt. Unfortunately, the two cylinders driving the belt induce additional disturbances. Later realizations by Robertson [91], Robertson and Johnson [92], Leutheusser and Chu [58], and Ahydin and Leutheusser [1] (Fig. 3.2b-d) improved the aspect ratio and used only one moving plate to apply hot-wire anemometry.

In 1992 Tillmark and Alfredsson [101] set up an apparatus (Fig. 3.3) similar to the one used by Reichardt; but additional cylinders squeezed the moving belt and improved the aspect ratio.

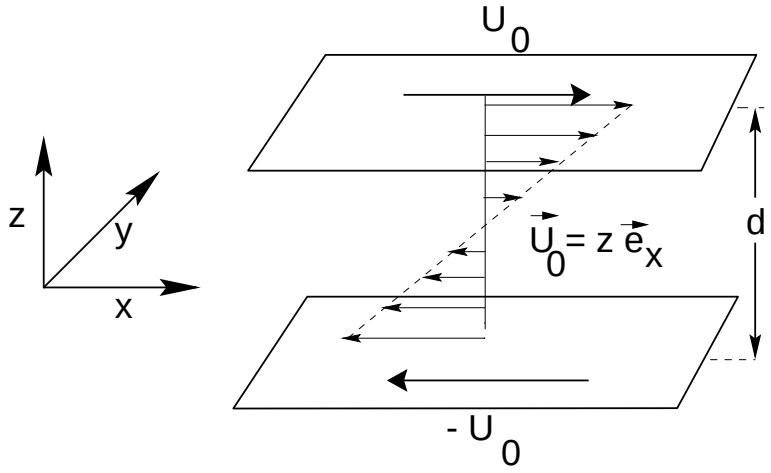

Figure 3.1: Sketch of the plane Couette flow geometry. Two infinite parallel plates shear a fluid between them. The gap width is d and the relative velocity of these plates equals $2\,U_0$.

All later investigations use this experimental architecture. Tillmark and Alfredsson used an aspect ratio of $1.50m : 0.36m : 0.01m$ (streamwise:spanwise:wall normal) [101]. The apparatus of Daviaud et al. was smaller but had a similar aspect ratio of $1.00m : 0.25m : 0.007m$ [11, 12, 32–34].

3.3 Former investigations of the plane Couette flow

3.3.1 Transition to turbulence

Experiments and numerical simulations show that the plane Couette flow undergoes a transition to turbulence if finite disturbances are introduced. The experiments done by Tillmark and Alfredsson [100, 101], Dauchot and Daviaud [32], and numerical investigations by Lundbladh and Johansson [62] focused on the evolution of spot like disturbances. These turbulent spots play an important role in bypass transition [90]. The bypass transition describes the transition to turbulence of a Blasius boundary layer in cases where the flow is linearly stable and the transition via Tolmien-Schlichting waves [35, 61] is not possible. In these cases one observes a fast spreading of the localized disturbance and a turbulent state in which streamwise streaks and vortices dominate the flow [2, 51, 53, 67].

For different experimental setups and different types of disturbances the critical Reynolds number, i.e. the Reynolds number where the first transition to turbulence can be observed, varies. Ahydin and Leutheusser observed a transition near $Re_c = 280$ [1]. By inducing jet-like perturbations Daviaud et al. measured $Re_c \sim 370$ [34], Bottin et al. $Re_c \sim 328$ [12], and Tillmark and Alfredsson $\mathrm{Re} = 360 \pm 10$ [101]. Lundbladh and Johansson [62] found in numerical simulations $Re_c \sim 375$. Furthermore, Daviaud, Hegseth and Bergé observed

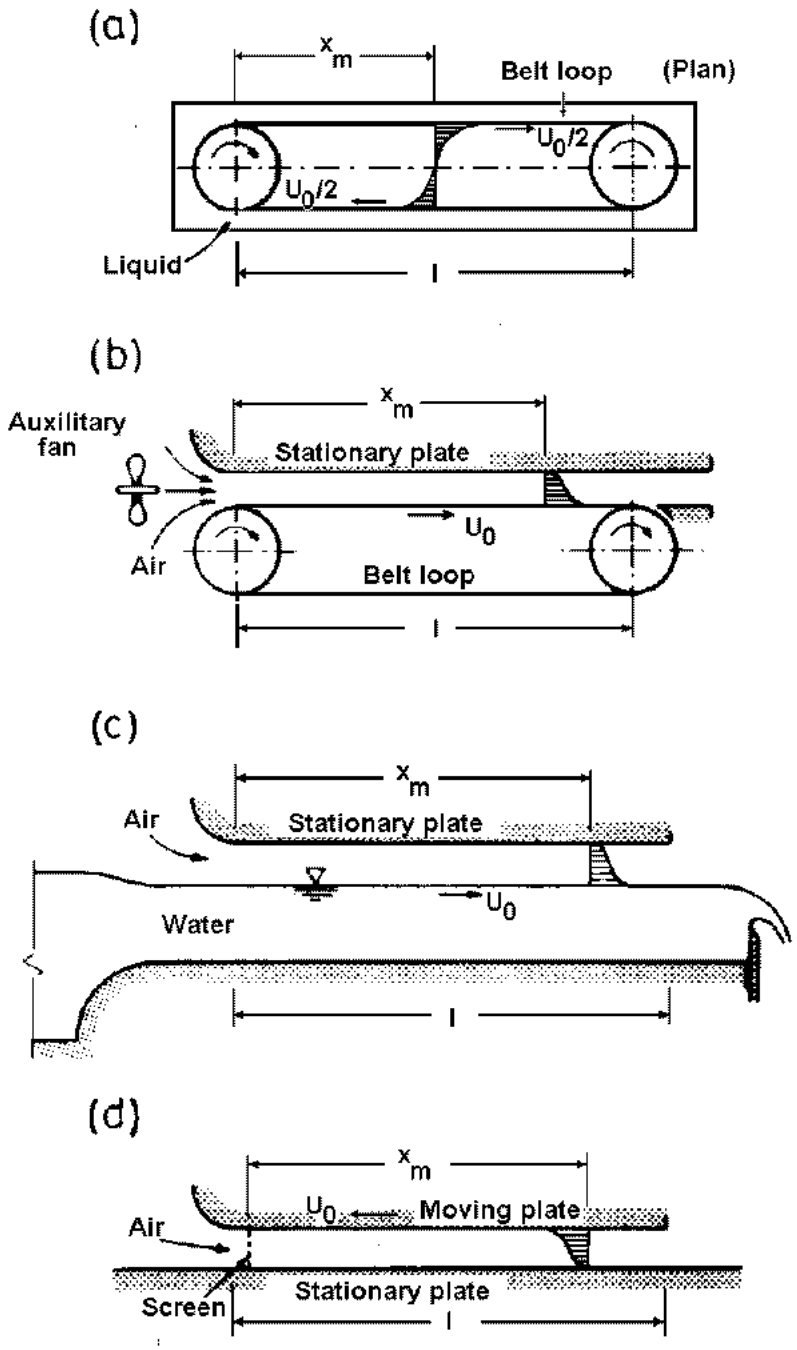

Figure 3.2: Different experimental realizations of the plane Couette flow. x_m describes the region of measurements [1].

a) Reichardt et al. [86]: $l = 2.00\text{m}$, $x_m = 1.00\text{m}$, $u_{0,\max} = 0.26\frac{\text{m}}{\text{s}}$

b) Reichardt et al. [87]: $l = 10.20\text{m}$, $x_m = 9.50\text{m}$, $u_{0,\max} = 9.00\frac{\text{m}}{\text{s}}$;
Robertson et al. [91, 92]: $l = 2.30\text{m}$, $x_m = 2.03\text{m}$, $u_{0,\max} = 21.34\frac{\text{m}}{\text{s}}$

c) Leutheusser and Chu [58]:$l = 7.32\text{m}$, $x_{m,\max} = 7.01\text{m}$, $u_{0,\max} = 3.00\frac{\text{m}}{\text{s}}$

d) Ahydin and Leutheusser [1]: $l = 2.30\text{m}$, $x_{m,\max} = 1.84\text{m}$, $u_{0,\max} = 3.04\frac{\text{m}}{\text{s}}$

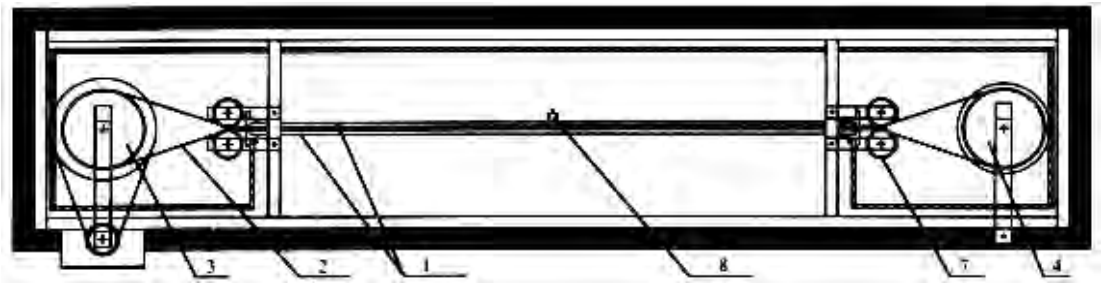

Figure 3.3: Experimental setup used by Tillmark and Alfredsson [101].

growing variations in the lifetime of perturbations near the critical Reynolds number [34].

These experimental observations indicate the existence of a turbulent state at some Reynolds number between 280 and 380 but little is known about the mechanism of this transition.

3.3.2 Coherent structures

Investigations of the turbulent state approached by bypass transition in the Blasius boundary layer at Reynolds numbers where the flow is linearly stable show the dominance of specific flow structures [50, 51, 67, 90]. These structures consist of streamwise streaks and streamwise vortices. Such coherent structures can also be observed in plane Couette flow [62, 100, 101]. In order to stabilize the observed streamwise streaks and streamwise vortices Bottin et al. modified the plane Couette flow by spanning a wire in the neutral plane along the spanwise direction. The streaks stabilized by this method were extended along the streamwise direction and periodic in the spanwise direction. They started to form at a Reynolds number of 160 and became unstable at 325, where a turbulent state established [12]. Barkly and Tuckerman tried to reproduce these results numerically [6]. They used a spectral element code and performed a two dimensional and three dimensional stability analysis of this modified Couette flow. Though the values for the first Reynolds number differ from the experimental values, they obtained a similar flow structure.

In their numerical investigations of the turbulent plane Couette flow, at a Reynolds number of 750, Lundbladh, Johansson and Komminaho studied coherent structure in a very large computational domain [55]. They observed large-scale elongated structures similar to the one observed by Dauchot et al. [32].

The origin of these coherent structures is yet unknown. They might be connected to the formation of nonlinear finite amplitude solutions of the steady Navier-Stokes equation. Nagata [68] and Busse and Clever [26] found such solutions born in a saddle-node bifurcation at $\mathrm{Re} = 129$. The node undergoes a hopf bifurcation at $\mathrm{Re} = 135$ and becomes linearly unstable. These states have been found by changing the flow geometry from the Couette-Taylor

flow [68] or Rayleigh-Bénard flow [26] to the plane Couette flow. At Reynolds numbers of about 1000 Cherhabili and Ehrenstein found additional solutions [21, 22] by investigating a plane Couette-Poiseuille flow. Similar investigations were done by Balakumar [5]. These states look different from the one observed by Nagata, Busse and Clever, which consists of streamwise vortices and streamwise streaks. The states found by Cherhabili, Ehrenstein and Balakumar are localized along the streamwise direction and have strong vortices at the walls.

3.3.3 Theoretical work on the transition

Although experiments prove that plane Couette flow can become turbulent the theoretical understanding is still rather limited. Linear stability analysis of the laminar flow field shows that it is linearly stable for all Reynolds numbers [93]. Watson [108] and later Ellingsen, Gjevik and Palm [40] performed a weakly nonlinear stability analysis of the laminar flow. For Reynolds numbers above 10^3 they were able to predict the existence of a threshold amplitude which scales like $(\alpha \mathrm{Re})^{-\frac{2}{3}}$ where α refers to the spatial periodicity.

Trefethen et al. [103] and Gebhardt and Grossmann [43] argued that the non normality of the linearized evolution equation can explain how a transition can occur though the laminar profile is linearly stable. The non normality is able to amplify an infinitesimal disturbance up to finite size though the linear operator has no unstable eigenmodes. Reddy and Hennigson [2, 85] and Butler and Farrell [17] investigated these amplification rates in case of plane Couette and plane Poiseuille flow and also in Blasius boundary layer. In pipe flow, which is also linearly stable for all Reynolds numbers, Boberg and Brosa identified the flow structures representing the effects of this non normal amplification [9]. If the disturbance has grown to finite size the nonlinearity can no longer be ignored. New effects take place which are not accessible via linear or weakly nonlinear analysis of the laminar flow field (see also [47]).

Some authors focus on the energy transfer in the turbulent motion. Since the linear terms of the linearized Navier-Stokes equation amplify energy and the nonlinear terms conserve energy, low dimensional models have been derived which consist of a non normal linear and an energy conserving nonlinear part [4, 43, 106]. These models illustrate the non normal amplification and the nonlinear redistribution of energy.

The interpretation of these results in terms of hydrodynamical systems was given by Waleffe et al. [41, 105, 107]. They interpret the turbulent motion as a self sustained process. In this process streamwise vortices amplify the streamwise streaks; these streaks perform a linear breakdown and their energy is transfered by nonlinear interactions. This energy transfer has been studied by Reddy [84] in a full DNS-code, with a reduced resolution in the spanwise and streamwise direction. It turns out that the mean flow plays an important role in the self sustaining process. Though this flow is not able to gain energy via the non normal

amplification it profits from the nonlinear redistribution of energy. Other modes benefit from this saved energy by a later nonlinear transport.

In the same spirit of Reddy's work Brosa and Grossmann [16] reduced the degrees of freedom of the Hagen-Poiseuille flow to the most relevant modes. They observed that almost 48 degrees of freedom are needed to sustain turbulent motions in pipe flow.

3.4 Equations of motion, their symmetry and numerical representation

3.4.1 Equations of motion

The problem is formulated in its dimensionless form. Lengths are measured in units of half the gap width $d/2$ and velocities in units of the velocity of one plate U_0. The turbulent flow field is decomposed into its laminar time independent part $\mathbf{U}_0 = z\,\mathbf{e}_x$ and a time dependent perturbation with a finite amplitude $\mathbf{u} = (u, v, w)$. The evolution equation for this disturbance follows to

$$\frac{\partial}{\partial t}\mathbf{u} = -(\mathbf{u}\cdot\nabla)\,\mathbf{u} - z\frac{\partial}{\partial x}\mathbf{u} - w\,\mathbf{e_x} - \text{grad}\,p + Re^{-1}\Delta\mathbf{u}\,, \tag{3.1}$$

where the Reynolds number is defined as

$$\mathrm{Re} = \frac{U_0 d}{2\nu}\,.$$

The incompressible disturbance $\mathbf{u}$ must fulfill the continuity equation,

$$\text{div}\,\mathbf{u} = 0\,, \tag{3.2}$$

and the boundary conditions,

$$\mathbf{u}|_{z=\pm1} = 0\,. \tag{3.3}$$

The flow is assumed to be periodic along the streamwise and spanwise direction. $L_{x,y}$ are the streamwise and spanwise lengths of the periodic box. Beside this discrete symmetry these equations conserve four additional basic symmetries:

$$\mathcal{P}: \begin{pmatrix} u \\ v \\ w \end{pmatrix}(x,y,z) = \begin{pmatrix} -u \\ -v \\ -w \end{pmatrix}(-x,-y,-z) \tag{3.4}$$

$$\mathcal{R}: \begin{pmatrix} u \\ v \\ w \end{pmatrix}(x,y,z) = \begin{pmatrix} u \\ -v \\ w \end{pmatrix}(x,-y,z) \tag{3.5}$$

$$\mathcal{T}_{\Delta x,\Delta y}: \begin{pmatrix} u \\ v \\ w \end{pmatrix}(x,y,z) = \begin{pmatrix} u \\ v \\ w \end{pmatrix}(x+\Delta x, y+\Delta y, z) \tag{3.6}$$

$\mathcal{P}$ corresponds to a point reflexion at $\mathbf{x} = (0,0,0)$, $\mathcal{R}$ equals a reflexion at the x,z-plane, and $\mathcal{T}_{\Delta x,\Delta y}$ are translations along the streamwise or the spanwise direction.

3.4.2 The NBC and the I symmetry groups

To simplify the investigation of nontrivial finite amplitude solutions in the plane Couette flow I reduced the phase space to members of two different symmetry groups. The first one, the NBC-group, corresponds to the symmetry group investigated by Nagata [68] and Busse and Clever [26, 27] where the first pair of stationary states bifurcates at $\mathrm{Re} = 129$. The NBC group consists of four elements: the unity **1**, the two symmetry operations $\mathcal{W}$ and $\mathcal{V}$, and the combination of both $\mathcal{WV}$. $\mathcal{W}$ and $\mathcal{V}$ are defined as:

$$\mathcal{W}: \begin{pmatrix} u \\ v \\ w \end{pmatrix}(x,y,z) = \begin{pmatrix} u \\ -v \\ w \end{pmatrix}(x + L_x/2, -y, z) \tag{3.7}$$

$$\mathcal{V}: \begin{pmatrix} u \\ v \\ w \end{pmatrix}(x,y,z) = \begin{pmatrix} -u \\ v \\ -w \end{pmatrix}(-x, y + L_y/2, -z)\ . \tag{3.8}$$

$\mathcal{W}$ refers to the waviness of the stationary states found in the Rayleigh-Bénard system and the Couette-Taylor flow [25, 26]. It supports an additional shear along the streamwise direction, where stationary states can benefit from. The $\mathcal{V}$ symmetry supports counter rotating vortices which transport high speed fluid from the wall region into the bulk. These two symmetries are combined in a way that stationary streaks benefit from both processes. $\mathcal{W}$ induces sheared streaks and $\mathcal{V}$ induces streamwise vortices, which transport the high-speed fluid into these streaks.

The NBC group supports streaks of equal width in the periodic box. To allow streaks of different width or even localized streaks I also investigate the I group. It is formed by the symmetry operations $\mathcal{P}$, the point reflexion at $\mathbf{x} = (0,0,0)$, and $\tilde{\mathcal{R}}$, a reflexion symmetry at $y = \frac{L_y}{4}$,

$$\mathcal{P}: \begin{pmatrix} u \\ v \\ w \end{pmatrix}(x,y,z) = \begin{pmatrix} -u \\ -v \\ -w \end{pmatrix}(-x,-y,-z) \tag{3.9}$$

$$\tilde{\mathcal{R}}: \begin{pmatrix} u \\ v \\ w \end{pmatrix}(x,y,z) = \begin{pmatrix} u \\ -v \\ w \end{pmatrix}(x, -y - L_y/2, z)\ , \tag{3.10}$$

the unity **1**, and the combination $\mathcal{P}\tilde{\mathcal{R}}$. $\mathcal{P}$ supports the formation of the streamwise vortices

but there is no spanwise correlation between these vortices. $\tilde{\mathcal{R}}$ supports the formation of streamwise streaks with a width of $L_y/4$.

3.4.3 The numerical representation

For the numerical representation of the flow field $\mathbf{u}$ is expanded in Fourier modes in the spanwise and streamwise directions and normalized Legendre polynomials $\phi_p(z)$ in the wall normal direction:

$$\mathbf{u}(\mathbf{x},t) = \sum_{n_x,n_y,p} \tilde{\mathbf{u}}_{n_x,n_y,p}(t) \exp\left(2\pi\, i \left(\frac{n_x x}{L_x} + \frac{n_y y}{L_y}\right)\right) \phi_p(z)\,. \tag{3.11}$$

L_x and L_y are the spanwise and streamwise lengths of the integration domain. Following Nagata [68] and Busse and Clever [27] I take $L_x = 2\pi\, d$ and $L_y = \pi\, d$. The wave vectors in these directions are constrained by $|n_x| + |n_y| \leq N$. I use $N = 6$ in my simulations. The maximum order N_z of Legendre polynomials used is $N_z = 9$ in the dynamical observations (chapter 4) and $N_z = 15$ for investigations of stationary states (chapter 5) and the chaotic repellor (chapter 6).

The conditions at the boundary (3.3) and on the divergence (3.2) are linear constraints and are accounted for by applying projections onto the allowed subspaces. These projections conserve energy and have to be applied to both the initial conditions and the equations of motion, where for the latter the Lagrange formalism of the first kind, familiar from classical mechanics, was used [44]. More details on the numerics are given in appendix A. See also appendix B for the spectral implementation of the investigated symmetries.

The code was tested and verified in three ways: I confirmed energy conservation in the Eulerian undriven case and checked the critical Reynolds number and stability of the steady states found by Nagata [68] and Busse and Clever [27]. The stability test required an increase in the number of Legendre polynomials to $N_z = 15$ but other aspects of the dynamics (fluctuations in mean energy and shear rate, for instance) did not change. Therefore most of the simulations presented here were done with $N_z = 9$ and thus 1192 independent and dynamically active degrees of freedom were used. I am confident that I can follow the time evolution up to a time of about $t_{\max} = 10000$ without changing the energy more than 0.01% using an Adams-Bashford method with an accuracy of 10^{-8}. For $d = 1$ cm, the viscosity of water $\nu = 0.01\frac{\mathrm{cm}^2}{\mathrm{s}}$, and a Reynolds number of $\mathrm{Re} = 400$ this corresponds to about 10 min.

For $N_z = 9$ and a numerical accuracy of 10^{-4} the numerical integration over a time interval of 100 time units needs on a DEC Alpha 500 workstation about 3 minutes CPU time. Using $N_z = 15$, which corresponds to 2212 active degrees of freedom, this integration takes about 14 minutes CPU time.

4 Transition of finite perturbations in plane Couette flow

Hätte ich zu Wardhöus einen Kirschkern in die See geworfen,
so hätte der Tropfen Seewasser den Myn Herr
am Kap von der Nase wischt nicht gnau an dem Ort gesessen.

G. C. Lichtenberg, D 54[60]

In this chapter the evolution of different finite perturbations in plane Couette flow is investigated. It will be shown that the lifetime of a finite perturbation for a fixed Reynolds number depends sensitively on its shape. Instead of connecting the transition to turbulence in plane Couette flow with a critical Reynolds number where a first transition can be observed it is more practical to define the *transitional Reynolds number* $\mathrm{Re}_{\mathrm{tr}}$ in a statistical sense. I will give an operational definition and calculate values of the transitional Reynolds number for different types of perturbations which vary between 305 and 320.

Three different types of states have been observed: linear and nonlinear transients and turbulent states. For different perturbations the statistical properties of the nonlinear transients and the turbulent state are the same. This suggests that the transition to turbulence is connected with the appearance of a chaotic repellor, which attracts perturbations, allows a chaotic motion on it, and repels them after some time. I will calculate some quantities of this chaotic repellor, namely the two time scales connected with such a repellor: the escape rate ϵ and the relaxation rate η. The first one gives information about the average lifetime of a state on this repellor. The latter contains information about the timescale needed to approach it. Its location in phase space will be estimated by calculating the distribution of the shear rate and the energy.

In order to follow turbulent states down to Reynolds numbers below the transitional Reynolds number, I performed annealing experiments. In these experiments the Reynolds number is slowly decreased, while the turbulent state follows the movement of the repellor. I will introduce the *annealing Reynolds number* $\mathrm{Re}_{\mathrm{anneal}}$, which gives the lower bounds for which turbulent motions can be followed down by these experiments.

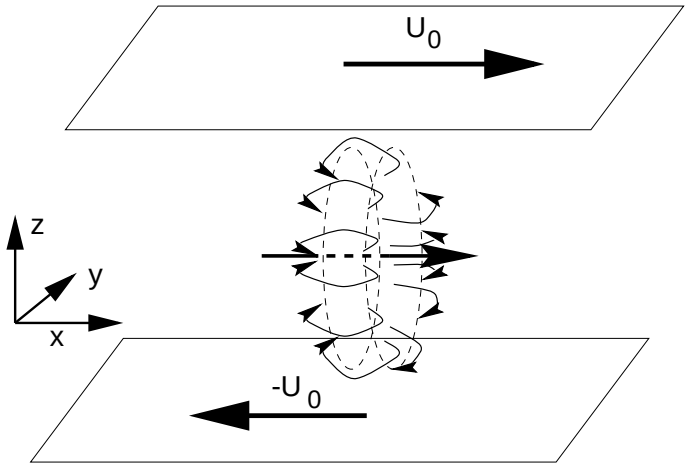

Figure 4.1: Sketch of a closed vortex filament with streamwise orientation.

4.1 Finite perturbations

I chose two different classes of perturbations, one initially imposed and the other dynamically induced. The first class consists of a closed vortex filament, the second class uses a body force that is slowly turned on and off for a finite time interval.

4.1.1 Finite vortex structures

It is known that for Reynolds number below 1000 transitional perturbations have to be intrinsically three dimensional [80]. A simple three dimensional flow structure is a closed vortex filament $\mathbf{u}(t=0) = \text{curl curl } (f(\mathbf{x})\mathbf{e})$, where the vector $\mathbf{e}$ is perpendicular to the area closed by the filament and corresponds to its orientation. Such a filament consists of vortices arranged on a torus (see Fig. 4.1). I chose

$$f(\mathbf{x}) = A\, e^{-\sigma(x^2+y^2+z^2)}\,,$$

where $\sigma = 8$. Such a vortex filament is localized in the streamwise and spanwise direction, but rather extended in the wall normal direction. The vortex filament was orientated along the streamwise, the spanwise or the wall normal direction, i.e. $\mathbf{e} = \mathbf{e}_{x,y,z}$.

These filaments preserve the $\mathcal{P}$ (3.4) and the $\mathcal{R}$ (3.5) symmetry of the Navier-Stokes equation (3.1). These symmetries are not broken by rotating the vortex filament as it was the case in the investigations of Lundbladh and Johansson [62]. Furthermore, the vortex filaments are normalized to the energy of the wall normal velocity w.

A closed vortex filament advects itselves along its axis [94]. The laminar flow shears and stretches it. The shear causes a rotation of the filament in the x,z-plane. Therefore a vortex filament initially orientated along the streamwise direction becomes similar to a vortex filament with a wall normal orientation. In both cases the self advection of the vortex filament

moves it into the wall region, where the vortices are able to transport high speed fluid from the wall region into the bulk.

The orientation of the vortex filament does not change if it is initially orientated along the spanwise direction. In this case the filament advects itself along the spanwise direction and not into the wall region. The stretching also leads to streamwise vortices and the advection amplifies the momentum transport from the boundary flow into the bulk.

4.1.2 Injected perturbations

In the experiments of Tillmark and Alfredsson [101], Daviaud, Hegseth and Bergé [34], Daviaud and Dauchot [32], and Malerud, Mâløy and Goldburg [63] the perturbation was induced by injecting water through a hole in the moving belt.

This perturbation corresponds to the application of a pulse acting in a small region near the wall affecting the velocity normal to the wall. It can be modeled by adding a time dependent volume force to the equation of motion (3.1), reading

$$\frac{\partial \mathbf{u}}{\partial t} = \mathbf{N}(\mathbf{u}) + f(t)\,\mathbf{F}(\mathbf{x}) \ . \tag{4.1}$$

$\mathbf{N}$ refers to the right hand side of the evolution equation (3.1). $f(t)$ fades the volume force in and out. For $0 \leq t \leq t_{\text{in}}$ it equals

$$f(t) = A_0 \left(\sin\left(\pi \left(2\,\frac{t}{t_{\text{in}}} - \frac{1}{2} \right) \right) + 1 \right) , \tag{4.2}$$

where A_0 is the maximum amplitude and t_{in} the time of injection. Two different kinds of injection forces $\mathbf{F}(\mathbf{x})$ have been used. The first one corresponds to a localized injection at one of the plates. The analytical form of the z-component is

$$F_z(\mathbf{x}) = e^{-\sigma\left(x^2+y^2\right)-\sigma_z(z+1)} , \tag{4.3}$$

with $\sigma = 32$ and $\sigma_z = 20$. The other components are also non-zero after projecting onto the divergence free subspace (see appendix A). In order to break the $\mathcal{P}$ symmetry no outflow at the opposite wall has been modeled. This force produces a localized vortex region, which contains most of the induced energy.

Figure 4.2 displays the evolution of the flow field at $\mathrm{Re} = 400$ for $t > t_{\text{in}} = 4$ in the $y = 0$ plane. Contours show the local energy $E = \frac{1}{2}\left((u+U_0)^2 + v^2 + w^2\right)$ of the fluid. The volume force generates a small region of high speed fluid within the boundary layer. This localized region is lifted into the bulk and generates spanwise vortices.

In order to break the $\mathcal{R}$ symmetry of the system a volume force with inflow and outflow in the wall region is used. It was modeled by performing a sine-transformation on the Fourier

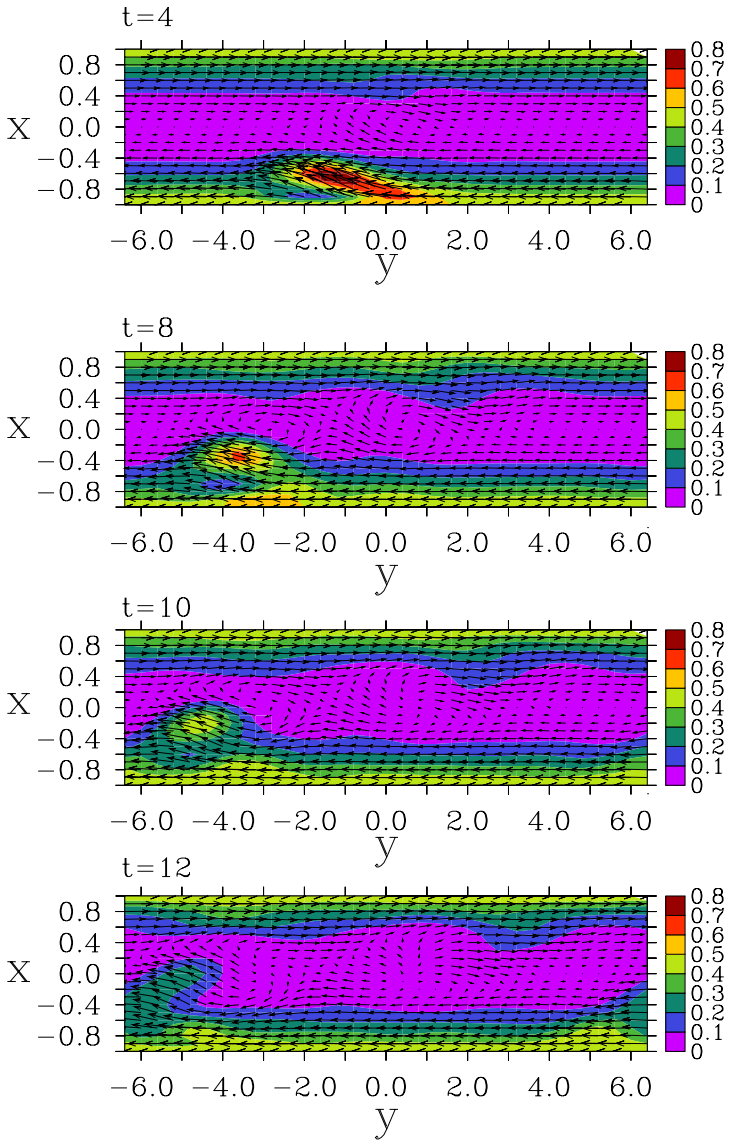

Figure 4.2: Evolution of the time dependent (4.3) perturbation at $\mathrm{Re} = 400$ for $t > t_{\mathrm{in}}$ at $t = 4, 6, 8, 10$. The arrows are the streamwise and wall normal component of $\mathbf{u} + \mathbf{U}_0$, the contour plot is the local kinetic energy $\frac{1}{2}(u + U_0)^2 + v^2 + w^2$.

components of the symmetric disturbance (4.3). Its analytical form is

$$\begin{aligned} F_z(\mathbf{x}) &= e^{-\sigma x^2 - 20(z+1)} \\ &\quad \cdot \int_0^\infty \mathrm{d}\,\tilde{\omega} \int_0^\infty \mathrm{d}\,\omega e^{-\sigma\,\omega^2} \cos(\omega\tilde{\omega}) \sin(\tilde{\omega} y)\, \mathbf{e}_z \\ &= e^{-\sigma x^2 - 20(z+1)} \\ &\quad \cdot \int_0^\infty \mathrm{d}\,\tilde{\omega} \frac{1}{2} \sqrt{\frac{\pi}{\sigma}} e^{-\frac{\tilde{\omega}^2}{4\sigma}} \sin(\tilde{\omega} y)\, \mathbf{e}_z \\ &= \sqrt{\pi} e^{-\sigma\left(y^2+x^2\right) - 20(z+1)} \int_0^{\sqrt{\sigma} x} \mathrm{d}\,\tilde{y}\, e^{-\tilde{y}^2} \mathbf{e}_z\,. \end{aligned} \tag{4.4}$$

4.2 Transition to turbulence

4.2.1 Different types of dynamical behavior

There are three different types of dynamical behavior [96, 97]: linear transients, nonlinear transients and turbulent states. They can be distinguished by investigating the temporal behavior of the energy density of the perturbation, expressed in terms of the energy of the laminar flow field E_0

$$E = \frac{1}{2V\,E_0}\int \mathbf{u}\cdot\mathbf{u}^*\,\mathrm{d}V \tag{4.5}$$

and the shear rate of the full flow field

$$S = \frac{1}{A}\int \frac{\partial}{\partial\, z}\,(u+z)\,|_{z=1}\,\mathrm{d}A\,. \tag{4.6}$$

If the amplitudes are sufficiently small the Navier-Stokes equation can be linearized and the perturbation decay with rates calculated earlier by Reddy and Hennigson [85]. Typical traces of the energy density and the shear rate are shown in figure 4.3a. Since the wall normal velocity transfers energy into the streamwise component the perturbation is able to gain energy until the former vanishes. This is the effect of the non normality of the linearized equations of motion [9, 43, 103] (see also chapter 5.4.2 for more details). The energy content of a perturbation will thus not decay monotonically but perhaps with a hump. If the amplitude in the wall normal component is sufficiently small the energy content will continue to decay monotonically. This allows to define the lifetime of a perturbation as the time it takes for the energy to decay below a threshold that a perturbation cannot recover. In the following investigations this limit was an energy in the wall normal component of 10^{-4}.

For larger amplitudes and Reynolds numbers a different behavior is observed. The perturbation can recover from a decay and a nonlinearly sustained oscillatory behavior occurs (see Fig. 4.3b). Energy is continually shifted between the components, but the lifetimes for all perturbations are finite since at some stage the energy content in the wall normal component drops below the critical value for regeneration. For slightly higher values of the Reynolds number and sufficiently large amplitudes of the perturbation the lifetimes seem to grow indefinitely (see Fig. 4.3c).

Later it will be shown that the properties of these turbulent states equal the properties of the nonlinear transients. In view of the large computing times the calculations were limited to $t_{max} = 3000$.

4.2.2 Lifetimes of perturbations

The figures 4.4, 4.5 and 4.6 show the lifetimes for perturbations orientated in the downstream, spanwise and wall normal direction, respectively, calculated on a dense grid of points in the

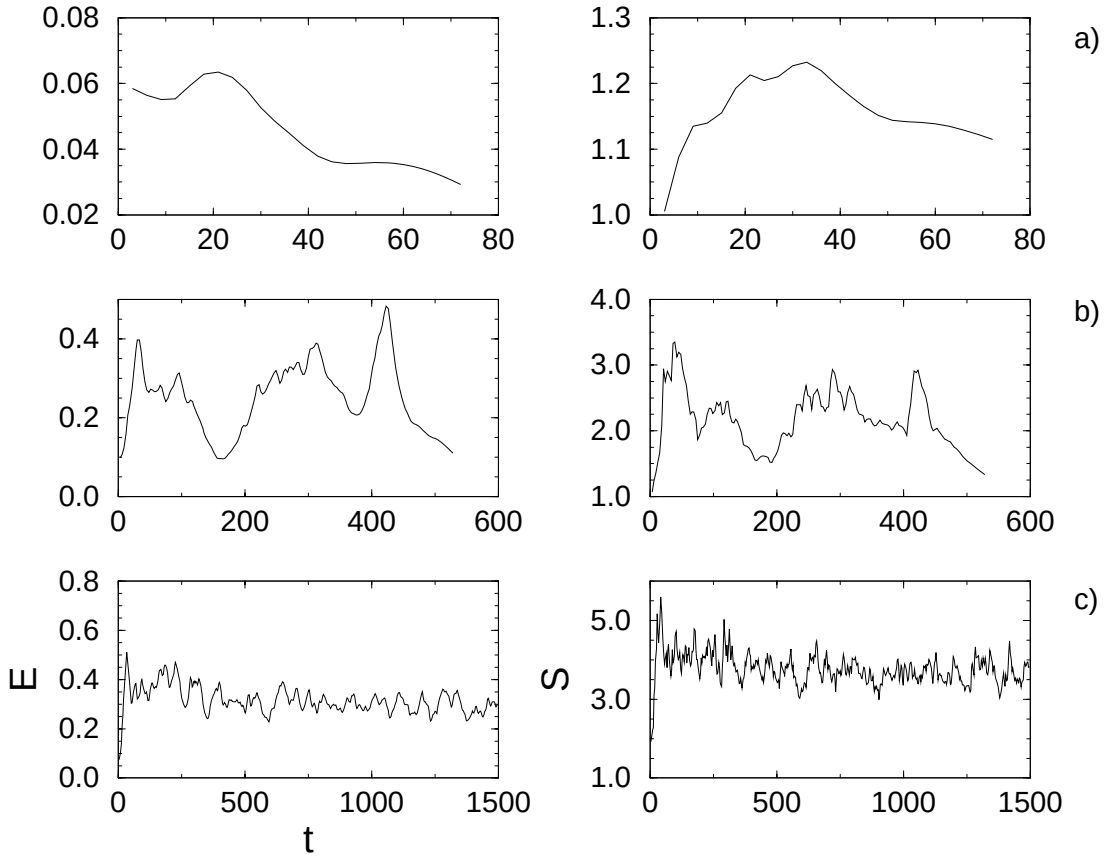

Figure 4.3: Time signals of energy (left column) and shear rate (right column) for the same initial state at Reynolds numbers 200, 300 and 400 (top to bottom). There are three different types of dynamical behavior: linear and nonlinear transients and turbulent dynamics. Note the different scales of both axes.

amplitude vs. Reynolds number plane. The location and width of the transition region differ for the three orientations of the filaments. The details of the pictures depend on the specific choice of the grid since a magnification shows large fluctuations due to small variations in amplitude and Reynolds number (Fig. 4.7). This strong dependence of the lifetime on the shape of the disturbance and the Reynolds number seems to be a generic feature of the transition in linearly stable shear flows [96]. It has been also observed by Darbyshire and Mullin in pipe flow [31] and Eckhardt and Mersmann in a low dimensional model of a linearly stable shear flow [38] (See also chapter 7 for more details on this model). To illustrate this feature, successive magnifications of amplitude and Reynolds number for a strongly localized filament $f(\mathbf{x}) = \delta(x, y)e^{-10z^2}$ with a streamwise orientation is shown in figure 4.8. The δ-function was approximated by setting the real parts of all Fourier-coefficients to one. These measurements were done using an aspect ratio of $d : 2\pi\, d : 2\pi\, d$ (wall normal: streamwise: spanwise), where the repellor is rather thin at $\mathrm{Re} = 400$.

In case of a streamwise orientated filament only linear transients are observed for Reynolds

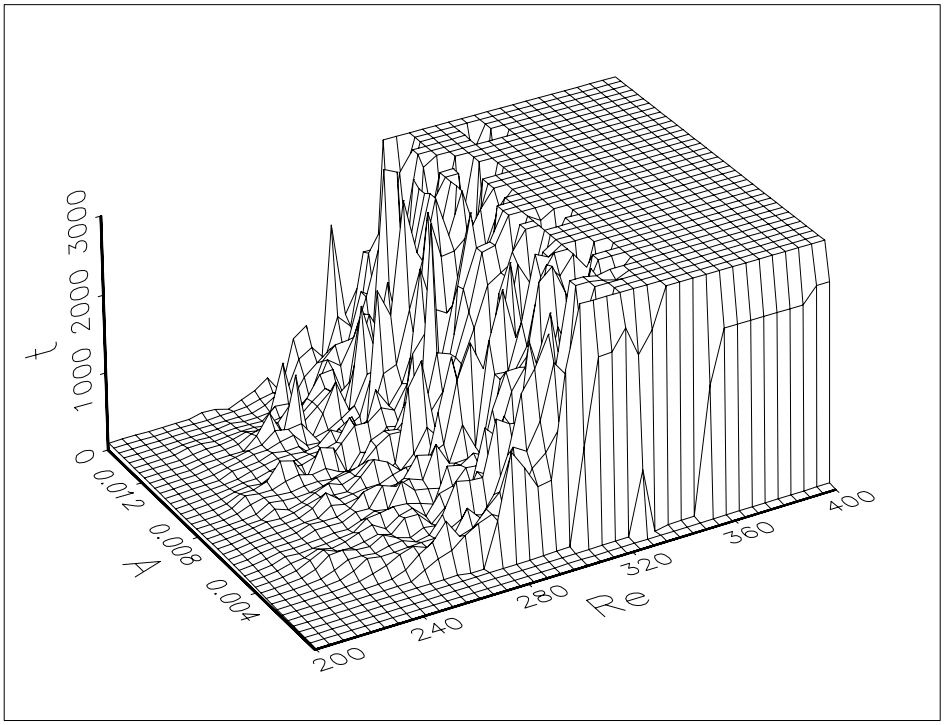

Figure 4.4: Lifetime of a streamwise orientated vortex filament for different values of the amplitude and Reynolds number.

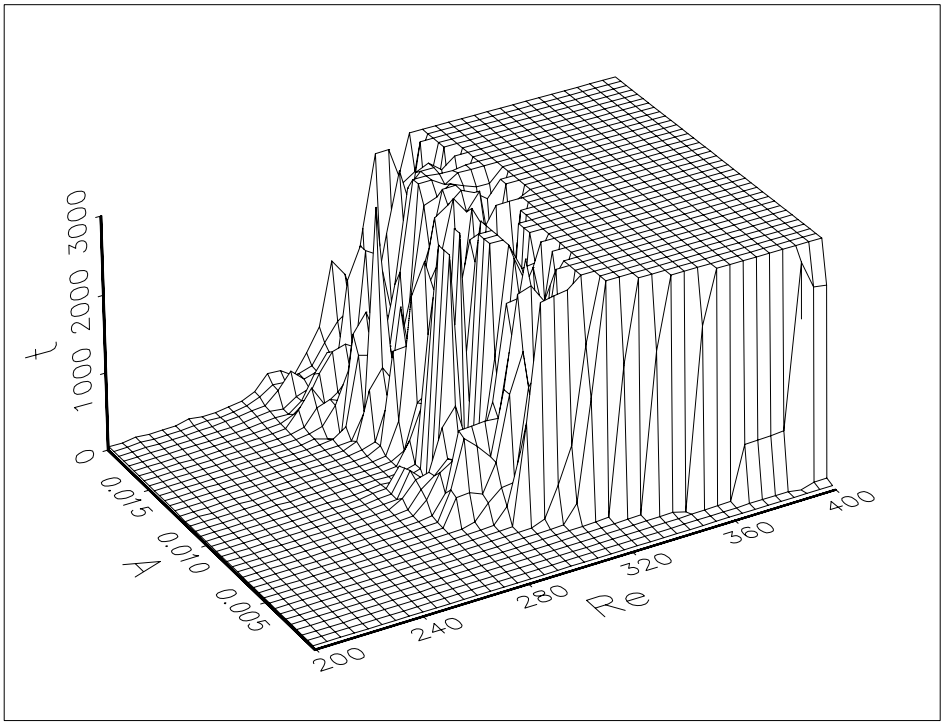

Figure 4.5: Lifetime of a vortex filament orientated along the wall normal direction for different values of the amplitude and Reynolds number.

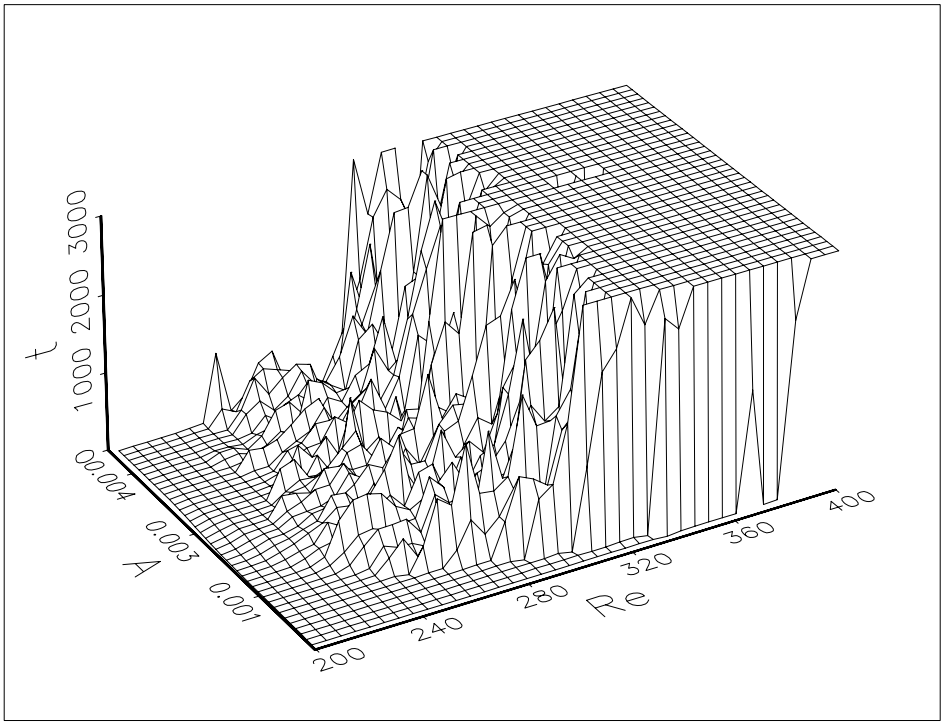

Figure 4.6: Lifetime of a spanwise orientated vortex filament for different values of the amplitude and Reynolds number.

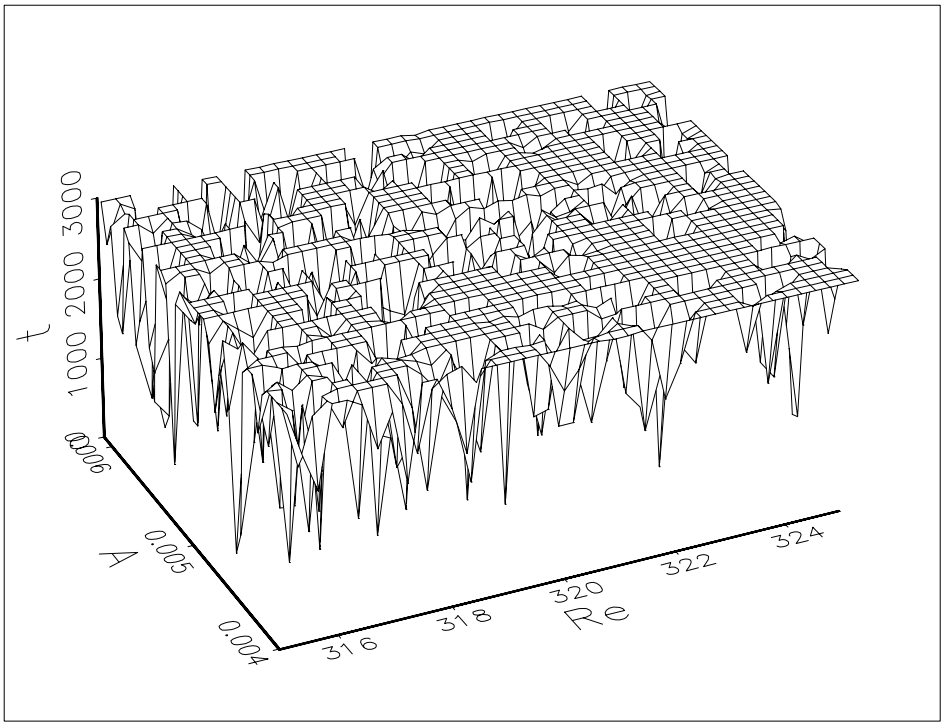

Figure 4.7: Magnification of a small subset of Fig. 4.4.

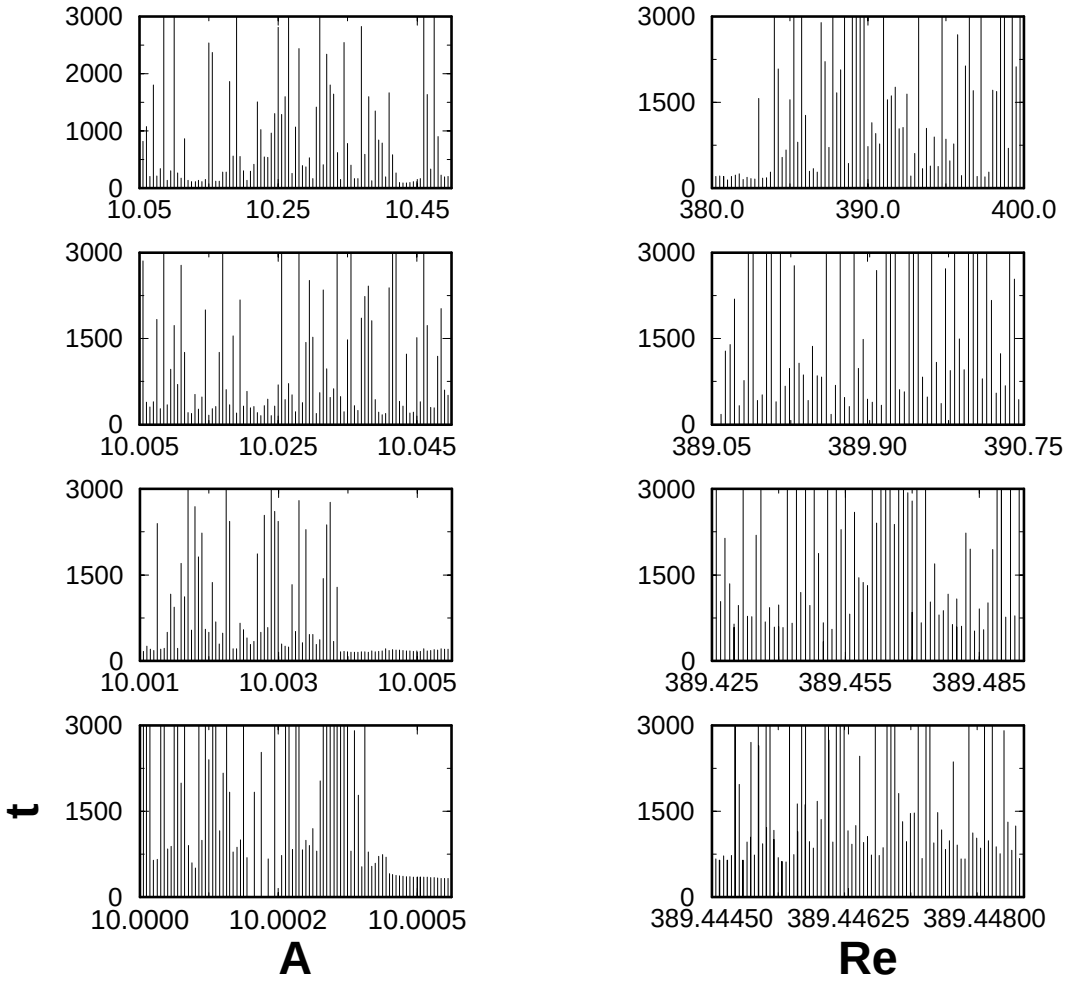

Figure 4.8: Successive magnifications of cuts through the lifetime distribution for $\mathrm{Re} = 380$ and varying amplitude (left column) and fixed $A = 10$ and varying Reynolds number (right column). These calculations have been done in an aspect ratio of $d : 2\pi\, d : 2\pi\, d$ (wall normal:spanwise: streamwise) with $f(\mathbf{x}) = \delta(x, y)e^{-10z^2}$ [96].

numbers below 220, then up to $\mathrm{Re} = 320$ the nonlinear transients dominates the dynamic. The appearance of nonlinear transients and turbulent states depends not only on the energy of the wall normal velocity but also on the shape of the perturbation. A spanwise orientated filament shows nonlinear transients at $\mathrm{Re} \approx 240$ with larger lifetimes for amplitudes which are four times smaller. The filament with a wall normal orientation shows only a very small region where nonlinear transients occur, starting at $\mathrm{Re} \approx 270$. The similar lifetimes for streamwise and wall normal orientated filaments are plausible since a streamwise orientated vortex filament is quickly rotated along the wall normal direction.

The lifetime distributions suggest that the number of long lived initial conditions increases with Reynolds number. The median and the maximal lifetime of each vortex filament are

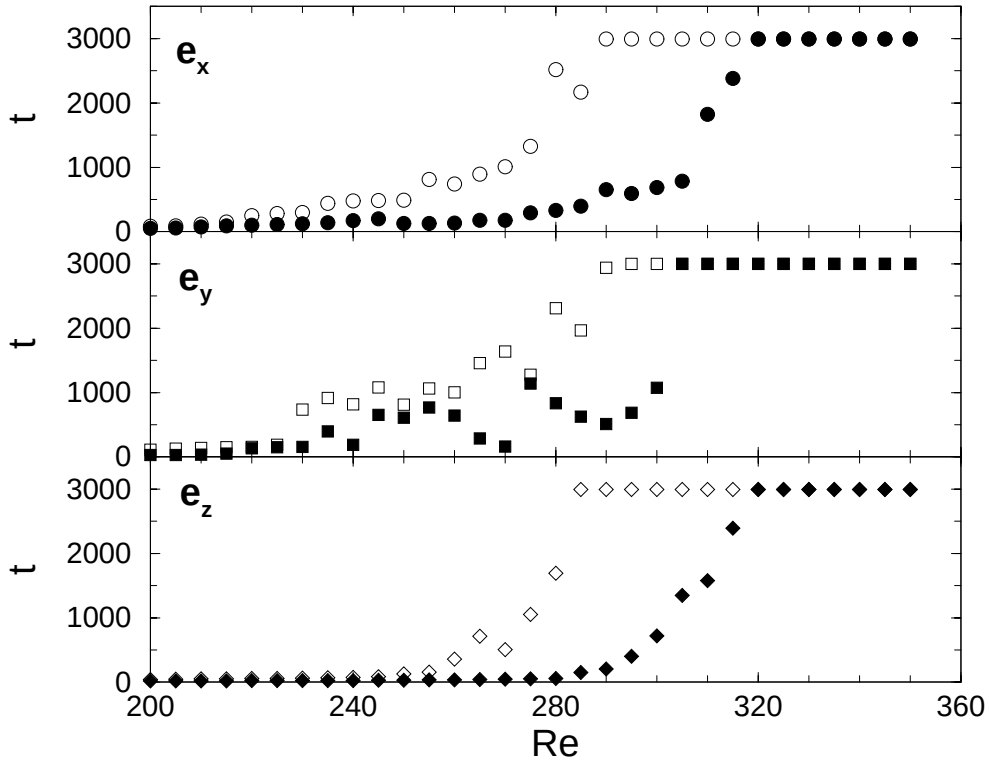

Figure 4.9: Median of the lifetimes that entered figures 4.4, 4.5 and 4.6 (filled symbols) and the observed maximum lifetime for fixed Reynolds number and different amplitudes (open symbols). $\mathbf{e}_{x,y,z}$ corresponds to the orientation of the introduced vortex filament.

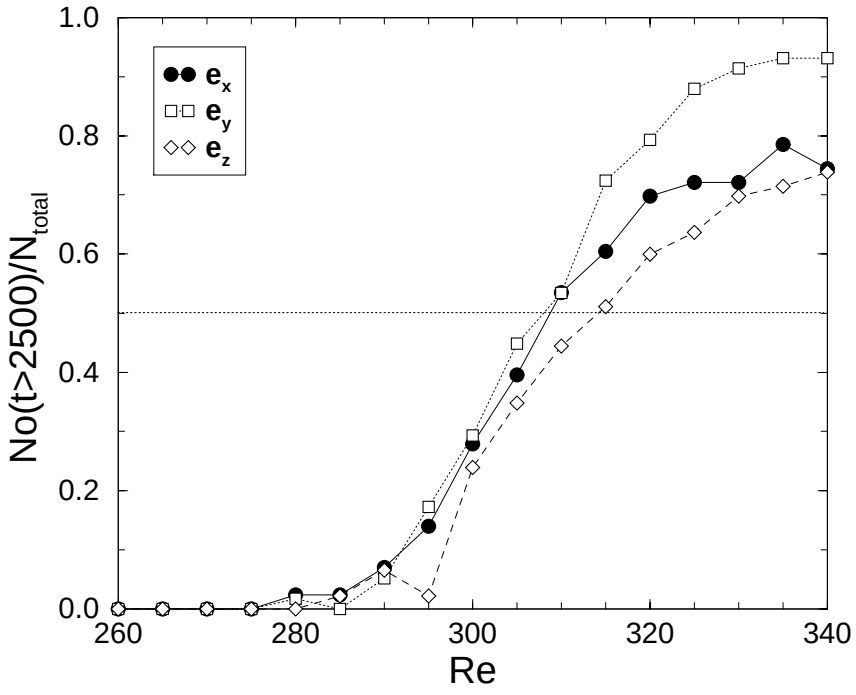

Figure 4.10: Number of initial conditions in the A/Re-plane having a lifetime greater than 2500. $\mathbf{e}_{x,y,z}$ corresponds to the orientation of the introduced vortex filament.

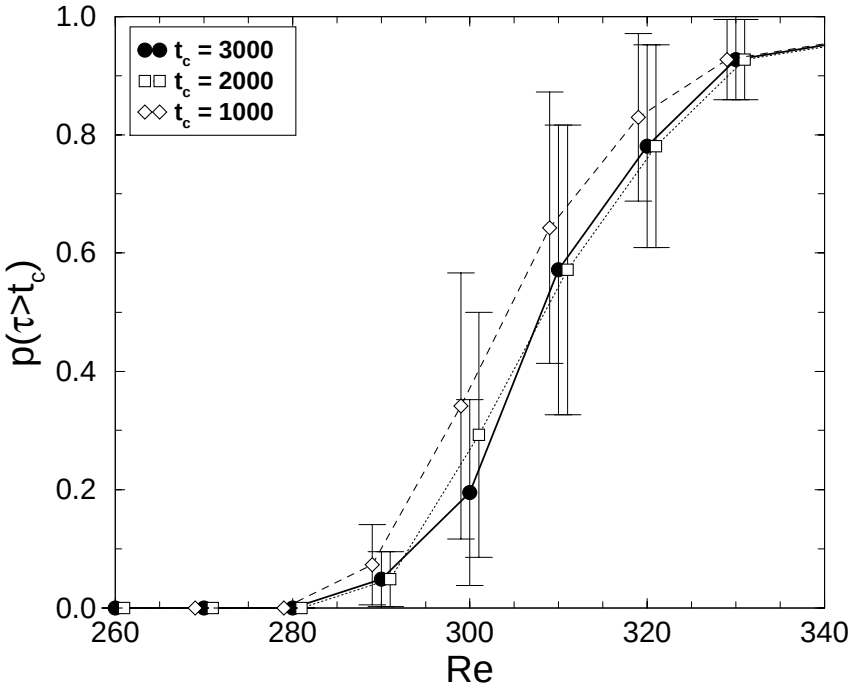

Figure 4.11: Probability of long living states for repeated experiments with similar amplitude ($A = 0.18 \pm 0.012$) as a function of the Reynolds number. The data points are derived from 40 repetitions of the lifetime experiment for Reynolds numbers in the interval ± 5. A state was defined as long lived if the time was above the levels t_c as indicated. A variance in p is obtained as $p(1-p)$ under the assumption of a binomial distribution.

collected for fixed Reynolds numbers (Fig. 4.9). In all three cases the median increases for Reynolds numbers between 285 and 320. In case of a spanwise orientated filament the median starts to grow at $\mathrm{Re} = 240$. In the other two cases this growth sets in later at about $\mathrm{Re} = 280$ and it shows an high increase at $\mathrm{Re} = 305$.

As a possible operational definition for the transition to turbulence the occurrence of the first states with lifetimes exceeding the observation time is less suitable since it depends sensitively on the initial conditions. A statistical measure such as the median is more stable and reproducible. The median exceeds the maximal integration time if half the initial conditions do so. Using this definition the transitional Reynolds number lies between of 305 and 320, since more than half the initial conditions life longer than the observation time. If the observation time is lowered to 2500 the fraction of initial conditions with life times exceeding this time is shown in figure. 4.10. More than half the initial conditions life longer than this time for Reynolds numbers above about 315; for spanwise orientation of the vortex the value is a bit lower. Experiments by Bottin and Chaté [11] with a cut-off of 20000 time units show a critical Reynolds number of about $\mathrm{Re} = 328$. Thus an increase in lifetimes about a factor of 8 changes the Reynolds numbers by only about 4%.

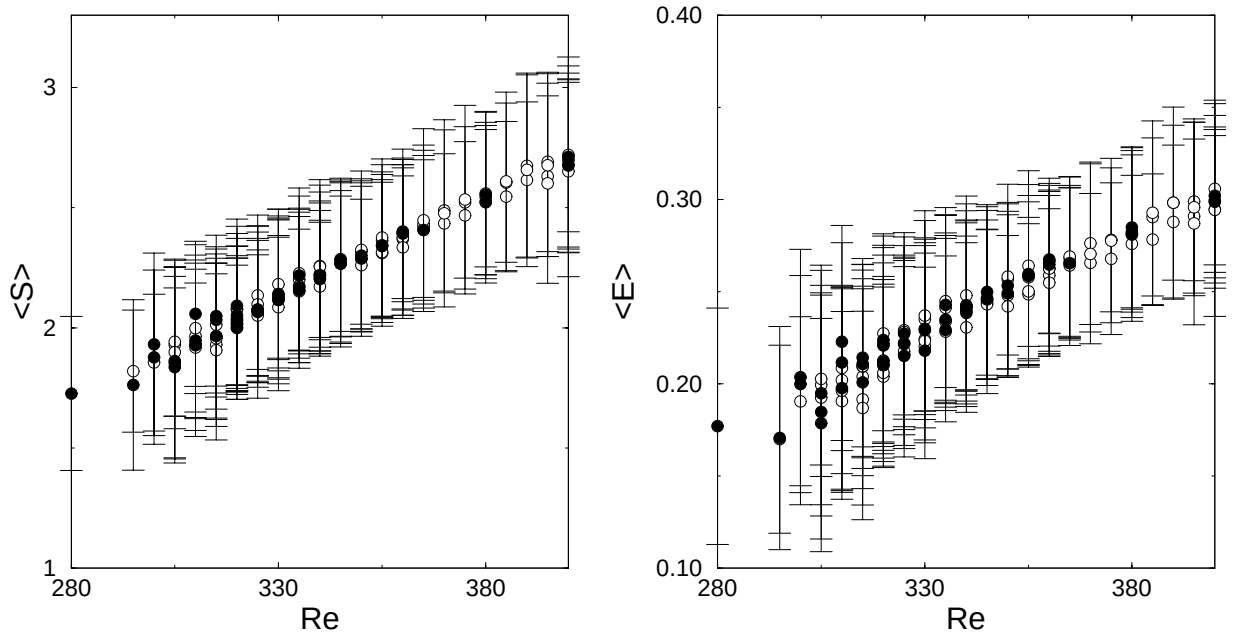

Figure 4.12: Energy and shear rate statistics for the long lived states in different intervals of Reynolds numbers. Indicated are the mean shear rate (left panel) and the mean energy (right panel) as well as the variances for all states with lifetimes longer than $t > 2500$ at the given values of Reynolds numbers. Open symbols correspond to the values of turbulent states originated from closed vortex filaments. Closed symbols correspond to the values of the symmetric and asymmetric induced perturbations.

Following Darbyshire and Mullin [31] I also studied the lifetime distributions observed in repeated experiments with similar initial conditions. The amplitude was taken from the fixed interval $A \in [0.18 \pm 0.12]$ and the Reynolds number was within an interval of ± 5 from the indicated value (the widths of the Reynolds number interval is the experimental resolution of Bottin et al. [12]). A state was classified as long lived if the time was above the level t_c as indicated. Figure 4.11 shows the probability to hit a long lived initial condition. On the assumption that the probabilities are drawn from a binominal distribution a variance of $p(1-p)$ can be assigned to each value. The probability of obtaining a long living state grows rapidly between $\mathrm{Re} = 290$ and $\mathrm{Re} = 325$. This interval shifts to higher Re for larger lifetimes. The probability does not reach 1 within the range of Reynolds numbers studied, indicating that nonlinear transients are still possible.

4.3 Properties of the turbulent state

In this section I study the statistical properties of the nonlinear transient and turbulent states. It turns out that their properties are independent of the symmetry and the shape of the imposed perturbation. Connecting the transition to turbulence to the formation of a chaotic

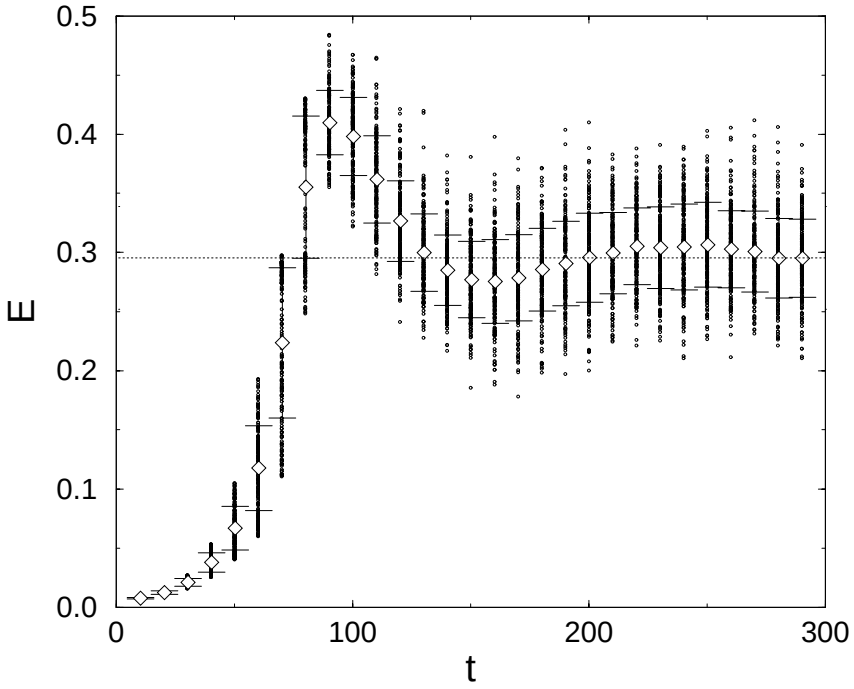

Figure 4.13: Time evolution of asymmetric time dependent perturbations (4.5) with randomly selected amplitudes $A = 0.035 \pm 0.005$ at $\mathrm{Re} = 400$. The dots are the energy of each perturbation at the given time. The line at $E = 0.3$ indicates the time average of a turbulent signal generated by a streamwise orientated filament. Also shown are the mean energy ($\diamond$) of the ensemble and its variance at each time step.

repellor suggests the existence of two different timescales: the escape rate and the relaxation rate. I measure these rates by evaluating the former lifetime measurements and turbulent time signals. In order to follow turbulent states down to Reynolds numbers below the transitional Reynolds number, annealing experiments have been performed, where the Reynolds number is dynamically decreased. These experiments allow the definition of the *annealing Reynolds number*, as the smallest Reynolds number where turbulent states have been followed down to.

4.3.1 Energy and shear rate statistics

The energy and shear rate statistics of the turbulent states and nonlinear transients indicate that the turbulent dynamic takes place in a distinct region of the phase space. Figure 4.12 shows the time averages of the energy

$$\langle E \rangle = \frac{1}{T} \int_T \mathrm{d}t \, E(t) \tag{4.7}$$

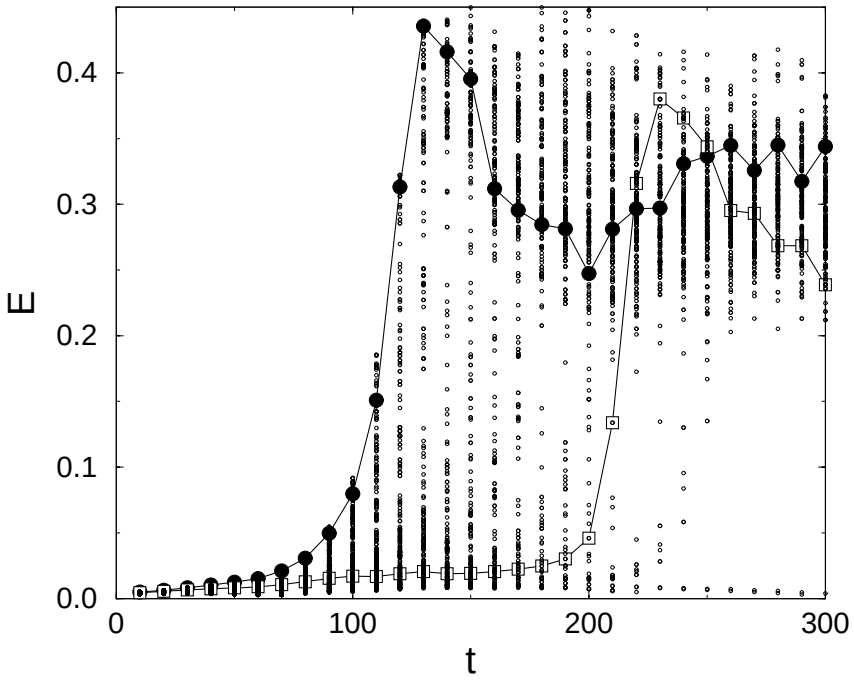

Figure 4.14: Time evolution of 100 asymmetric time dependent perturbations with randomly selected amplitudes of $A = 0.025 \pm 0.005$ at $\mathrm{Re} = 400$. The full temporal behavior is shown for two perturbations. For the other runs only the instantaneous values are indicated by dots. The dots become denser for energies less that 0.1 and energies around 0.3.

and the shear rate

$$\langle S \rangle = \frac{1}{T} \int_T \mathrm{d}t \, S(t), \tag{4.8}$$

of long living nonlinear transients and turbulent states approached by vortex filaments with different orientations and their variance. Also long living nonlinear transients and turbulent states reached by symmetric (4.3) and asymmetric (4.5) time dependent perturbations entered the figure. There is no significant difference between nonlinear transient and turbulent states. The dynamics take place in the same region of phase space, which is independent of the nature of the perturbations.

In Fig. 4.13 the time signals of 100 asymmetric time dependent perturbations (4.5) with randomly selected amplitudes of $A = 0.035 \pm 0.005$ and a time of injection of 10 time units at a Reynolds number of 400 are shown. Figure 4.13 shows the energy of each calculated state and the ensemble average with its variance at a given time. At about 100 time units the average energy approach a value of 0.3. The turbulent time signal of a streamwise orientated filament show the same average energy and the same variation (horizontal line). Hence, the perturbations evolve to the same region in phase space, independent of the shape and the symmetry of the perturbation. The time needed to begin the approach to this region depends

sensitively on the perturbation. Even small variations in the amplitude can cause a drastic change. In Fig. 4.14 the time signals of 100 asymmetric time dependent perturbations (4.5) with randomly selected amplitudes of $A = 0.025 \pm 0.005$ at $\mathrm{Re} = 400$ are shown. The full temporal behavior of two perturbations illustrates this sensitivity. Between $t = 100$ and $t = 200$ the ensemble spreads into two parts, one decaying into the laminar state and another part approaching the turbulent state.

4.3.2 The distribution of energy and the shear rates of the turbulent state

The changes in the energy as well as the shear rate and their variances shown in figure 4.12 suggest that the turbulent state is not only moving in phase space but also changes its shape for varying Reynolds number.

To get the distribution of energy and shear rate two turbulent time signals at $\mathrm{Re} = 320$ up to $\mathrm{Re} = 400$ have been measured imposing a symmetric (4.3) and an asymmetric (4.5) time dependent perturbation. The symmetric perturbation had an amplitude of $A_0 = 3$ and the asymmetric perturbation had an amplitude of $A_0 = 0.5$. The injection time was 5 time units for both perturbations and their evolution was followed up for 6000 time units. The investigation of the energy and the shear rate of the turbulent state started after the first 150 time units. These time signals are combined and the integrated probability distribution of the energy and the shear rates was calculated. Then a cubic spline fit with 50 points on the normalized integrated distributions was applied. Using a center differentiation scheme one obtains the distributions of energy P_E and shear rates P_S. These distributions are asymmetric for lower Reynolds numbers with a fast decay to smaller energies and shear rates (See Figure 4.15). This asymmetry becomes less significant for increasing Reynolds numbers and presumably vanishes at sufficiently high Reynolds numbers. While the maximum of P_E increases and therefore the variation decreases the maximum of the shear rate distribution becomes smaller and the variance increases. For growing Reynolds numbers the active degrees of freedom increase and the dynamic also take place on smaller lengthscales. Therefore the energy is evenly distributed and large fluctuations becomes less possible. On the other hand, since velocity fluctuations also occurs on smaller lengthscales larger gradients appear which shift the shear rate to higher values.

4.3.3 Escape rate and relaxation rate: timescales on a repellor

Two different timescales characterize a chaotic repellor [36, 54, 59]: The escape rate ϵ and the relaxation rate η. The probability $\rho(t)$ of staying on a repellor at a time t decays like $\rho(t) \propto \exp(-\epsilon\, t)$. The escape rate ϵ is accessible by the former calculations. One is able to calculate the probability that a perturbation has left the repellor at a time t, which equals $1 - \rho(t)$.

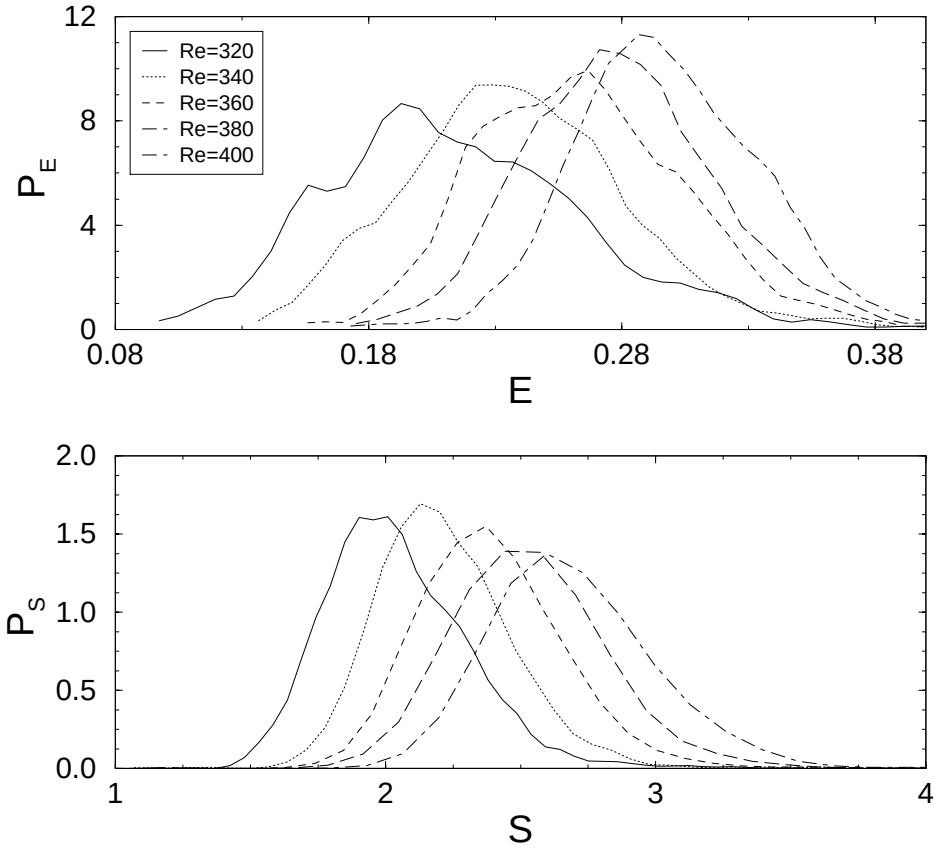

Figure 4.15: Distribution of energy (upper panel) and mean squared shear rates (lower panel) taken from two turbulent time signal with a cut-off of $t_{\max} = 6000$ for a symmetric and an asymmetric time dependent perturbation at $\mathrm{Re} = 320$ up to $\mathrm{Re} = 400$.

Assuming that such timescale also exists for the nonlinear transients, one is able to calculate ϵ by evaluating $1 - \rho(t)$ from the previous lifetime measurements. For high escape rates one needs good initial conditions and for lower ones long lifetime measurements, therefore one is only able to calculate ϵ in a small region of Reynolds number.

A state staying at a distance d on the stable manifold of a repellor will be attracted to the repellor. Such behavior has also been observed in the previous section. Any non decaying perturbation relaxates on the same turbulent state. d decreases like $d(t) \propto \exp(-\eta\, t)$. In order to estimate this rate, the relaxation of an ensemble of initial perturbations was studied since the position of the stable manifold is not known. For sufficiently high amplitudes the ensemble approached the turbulent state before it spreads (Fig. 4.13). The ensemble average of the distance $d = E(t) - \langle E \rangle$ also decreases like $d(t) \propto \exp(-\eta\, t)$. Figure 4.13 shows that this decrease consists of an oscillating part and an exponential decay. The frequence of oscillation ω was determed by calculating the time interval between the first maxima of the distance d of the ensemble averages, the interval between the first minima, and the interval between the first two times where $E(t)$ equals $\langle E \rangle$ and calculate the average of these times.

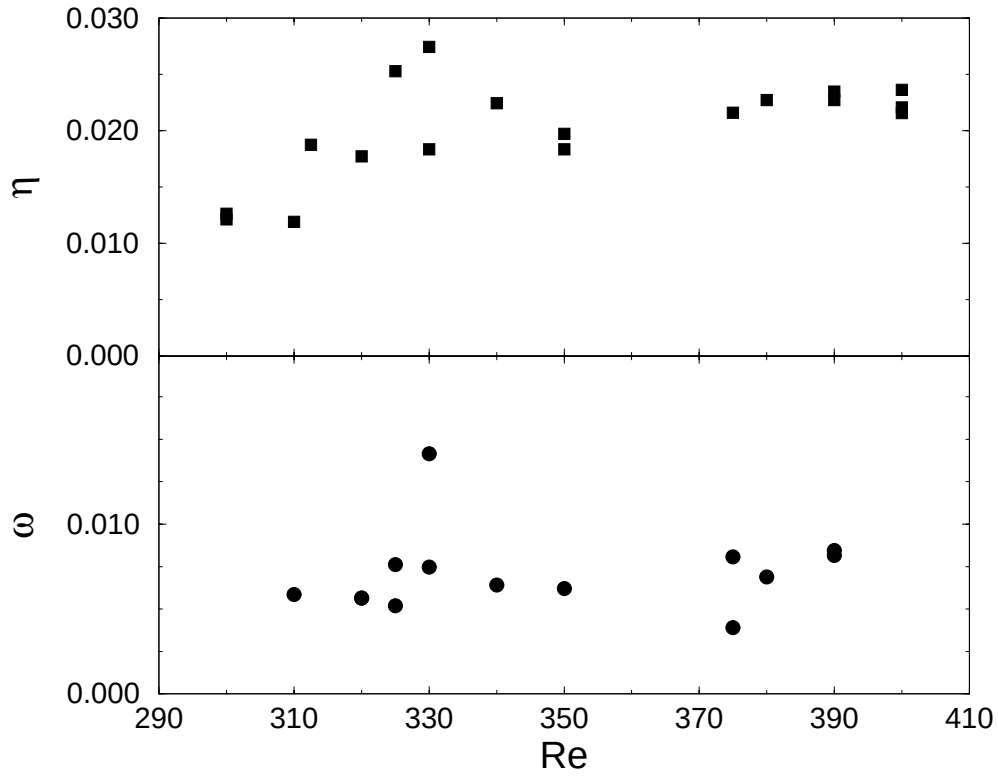

Figure 4.16: Relaxation rate η and oscillation frequency ω for the approach to the turbulent state as a function of the Reynolds number. The data points are based on 100 realizations of time dependent perturbations as in Fig. 4.13.

Values of the relaxation rate η and the frequency of oscillation ω are shown in figure 4.16. They were only calculated for higher Reynolds numbers because the turbulent state is more attractive at higher Reynolds numbers. The relaxation rate η shows a slight increased which indicates a stabilization of the turbulent state. The values of ω do not change in the observed range of Reynolds number. This suggests that the oscillation is only slightly influenced by the linear terms, which would show a scaling proportional to Re^{-1}, but dominated by the nonlinear effects, which are independent from the Reynolds number.

Figure 4.17 shows values of η and ϵ. ϵ decays for a Reynolds number of about 270. η is larger than ϵ but grows slowly. Extrapolation of both rates suggest a Reynolds number of $\mathrm{Re} \approx 240$ where the escape rate equals the relaxation rate.

4.4 Annealing experiments

In order to follow the turbulent states down to Reynolds numbers below the transitional Reynolds number annealing experiments have been performed. In these experiments the Reynolds number decreases slowly in time. This corresponds to a change of the viscosity

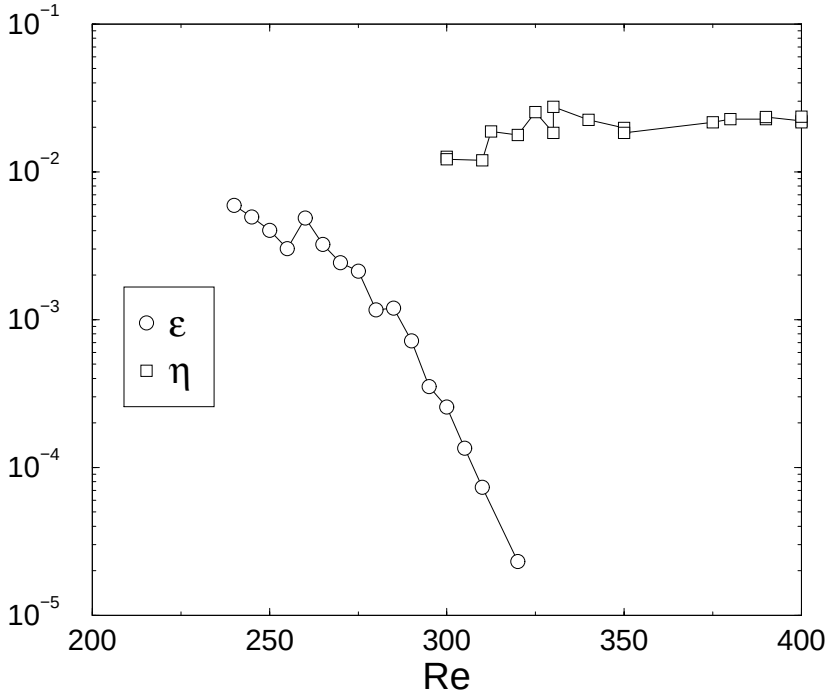

Figure 4.17: Escape rates ϵ and relaxation rates η. ϵ is taken from lifetime measurements for different vortex filaments. η is extracted by relaxation experiments shown in Fig. 4.13. Extrapolation of both rates show that the escape rate equals the relaxation rate at a Reynolds number of about 240.

because a change of the velocity of the plates would introduce a time dependent laminar profile in the equation of motions (3.1).

In the same spirit Bottin and Chaté performed quench experiments [11] where they decreased the velocity of the plates abruptly. They observed a minimal Reynolds number of $\mathrm{Re} = 323 \pm 2$ which equals the transitional Reynolds number observed by their experiments. Since the statistical properties of the repellor change with the Reynolds number, a quenched turbulent state may decay since it is no longer near the repellor. Therefore, it is more practical to reduce the Reynolds number slowly. Then the turbulent state lies always near the repellor, until it leaves the repellor via the unstable manifold. In these experiments about 20 turbulent states at $\mathrm{Re}_0 = 320$ were taken. This Reynolds number is lowered at a rate c, $\mathrm{Re}(t) = \mathrm{Re}_0 - c\,t$. Typical energy curves for a specific turbulent state are shown in figure 4.18.

For the very small lowering rate $c = 2^{-10} \approx 0.00097$ the turbulent state disappears after $t \approx 2500$, corresponding to a final Reynolds number of about 317. Since here the decay rate is much smaller than the escape rate, this should be the regular decay of the turbulent state. For a somewhat larger rate $c = 2^{-6} \approx 0.015$ the turbulent state can be followed all the way to a Reynolds number of $\mathrm{Re} = 291$. This is less than the transitional Reynolds number

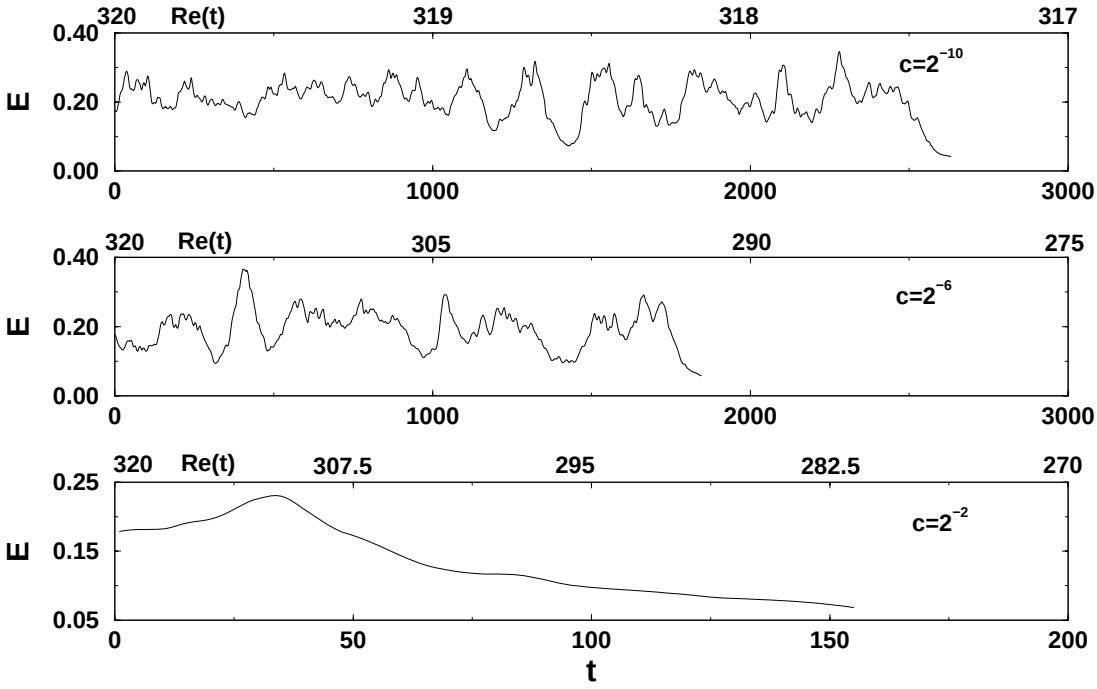

Figure 4.18: Temporal behavior of a turbulent perturbation for different annealing rates. The lower abscissa give the time, the upper labels the Reynolds number reached at that time.

but compatible with the appearance of the first maximal lifetime at $\mathrm{Re} = 290$ observed in the previous section. Moreover, the fluctuations before the decay show no indications that the end of the turbulent state is reached. I take this as an evidence that until shortly before the decay the dynamics is still dominated by the turbulent behavior and that indeed a continuation of the turbulent state to lower Reynolds number is visible. At the even faster annealing rate $c = 0.25$ the dynamics is markedly different. It shows a gradual decay to zero without any turbulent revivals as in the other cases.

The results for many such annealing experiments are collected in Fig. 4.19. For fast annealing rates the lifetimes cluster tightly, around about 30 for $c = 8$. Decreasing c the lifetime increases, as do the variations between the experiments. For slower annealing rates the variability increases drastically, lifetimes differ by one order of magnitude, and the dynamics changes, as indicated by the traces in Fig. 4.18. It is here that the longest living states indeed seem to follow the turbulent state down to Reynolds numbers of about $\mathrm{Re} = 240$. For even slower annealing rates the lifetimes increase drastically, with fluctuations covering almost two decades. For such small annealing rates the escape rate dominates the lifetime distribution and the large fluctuations are the ones known from lifetime measurements. Note that I calculated the lifetime up to 20000, which is much higher than the numerical cut-off used in previous investigations.

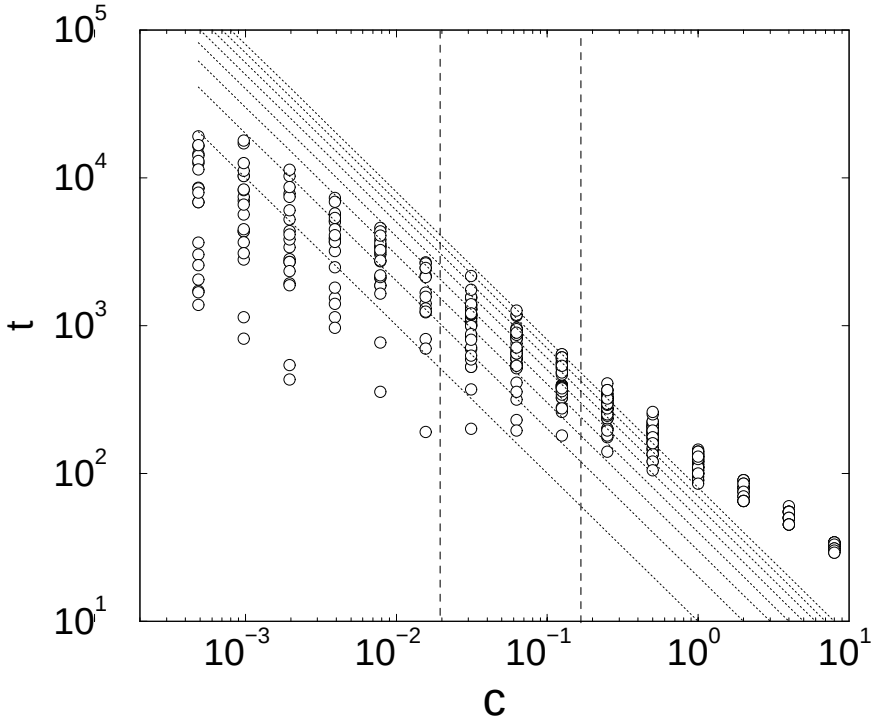

Figure 4.19: Final points for annealing experiments with different annealing rates c. The ordinate gives the time for which the wall normal energy in the perturbation is larger than 10^{-4}. The dashed lines are lines of constant Reynolds number. Starting at $\mathrm{Re} = 310$ down to $\mathrm{Re} = 240$ (from left to right). The vertical dashed line marks the region, where neither the escape rate nor the relaxation rate dominates the dynamics.

The ranges of annealing rates that showed the lowest Reynolds numbers with turbulent behavior are indicated in figure 4.19 by vertical bars. The slowest limit is about a factor of three above the escape rate of the turbulent state, to avoid spontaneous decay of the perturbation. The upper limit is about a factor of five faster than the relaxation rates η of the turbulent state. This can be justified by the fact that in the annealing experiments the deviations from the turbulent state will be much smaller than in the strong perturbation experiments used to determine η, so that even with faster annealing rates the dynamics has a chance to follow the turbulent state.

It seems possible to follow adiabatically a turbulent state from a higher Reynolds number to values as small as $\mathrm{Re} = 240$ if the annealing rate lies between 0.02 and 0.1. This value is close to the one where the nonlinear transients and turbulent states were observed but still much larger than the bifurcation value for the first stationary states, which will be discussed in the next chapter. This suggests that the domain of attraction for the turbulent state shrinks rapidly with decreasing Reynolds number and becomes almost negligible for Reynolds numbers around $\mathrm{Re} = 250$.

4.5 Conclusions

The above investigations show that the lifetime depends strongly on the shape of the perturbation and the Reynolds number. Therefore the transition is best described in a statistical sense. The transitional Reynolds number $\mathrm{Re}_{\mathrm{tr}}$ is defined as the Reynolds number where the probability of finding perturbations with life times above 3000 exceed a value of 50%. For a streamwise orientated closed vortex filament $\mathrm{Re}_{\mathrm{tr}}$ equals 320, which equals the value of a filament with a wall normal orientation. A vortex filament orientated along the spanwise direction shows an earlier transition at 305. These values suggest a general transition at $\mathrm{Re}_{\mathrm{tr}} = 315 \pm 10$.

There are three different types of states: linear and nonlinear transients and turbulent states. The statistics of a turbulent state equal the statistics of the nonlinear transients and are independent of the shape and the symmetry of the initial perturbation. These observations suggest that the transition to turbulence comes along with the formation of a chaotic repellor, which attracts perturbations on a timescale η, the relaxation rate, but repels them on a timescale ϵ, the escape rate.

The repellor already exists at values below $\mathrm{Re}_{\mathrm{tr}}$. One can follow the turbulent motion down to Reynolds number below 315 ± 10 by performing annealing experiments where the Reynolds number is slowly decreased. The annealing Reynolds number $\mathrm{Re}_{\mathrm{anneal}}$ is the lowest value of a Reynolds number where a turbulent dynamic was sustained. This value is about 240, which is similar to the occurrence of first nonlinear transients for the propagation of a vortex filament with a spanwise orientation.

At a value of $Re = 240$ a couple of stationary states already exist. They are presumably responsible for the formation of this repellor. The properties of these stationary states are discussed in the next chapter. In chapter 6 I will discuss and illustrate how these states are presumably responsible for the formation of the repellor.

5 Stationary states in plane Couette flow

Palmström bekam ein Operglas geschenkt
womit er sich nun in die Welt versenkt.
Doch glaub nicht, daß man ihn beneiden darf:
denn ach! Es ist für seine Welt zu scharf.

Die Welt, die ihn umfängt und interessiert,
mißt dreihundert Meter im Geviert.
Das Fernglas aber zeigt immer Gegenstände,
die viel, viel weiter draußen im Gelände

Er sieht mit seinen Linsen lediglich
ein gewissen Nebelreich um sich,
ja, Zirkus selbst, Konzertsaal und Theater
sind nicht wie einige verschwommne Krater

Palmstöm versucht hierauf nach solchem Scheitern
den Horizont behutsam zu erweitern.
Umsonst! es weiß der wundervolle "Zeiss"
allein von Solchem, wovon er nichts weiß.

Das achtfache Glas, C. Morgenstern[66]

Recent investigations focused on finite amplitude solutions of the time independent Navier-Stokes equation in the plane Couette flow. Since the birth of a new finite amplitude solution and its secondary bifurcation marks a well-known route to turbulence in linearly unstable flows, one would expect these states to play also an important role in the transition to turbulence in plane Couette flow. It is known that one pair of stationary states bifurcates at $\mathrm{Re} = 129.75$, which was found by Nagata [68, 69], Busse and Clever [27]. Nagata found an additional pair of states bifurcating at $\mathrm{Re} = 200$ [71]. At a Reynolds number of about 1000 Cherhabili and Ehrenstein [21] and later Balakumar [5] found a two dimensional stationary solution. From this solution a three dimensional solution bifurcates at a higher Reynolds number [22].

All these states have been found by applying path-following methods. These methods modify the plane Couette flow by adding additional forces to the equation of motions, which desta-

bilize the laminar flow and allow primary and secondary bifurcations. Cherhabili, Ehrenstein and Balakumar add a pressure gradient, Nagata used centrifugal forces and Busse and Clever used a temperature gradient.

My investigations show that there are various stationary states beside the ones observed by Nagata, Busse and Clever, Cherhabili and Ehrenstein, and Balakumar. In this chapter I discuss these various states. The numerical methods of the investigation, the observed stationary states, different topologies of the stationary state are described and the states are classified. Some of the characteristics of these states can be explained with simple, linear arguments. This chapter is closed with a discussion of these arguments.

5.1 Numerical methods

Stationary states are solutions of the time independent evolution equation:

$$\mathbf{0} = -(\mathbf{u}\cdot\nabla)\,\mathbf{u} - z\frac{\partial}{\partial x}\mathbf{u} - w\,\mathbf{e_x} - \operatorname{grad} p + \mathrm{Re}^{-1}\Delta\mathbf{u}\,, \tag{5.1}$$

which fulfill also the continuity equation,

$$\operatorname{div}\mathbf{u} = 0\,, \tag{5.2}$$

and satisfy the boundary conditions,

$$\mathbf{u}|_{z=\pm1} = 0\,. \tag{5.3}$$

The search is restricted to members of the two symmetry groups `I` and `NBC` (see chapter 3.4). The latter equals to the symmetry group investigated by Nagata [68–70] and Busse and Clever [25–27], where the first pair of stationary states have been found. In accordance to their work I used an aspect ration of $d : 2\pi\,d : \pi\,d$ (wall normal:streamwise:spanwise), where d is the gap width. Solution branches of members of the `NBC` group are named in Greek letters, members of the `I` group in capital Latin letters.

In order to find a solution of equation (5.1) also solving equations (5.2) and (5.3), I used the Lagrangian formalism of the second kind (see appendix A), i.e. the flow field $\mathbf{u}$ is expanded in terms of incompressible vector fields vanishing at the boundary. The resulting formulation can be solved with a standard Newton-Raphson method [83]. The initial conditions for this method are taken from the turbulent state. The Pittsburgh path-following program PITCON [88, 89] is used to follow the solution branch to different Reynolds numbers.

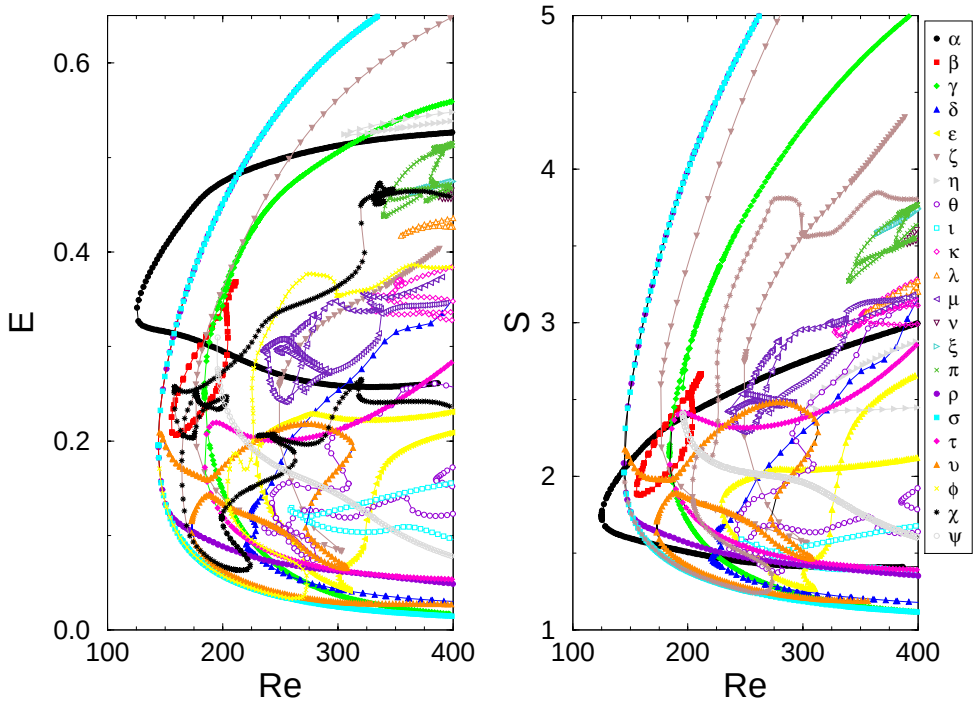

Figure 5.1: Energy and shear rate of various stationary states found in plane Couette flow reduced to the NBC symmetry group. Each symbol corresponds to a stationary solution found at a given Reynolds number. They are connected by lines to sketch the solution branch.

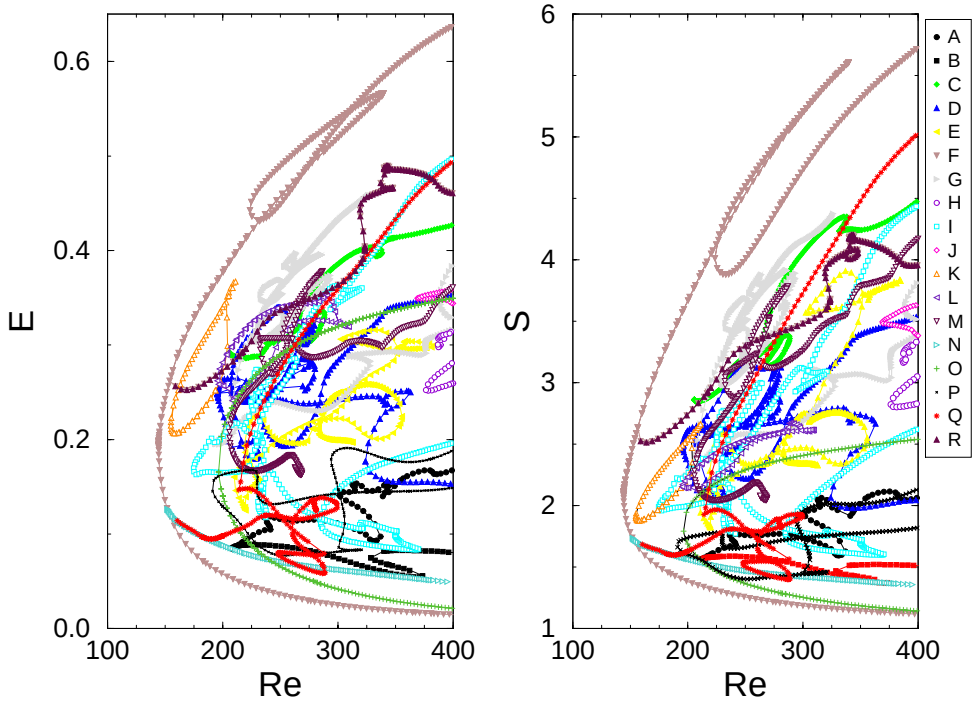

Figure 5.2: Energy and shear rate of various stationary states found in plane Couette flow reduced to the I symmetry group. Each symbol corresponds to a stationary solution found at a given Reynolds number. They are connected by lines to sketch the solution branch.

5.2 Classes of stationary states in plane Couette flow

In this section I introduce the stationary states found in plane Couette flow in the investigated symmetric subspaces. It turns out that the states found by Nagata [68, 69] and Busse and Clever [27] are only a few members of a great variety of stationary states. Figure 5.1 shows the energy and the shear rate of the stationary states which are member of the `NBC` group (See also D.1). Figure 5.2 show the same in the `I` group (See D.2). Each symbol corresponds to a found stationary solution at a given Reynolds number. They are connected to sketch the solution branch.

The first pair of states bifurcates at $\mathrm{Re} = 125$. This value is slightly below the value of the state found by Nagata [68, 69] and Busse and Clever [27]. The difference is presumably caused by the different applied numerical methods and spectral representation.

At $\mathrm{Re} = 140$ a new pair of states bifurcates being member of the `NBC` group. New solutions split off from this branch at $\mathrm{Re} = 142$ from the upper part and at $\mathrm{Re} = 146$ from the lower part. A new pair bifurcates in both groups at $\mathrm{Re} = 155$ and vanishes at $\mathrm{Re} = 210$. For Reynolds numbers larger than 200 various additional states bifurcate. The energy and the shear rates of the states of the `I` group lie between the upper and the lower part of the solution branch of the first pair of states. It is also the state bifurcating at $\mathrm{Re} = 140$ in the `NBC` symmetry group which marks the highest and the lowest energy and shear rate. The upper and the lower part of the solution branch of the state bifurcating at $\mathrm{Re} = 125$ does not spread in this way.

While the members of the `I` group perform a complex framework of backward and forward bifurcations, most of the members of the `NBC` group show only few additional backward and forward bifurcations. Such complex bifurcations occur only at higher Reynolds numbers in the `NBC` group.

The topological features of these stationary states are all the same. These features are described in the next section.

5.3 Topological characterization of the stationary states

Figure 5.3 shows the flow field $\mathbf{u}$ of the first state of the `NBC` group at the bifurcation point at $\mathrm{Re} = 125$. The streamwise velocity (contour) and the spanwise and wall normal velocity (vectors) are shown at $x = 0, \frac{\pi}{4}, \frac{\pi}{2}, \frac{3}{4}\pi$. The whole flow can be reconstructed by applying the $\mathcal{W}$ (3.7) and the $\mathcal{V}$ (3.8) symmetry operation. The state consists of two localized regions with a high fluid transport along the streamwise direction, referred as streamwise streaks.

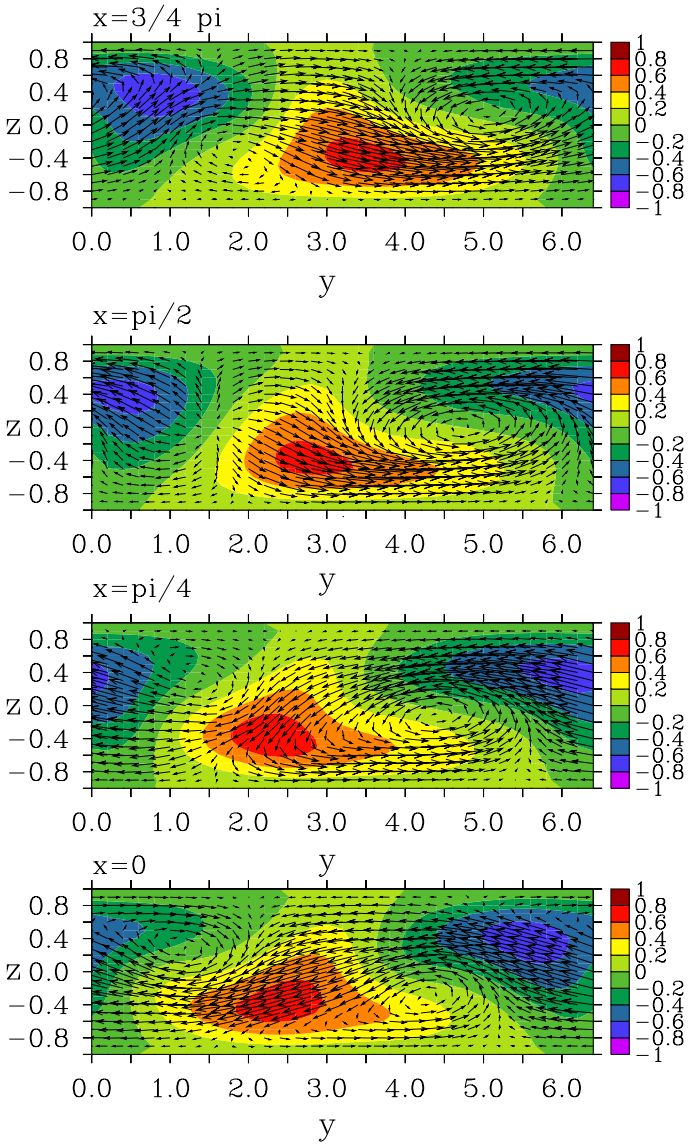

Figure 5.3: Flow field $\mathbf{u}$ of the first state bifurcating in the NBC group at $\mathrm{Re} = 125$. The streamwise velocity (contour) and the spanwise and wall normal velocity (vectors) are shown at $x = 0, \frac{\pi}{4}, \frac{\pi}{2}, \frac{3}{4}\pi$. The whole flow can be reconstructed by applying the $\mathcal{W}$ (3.7) and the $\mathcal{V}$ (3.8) symmetry operation.

Averaging the flow field along the streamwise direction

$$\langle \mathbf{u} \rangle = \int_{L_x} \mathrm{d}x \, \mathbf{u}(x, y, z), \tag{5.4}$$

filters the variation along the streamwise direction and clarifies the topology of these state (Fig. 5.4 left panel).

To study the spanwise and streamwise dependence of these states the positive streamwise

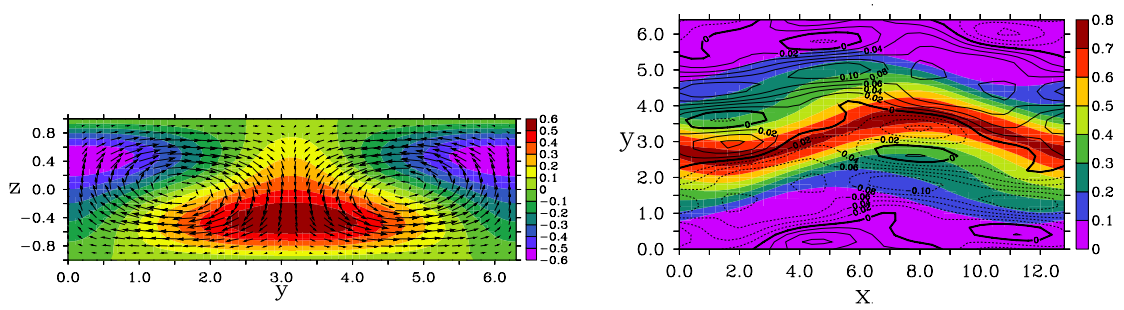

Figure 5.4: Flow field $\mathbf{u}$ of the first state of the NBC group at the bifurcation point ($\mathrm{Re} = 125$) averaged along the streamwise direction (left panel) and u_+ (shade contour) and Ω (contour lines) of the this state (right panel).

velocity is integrated along the wall normal direction, i.e.

$$u_+(x,y) = \int_{-1}^{1} \mathrm{d}z'\, u(x,y,z')\, \Theta\left(u(x,y,z')\right) \;, \tag{5.5}$$

where Θ is the Heaviside function,

$$\Theta(x) = \begin{cases} 0 & x < 0 \\ 1 & x \geq 0 \end{cases} \quad . \tag{5.6}$$

The right panel of Fig. 5.4 shows u_+ of the first state of the NBC group. The wavy structure of this state imposed by the $\mathcal{W}$ symmetry is clearly visible.

Figure 5.3 shows that these streaks are penetrated by two strong vortices which transport fluid between them. When the streamwise vorticity $\omega_x = \frac{\partial}{\partial y} w - \frac{\partial}{\partial z} v$ is integrated along the wall normal direction,

$$\Omega(x,y) = \int_{-1}^{1} \mathrm{d}z'\, \omega_x(x,y,z') \;, \tag{5.7}$$

it becomes visible that these vortices follow the movement of the streaks (Fig. 5.4 right panel).

Further studies of other stationary states show that this is the universal structure of the observed stationary states. All states consist of streamwise streaks and vortices which transport fluid between the streaks. The arrangement differs, i.e. the streaks can be staggered in a way that no average fluid transport between the neutral plane occurs. Additional topological changes are also possible.

There are four different basic streak topologies: S-, Φ-, H- and I-streaks. The S-streak is shown in figure 5.4, the other ones are displayed in figure 5.5.

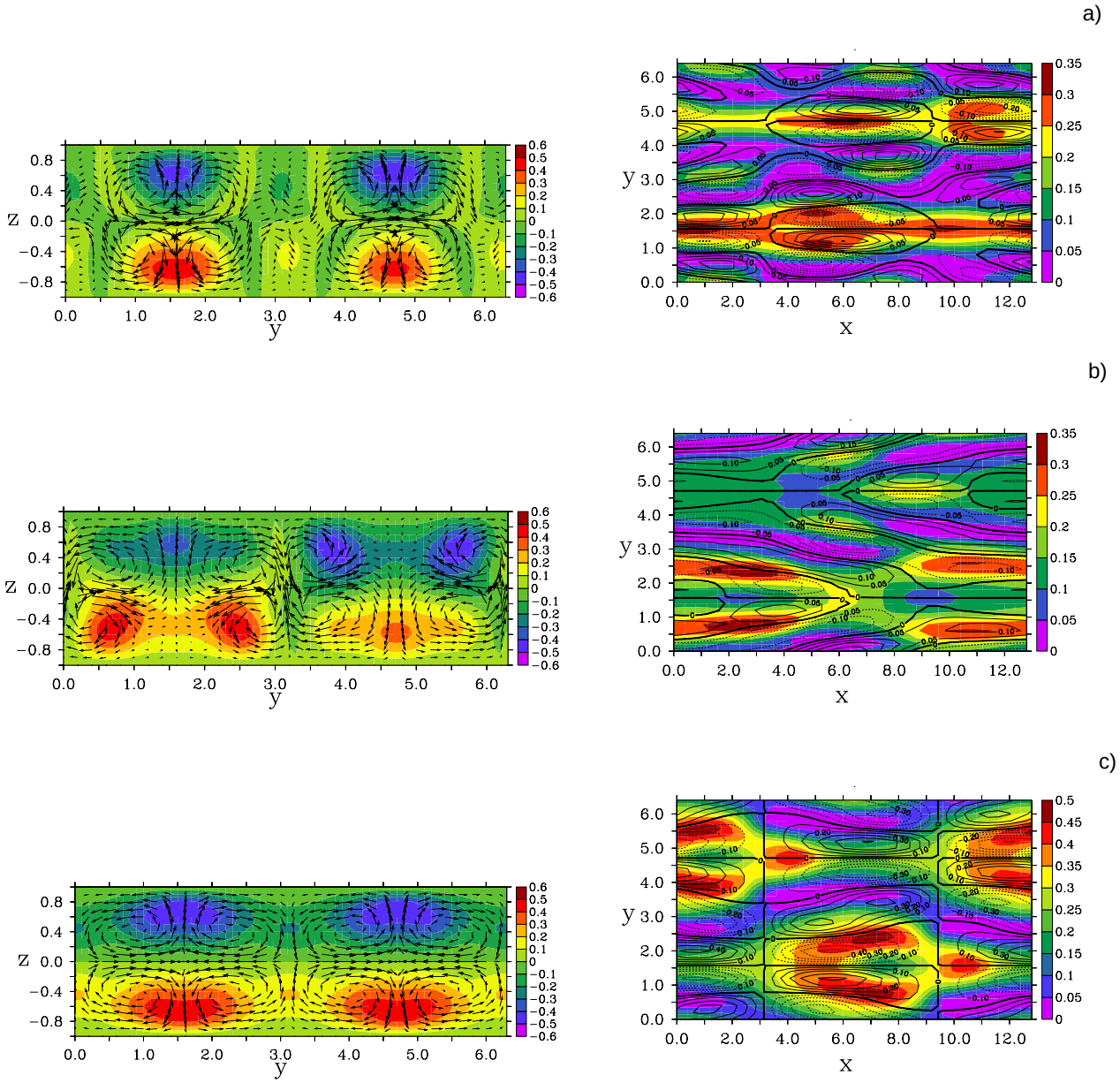

Figure 5.5: The different topologies of the stationary states, which can be identified by $\langle \mathbf{u} \rangle$, u_+ and Ω. There are four different basic streak topologies: S-, I- a), H- b) and Φ-streaks c). The S-streak is shown in figure 5.4.

S-streaks consists of elongated streamwise streaks. These streaks not always extend over the whole spanwise box length. The sign of the velocity inside the streaks alternate along the spanwise direction. There exist states with two layers of streaks. These states are similar to the I-streaks (Fig. 5.5a), which are localized along the spanwise direction. I-streaks only occurs in the $\mathtt{I}$ symmetry group. They do not show the streamwise waviness as the S-streaks do, and they are always staggered in two layers with a fluid transport in opposite directions (Fig. 5.5a).

Additional topological changes are possible. Two streaks can combine and split again. These kind of streaks are referred as H-streaks (Fig. 5.5b) and they are similar to the Φ-streaks, where one streak splits into two streaks, which unify again (Fig. 5.5c).

Different streak topologies can be observed within the same stationary state. In the state shown in figure 5.5a I-streaks coexist with little S-streaks. Since at higher Reynolds numbers lengthscales and the spatial correlation of the flow field decrease, more states with different coexisting streak topologies may exist for sufficient high Reynolds numbers.

The different states found in plane Couette flow can be classified by the symmetry properties of $\langle \mathbf{u} \rangle$, u_+ and Ω and the number of streaks and streak layers. Two different reflexion symmetries can be observed:

$$\mathcal{R}_y : \begin{pmatrix} u \\ v \end{pmatrix}(x,y) = \begin{pmatrix} u \\ -v \end{pmatrix}(x,-y) \tag{5.8}$$

$$\mathcal{R}_z : \begin{pmatrix} u \\ v \\ w \end{pmatrix}(x,y) = \begin{pmatrix} u \\ v \\ -w \end{pmatrix}(x,y,-z) \tag{5.9}$$

Furthermore, some of these solution show a translation symmetry along the spanwise or the streamwise direction or a diagonal translation:

$$\mathcal{T}_{\Delta x,\Delta y} : \begin{pmatrix} u \\ v \end{pmatrix}(x,y) = \begin{pmatrix} u \\ v \end{pmatrix}(x+\Delta x, y+\Delta y)\ . \tag{5.10}$$

$\langle \mathbf{u} \rangle$, u_+ and Ω of all classes of states are given in appendix E. The linear stability analysis of the stationary states shows, that they are all linearly unstable except the α-node at low Reynolds numbers. In the following, I discuss the characteristics of the different classes in the `NBC` and the `I` symmetry group. Table 5.1 and table 5.2 summarize the results of these classifications.

5.3.1 Stationary states in the `NBC` symmetry group

$\mathcal{A}$ class

This class consists of S-streaks, long wavy streamwise streaks extending over the whole streamwise box length. The streaks lie next to each other and show an alternate sign. The α-branch, i.e. the state found by Nagata[68, 69] and Busse and Clever [27], is the first member of the $\mathcal{A}$ class. At $\mathrm{Re} = 280$ the η-branch bifurcates. This state is similar to the α-branch but shows a weaker modulation along the spanwise direction. The ι-branch, $\mathcal{A}_3$, is the third member of this group. It bifurcates at $\mathrm{Re} = 256$ and consists of three streamwise streaks.

Name	branch	No. of streaks	No. of streak layers	Symmetries	$Re_{\mathrm{cr.}}$
$\mathcal{A}_1$	α	1	1		125
$\mathcal{A}_2$	η	1	1		280
$\mathcal{A}_3$	ι	3	1	$\mathcal{T}_{L_x/3}, \mathcal{T}_{L_y/3}$	256
$\mathcal{B}_1$	γ	4	2	$\mathcal{T}_{L_x/2,L_y/4}, \mathcal{R}_z$	183
$\mathcal{B}_2$	ψ	4	2	$\mathcal{T}_{L_x/2,L_y/4}, \mathcal{R}_z$	223
$\mathcal{B}_2'$	ϵ	4	2	$\mathcal{R}_z$	229
$\mathcal{B}_2''$	θ	4	2		235
$\mathcal{B}_3$	δ	6	2		220
$\mathcal{B}_4$	σ	8	2	$\mathcal{T}_{L_x/4,L_y/4}, \mathcal{R}_y, \mathcal{R}_z$	235
$\mathcal{B}_4'$	χ	8	2	$\mathcal{T}_{L_x/2,L_y/2}, \mathcal{R}_z$	154
$\mathcal{B}_5$	ζ	12	4	$\mathcal{T}_{L_x/2,L_y/2}, \mathcal{R}_z$	172
$\mathcal{B}_6$	τ	16	4	$\mathcal{T}_{L_x/2,L_y/2}, \mathcal{R}_y, \mathcal{R}_z$	387
$\mathcal{C}_1$	ρ	8	2	$\mathcal{T}_{L_x/2,L_y/2}, \mathcal{R}_y$	153
$\mathcal{C}_2$	ϕ	8	2		258
$\mathcal{C}_3$	υ	8	2	$\mathcal{R}_z$	144
$\mathcal{D}_1$	β	4	2	$\mathcal{T}_{L_x/2,L_y/2}, \mathcal{R}_y, \mathcal{R}_z$	153
$\mathcal{D}_1'$	ξ	4	2		364
$\mathcal{D}_2$	λ	4	2		353
$\mathcal{D}_3$	π	4	2		183
$\mathcal{D}_4$	ν	4	2		387
$\mathcal{D}_5$	μ	4	2		326
$\mathcal{D}_6$	κ	4	2		233

Table 5.1: Classification of the different solution branches in the NBC symmetry group.

The energy and the shear rate of the three solution branches are shown in Fig. 5.6. All states are born in saddle node bifurcations and are not connected with each other.

$\mathcal{B}$ class

Members of the $\mathcal{B}$ class consist of streaks with alternate sign along the streamwise and spanwise direction. Figure 5.7 shows the basic state $\mathcal{B}_1$, the γ-branch. This state conserves the $\mathcal{T}_{L_x/2,L_y/4}$ and the $\mathcal{R}_z$ symmetries. The later implies that there is no average fluid transport between the neutral plane. The ψ-branch is similar to the $\mathcal{B}_1$ state but its streaks a more elongated. The ϵ-branch and the θ-branch break the observed symmetries. The ψ-branch, referred as $\mathcal{B}_2$, is connected with the γ-branch via a pitchfork bifurcation at $Re = 223$. The θ-branch, $\mathcal{B}_2''$, and the ϵ-branch, $\mathcal{B}_2'$, are not connected to the γ-branch.

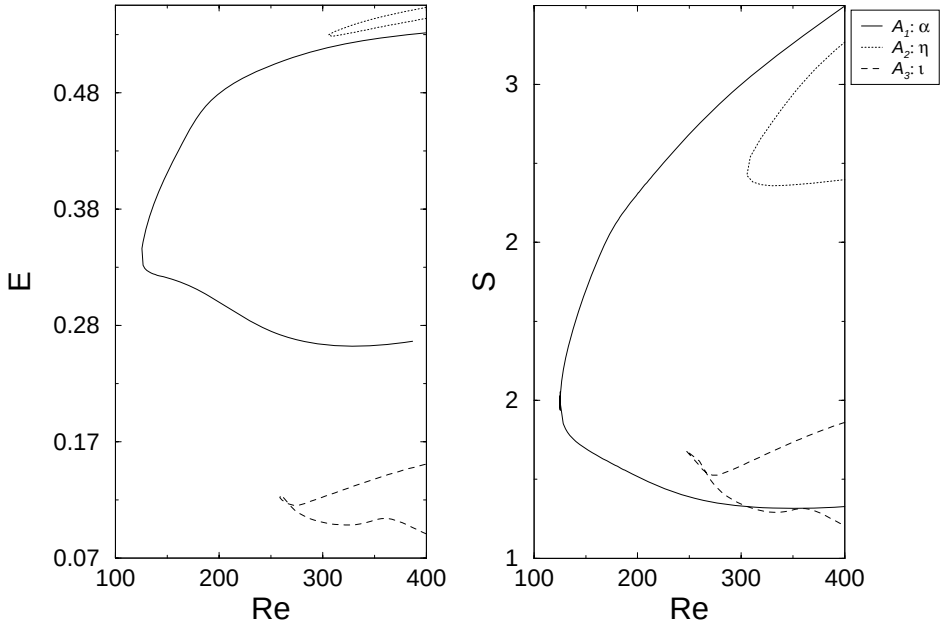

Figure 5.6: Energy and shear rate of the members of the $\mathcal{A}$ class.

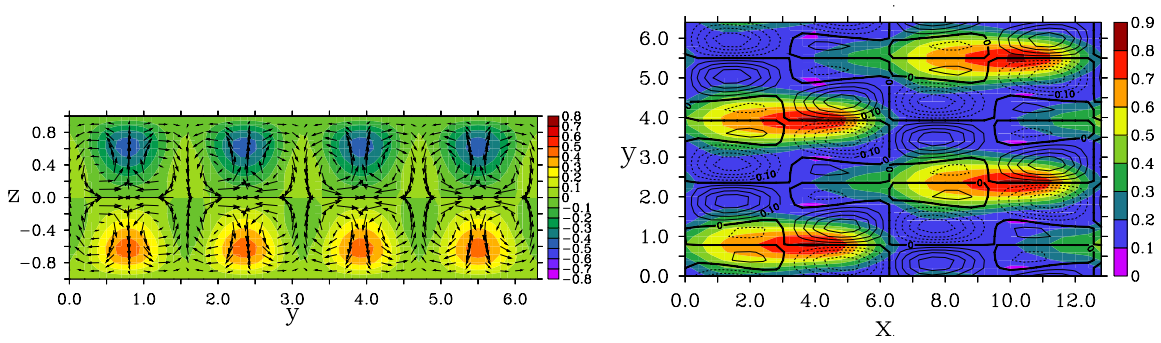

Figure 5.7: $\langle \mathbf{u} \rangle$, u_+ and Ω of a state of the γ-branch. This branch is the first state of the $\mathcal{B}$ class.

The bifurcation diagram of this class (Fig. 5.8) shows that except the ψ-branch all states are born by saddle node bifurcations and are not connected with each other. $\mathcal{B}_5$ and $\mathcal{B}_6$ consist of four streak layers. Since the sign of these streaks changes on each layer, there are streaks with an high fluid transport along the direction of the mean flow. These regions are smaller and less intensive than the dominant streaks at the plates, which show the familiar transport opposite to the laminar flow.

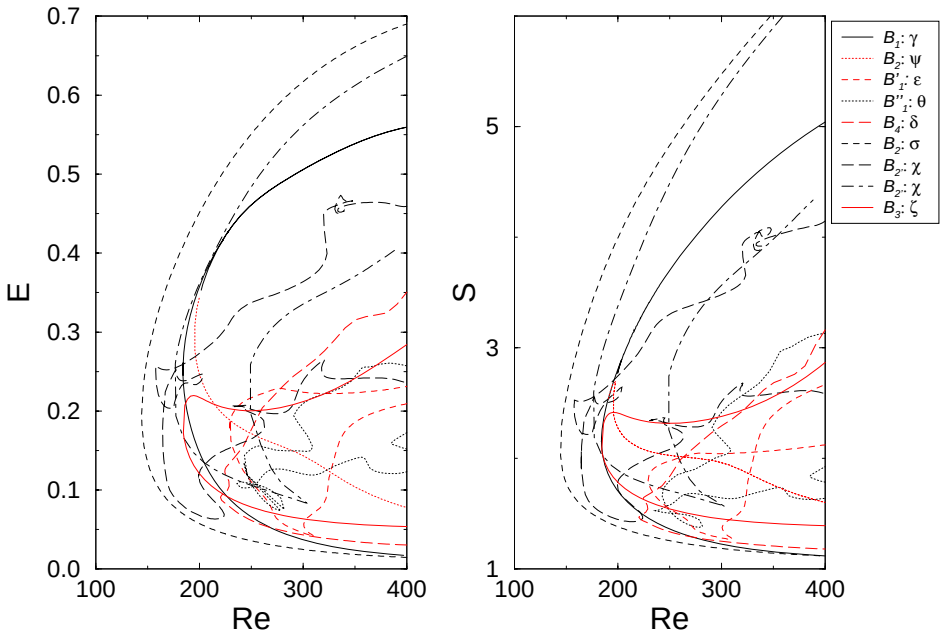

Figure 5.8: Energy and shear rate of the members of the $\mathcal{B}$ class.

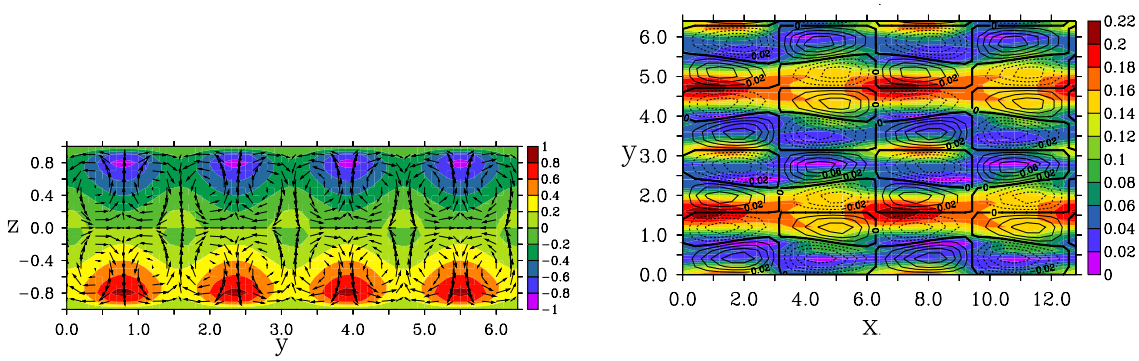

Figure 5.9: $\langle \mathbf{u} \rangle$, u_+ and Ω of a state of the ρ-branch. This branch is the first state of the $\mathcal{C}$ class.

$\mathcal{C}$ class

All states of the $\mathcal{C}$ class are born in pitchfork bifurcations of the σ-branch, $\mathcal{B}_2$ (Fig. 5.10). They all consist of eight streaks on two layers and break the symmetries of the σ-branch. The intensity and the spatial extension of these streaks changes. The ϕ-branch, $\mathcal{C}_1$, has four intensive streaks and four weaker streaks with a diffusive border (Fig. 5.9). The ρ-branch, $\mathcal{C}_2$, also shows four intensive and four weak streaks, which are elongated along the streamwise direction with a sharp border in the spanwise direction. The υ-branch, $\mathcal{C}_3$, has only two intensive and six weaker streaks of nearly equal width.

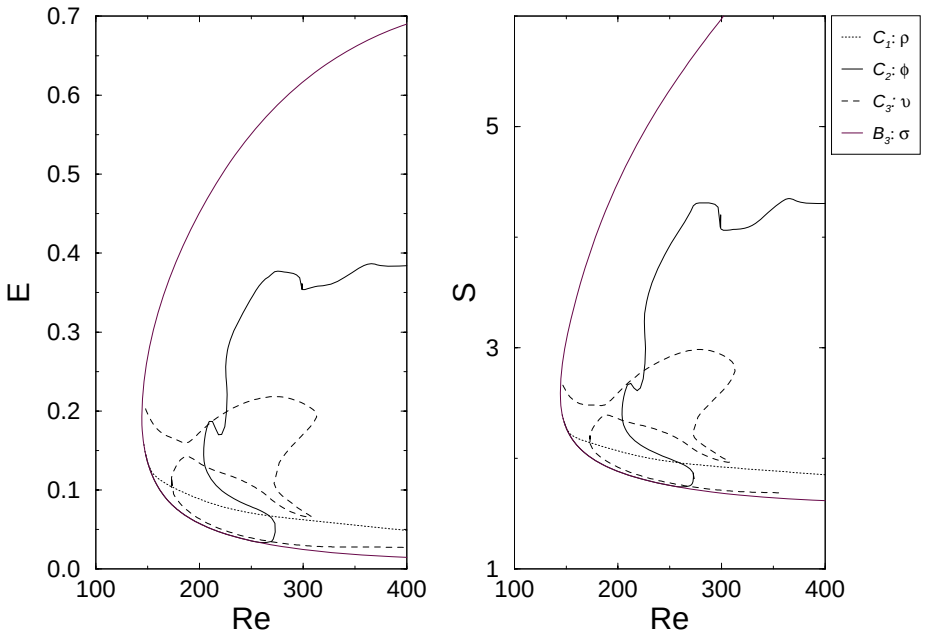

Figure 5.10: Energy and shear rate of the members of the $\mathcal{C}$ class. Since all states are born by a pitchfork bifurcation of the σ-branch, the σ-branch, $\mathcal{B}_2$, is also shown.

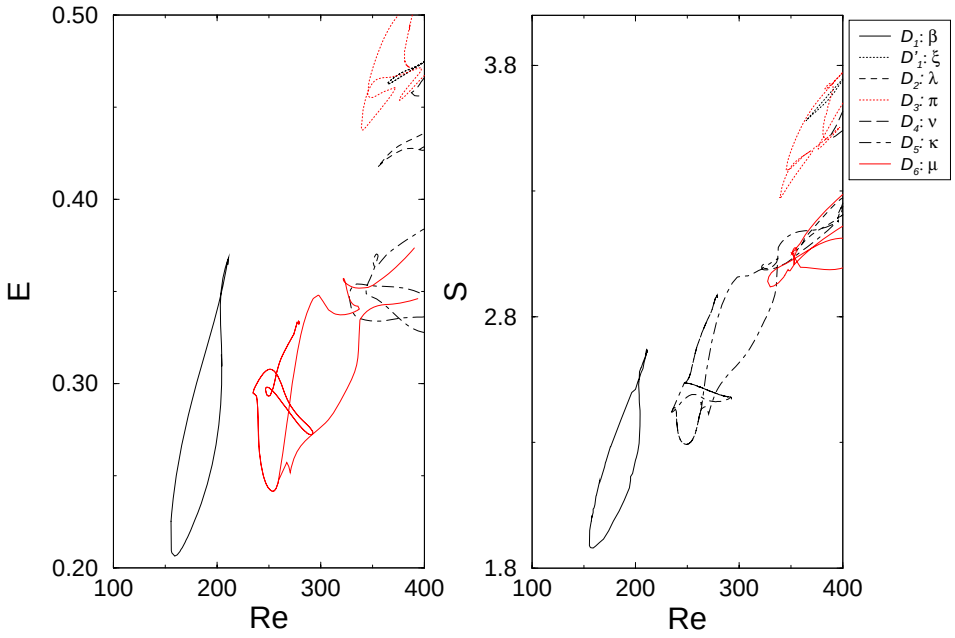

Figure 5.11: Energy and shear rate of the members of the $\mathcal{D}$ class.

$\mathcal{D}$ class

The $\mathcal{D}$ class consists of spatial localized streaks which undergo topological changes. Φ- and H-streaks of the NBC belong to this class. The state shown in figure 5.5c belongs to the β-branch, $\mathcal{D}_1$. It conserves the $\mathcal{T}_{L_x/2,L_y/2}$, $\mathcal{R}_y$, $\mathcal{R}_z$ symmetries. These symmetries are broken

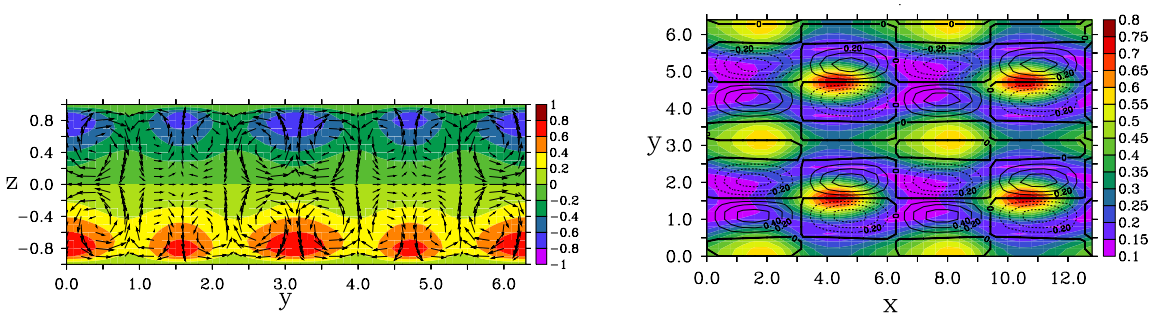

Figure 5.12: $\langle \mathbf{u} \rangle$, u_+ and Ω of a state of the F-branch. This branch is the first state of the $\mathcal{E}$ class and the first stationary state bifurcating in the I symmetric subspace.

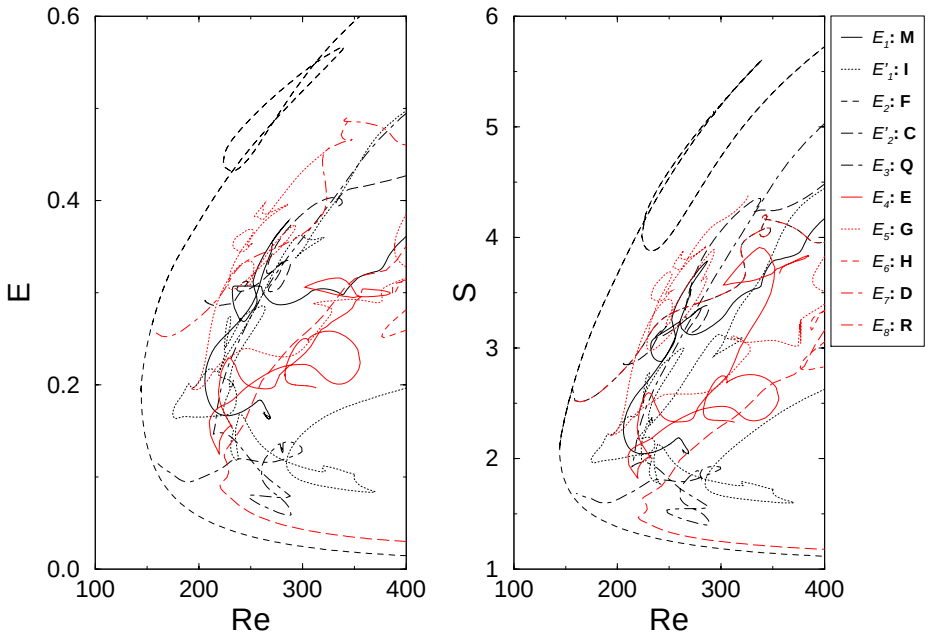

Figure 5.13: Energy and shear rate of the members of the $\mathcal{E}$ class.

by the other members. Due to its high symmetry the β-branch, $\mathcal{D}_1$, exists in both symmetry groups NBC and I. The bifurcation diagram (Fig. 5.11) shows that this state exists only in a distinct range of Reynolds numbers. It is born by a forward saddle node bifurcation and vanishes by performing a back saddle node bifurcation.

5.3.2 Stationary states in the I symmetry group

$\mathcal{E}$ class

States of the $\mathcal{E}$ class are similar to the members of the $\mathcal{B}$ class. They consist of localized streaks with alternating sign arranged on a grid with a grid space of $L_{x,y}/2$. The first state of

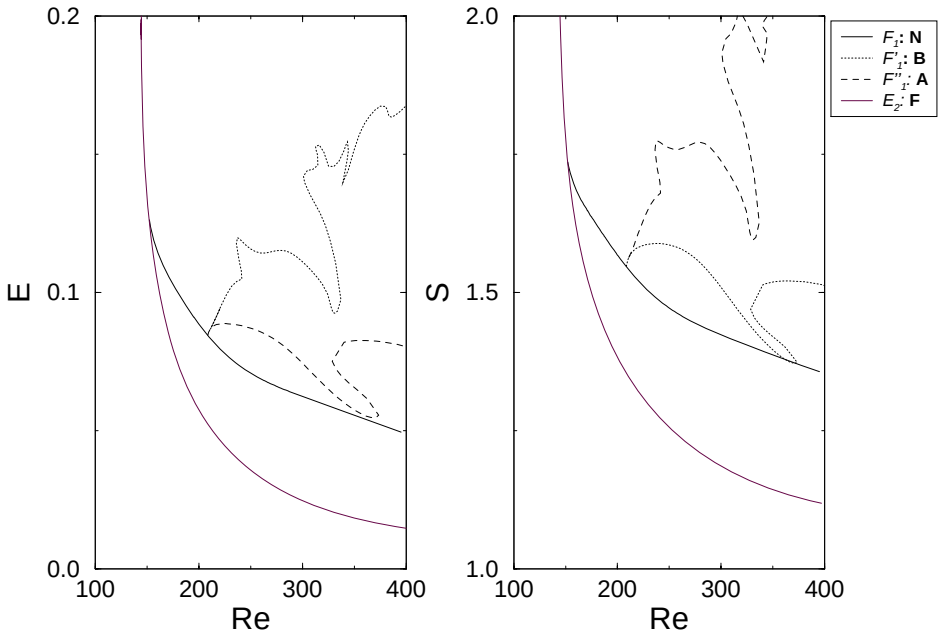

Figure 5.14: Energy and shear rate of the members of the $\mathcal{F}$ class. The N-branch, $\mathcal{E}_2$ bifurcates from the F-branch, which also entered the figure.

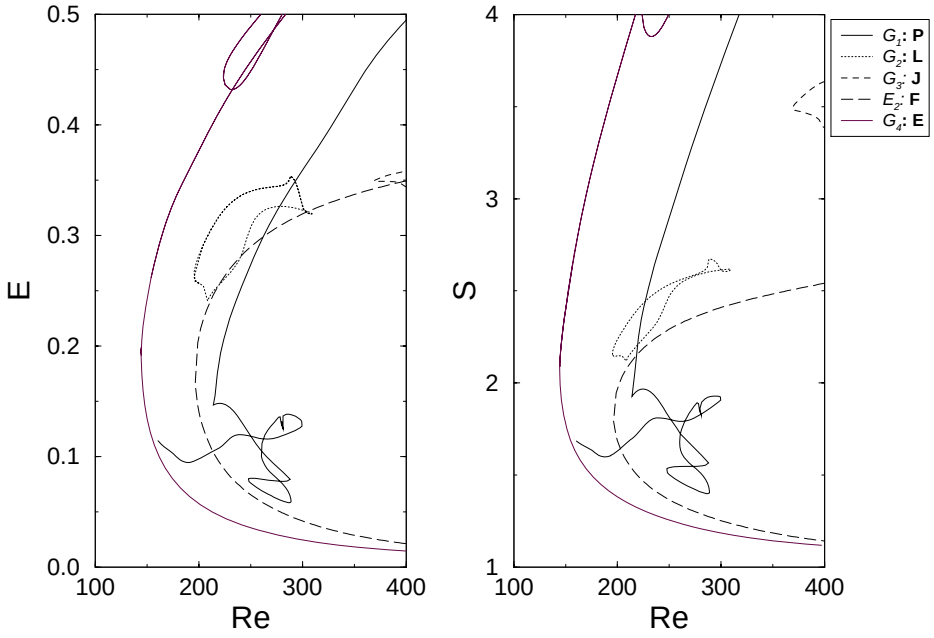

Figure 5.15: Energy and shear rate of the members of the $\mathcal{G}$ class.

the I symmetry group, the F-branch (Fig. 5.12) is member of this class. There are four intensive streaks and four weaker streaks on two layers. There is no average transport between these two layers.

The Q-branch and the R-branch bifurcate from the F-branch and break the $\mathcal{T}_{L_x/2,L_y/2}$ sym-

Name	branch	No. of streaks	No. of streak layers	Symmetries	$Re_{\mathrm{cr.}}$
$\mathcal{E}_1$	M	6	2	$\mathcal{R}_y$	208
$\mathcal{E}_1'$	I	6	2	$\mathcal{R}_y$	173
$\mathcal{E}_2$	F	8	2	$\mathcal{T}_{L_x/2,L_y/2}$, $\mathcal{R}_y$, $\mathcal{R}_z$	144
$\mathcal{E}_2'$	C	8	2		208
$\mathcal{E}_3$	Q	8	2	$\mathcal{T}_{L_x/2}$, $\mathcal{R}_y$, $\mathcal{R}_z$	191
$\mathcal{E}_4$	E	8	2	$\mathcal{T}_{L_x/2}$	210
$\mathcal{E}_5$	G	8	2	$\mathcal{T}_{L_x/2}$	197
$\mathcal{E}_6$	H	8	2		375
$\mathcal{E}_7$	D	8	2	$\mathcal{T}_{L_x/2,L_y/2}$	220
$\mathcal{E}_8$	R	10	4	$\mathcal{R}_z$	155
$\mathcal{F}_1$	N	8	2	$\mathcal{T}_{L_x/4,L_y/4}$, $\mathcal{R}_y$, $\mathcal{R}_z$	151
$\mathcal{F}_1'$	B	8	2	$\mathcal{T}_{L_x/2,L_y/2}$, $\mathcal{R}_z$	206
$\mathcal{F}_1''$	A	8	2		206
$\mathcal{G}_1$	P	4	2		186
$\mathcal{G}_2$	L	6	2		194
$\mathcal{G}_3$	J	8	2		368
$\mathcal{G}_4$	O	10	2	$\mathcal{T}_{L_x/4,L_y/2}$, $\mathcal{R}_y$, $\mathcal{R}_z$	195

Table 5.2: Classification of the different solution branches in the I symmetry group.

metry. So does the N-branch, but this branch belongs to the $\mathcal{F}$ class.

$\mathcal{F}$ class

The first state of the $\mathcal{F}$ class, the N-branch, bifurcates from the F-branch. The other states of this group bifurcate from this branch via pitchfork bifurcations. Therefore, they have all a similar topology. They consist of I-streaks. A state of the N-branch is displayed in figure 5.5a. These elongated streaks extend over the whole spanwise periodic box. Weak S-streaks lie between these long intensive streaks. All streaks on one layer have the same sign and only the A-branch, $\mathcal{F}_1''$, show an average transport between the neutral plane.

$\mathcal{G}$ class

Spatial extended structures characterize the member of this class. They consist of Φ- and H-streaks and are similar to the members of the $\mathcal{D}$ class of the NBC symmetry group. The basic state, the P-branch, $\mathcal{G}_1$, preserves none of the additional symmetries (See figure 5.5b).

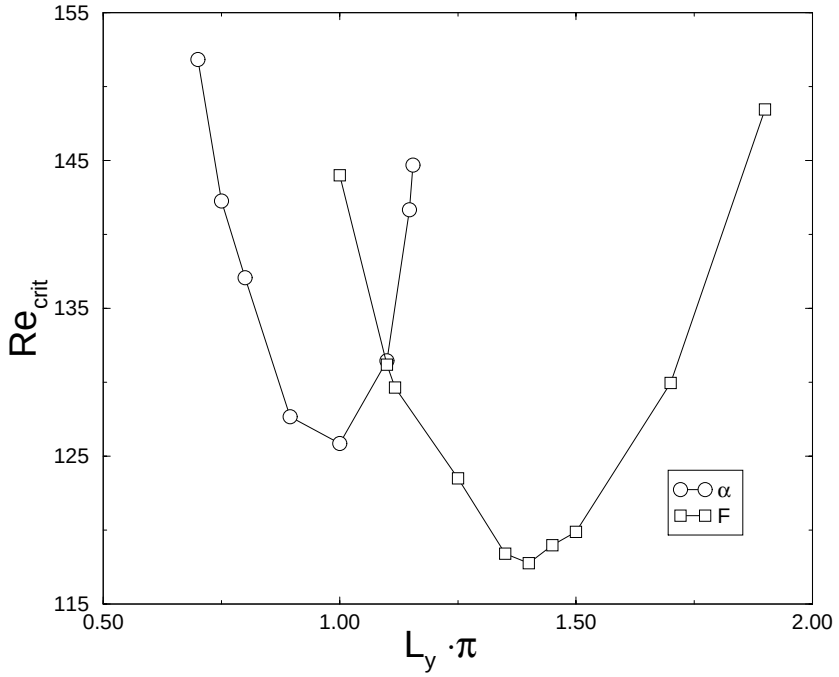

Figure 5.16: Critical Reynolds numbers for the α- and the F-branch for different spanwise extensions and $L_x = 2\pi\, d$. The α-branch shows an optimal aspect ratio of $d : 2\pi\, d : \pi\, d$ (wall normal: streamwise: spanwise), where its critical Reynolds number equals $\mathrm{Re}_{\mathrm{cr}} = 125$. The F-branch has an optimal aspect ratio of $d : 2\pi\, d : 1.39\pi\, d$. In this aspect ratio, it bifurcates at $\mathrm{Re}_{\mathrm{cr}} = 117.4$.

5.4 The wavelength selection

In this section, I investigate the optimal aspect ratio of the first branch of the `NBC` and the `I` group. Then I will show how the basic physical mechanisms responsible for the formation of the stationary state determine the aspect ratio. The ideas follow the work done by Waleffe [105], though he applied these ideas on the self sustaining process in turbulent flow instead for the structure of stationary states in plane Couette flow. I will show that the basic properties of the stationary states can be interpreted by the two basic mechanisms of this self sustained process.

5.4.1 The optimal aspect ratio for the α- and the F-branch

The α- and the F-branch are the first stationary states bifurcating in the `NBC` and the `I` symmetry group, respectively. While the α-states consist of two neighboring S-streaks (Fig. 5.4), the F-states consist of two layers of streaks (Fig. 5.12 left panel). The streaks of the α-branch show a width of $\frac{\pi}{2}d$ and fill the gap. The F-branch are only of $\frac{d}{2}$ height and have a width of $\frac{\pi}{4}d$, but their length does not equal the half box length along the streamwise direction (Fig. 5.12 right panel).

Varying the spanwise boxlength L_y for fixed gap size and streamwise extension $L_x = 2\pi\, d$ shows that the two branches have a different optimal aspect ratio (Fig. 5.16). The α-branch has an optimal aspect ratio of $d : 2\pi\, d : \pi\, d$ (wall normal: spanwise: streamwise), which is in agreement with the results obtained by Busse and Clever [27]. In this aspect ratio the F-branch has a critical Reynolds number of 144. However, the optimal critical Reynolds number for the F-branch lies below this value. For a ratio of $d : 2\pi\, d : 1.39\pi\, d$ it bifurcates at $\mathrm{Re}_{\mathrm{cr}} = 117.4$.

To understand qualitatively the existence of optimal wavelengths, I discuss the basic mechanism which are responsible for the topological structure of the stationary states: the lift-up effect and the streak breakdown.

5.4.2 The lift-up effect

Consider the linearized evolution equation (3.1) for an infinitesimal disturbance of the plane Couette flow without streamwise dependence:

$$\begin{aligned} \frac{\partial}{\partial\, t} u &= -w + \frac{1}{Re}\Delta u \\ \frac{\partial}{\partial\, t} v &= -\frac{\partial}{\partial\, y} p + \frac{1}{Re}\Delta v \\ \frac{\partial}{\partial\, t} w &= -\frac{\partial}{\partial\, z} p + \frac{1}{Re}\Delta w\,. \end{aligned} \tag{5.11}$$

$\mathbf{u}$ vanishes at the plates since no-slip boundary conditions are applied:

$$\mathbf{u}|_{z=\pm\frac{1}{2}} = 0.$$

Note, that in this investigations the gap width is set to one and not to two. Since there is no streamwise dependence the continuity equation simplifies to

$$\text{div}\ \mathbf{u} = \frac{\partial}{\partial\, y} v + \frac{\partial}{\partial\, z} w = 0. \tag{5.12}$$

The equations of motion for v and w decouple from $\frac{\partial}{\partial t} u$. The evolution equation for u equals a passive scalar problem where u is driven by w. Such type of equation have been studied by Pearson and Abernathy [81] and Moore [65]. (v, w) are expressed in terms of a stream function ψ, i.e. $(v, w) = \text{curl}\ (\psi\, \mathbf{e}_x)$. The equation of motion for ψ equals

$$\frac{\partial}{\partial\, t}\Delta\psi = \mathrm{Re}^{-1}\Delta\Delta\psi\,, \tag{5.13}$$

and the no-slip boundary conditions for v and w give the following boundary conditions for ψ:

$$\psi|_{z=\pm\frac{1}{2}} = \frac{\partial}{\partial z}\psi|_{z=\pm\frac{1}{2}} = 0\,. \tag{5.14}$$

One can apply a Fourier-expansion in u and ψ along the spanwise direction. Along the wall normal direction two different expansions are needed since u and ψ fulfill different boundary conditions.

ψ can be expanded in terms of the even and odd Chandrasekhar-beam-functions $C_i(x)$ and $S_i(x)$ [20], where

$$C_m(x) = \frac{\cosh \lambda_m x}{\cosh \frac{1}{2}\lambda_m} - \frac{\cos \lambda_m x}{\cos \frac{1}{2}\lambda_m} \tag{5.15}$$

$$S_m(x) = \frac{\sinh \mu_m x}{\sinh \frac{1}{2}\mu_m} - \frac{\sin \mu_m x}{\sin \frac{1}{2}\mu_m} \tag{5.16}$$

and λ_m and μ_m are roots of the characteristic equations

$$0 = \tanh \frac{1}{2}\lambda + \tan \frac{1}{2}\lambda \tag{5.17}$$

$$0 = \coth \frac{1}{2}\mu - \cot \frac{1}{2}\mu \,. \tag{5.18}$$

Expanding the stream function ψ only in terms of $C_m(x)$ a solution of (5.13) reads

$$\psi = \sum_{n=1}^{\infty} \sum_{l=-\infty}^{\infty} \tilde{\psi}_{nl} C_n(z) \exp\left(\frac{2\pi\, il}{L_y} y - \frac{1}{\mathrm{Re}} \left(\frac{4\pi^2 l^2}{L_y^2} + \tilde{\omega}_n \right) t \right) \,, \tag{5.19}$$

where the coefficients $\tilde{\omega_n}$ are

$$\tilde{\omega}_n = \int_{-\frac{1}{2}}^{\frac{1}{2}} \mathrm{d}z\, C_n(z) \frac{\partial^2}{\partial z^2} C_n(z) \,.$$

u is expanded in a Cosine expansion, which also fulfills the boundary conditions:

$$u = \sum_{n=0}^{\infty} \sum_{l=-\infty}^{\infty} \tilde{u}_{n,l}(t) \cos\left((2n+1)\, \pi\, z \right) \exp\left(\frac{2\pi\, il}{L_y} y \right) \,. \tag{5.20}$$

The reality of both u and ψ demands further that $\tilde{u}_{n,l} = \tilde{u}^*_{n,-l}$ and $\tilde{\psi}_{n,l} = \tilde{\psi}^*_{n,-l}$.

The evolution equation for the coefficients $\tilde{u}_{n,l}(t)$ equals

$$\frac{\partial}{\partial\, t} \tilde{u}_{n,l}(t) = -\sum_{m=0}^{\infty} \frac{2\pi i\, l}{L_y} P_{m,n} \tilde{\psi}_{m,l} - \frac{\pi^2}{\mathrm{Re}} \left(\frac{4}{L_y^2} l^2 + (2n+1)^2 \right) \tilde{u}_{n,l} \,, \tag{5.21}$$

where $P_{m,n}$ is the projection of the even C_{m+1} onto the cosine:

$$P_{m,n} = \int_{-\frac{1}{2}}^{\frac{1}{2}} \mathrm{d}z \cos((2n+1)\, \pi z) C_{m+1}(z) \,. \tag{5.22}$$

The vortex ψ transfers energy from the mean flow into the streamwise velocity u and build up the streaks. Since the vortex vanishes for $t \to \infty$ this amplification is only of transient nature. The imaginary unit i induces the observed phase shift and the width of the streak equals the width of the vortices.

Using one distinct wavelength and only the first coefficient for the expansions of ψ and u in the wall normal direction simplifies the equations. Setting $l = 1$, $n = 0$, using $\lambda = \frac{1}{\mathrm{Re}}\left(\frac{4\pi^2}{L_y^2} + \tilde{\omega}_1\right)$, $\mu = \frac{\pi^2}{\mathrm{Re}}\left(\frac{4}{L_y^2} + 1\right)$, and $A = \frac{2\pi i}{L_y} P_{1,1}\tilde{\psi}$, equation (5.21) reduces to

$$\frac{\partial}{\partial t}\tilde{u}(t) = -Ae^{-\lambda t} - \mu\tilde{u}(t)\,, \tag{5.23}$$

which has the solution

$$\tilde{u}(t) = \frac{A}{\mu - \lambda}\left(e^{-\mu t} - e^{-\lambda t}\right)\,. \tag{5.24}$$

The amplitude of $\tilde{u}(t)$ shows a growth followed by an exponential decay. It reaches its maximum at $t_{\max} = \frac{\ln\lambda - \ln\mu}{\lambda - \mu}$ and the maximum amplitude is

$$u_{\max}(t_{\max}) = \frac{A}{\mu - \lambda}\left(\left(\frac{\lambda}{\mu}\right)^{-\frac{\mu}{\lambda-\mu}} - \left(\frac{\lambda}{\mu}\right)^{-\frac{\lambda}{\lambda-\mu}}\right)\,. \tag{5.25}$$

Since λ and μ are proportional to Re^{-1} the maximum of $\tilde{u}(t)$ grows linear with Re. Fig. 5.17 shows $u_{\max}$ at a Reynolds number of 100 and $\tilde{\psi} = -\frac{i\,L_y}{2\pi P_{1,1}}$ for different spanwise extensions L_y. The optimal width equals $\tilde{L}_y = 1.8889$.

The above investigations are the hydrodynamical interpretation of the non normality of the linear evolution equation for infinitesimal disturbances of parallel shear flows [4, 43, 46, 47, 105, 106]. Butler and Farrell studied the general case of the linearized evolution equation [17]. They calculate an optimal spanwise length for a streamwise vortex at $\mathrm{Re} = 100$ of 1.66.

Though the stationary states are intrinsically time independent this mechanism is responsible, because it is the only mechanism to amplify energy. In the next section, I will show how an additional linear mechanism selects the lengths of the streaks: the breakdown of streamwise streaks.

5.4.3 Streak breakdown

The vortices feed the streaks by the lift-up effect. Since the fluid is sheared between these streaks a shear instability occurs which breaks down the streaks. The above discussion showed that the amplitude of the streak is of the order Re. Since the investigated streaks are not staggered one can simplify the stability analysis to a two dimensional streak having

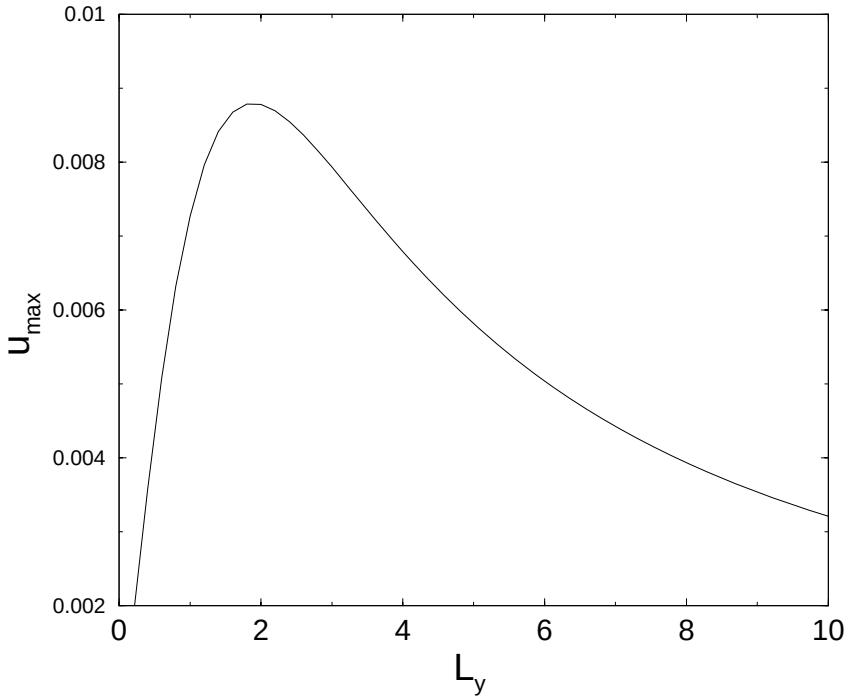

Figure 5.17: The maximum amplitude of the streamwise velocity $\tilde{u}(t)$ amplified by a streamwise vortex ψ for different spanwise extensions of the box (5.25), with $\mathrm{Re} = 100$ and $\tilde{\psi} = -\frac{iL_y}{2\pi P_{1,1}}$.

only a streamwise and a spanwise dependence. The linear evolution of a $2d$ disturbance represented by a stream function $\phi(x, y, t)$ of a time independent laminar flow $\Phi(y)$ equals:

$$\frac{\partial}{\partial t}\Delta\phi = \frac{\partial}{\partial x}\phi\frac{\partial}{\partial y}\Delta\Phi - \frac{\partial}{\partial y}\Phi\frac{\partial}{\partial x}\Delta\phi + \frac{1}{\mathrm{Re}}\Delta\Delta\phi\,. \tag{5.26}$$

Since $\frac{\partial}{\partial y}\Phi = u$, this equation reduces to the Orr-Sommerfeld equation: [35, 61]

$$\frac{\partial}{\partial t}\Delta\phi = \left(\frac{\partial^2}{\partial y^2}u\right)\frac{\partial}{\partial x}\phi - u\frac{\partial}{\partial x}\Delta\phi + \frac{1}{\mathrm{Re}}\Delta\Delta\phi\,. \tag{5.27}$$

The streak corresponds to

$$u(y) = u_0\cos\left(\frac{2\pi}{L_y}y\right) = u_0\cos(\alpha y)\,, \tag{5.28}$$

and the disturbance is expressed in a Cosine-expansion,

$$\phi(x, y, t) = \sum_{m=-\infty}^{\infty}\exp\left(im\gamma x\right)\sum_{n=0}^{\infty}g_{m,n}\cos\left(\alpha\, ny\right)e^{\lambda t}\,, \tag{5.29}$$

with $g_{m,n} = g^*_{-m,n}$. Using only the first two terms of the Cosine-expansion, taking only one wave in streamwise direction, i.e. $|m| = 1$, and substituting equation (5.28) and (5.29) into

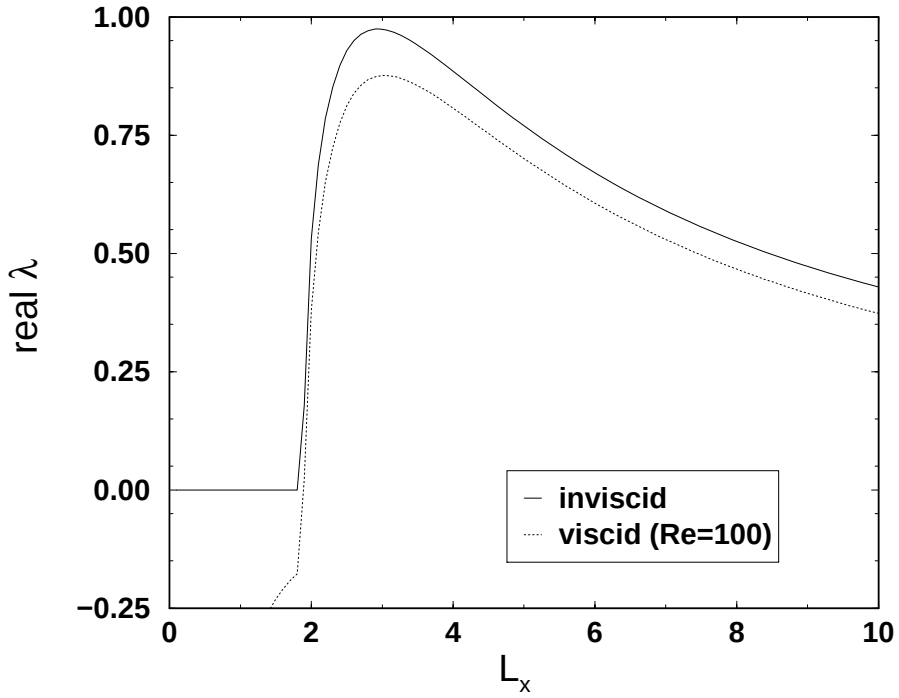

Figure 5.18: Real part of the leading eigenvalue of the Orr-Sommerfeld equation for the infinitesimal perturbation of a periodic two dimensional streamwise streak, with a spanwise width of $\tilde{L}_y = 1.8889$ and an amplitude of $u_0 = 1$. In the inviscid case and the viscid case at $\mathrm{Re} = 100$.

equation (5.27) leads to an eigenvalue problem for the vector (g_0, g_1):

$$\lambda g_0 = -\frac{i\gamma u_0}{2} g_1 - \frac{\gamma^2}{\mathrm{Re}} g_0 \tag{5.30}$$

$$\lambda g_1 = i\gamma u_0 \frac{\alpha^2 - \gamma^2}{\alpha^2 + \gamma^2} g_0 - \frac{\alpha^2 + \gamma^2}{\mathrm{Re}} g_1 \,. \tag{5.31}$$

In the inviscid case, i.e neglecting the dissipative terms, the eigenvalues are

$$\lambda_{1,2} = \frac{|\gamma u_0|}{\sqrt{2}} \sqrt{\frac{\alpha^2 - \gamma^2}{\alpha^2 + \gamma^2}} \,. \tag{5.32}$$

Disturbances with a wavelength smaller than the streak width are marginally stable and show an oscillatory instability in the inviscid and a damped oscillatory decay in the viscid case. All disturbances with a wavelength larger than the streak width are linearly unstable. In figure 5.18 values for the leading eigenvalue λ in the inviscid and the viscid case at $\mathrm{Re} = 100$ are shown. The width of the streak was chosen as the optimal value calculated in the above section 5.4.2, $\tilde{L}_y = 1.8889$. The amplitude of the streak was set to $u_0 = 1$. The maximum of the leading eigenvalue lies for the inviscid case $\tilde{L}_x = 2.935$, and at $\tilde{L}_x = 3.035$, in the viscid case.

After the streak instability occurs vortex filaments start to grow at the shear layer. These vortex filaments are rotated by the shearing of the laminar flow field and change their orientation into the streamwise direction. Then they start to build up new streamwise streaks via the lift up effect.

The above mechanisms are also relevant for the stationary states. Since the lift-up effect is the only mechanism which compensates the energy loss by viscous effects, stationary states have to consist of streamwise vortices. The optimal width of the vortex corresponds to the optimal energy input. These vortices feed streaks which have a shear instability. The most unstable disturbance will break down these streaks and transfer most of the energy into vortex filament, which are coupled via nonlinear effects to the streamwise vortices. Hence, the width of the streaks presumably corresponds to the optimal width of the streamwise vortices and their length corresponds to the most unstable wavelength of the shear instability. These two wavelengths give an optimal energy flow and lead to the following optimal aspect ratios: for the inviscid case, the optimal ratio is about $d : 1.553\tilde{L}_y\, d : \tilde{L}_y\, d$ (streamwise:spanwise) and in the viscid case the ratio equals $d : 1.605\tilde{L}_y\, d : \tilde{L}_y\, d$.

The values of the obtained aspect ratio are between the observed values. The differences have their origin in the strong simplifications which have been applied in the above investigations. In fact, the streamwise vortices and the streamwise streaks have a streamwise dependence and the nonlinear coupling between the streak breakdown and the streamwise streaks has not been investigated here. The influence of the symmetries which imply a streamwise dependence and spatial correlations between vortices and streaks have also been ignored.

However, the above results illustrate the effects leading to a selection of the wavelengths and the basic mechanisms being responsible for the formation of stationary states.

5.5 Conclusions

There is a great variety of stationary states in plane Couette flow. These states consist of streamwise vortices and streamwise streaks and show four different streak topologies: $S-$, $I-$, $H-$ and Φ streaks. All states are born in saddle node or pitchfork bifurcations. All states are linearly unstable, except the α-node (See chapter 6.2.1 for a further discussion of its stability properties). A further classification of the stationary states show that there are four different classes of states in the NBC symmetry group and three classes in the I symmetry group. The members of these classes can be distinguish by the number streaks and streak layers, and the symmetry properties of $\langle \mathbf{u} \rangle$, u_+ and Ω.

The first state of the NBC symmetry group, the α-branch, has an optimal aspect ratio of $d : 2\pi\, d : \pi\, d$, where it bifurcates at $\mathrm{Re}_{\mathrm{cr}} = 125$. In this aspect ratio, the F-branch,

the first state in the `I` symmetry group, bifurcates at 144. Changing the aspect ratio to $d : 2\pi\, d : 1.39\pi\, d$ shows that its critical Reynolds number equals 117.4.

The mechanisms responsible for the formation of the stationary states are the linear lift-up effect and the streak breakdown. Both effects are linear and have been studied by Waleffe et al. to explain the self-sustaining process in turbulent motions [41, 42, 105, 107]. Looking for the optimal coupling between these two mechanism suggests an optimal aspect ratio of about $d : 1.606\, \tilde{L}_y\, d : \tilde{L}_y\, d$, where $\tilde{L}_y \approx 1.8889$.

So far, the role of this stationary states for the transition to turbulent has not been investigated. In the next chapter, I will discuss their influence on this transition.

6 Stationary states and the transition to turbulence

Blödem Volke unverständlich
treiben wir des Lebens Spiel.
Gerade das, was unabwendlich,
fruchtet userm Spott als Ziel.

Magst es Kinder-Rache nennen
an des Daseins tiefem Ernst;
wirst das Leben besser kennen,
wenn du uns verstehen lernst.

Galgenberg, C. Morgenstern[66]

There are various stationary states in plane Couette flow. At $\mathrm{Re} = 125$ a first pair of states bifurcates in the NBC group. Further pairs bifurcate at $\mathrm{Re} \approx 140$ in both symmetry groups. The number of stationary states increases rapidly for higher Reynolds number. In this chapter, I will show how these stationary states change the flow in the phase space. Energy, shear rates and an additional shear measure for the stationary states are compared with the time averaged values of the turbulent state, measured in chapter 4, and give another interpretation of the results obtained in the annealing experiments. The different types of possible heteroclinic connections are discussed and the flow between the stationary states is investigated at $\mathrm{Re} = 200$ and $\mathrm{Re} = 240$.

6.1 Statistical properties of the stationary states and the turbulent state – an interpretation of the annealing experiment.

The lifetime statistics of finite perturbations in chapter 4 have shown that the transitional Reynolds number is about $\mathrm{Re} = 315 \pm 10$. By performing annealing experiments it was also possible to follow the turbulent dynamics down to Reynolds numbers of about 240. The turbulent dynamic take place in a distinct region of the phase space, which is independent of the nature of the perturbation. The region shifts for different Reynolds numbers. The annealing experiments take care of this shift. The perturbation lies always in the vicinity of the turbulent state and can relax onto this state, while the Reynolds number is decreased.

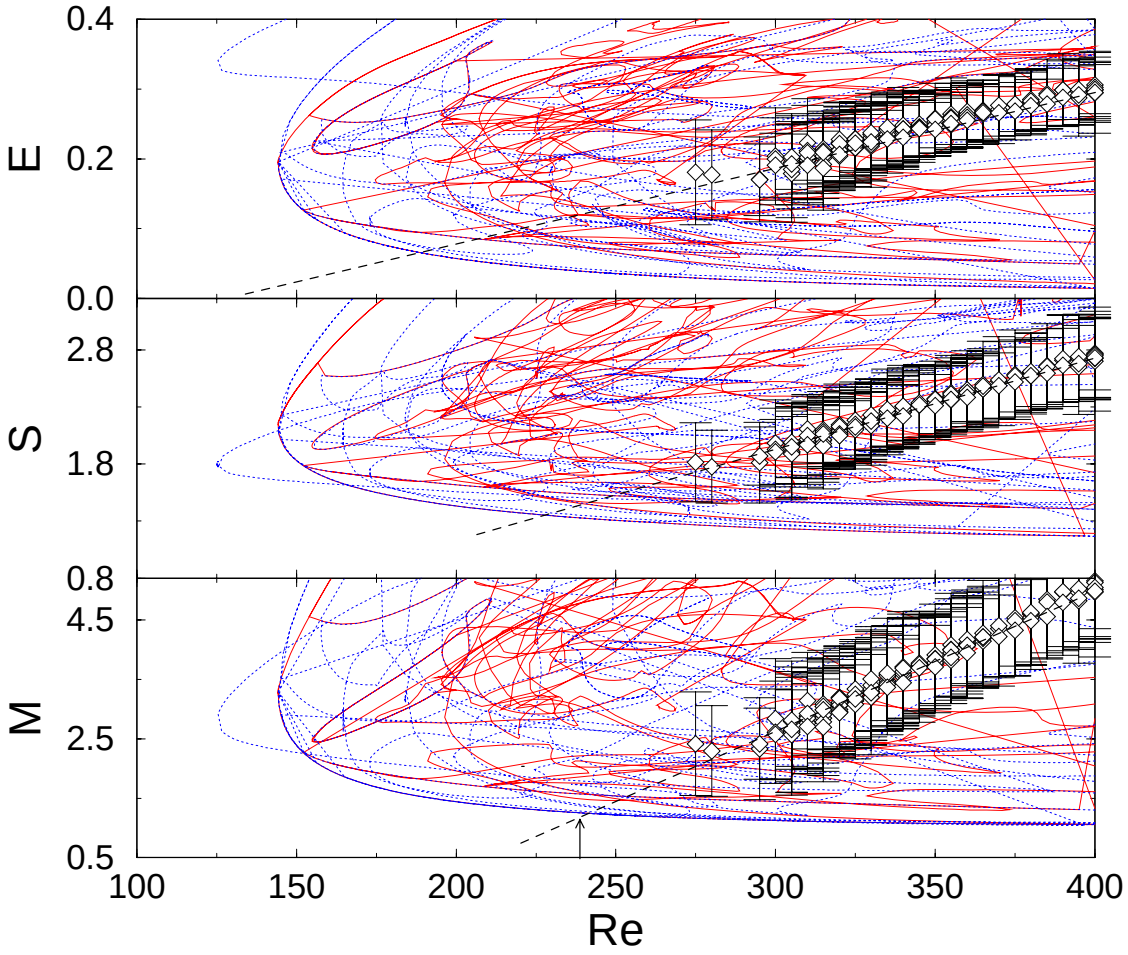

Figure 6.1: Energy (upper panel), the shear rate (middle panel), and the average shear measure (6.1) (lower panel) of the stationary states of the `NBC` (dotted lines) and the `I` (solid lines) symmetry group, and the time average of turbulent perturbations calculated in chapter 4 ($\diamond$) for different Reynolds numbers. The dashed lines extrapolate the shift of the turbulent state to lower Reynolds numbers. At $\mathrm{Re} \approx 240$ the shear measure of the time average quantity falls below the value of the stationary states.

The perturbation is able to follow the movement of the turbulent state until it escapes via the unstable manifold of the turbulent state.

Figure 6.1 shows the time averaged energy and the shear rate of the turbulent state measured in chapter 4 and the values of the stationary states. Since the shear rate reflects only the shearing at one plate and ignores internal shearing due to staggered streaks, an average shear measure, defined by

$$M = \frac{1}{A} \int_{-1}^{1} \mathrm{d}z \left(\int_A \frac{\partial}{\partial z} (u + z) \right)^2 , \tag{6.1}$$

also entered Figure 6.1.

At Reynolds numbers above $\mathrm{Re}_{\mathrm{tr}}$ the turbulent state lies in regions of the phase space, where a couple of stationary states exists. For decreasing Reynolds numbers the values of the energy, shear rate, and the shear measure decrease. Linear extrapolation of this shift to lower Reynolds numbers shows that the value of the average shear measure falls below the values of the stationary states at $\mathrm{Re} \approx 240$ (Fig. 6.1). This observation suggests that the turbulent state can only sustain in the vicinity of the stationary states. And that the turbulent state approached by time dependent perturbations and close vortex filaments, which dominates the phase space at higher Reynolds numbers, leaves the vicinity of the stationary states at $\mathrm{Re} \approx 240$.

On the other hand, stationary states exists for Reynolds numbers below 240 and nonlinear transients and even turbulent states might be observed if the perturbation starts in the vicinity of these stationary states. The statistical properties of these states are different from the one of the turbulent state which dominates the phase space at higher Reynolds numbers. This observation suggest that these turbulent states become less dominant at higher Reynolds numbers and might even unify with the observed dominant turbulent state.

The responsible phase space structure might be heteroclinic or homoclinic connections between the stationary states. These connections are able to generate a nontrivial flow between different stationary states and allow a perturbation starting on this flow to sustain before it decays.

6.2 Investigation of heteroclinic and homoclinic connecting flows

In this section I will focus on the heteroclinic and homoclinic flows in the vicinity of the stationary states, which are presumably generated by heteroclinic connections and homoclinic orbits. Additionally, I study the dynamic in the vicinity of the α-branch, which allows periodic and nonlinear transient motions at Reynolds numbers below 240 in regions of the phase space not approached by the turbulent state studied in chapter 4.

I start with an investigation of the stability of the α-branch. Then I discuss the different types of the known heteroclinic connections build up by saddle node and pitchfork bifurcations and investigate the formation of heteroclinic and homoclinic flows for $\mathrm{Re} = 200$ and $\mathrm{Re} = 240$.

6.2.1 Hopf bifurcations of the α-node

Busse and Clever showed that in a small region of the parameter space the node of the α-branch is linearly stable until it undergoes a stable Hopf bifurcation [27]. Figure 6.2 shows the real part of the eigenvalues of the Jacobian of the α-branch. At $\mathrm{Re} = 128$ a first pair

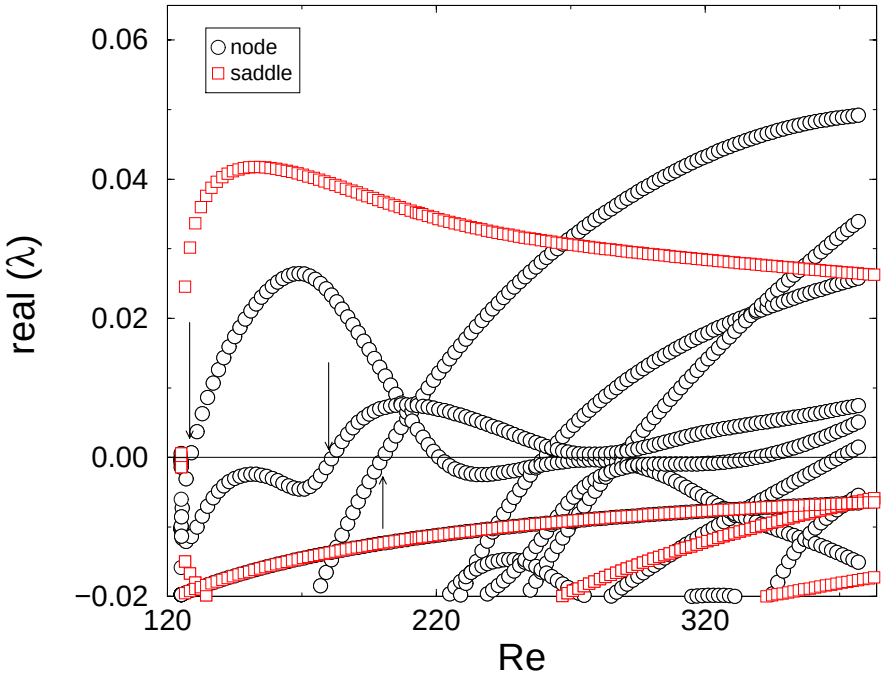

Figure 6.2: Largest real parts of the eigenvalues of the Jacobian of the α-branch for different Reynolds numbers. Circles correspond to the eigenvalues of the node. Squares corresponds to the eigenvalues of the saddle. The node undergoes additional Hopf bifurcations at $\mathrm{Re} = 128$, $\mathrm{Re} = 180$ and $\mathrm{Re} = 199$ (arrows).

of complex conjugate eigenvalues crosses the real axis and generates a stable limit cycle [3, 48, 64, 109].

The singular eigenvalue of the node becomes complex after the saddle node bifurcation at $\mathrm{Re} = 125$ and crosses the real axis at $\mathrm{Re} = 181$. Since the eigenvalue of the center manifold of the saddle is the most unstable eigenvalue, perturbations move from the saddle to the node. The second bifurcation at $\mathrm{Re} = 181$ adds a new unstable manifold to the node. The formerly stable limit cycle changes into an unstable torus. This is illustrated in Figure 6.3 where the time signal of a perturbation starting near the node of the α-branch at $\mathrm{Re} = 200$ is shown: the time signal is not able to approach the formerly stable limit cycle since an additional unstable manifold exists.

The node of the α-branch allows long living states at low Reynolds numbers. Below $\mathrm{Re} = 130$ the node is linearly stable and between 130 and 181 a stable limit cycle exists, which allows a periodic dynamic. Above 181 nonlinear transients are possible since the limit cycle changes into an unstable torus. The energy, shear rate and the shear measure of this orbit and values of the observed nonlinear transients are different from the ones for the turbulent state (See chapter 4 and figure 6.1). Furthermore, its basin of attraction is rather small as the former investigation of finite perturbations suggests. Although the α-branch allows a

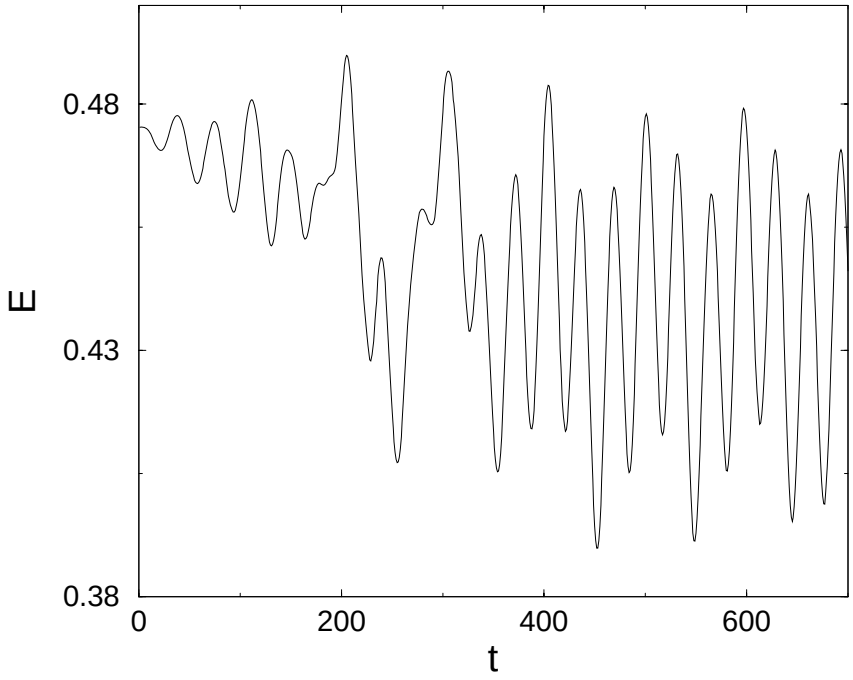

Figure 6.3: Time signal of a perturbation starting at the node of the α-branch at $\mathrm{Re} = 200$, which has already undergone three stable Hopf bifurcations. The time signal is not able to approach the formerly stable periodic orbit since additional unstable manifolds exist.

complex motion it is not responsible for the formation of the turbulent state observed at higher Reynolds numbers.

6.2.2 The origin of heteroclinic connections – pitchfork bifurcations and back saddle node bifurcations

The linear stability analysis of the stationary states shows that there are two types of local bifurcations, which are responsible for the formation of stationary states: pitchfork bifurcations and backward saddle node bifurcations. The term *backward and forward bifurcation* is related to a bifurcation where the Reynolds number is the control parameter.

Figure 6.4 illustrates the effect of these two types of bifurcations. Suppose a saddle node pair. This pair is connected with each other via the center manifold. If one of the members of the pair undergoes a pitchfork or a backward saddle node bifurcation a heteroclinic connection between the new saddle node pair and the other member exists.

An example of a backward saddle node bifurcation is the υ-branch, which undergoes a backward saddle node bifurcation at $\mathrm{Re} = 308$ and is born by a forward saddle node bifurcation at $\mathrm{Re} = 172$ (Fig. 6.5). Part a of the branch is connected with b via the center manifold. At $\mathrm{Re} = 271$, where the c branch exists, the a part is connected with the center manifold

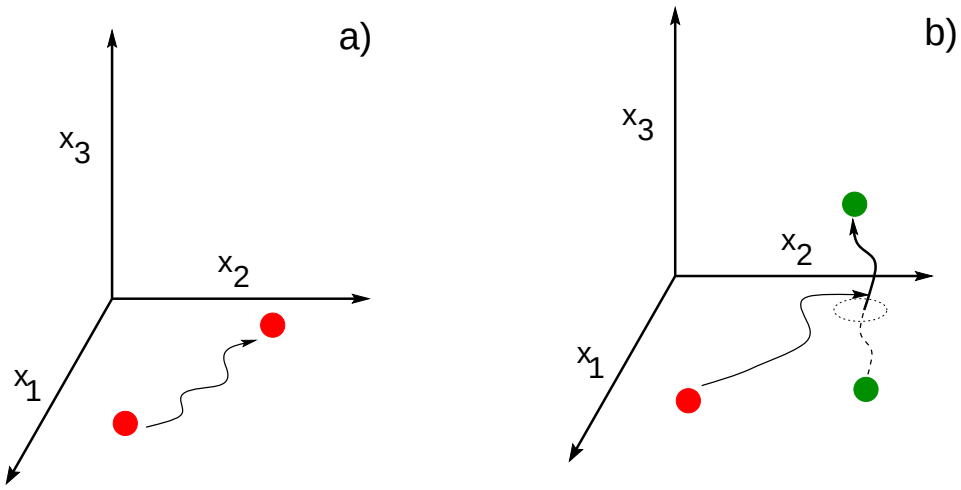

Figure 6.4: Birth of a heteroclinic connection by a pitchfork bifurcation or a backward saddle node bifurcation. A saddle node pair is connected via the center manifold a). This connection still exists though the node undergoes a pitchfork bifurcation b). Now, the saddle is connected with both new states. In case of a backward saddle node bifurcation an existing second connection vanishes because the two states unify b)$\rightarrow$ a).

connecting b and c.

In the NBC subspace the first pitchfork bifurcation occurs at $\mathrm{Re} = 144$, where the υ-branch leaves the γ-branch. This type of bifurcation is symmetry breaking and the γ-branch consists of two states with the same symmetry and equal energy, shear rate and values of the shear measure (See also appendix E).

The first pitchfork bifurcation in the I subspace occurs at $\mathrm{Re} = 151$. The lower part of the F-branch undergoes a pitchfork bifurcation at 160 while the upper part of the branch undergoes a pitchfork bifurcation at 156. These four branches are connected via different heteroclinic connections. The first backward saddle node bifurcation occurs at $\mathrm{Re} = 157$ in the NBC subspace on the χ-branch. The D-branch undergo such bifurcations at $\mathrm{Re} = 218$.

Most stationary states undergo backward and forward saddle node bifurcations. As the number of states generated by bifurcations increases for growing Reynolds numbers the number of heteroclinic connections also increases. However, this mechanism can only generate a global flow between states of the same solution branch. The flow becomes even more complex if a heteroclinic connection between different branches occurs. Furthermore, most of the connections are unstable, i.e. the saddle has an additional unstable eigenspace with a higher growth rate than the one of the center manifold. In cases, where the node also has additional unstable eigenspaces the flow induced by the center manifold is no longer observable.

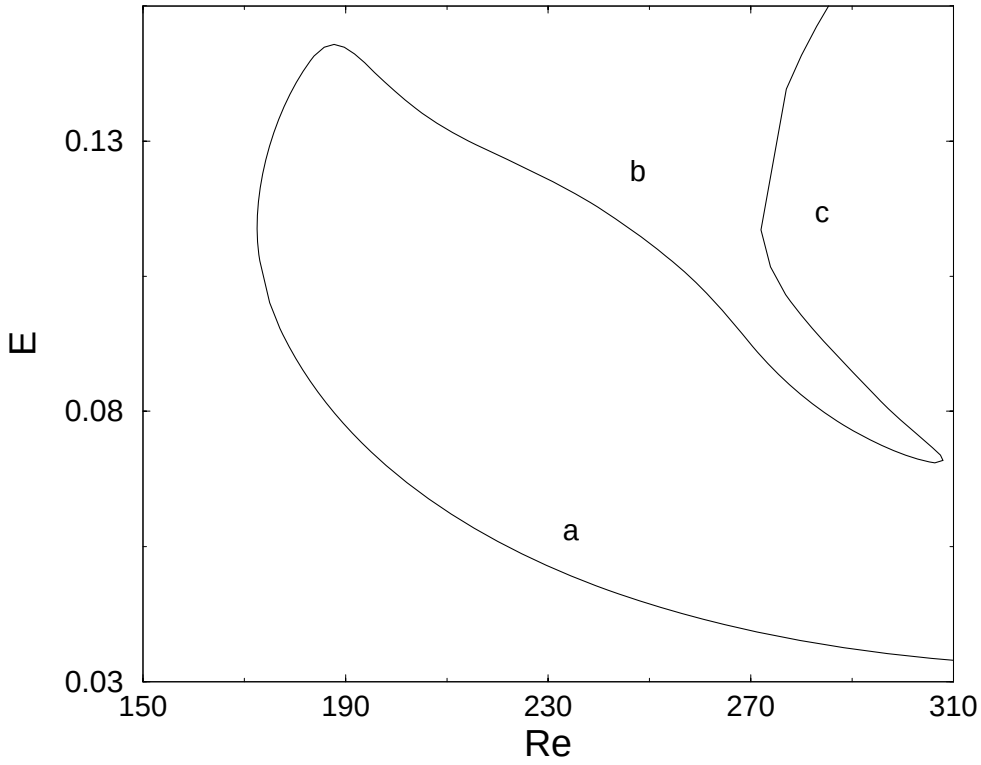

Figure 6.5: Example of a backward saddle node bifurcation. The v-branch is born in a saddle node bifurcation at $\mathrm{Re} = 172$ and undergoes a backward saddle node bifurcation at $\mathrm{Re} = 308$. The branch a is connected with the branch b via the center manifold. At $\mathrm{Re} = 271$, where the c branch exists, the a branch is connected to the center manifold of b and c.

6.2.3 Investigations of the global flow

In the former section I have illustrated how the bifurcation of stationary states and additional backward and forward bifurcations or pitchfork bifurcations can generate complex heteroclinic connections. Unfortunately, the numerical search for heteroclinic connections for systems with many degrees of freedom is an difficult task [8].

Problems arise from the mathematical definition of a heteroclinic connection: if $\mathbf{x}_{1,2}$ are two stationary states of a given flow $\mathbf{F}$, then a solution $\tilde{\mathbf{x}}(t)$ of the dynamical system $\frac{\mathrm{d}}{\mathrm{d}\,t}\,\mathbf{x} = \mathbf{F}(\mathbf{x})$ is referred to a heteroclinic connection, if

$$\lim_{t\to-\infty} \tilde{\mathbf{x}}(t) = \mathbf{x}_1 \tag{6.2}$$

$$\lim_{t\to\infty} \tilde{\mathbf{x}}(t) = \mathbf{x}_2\,. \tag{6.3}$$

If $\mathbf{x}_1 = \mathbf{x}_2$ this connection is a homoclinic orbit.

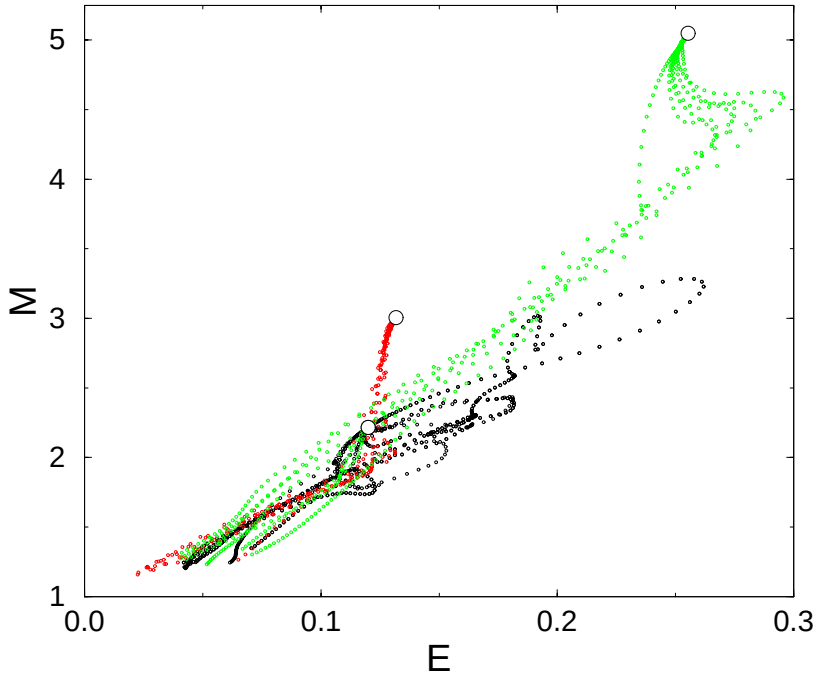

Figure 6.6: Illustration of the flow between the states of the N-branch at $\mathrm{Re} = 240$. The circles correspond to the stationary states of the N-branch. The evolution of an ensemble of 20 perturbations of each stationary state is shown. There is a flow from the two states at higher energies and values of the shear measure down to the third one.

One can weaken this definition by setting the infinite time interval to a finite one. To reformulate this problem into a boundary value problem, one uses projection boundary conditions [8]. $\Lambda_{1,2}^{\pm\, i}$ is the i^{th} eigenvector of the $N_{1,2}^{\pm}$ dimensional stable (-) or unstable (+) manifold at $\mathbf{x}_{1,2}$. Using an inner product $(\cdot,\cdot)$ the projection boundary conditions equal:

$$\forall i = 1, ..., N_1^- \,:\, \left(\Lambda_1^{-\, i}, \tilde{\mathbf{x}}(T_-) - \mathbf{x}_1\right) = 0 \tag{6.4}$$

$$\forall i = 1, ..., N_2^+ \,:\, \left(\Lambda_2^{+\, i}, \tilde{\mathbf{x}}(T_+) - \mathbf{x}_2\right) = 0\,. \tag{6.5}$$

$T_\pm$ is the maximal investigated time. Equation (6.4) consists of N_1^- equations and (6.5) consists of N_2^+ equations. The sum of N_1^- and N_2^+ does not always equal the active degrees of freedom. In general, the above problem is under- or overestimated. In case of an overestimated problem one can formulate a well defined problem by introducing additional parameters. However, this needs a knowledge about the presumably connected states.

Furthermore, a time integration of the dynamical system in the interval $T_\pm$ is needed. The time integration of the plane Couette flow reduced to the `I` symmetry with $N_z \leq 9$ and $N \leq 6$, corresponding to 547 active degrees of freedom, and a temporal accuracy of 10^{-8} for a time interval of 100 time units, takes about 4 minutes on a DEC Alpha 500 workstation. Using

a shooting method also the numerical calculation of the Jacobian is needed. Calculating the Jacobian via a finite difference method of first order takes about 22 hours. Hence, the computation of one correction of the initial guess needs about one day of CPU time.

Therefore, I applied another method which focuses on the flow between the stationary states. If there is a presumably unstable connection an ensemble of states starting at $\mathbf{x}_1$ will follow this connection into the vicinity of $\mathbf{x}_2$.

I show such an experiment in figure 6.6. An ensemble of 20 perturbations with a distance of 0.0075 was randomly distributed in the vicinity of a stationary state. By studying the evolution of such an ensemble one can identify the dominant existing connections. Figure 6.6 shows the flow between the states of the N-branch at $\mathrm{Re} = 240$. There is a flow from the two states at higher energies and values of the shear measure down to the third one.

To investigate the heteroclinic and homoclinic connecting flows, I study the evolution of an ensemble of states lying near a stationary state and follow their evolution. I restrict myself to investigations within the energy-shear measure space. It is reasonable to investigate the evolution in this space because any measurement of distances between the perturbations and the stationary states has to deal with the multiplicity of each state, since the application of one of the symmetry operations $\{\mathcal{P}, \mathcal{S}, \mathcal{T}_{\Delta x, \Delta y}\}$ and combinations of them produces a new state. The energy and the shear measure do not change after the application of these symmetric operations and one is always able to identify a stationary state in terms of its energy and its shear measure. Furthermore, the investigations of the time averages of the turbulent states and the energy, shear rate and shear measure of the stationary states showed that the shear measure characterizes the location of the turbulent state better than the shear rate does. Since these investigations base on an investigation of a two dimensional projection of a high dimensional dynamic, the obtained results may be misleading, but the investigation of stationary states showed that those cases are rare and these two scalars identify different states very well.

Connecting flows at $\mathrm{Re} = 200$

Although no nonlinear transient states have been observed at a Reynolds number of 200 (See chapter 4) almost 30 stationary states exist at this Reynolds number. Most stationary states have a dominant unstable manifold which generates a flow to the laminar profile. Only a few stationary states generate a non decaying flow. In Figure 6.7 all stationary states are shown in the E/M-plane at $\mathrm{Re} = 200$. Stationary states marked by open circles show only a flow to the laminar state. Though their lifetime is higher than the lifetime of a finite perturbation one can not speak off a nonlinear transient dynamic. Since, after the perturbation leaves the stationary state the time signal shows an exponential decay.

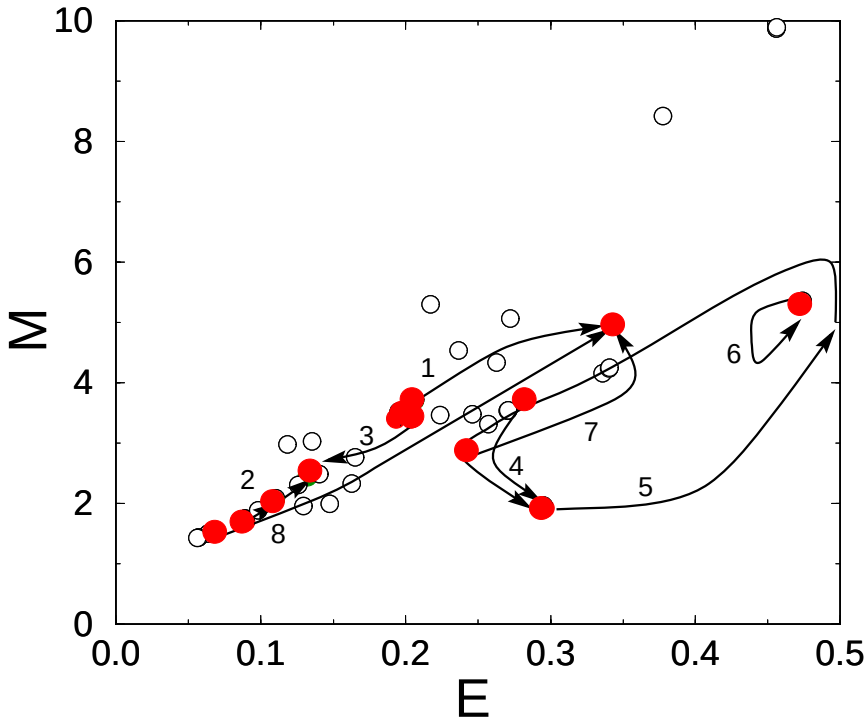

Figure 6.7: Heteroclinic and homoclinic flows extracted from investigations of the global flow at $\mathrm{Re} = 200$. Each circle corresponds to a stationary state. The flow in the vicinity of the open circles goes to the laminar flow. Only the nontrivial flow between stationary states is displayed. Numbers mark the connections, which are shown in table 6.1.

Some stationary states show a different behavior. A heteroclinic flow between these states is visible. These nontrivial connecting flows are listed in table 6.1. There are flows between different branches, like the connection between the D- and the L-branch, and connections of members of different symmetry groups, like the C-α and the C-β connection. The node of the C-branch shows a heteroclinic connecting flow to the β-node (Fig. 6.7-1). Another heteroclinic connecting flow which connects states of the `NBC` and the `I` group connects the L-node with the α-saddle of the (Fig. 6.7-3). Both, the α-saddle and the α-node show homoclinic connecting flows (Fig. 6.7-5 and Fig. 6.7-6). Though there is a connection between these two states via the center manifold no flow have been observed.

Connecting flow at $\mathrm{Re} = 240$

At a Reynolds number of 240 almost 67 stationary states have been observed. There are still many stationary states showing only a flow to the laminar state but there exist at least 11 nontrivial heteroclinic connecting flows which are able to amplify the energy and the shear measure of a perturbation. Figure 6.8 shows these stationary states and the global, nontrivial

1	C $\rightarrow \gamma$
2	D$\rightarrow$ L
3	C $\rightarrow$ L
4	C $\rightarrow \alpha$
5	$\alpha \rightarrow \alpha$ (saddle)
6	$\alpha \rightarrow \alpha$ (node)
7	N $\rightarrow \gamma$
8	$\upsilon \rightarrow \gamma$

Table 6.1: Nontrivial heteroclinic flows at $\mathrm{Re} = 200$. The flow within the E/M-plane is shown in figure 6.7.

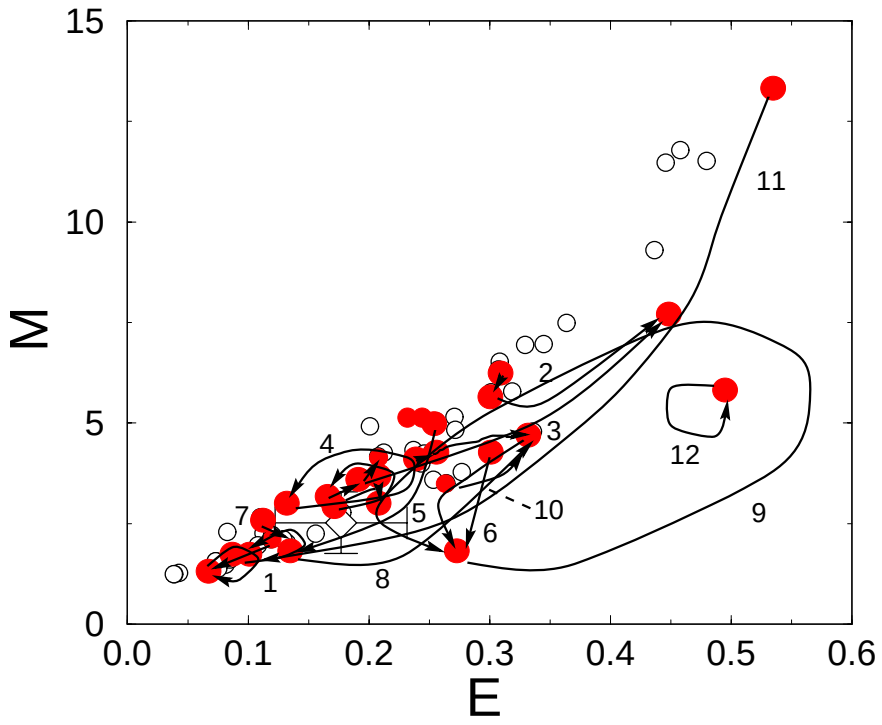

Figure 6.8: Heteroclinic and homoclinic flows extracted from investigation of the flow at $\mathrm{Re} = 240$. Each circle corresponds to a stationary state. The flow in the vicinity of the open circles decays to the laminar flow. Only the non trivial flow between stationary states is shown. The diamond marks the average energy and shear measure and the bars mark its variation, extracted from turbulent time signals 4 at a Reynolds number of about 280.

flow in the E/M-plane. To illustrate the region where turbulent motion takes place at higher Reynolds number the average energy and shear measure, extracted from a turbulent time signal at $\mathrm{Re} = 280$, and its variations are shown. The turbulent state appears in a region of

1)	B $\rightarrow$ B
2)	C $\rightarrow \gamma$
3)	$\delta \rightarrow$ L
4)	I $\rightarrow$ I
5)	E$\rightarrow \beta$
6)	L $\rightarrow \alpha$
7)	O $\rightarrow$ L
8)	N $\rightarrow$ L
9)	$\alpha \rightarrow \alpha$ (saddle)
10)	$\upsilon \rightarrow \beta$
11)	$\sigma \rightarrow \upsilon$
12)	$\alpha \rightarrow \alpha$ (node)

Table 6.2: Nontrivial heteroclinic flows at $\mathrm{Re} = 240$. The flow within the E/M-plane is shown in figure 6.8.

the E/M-plane where at a Reynolds number of 240 many heteroclinic connecting flows are observed. The unstable homocline flow of the α-saddle approaches this region (Fig. 6.8-9). Some of the former heteroclinic flows have vanished, for example the connection between the G-branch and the γ-branch (Fig. 6.7-2). Other branches form additional connections: the υ-branch which is connected to the γ-branch (Fig.6.7-6) connects with the β-branch (Fig.6.8-10) and with the σ-branch.

At a Reynolds number of $\mathrm{Re} = 200$ unstable homoclinic flows exist in the vicinity of the α-branch. A perturbation is only able to move from one stationary state to another. At a Reynolds number of $\mathrm{Re} = 240$ heteroclinic flows to the existing homoclinic flows of the states at the α, the B-, I-, and the N-branches are possible. In table 6.3 the different connections leading to such closed flows are listed.

The formation of the turbulent state

The former investigation shows that there are two different phase space structures which allow nonlinear transients. The first one is built up by the α-branch at $\mathrm{Re} = 128$ where a Hopf bifurcation generates a stable limit cycle around the α-node. This bifurcation has already been investigated by Busse and Clever. These authors proposed that these states are responsible for the transition to turbulence [27]. The dynamic in the vicinity of the α-node shows significantly longer lifetimes even after the birth of additional unstable directions at $\mathrm{Re} = 181$ and $\mathrm{Re} = 199$. But as the leading eigenvalue of the additional unstable eigenspace grows the lifetime of perturbations starting in the vicinity of the α-node decreases for higher

1)	$1 \rightarrow 1$
3)	$3 \rightarrow 6 \rightarrow 9 \rightarrow 9$
4)	$4 \rightarrow 4$
5)	$5 \rightarrow 8 \rightarrow 3 \rightarrow 6 \rightarrow 9 \rightarrow 9$
6)	$6 \rightarrow 9 \rightarrow 9$
7)	$7 \rightarrow 1 \rightarrow 1$
8)	$8 \rightarrow 3 \rightarrow 6 \rightarrow 9 \rightarrow 9$
9)	$9 \rightarrow 9$
10)	$10 \rightarrow 3 \rightarrow 6 \rightarrow 9 \rightarrow 9$
11)	$10 \rightarrow 7 \rightarrow 1 \rightarrow 1$
12)	$12 \rightarrow 12$

Table 6.3: List of combinations of the heteroclinic and homoclinic flows between different branches to perform closed orbits. The numbers correspond to the number in figure 6.8 and table 6.2.

Reynolds number. The basin of attraction of this structure is rather low. Only states starting near the α-node approach it. Small but finite perturbations of the laminar flow do not approach this structure, as the investigation in chapter 4 showed.

Furthermore, the statistical properties of the timesignals of perturbation on this phase space structure are different from the ones observed by lifetime measurements done in chapter 4. Figure 6.9 shows the dynamics of two perturbations starting at the α-saddle and the α-node at $\mathrm{Re} = 240$ and $\mathrm{Re} = 320$ in the E/M-plane (left panel) and the time signals of the shear measure (right panel). The dynamic of the perturbation starting on the α-saddle consist of a burst of energy but the perturbation is not able to regenerate because it falls off the homoclinic connecting flow. The perturbation starting at the α-node follows the flow to the limit cycle but falls off this cycle since the unstable manifold already dominates.

At a Reynolds number of $\mathrm{Re} = 320$ the homoclinic connecting flow of the α-saddle reaches the regions of the phase space where the turbulent state have been observed. The diamond marks the time averaged energy and the shear measure, obtained in chapter 4. The orbit in the vicinity of the α-node is more unstable and the perturbation leaves this region rather fast to approach the turbulent state.

This turbulent state is formed by the complex framework of heteroclinic connecting flows. These flows have their origin in pitchfork bifurcations and backward saddle node bifurcations, but also connecting flows between different branches occurs. A first pitchfork bifurcation occurs at $\mathrm{Re} = 157$ in both symmetric subspaces, where the δ-branch and the F-branch undergo further bifurcations. First backward saddle node bifurcations occur at $\mathrm{Re} = 157$

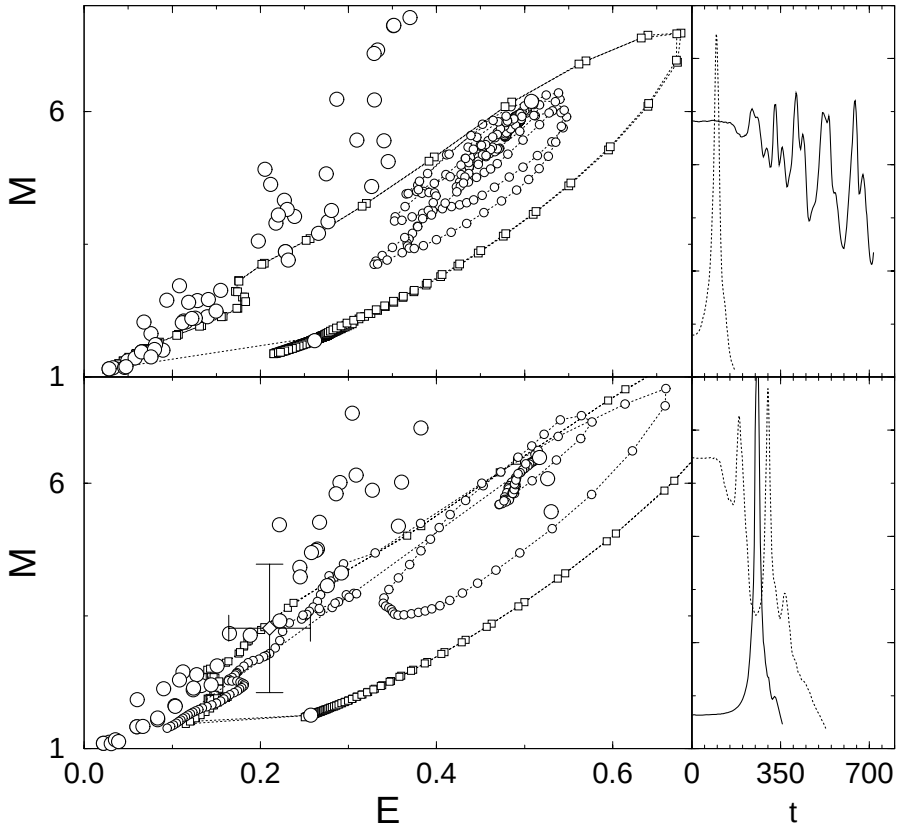

Figure 6.9: Evolution of a perturbation starting at the saddle (squares) and the node (circles) of the α-branch at $\mathrm{Re} = 240$ (upper) and $\mathrm{Re} = 320$ (lower) in the E/M-plane. The open circles correspond to the stationary states at the given Reynolds number. The right panel shows the timesignal of the shear measure. The solid line is the dynamic of a perturbation starting near the node. The dotted line is the dynamic of a perturbation starting near the saddle. The diamond marks the time averaged energy and shear measure of a turbulent state.

and $\mathrm{Re} = 218$. At such small Reynolds numbers no nonlinear transient dynamics has been observed.

The formation of this second structure is a collective phenomenon. For Reynolds numbers above 157 the network of heteroclinic connecting flows starts to grow. At $\mathrm{Re} = 240$ the framework of different connecting flows becomes thick enough to support nonlinear transient dynamics besides the dynamics in the vicinity of the α-node.

While the leading eigenvalue of the α-node increases the escape rate of the second repellor decreases and its relaxation rate increases (chapter 4). At Reynolds numbers above $\mathrm{Re} = 200$ the dominance of the turbulent state in the vicinity of the α-node starts to vanish because the leading eigenvalue of the unstable manifold of the α-node grows and additional unstable eigendirections occurs at $\mathrm{Re} = 260, 288, 339, 369$.

6.3 Conclusions

Two different phase space structures have been identified to be responsible for a transition to turbulence in the plane Couette flow. The first one arises from a stable Hopf bifurcation which has already been investigated by Busse and Clever [27]. This limit cycle is born at a $\mathrm{Re} = 128$. Additional Hopf bifurcations of the α-node destabilized this cylces and supports the formation of an unstable torus. Its basin of attraction is rather small, only perturbations lying in the vicinity of the α-branch approach this structure. Finite but small perturbations of the laminar profile do not seem to be able to approach this cycle.

The second phase space structure is formed by a complex framework of heteroclinic flows. First connections are generated at a Reynolds number of $\mathrm{Re} = 144$ by a pitchfork bifurcation. The first backward saddle node bifurcation occurs at $\mathrm{Re} = 157$. While the connected stationary states approach different regions of the phase space this structure grows rapidly. Additional stationary states bifurcate and add their heteroclinic flows to it.

These two different phase space structures unify at higher Reynolds number. Since the unstable torus at the α-node becomes more and more unstable for higher Reynolds numbers, it looses its dominant role in the phase space and plays only a part in the framework of the turbulent state.

7 Transition to turbulence in a low dimensional model

Ein Paradigma aufzusuchen,
wo[r]nach man dieses deklinieren kann.

G.C. Lichtenberg, J 1257[60]

In order to get a deeper understanding of the transition to turbulence in linearly stable shear flows, a low dimensional model of such a flow is studied. This model, derived by Eckhardt and Mersmann [38], consists of 19 degrees of freedom. Further symmetric decompositions are applied and decrease its degrees of freedom down to 9.

After an introduction to the model and the successive simplification leading to a reduction from 19 down to 9 degrees of freedom, I will show that this system also undergoes a transition to turbulence. It turns out that stationary states bifurcate after the turbulent state has already established. The responsible phase space structures forming this turbulent state are unstable periodic orbits which are not formed by heteroclinic connections and homoclinic orbits of stationary states.

The bifurcations of these periodic orbits are studied and the chapter is closed by evaluating the escape rate and the leading Lyapunov exponent of this turbulent state.

7.1 The model

Consider a plane shear flow. Following the notation of Eckhardt and Mersmann [38], x refers to the spanwise, y to the streamwise and z to the wall normal direction. The incompressible fluid is described by toroidal and poloidal vector fields and two additional flow fields for the mean flow in spanwise and streamwise direction:

$$\mathbf{u} = \text{curl curl } \left(\Phi\left(\mathbf{x}\right)\mathbf{e}_z\right) + \text{curl } \left(\Psi\left(\mathbf{x}\right)\mathbf{e}_z\right) + f\left(z\right)\mathbf{e}_x + g\left(z\right)\mathbf{e}_y\,. \tag{7.1}$$

The flow is periodic in the streamwise and spanwise direction and solves stress-free boundary conditions in the wall normal direction:

$$\frac{\partial}{\partial z}u|_{z=0,z=\pi} = \frac{\partial}{\partial z}v|_{z=0,z=\pi} = w|_{z=0,z=\pi} = 0\,. \tag{7.2}$$

The velocity fields are expressed by Fourier modes. In this representation the poloidal and toroidal vector fields look like:

$$(\text{curl curl } (\Phi(\mathbf{x})\,\mathbf{e}_z))_{\mathbf{k}} = \frac{1}{\sqrt{1+\frac{k_z^2}{k_x^2+k_y^2}}} \begin{pmatrix} -\frac{k_x\,k_z}{k_x^2+k_y^2} \\ -\frac{k_y\,k_z}{k_x^2+k_y^2} \\ 1 \end{pmatrix}$$

$$(\text{curl } (\Psi(\mathbf{x})\,\mathbf{e}_z))_{\mathbf{k}} = \frac{1}{\sqrt{k_x^2+k_y^2}} \begin{pmatrix} k_y \\ -k_x \\ 0 \end{pmatrix} . \tag{7.3}$$

and the full velocity field is expressed by:

$$\begin{aligned} \mathbf{u}(\mathbf{x},t) &= \sum_{\mathbf{k}} \mathbf{u}_{\mathbf{k}}(t) e^{i\mathbf{k}\mathbf{x}} \\ &= \sum_{\mathbf{k}} \left(\alpha_{\mathbf{k}}(t)\,(\text{curl curl } (\Phi(\mathbf{x})\,\mathbf{e}_z))_{\mathbf{k}} + \beta_{\mathbf{k}}(t)\,(\text{curl } (\Psi(\mathbf{x})\,\mathbf{e}_z))_{\mathbf{k}}\right) e^{i\mathbf{k}\mathbf{x}} . \end{aligned} \tag{7.4}$$

The Navier-Stokes equation for the amplitudes $\mathbf{u}_{\mathbf{k}}(t)$ reads

$$\frac{\partial}{\partial t}\mathbf{u}_{\mathbf{k}}(t) = -ip_{\mathbf{k}}\mathbf{k} - i\sum_{\mathbf{p}+\mathbf{q}=\mathbf{k}} (\mathbf{u}_{\mathbf{p}}(t)\cdot\mathbf{p})\,\mathbf{u}_{\mathbf{q}}(t) - \nu\mathbf{k}^2\mathbf{u}_{\mathbf{k}}(t) + \mathbf{F}_{\mathbf{k}} , \tag{7.5}$$

where $p_{\mathbf{k}}$ is the $\mathbf{k}^{\text{th}}$ Fourier component of the pressure (divided by the density) and ν is the kinematic viscosity.

The pressure vanishes in the evolution equation of Φ, Ψ, f and g because these quantities are orthogonal to $\mathbf{k}$. To sustain a laminar shear flow a volume force $\mathbf{F}$ with its corresponding Fourier component $\mathbf{F}_{\mathbf{k}}$ is introduced. $\mathbf{F}$ is chosen in a way that the resulting flow field $\mathbf{U}_0$ equals

$$\mathbf{U}_0 = \frac{16}{\pi^2}\cos(z)\mathbf{e}_z , \tag{7.6}$$

which corresponds to the first term of the Fourier expansion of a linear flow field with an amplitude of ± 2 at the boundaries. To compare the results with plane Couette flow the velocity is measured in units of the approximated mean flow at $z=\pi$, $U_0=2$, instead of units of the actual mean flow $U_0=\frac{16}{\pi^2}$. Lengths are measured in units of the half gap width $\frac{d}{2}$. Together with the kinematic viscosity ν, the Reynolds number equals

$$Re = \frac{\pi}{\nu} . \tag{7.7}$$

To reduce the degrees of freedom only a finite set of wave vectors was used. Three wave

vectors along the wall normal direction;

$$\mathbf{k}_i = \begin{pmatrix} 0 \\ 0 \\ i \end{pmatrix}, i = 1, 2, 3\,, \tag{7.8}$$

and a triangle in each k_x, k_y plane;

$$\mathbf{k}_4 = \begin{pmatrix} 2\alpha \\ 0 \\ 0 \end{pmatrix}, \mathbf{k}_5 = \begin{pmatrix} \alpha \\ \beta \\ 0 \end{pmatrix}, \mathbf{k}_6 = \begin{pmatrix} \alpha \\ -\beta \\ 0 \end{pmatrix}. \tag{7.9}$$

There are 12 additional wave vectors:

$$\begin{aligned}
\mathbf{k}_7 &= \mathbf{k}_1 + \mathbf{k}_4 \quad \mathbf{k}_8 = \mathbf{k}_1 + \mathbf{k}_5 \quad \mathbf{k}_9 = \mathbf{k}_1 + \mathbf{k}_6 \\
\mathbf{k}_{10} &= \mathbf{k}_1 - \mathbf{k}_4 \quad \mathbf{k}_{11} = \mathbf{k}_1 - \mathbf{k}_5 \quad \mathbf{k}_{12} = \mathbf{k}_1 - \mathbf{k}_6 \\
\mathbf{k}_{13} &= \mathbf{k}_2 + \mathbf{k}_4 \quad \mathbf{k}_{14} = \mathbf{k}_2 + \mathbf{k}_5 \quad \mathbf{k}_{15} = \mathbf{k}_2 + \mathbf{k}_6 \\
\mathbf{k}_{16} &= \mathbf{k}_2 - \mathbf{k}_4 \quad \mathbf{k}_{17} = \mathbf{k}_2 - \mathbf{k}_5 \quad \mathbf{k}_{18} = \mathbf{k}_2 - \mathbf{k}_6\,.
\end{aligned} \tag{7.10}$$

In order to fulfill the boundary conditions some $\alpha_{\mathbf{k}}$ and $\beta_{\mathbf{k}}$ are related to each other:

$$\begin{aligned}
\alpha_{\mathbf{k}_{10}} &= -\alpha^*_{\mathbf{k}_8} \quad \alpha_{\mathbf{k}_{11}} = -\alpha^*_{\mathbf{k}_7} \quad \alpha_{\mathbf{k}_{13}} = -\alpha^*_{\mathbf{k}_9} \\
\alpha_{\mathbf{k}_{16}} &= -\alpha^*_{\mathbf{k}_{13}} \quad \alpha_{\mathbf{k}_{17}} = -\alpha^*_{\mathbf{k}_{14}} \quad \alpha_{\mathbf{k}_{18}} = -\alpha^*_{\mathbf{k}_{15}} \\
\beta_{\mathbf{k}_{10}} &= -\beta^*_{\mathbf{k}_8} \quad \beta_{\mathbf{k}_{11}} = -\beta^*_{\mathbf{k}_7} \quad \beta_{\mathbf{k}_{13}} = -\beta^*_{\mathbf{k}_9} \\
\beta_{\mathbf{k}_{16}} &= -\beta^*_{\mathbf{k}_{13}} \quad \beta_{\mathbf{k}_{17}} = -\beta^*_{\mathbf{k}_{14}} \quad \beta_{\mathbf{k}_{18}} = -\beta^*_{\mathbf{k}_{15}}\,.
\end{aligned} \tag{7.11}$$

Using this set of wave vectors and relations, the resulting model consists of 36 degrees of freedom. Restricting the flow to a point symmetry $\mathcal{P}$ reduces the dynamics down to a 19 dimensional subspace. Eckhardt and Mersmann number these degrees of freedom in the

following way:

$$
\begin{aligned}
\alpha_{\mathbf{k}_1} &= y_1 & \beta_{\mathbf{k}_1} &= y_2 \\
\alpha_{\mathbf{k}_3} &= y_3 & \beta_{\mathbf{k}_3} &= y_4 \\
& & \beta_{\mathbf{k}_4} &= iy_5 \\
& & \beta_{\mathbf{k}_5} &= iy_6 \\
& & \beta_{\mathbf{k}_6} &= iy_7 \\
\alpha_{\mathbf{k}_7} &= y_8 & \beta_{\mathbf{k}_7} &= y_9 \\
\alpha_{\mathbf{k}_8} &= y_{10} & \beta_{\mathbf{k}_8} &= y_{11} \\
\alpha_{\mathbf{k}_9} &= y_{12} & \beta_{\mathbf{k}_9} &= y_{13} \\
\alpha_{\mathbf{k}_{13}} &= iy_{14} & \beta_{\mathbf{k}_{13}} &= iy_{15} \\
\alpha_{\mathbf{k}_{14}} &= iy_{16} & \beta_{\mathbf{k}_{14}} &= iy_{17} \\
\alpha_{\mathbf{k}_{15}} &= iy_{18} & \beta_{\mathbf{k}_{15}} &= iy_{19}\ .
\end{aligned}
\tag{7.12}
$$

This 19-model has 3 additional discrete symmetries:

$$
\begin{aligned}
\mathcal{R}: \begin{pmatrix} u \\ v \\ w \end{pmatrix}(x,y,z) &= \begin{pmatrix} -u \\ v \\ w \end{pmatrix}(-x,y,z) \\
\mathcal{T}_1: \begin{pmatrix} u \\ v \\ w \end{pmatrix}(x,y,z) &= \begin{pmatrix} u \\ v \\ w \end{pmatrix}(x+L_x/2,y,z) \\
\mathcal{T}_2: \begin{pmatrix} u \\ v \\ w \end{pmatrix}(x,y,z) &= \begin{pmatrix} u \\ v \\ w \end{pmatrix}(x+L_x/2,y+L_y/2,z)\ .
\end{aligned}
$$

These symmetries plus the unity form nine symmetry groups. Restricting the dynamics to members of these groups reduces the degrees of freedom down to 10, 9 or 4 (See table 7.1).

$\{\mathbf{1}, \mathcal{R}\mathcal{T}_2\}$	10
$\{\mathbf{1}, \mathcal{R}\}$	9
$\{\mathbf{1}, \mathcal{T}_1\}$	9
$\{\mathbf{1}, \mathcal{T}_2\}$	9
$\{\mathbf{1}, \mathcal{R}\mathcal{T}_1\}$	9
$\{\mathbf{1}, \mathcal{T}_2\mathcal{T}_1\}$	9
$\{\mathbf{1}, \mathcal{T}_1, \mathcal{T}_2, \mathcal{T}_1\mathcal{T}_2\}$	4
$\{\mathbf{1}, \mathcal{T}_1, \mathcal{R}, \mathcal{R}\mathcal{T}_1\}$	4
$\{\mathbf{1}, \mathcal{T}_2, \mathcal{R}, \mathcal{R}\mathcal{T}_2\}$	4
$\{\mathbf{1}, \mathcal{T}_1, \mathcal{T}_2, \mathcal{R}, \mathcal{R}\mathcal{T}_1, \mathcal{R}\mathcal{T}_2, \mathcal{T}_1\mathcal{T}_2\}$	4

Table 7.1: Degrees of freedom of the 19-model reduced to the above symmetry groups. The investigations in this chapter are done in the $\{\mathbf{1}, \mathcal{R}\mathcal{T}_1\}$ symmetry group. Note, that the dynamical system reduced to 4 degrees of freedom has a trivial dynamic shown in equation (7.14).

The equations in case of 4 degrees of freedom reads

$$\begin{aligned}
\frac{\partial}{\partial t} x_1 &= \frac{8\nu}{\pi^2} - \sqrt{2} x_3 x_4 - \nu x_1 \\
\frac{\partial}{\partial t} x_2 &= -3\sqrt{2} x_3 x_4 - 9\nu x_2 \\
\frac{\partial}{\partial t} x_3 &= \frac{3}{2}\sqrt{2} x_2 x_4 + \frac{1}{2}\sqrt{2} x_1 x_4 - 5\nu x_3 \\
\frac{\partial}{\partial t} x_4 &= -8\nu x_4 \,.
\end{aligned} \tag{7.13}$$

The dynamics of this system is simple: while x_4 decays exponentially it amplifies x_3, which is coupled with the other two components. After x_4 has vanished there is no drive and the other components also vanish. This system shows only a nonlinear transient dynamic.

In case of 10, 9 degrees of freedom the system is able to show a chaotic behavior. The following investigations were done for members of the $\{\mathbf{1}, \mathcal{R}\mathcal{T}_1\}$ symmetry group. This choice is motivated by the fact that streamwise vortices solve the $\mathcal{P}$ symmetry which is already conserved and streamwise streaks solve the $\mathcal{R}$ symmetry. To allow streaks and vortices $\mathcal{R}\mathcal{T}_1$ was

imposed. This gives the following constraints to x_i:

$$\begin{aligned} x_1 = x_3 = x_5 = x_8 = x_{15} &= 0 \\ x_6 = -x_7, \;\; x_{10} &= x_{12} \\ x_{11} = -x_{13}, \;\; x_{16} = x_{18}, \;\; x_{17} &= -x_{19} \,. \end{aligned} \tag{7.14}$$

The dynamic active degrees of freedom are numbered in the following way:

$$\begin{aligned} y_1 = x_2 \quad y_2 = x_4 \quad y_3 &= x_6 \\ y_4 = x_9 \quad y_5 = x_{10} \quad y_6 &= x_{11} \\ y_7 = x_{14} \quad y_8 = x_{16} \quad y_9 &= x_{17} \,. \end{aligned} \tag{7.15}$$

The original model used a specific spanwise and streamwise periodicity, i.e. $\alpha = 1/2$ and $\beta = \sqrt{3}/2$, which are now two additional parameters. Since $y_1 = \frac{8\nu}{\pi^2}$ corresponds to the laminar profile, $\frac{8\nu}{\pi^2}$ was subtracted from y_1. The resulting equations correspond to the equations of motion of a finite perturbation of the laminar profile. The general form of these equations is shown in appendix C. Most of the investigations in this chapter have been done with an aspect ration of $d : 2\pi\, d : \pi\, d$ (wall normal: streamwise: spanwise). For this aspect ratio the equations of motions are

$$\begin{aligned}
\frac{\mathrm{d}}{\mathrm{d}\,t}\, y_1 &= \frac{8}{\sqrt{5+\pi^2}} y_5 y_3 - \frac{4}{\sqrt{\pi^2+4}} y_4 y_7 + \left(\frac{-12\,\pi}{\sqrt{5+\pi^2}\sqrt{5+4\,\pi^2}}\, y_8 - \frac{8}{\sqrt{5+\pi^2}} y_9 \right) y_5 \\
&\quad - \frac{8}{\sqrt{5+4\,\pi^2}} y_6 y_8 - \nu\, y_1 \\
\frac{\mathrm{d}}{\mathrm{d}\,t}\, y_2 &= 12 \left(- \frac{1}{\sqrt{\pi^2+4}} y_7 y_4 + \left(\frac{\pi}{\sqrt{5+4\,\pi^2}\sqrt{5+\pi^2}}\, y_8 + \frac{2}{\sqrt{5+\pi^2}} y_9 \right) y_5 \right. \\
&\quad \left. - \frac{2}{\sqrt{5+4\,\pi^2}} y_8 y_6 \right) - 9\,\nu\, y_2 \\
\frac{\mathrm{d}}{\mathrm{d}\,t}\, y_3 &= \left(- \frac{4}{\sqrt{5+\pi^2}} y_5 - \frac{2}{\pi} y_6 \right) y_1 - \frac{5\nu}{\pi^2} y_3 + \left(- \frac{4}{5\sqrt{5+\pi^2}} y_5 + \frac{22}{5\,\pi} y_6 \right) y_4 \\
&\quad - \frac{32}{\pi^2\sqrt{5+\pi^2}} y_5 - \frac{16}{\pi^3} y_6 + \left(-\frac{44}{5} \frac{\pi}{\sqrt{\pi^2+4}\sqrt{5+4\,\pi^2}}\, y_8 - \frac{4}{5\sqrt{\pi^2+4}} y_9 \right) y_7 \\
\frac{\mathrm{d}}{\mathrm{d}\,t}\, y_4 &= 6 \left(\frac{\pi}{\sqrt{5+\pi^2}\sqrt{5+4\,\pi^2}}\, y_8 + \frac{2}{\sqrt{5+\pi^2}} y_9 \right) y_5 - \frac{12}{\sqrt{5+4\,\pi^2}} y_8 y_6 + \frac{16}{\sqrt{\pi^2+4}\pi^2} y_7 \\
&\quad \frac{2}{\sqrt{\pi^2+4}} y_7 y_1 + \frac{6}{\sqrt{\pi^2+4}} y_2 y_7 + \frac{4}{\sqrt{5+\pi^2}} y_5 y_3 - \nu \left(1 + \frac{16}{\pi^2} \right) y_4
\end{aligned}$$

$$
\begin{aligned}
\frac{\mathrm{d}}{\mathrm{d}\,t}\,y_5 &= \frac{(5+3\pi^2)}{\sqrt{5+\pi^2}\sqrt{5+4\,\pi^2}}y_8\,y_1 + 5\,\frac{(\,\pi^2-1)}{\sqrt{5+\pi^2}\sqrt{5+4\,\pi^2}\pi}\,y_8\,y_2 - \frac{8}{5\sqrt{5+\pi^2}}y_3y_4 \\
&\quad + \frac{1}{5\,\sqrt{5+\pi^2}}\left(\frac{(17\pi^2-25)}{\sqrt{5+4\,\pi^2}\pi}y_8 - y_9\right)y_4 + \left(-\frac{4}{5\sqrt{\pi^2+4}}y_7 - \nu\left(1+\frac{5}{\pi^2}\right)\right)y_5 \\
&\quad \frac{(-8\,\pi^2-40)}{\sqrt{5+\pi^2}\sqrt{\pi^2+4}\pi}y_7y_6 + \frac{(20+24\pi^2)}{\sqrt{5+\pi^2}\sqrt{5+4\,\pi^2}\pi^3}y_8 \\
\frac{\mathrm{d}}{\mathrm{d}\,t}\,y_6 &= \left(\frac{1}{\pi}y_3 + \frac{2}{\sqrt{5+4\,\pi^2}}y_8 + \frac{1}{\pi}y_9\right)y_1 + \left(\frac{6}{\sqrt{5+4\,\pi^2}}y_8 + \frac{1}{\pi}y_9\right)y_2 \\
&\quad + \left(-\frac{11}{5\pi}y_4 + 8\,\pi^{-3}\right)y_3 + \left(\frac{14}{5\sqrt{5+4\,\pi^2}}y_8 - \frac{11}{5\pi}y_9\right)y_4 + \frac{2\pi}{5\sqrt{\pi^2+4}\sqrt{5+\pi^2}}y_7y_5 \\
&\quad + \left(\frac{4}{5\sqrt{\pi^2+4}}y_7 - \nu\,\frac{5+\pi^2}{\pi^2}\right)y_6 + \frac{16}{\pi^2\sqrt{5+4\,\pi^2}}y_8 + \frac{8}{\pi^3}y_9 \\
\frac{\mathrm{d}}{\mathrm{d}\,t}\,y_7 &= \frac{4}{5}\left(\frac{11\,\pi^2+20}{\pi\sqrt{5+4\,\pi^2}\sqrt{\pi^2+4}}y_8 - 4\,\frac{1}{\sqrt{\pi^2+4}}y_9\right)y_3 \\
&\quad + \frac{4}{5}\left(\frac{1}{\sqrt{\pi^2+4}}y_5^2 + \frac{(3\,\pi^2+20)}{\sqrt{5+\pi^2}\pi\sqrt{\pi^2+4}}y_6y_5\right) \\
&\quad + \frac{4}{5}\left(-2\,\frac{1}{\sqrt{\pi^2+4}}y_6^2 + 5\nu\left(-1-\frac{4}{\pi^2}\right)y_7\right) \\
\frac{\mathrm{d}}{\mathrm{d}\,t}\,y_8 &= -\frac{1}{\pi\sqrt{5+\pi^2}\sqrt{5+4\pi^2}}\left(5y_5y_1 + \left(8\,\pi^2-5\right)y_5y_2\right) - \frac{8}{\pi\,\sqrt{5+4\,\pi^2}\sqrt{\pi^2+4}}y_3y_7 \\
&\quad + \frac{1}{5\sqrt{5+4\pi^2}}\left(-\frac{(32\,\pi^2-25)}{\sqrt{5+\pi^2}\pi}y_5 + 16y_6\right)y_4 - \frac{40}{\sqrt{5+\pi^2}\pi^3\sqrt{5+4\,\pi^2}}y_5 \\
&\quad - \nu\left(\frac{5}{\pi^2}+4\right)y_8 \\
\frac{\mathrm{d}}{\mathrm{d}\,t}\,y_9 &= \left(\frac{2}{\sqrt{5+\pi^2}}y_5 - \frac{1}{\pi}y_6\right)y_1 + \left(-\frac{6}{\sqrt{5+\pi^2}}y_5 - \frac{1}{\pi}y_6\right)y_2 + \frac{2}{\sqrt{\pi^2+4}}y_3y_7 \\
&\quad + \left(-\frac{22}{5\sqrt{5+\pi^2}}y_5 + \frac{11}{5\,\pi}y_6\right)y_4 + \frac{16}{\pi^2\sqrt{5+\pi^2}}y_5 - \frac{8}{\pi^3}y_6 \\
&\quad - \nu\left(\frac{5}{\pi^2}+4\right)y_9
\end{aligned}
$$

7.2 Transitional behavior

The 19-model and the 9-model show a similar transitional behavior as the plane Couette flow. The lifetimes of a finite perturbation depends sensitively on the amplitude and the Reynolds number [37, 38]. An example of this sensitivity is given in figure 7.1, where the lifetime of a random initial condition is shown in the amplitude-Reynolds number plane. To separate the influence of the nonlinear effects from the linear ones, the lifetimes of the perturbations

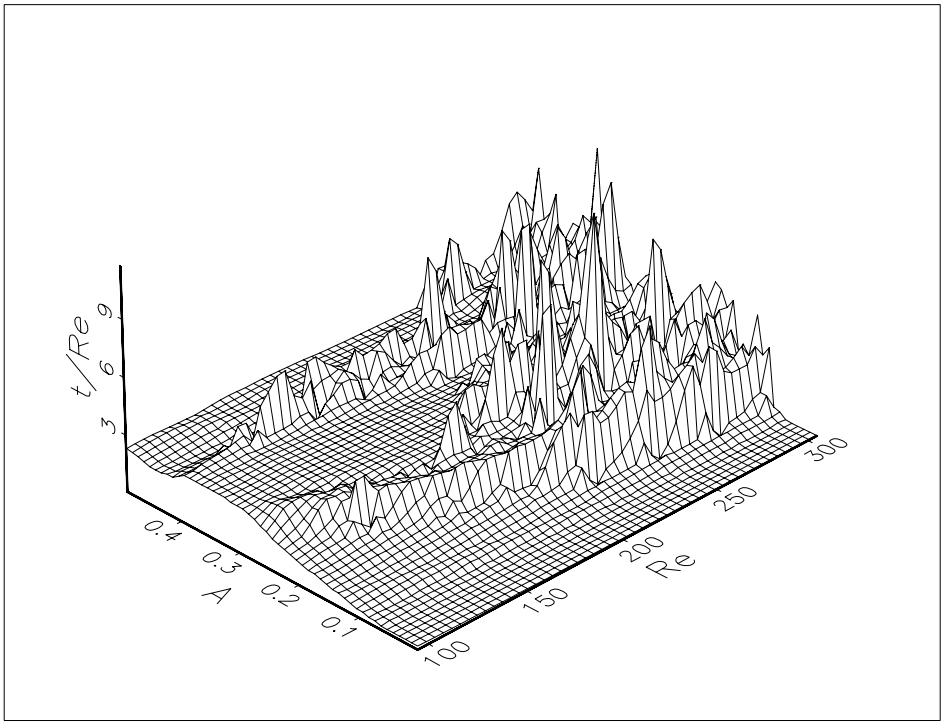

Figure 7.1: The lifetime of a specific finite random initial condition of the 9-model as a function of the amplitude and the Reynolds number. Note that the lifetime t is divided by the Reynolds number to split the nonlinear influence on the lifetime from the linear one.

are divided by the Reynolds number. First chaotic transients occur at $\mathrm{Re} = 132$. At a Reynolds number of about 240 most perturbations show a significantly long lifetime. In these calculations the lifetime was defined as the time, until the energy of the disturbances drop below a given threshold, here $\mathbf{y}^2 \leq 10^{-6}$.

Since the lifetime also depends on the specific type of perturbation the median of 100 perturbations with a distinct amplitude A is calculated. It shows a change at $\mathrm{Re} = 160$ and $\mathrm{Re} = 240$ (Fig. 7.2). This suggests that the turbulent state is rather thin at $\mathrm{Re} = 132$ and grows at $\mathrm{Re} = 160$ and $\mathrm{Re} = 240$. The maximum lifetime observed in these runs shows a sudden increase at $\mathrm{Re} = 140$ and a decrease at $\mathrm{Re} = 180$. The lifetime grows between these two values and shows transient trajectories with lifetimes up to 2880 time units.

7.3 Stationary states

The 19-model shows an increasing number of stationary states [38]. The first state bifurcates at $\mathrm{Re} = 790$, with $\alpha = 1/2$ and $\beta = \sqrt{3}/2$ and all these solutions are linearly unstable.

In order to find stationary solutions in the 9-model a Newton-Raphson method was applied [83]. The initial conditions are taken from the chaotic time signal and the found solutions are

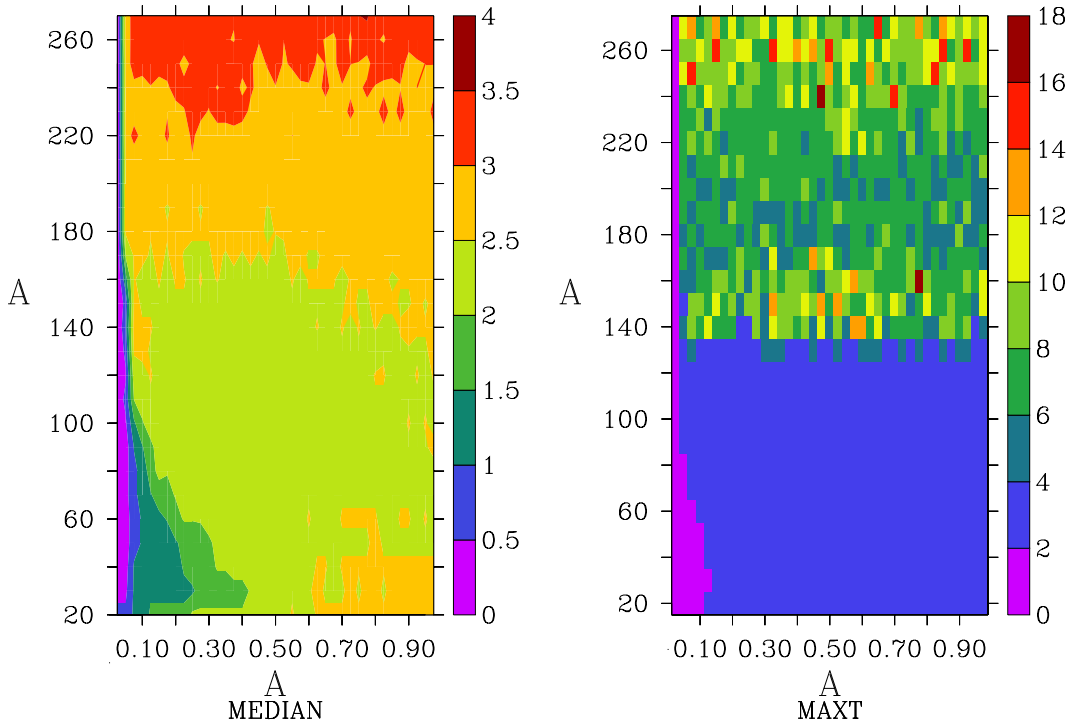

Figure 7.2: Median of the distribution of lifetime (left panel) and maximum lifetime (right panel) of an ensemble of 100 random initial conditions of the 9-model with a distinct amplitude A. Note that the lifetime t is divided by the Reynolds number to split the nonlinear influence on the lifetime from the linear one.

followed to different Reynolds numbers using the Pittsburgh continuation program PITCON [88, 89].

7.3.1 Bifurcation of stationary states

For Reynolds numbers up to 2000 only two pairs of stationary states exist. The first pair bifurcates at $\mathrm{Re} = 790.81$, the second one at $\mathrm{Re} = 847.27$ (Fig. 7.3). Both pairs are born in a saddle-node bifurcation. Figure 7.4 displays the real parts of the highest eigenvalues of the first pair of states for the upper and the lower branch. After the bifurcation the singular eigenvalue becomes negative for the lower branch, the node, and positive for the upper one, the saddle. Both branches have additional positive eigenvalues, hence both states are linearly unstable. The real parts of two eigenvalues of the upper branch meets at $\mathrm{Re} = 800$, where they form a complex conjugate pair of eigenvalues. These eigenvalues become positive at higher Reynolds numbers and make a forward Hopf bifurcation.

The second pair bifurcates from a saddle-node bifurcation in a similar way (Fig. 7.5). The singular eigenvalue becomes negative for the lower and positive for the upper branch. Both

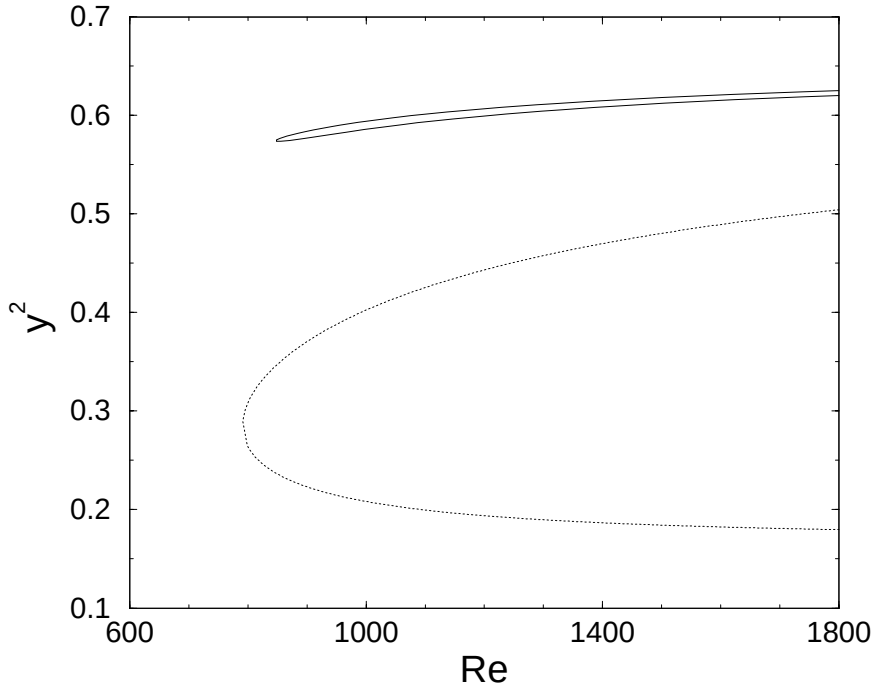

Figure 7.3: Stationary states for the 9-model in the case of $\alpha = 2\pi^{-1}$ and $\beta = \pi^{-1}$.

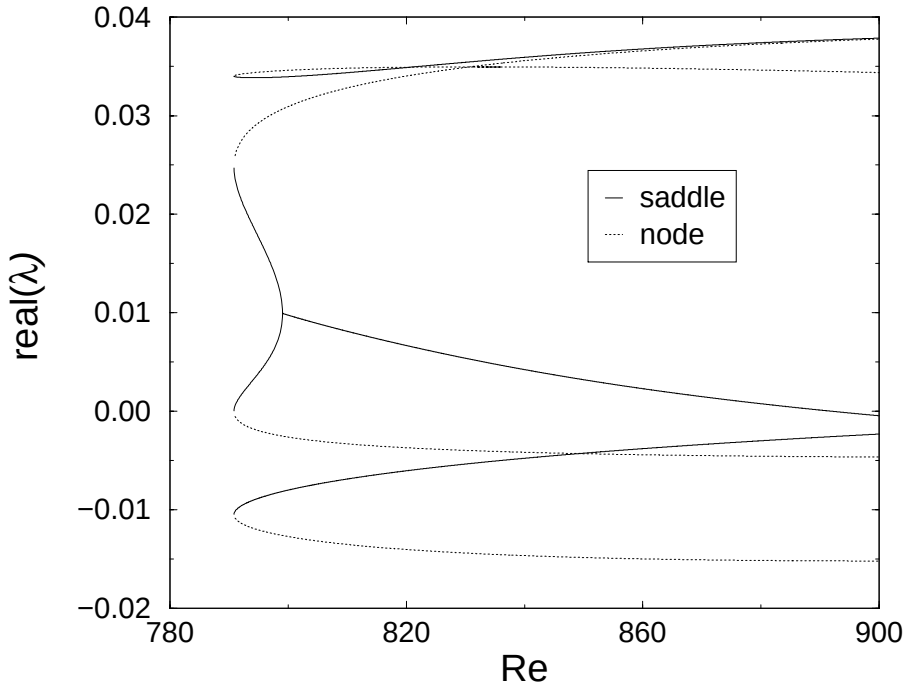

Figure 7.4: Real parts of the largest eigenvalues of states of the saddle and the node of the first pair of stationary states for $\alpha = 2\,\pi^{-1}$ and $\beta = 2\pi^{-1}$ at different Reynolds numbers.

states have additional positive eigenvalues. Two eigenvalues of the upper branch start to form a complex conjugate pair of eigenvalues at $\mathrm{Re} = 950$ but they do not undergo a Hopf

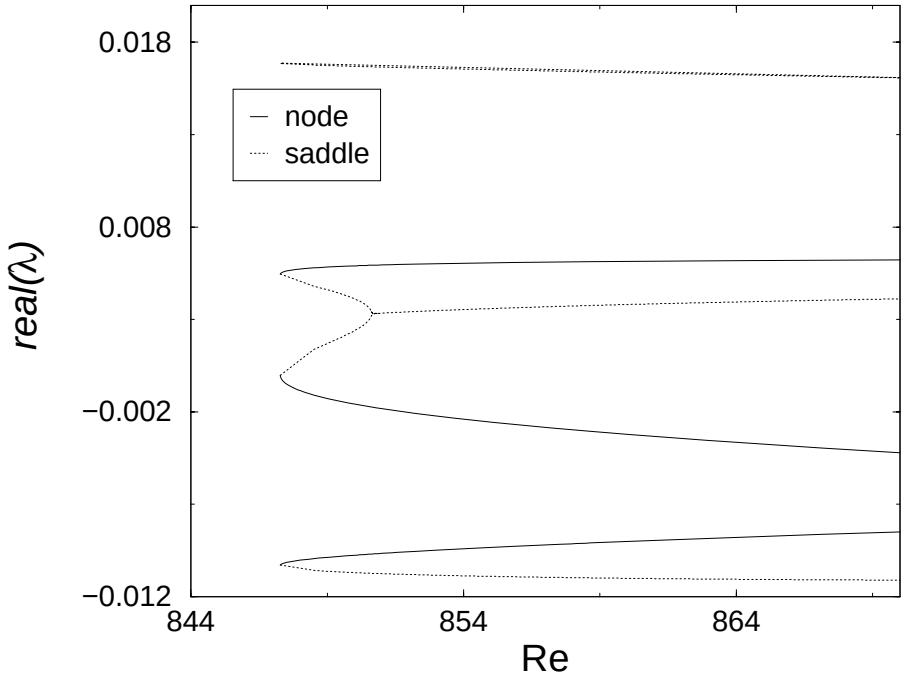

Figure 7.5: Real parts of the largest eigenvalues of states of the saddle and the node of the second pair of stationary states for $\alpha = 2\,\pi^{-1}$ and $\beta = 2\pi^{-1}$ at different Reynolds numbers.

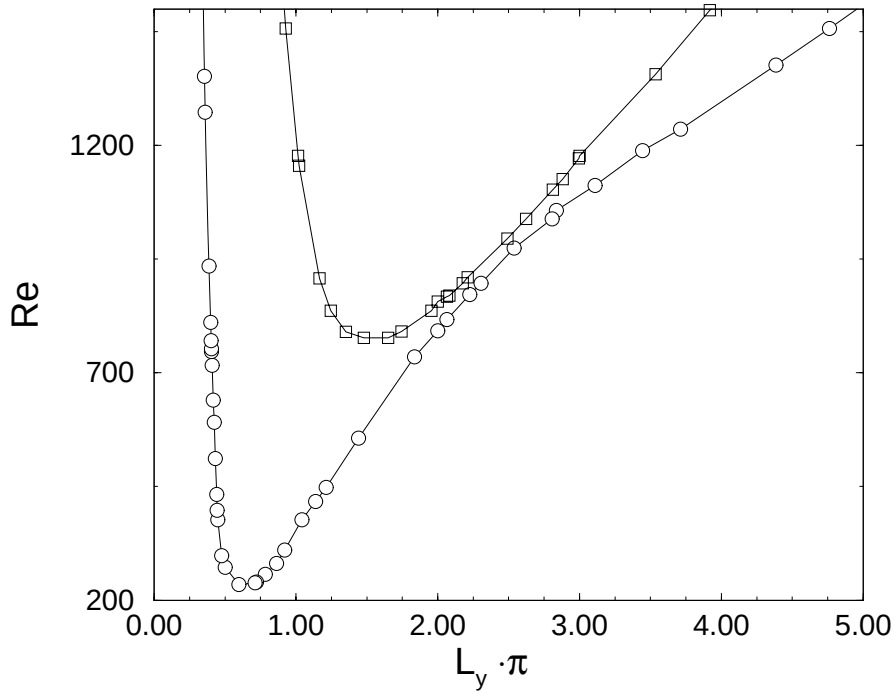

Figure 7.6: Critical Reynolds number as a function of L_y. Each point corresponds to a calculated $\mathrm{Re}_{\mathrm{crit}}$. The circles correspond to the critical Reynolds numbers of the first pair of stationary states, the squares to the second one.

bifurcation for Reynolds numbers less than 2000.

Variation of L_y, i.e. the periodicity along the streamwise direction, shows that the first pair of states have a critical Reynolds number of $\mathrm{Re}_{\mathrm{crit}} \approx 234$ at $Ly \approx 0.64\pi$ (Fig.7.6). In this geometry the second state does not bifurcate for Reynolds number less than 2000. Their optimal aspect ratio equals $d : 0.64\pi\, d : \pi\, d$ (wall normal: streamwise: spanwise).

The second pair of stationary states bifurcates at a critical Reynolds number of $\mathrm{Re}_{\mathrm{crit.}} \approx 754$ at $L_y = 1.61\pi$. In this case, the first state bifurcates at $\mathrm{Re}_{\mathrm{crit.}} = 612$. Their optimal aspect ratio equals $d : 1.61\pi\, d : \pi\, d$, which is in good agreement to the investigation made in chapter 5.4.

7.3.2 Are stationary states responsible for the formation of the turbulent state?

The linear stability analysis shows that the dynamics around these stationary states are dominated by one unstable direction (Fig. 7.4 and Fig. 7.5). Starting near these stationary states shows the dominance of the unstable manifold. In Fig. 7.8 the propagation of two ensembles of perturbations near the states of the first pair of states at $\mathrm{Re} = 1000$ is displayed in the y_1,y_2-plane. None of the two ensembles follows the connecting center manifold. At $t = 200$ the ensembles are stretched along the unstable manifold. Then each trajectory spirals away from the center manifold. At $t = 300$ the ensemble is spread over the turbulent state.

The dynamical influence of the stationary states seems to be negligible. Every perturbation is repulsed by these states and attracted by the turbulent state. These stationary states are not perceivable. The investigation of lifetimes supports this conclusion. Long living nonlinear transients can be observed before stationary states bifurcate (Fig.7.1). This behavior is different from the transition in plane Couette flow where the first stationary states bifurcates at $\mathrm{Re} = 125$ and transitions occur at Reynolds numbers two times higher.

7.4 Periodic orbits

It is known that periodic orbits together with unstable stationary states, heteroclinic connections and homoclinic orbits form the skeleton of a chaotic attractor or repellor. Christiansen, Cvitanović and Putkaradze [24] showed that in case of the Kuramoto-Sivashinsky equation the turbulent state can be characterized by periodic orbits. For plane shear flows Waleffe [105, 106] suggests a self sustaining process to be responsible for the turbulent dynamic, where streamwise vortices induce streamwise streaks and gain energy by the breakdown of these streaks via a nonlinear feedback mechanism (See chapter 5.4 for more details). This picture suggests the existence of periodic orbits which might be responsible for the turbulent motion. The 9-model has unstable periodic orbits, which start to fill the phase space before

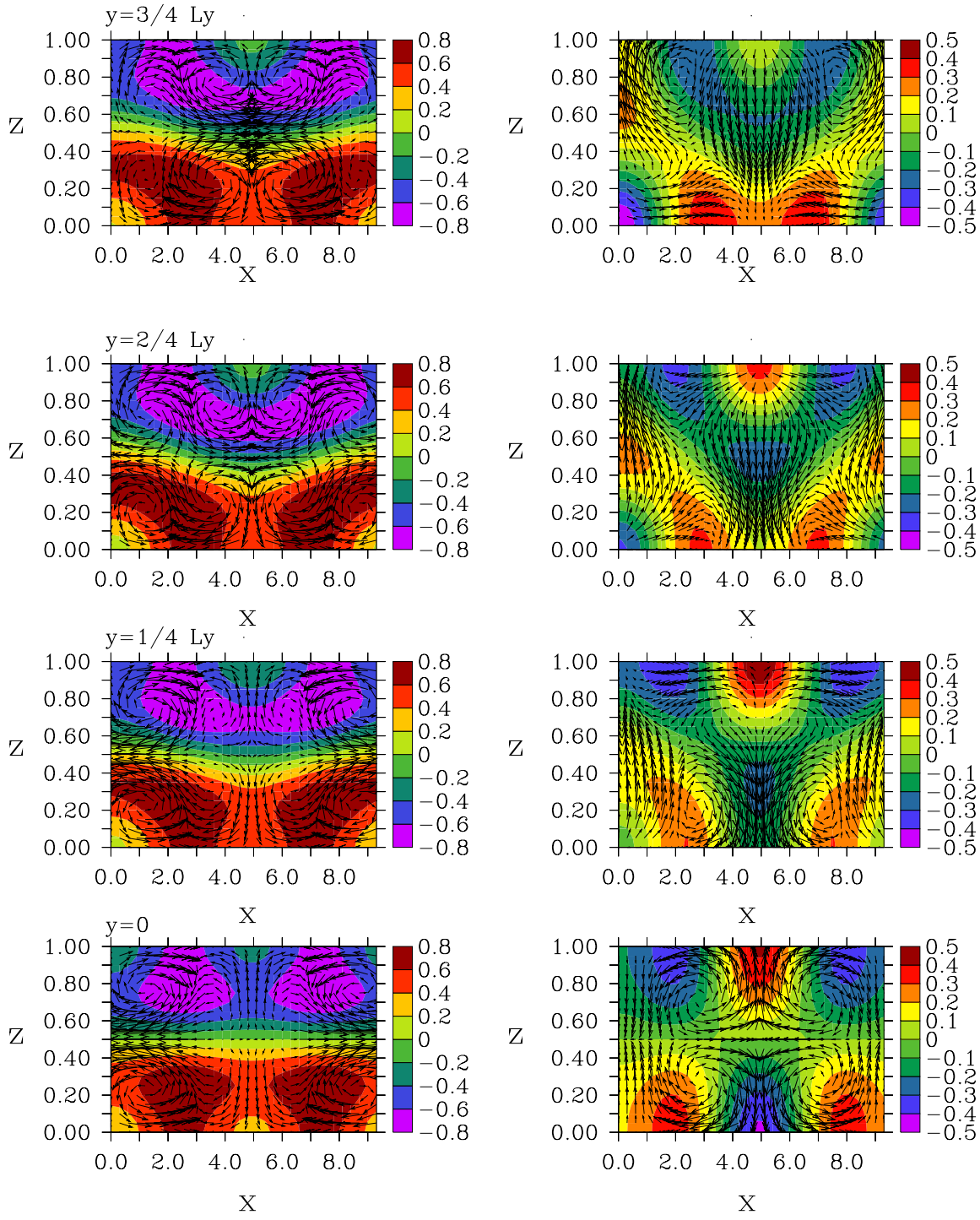

Figure 7.7: Streamwise velocity (contour) and spanwise and wall normal velocity (vectors) of states of the lower branch of the first (left column) and the second (right column) pair of stationary states at $\mathrm{Re} = 900$ at $x = 0, L_y/4, L_y/2\,d, 3/4\,L_y$.

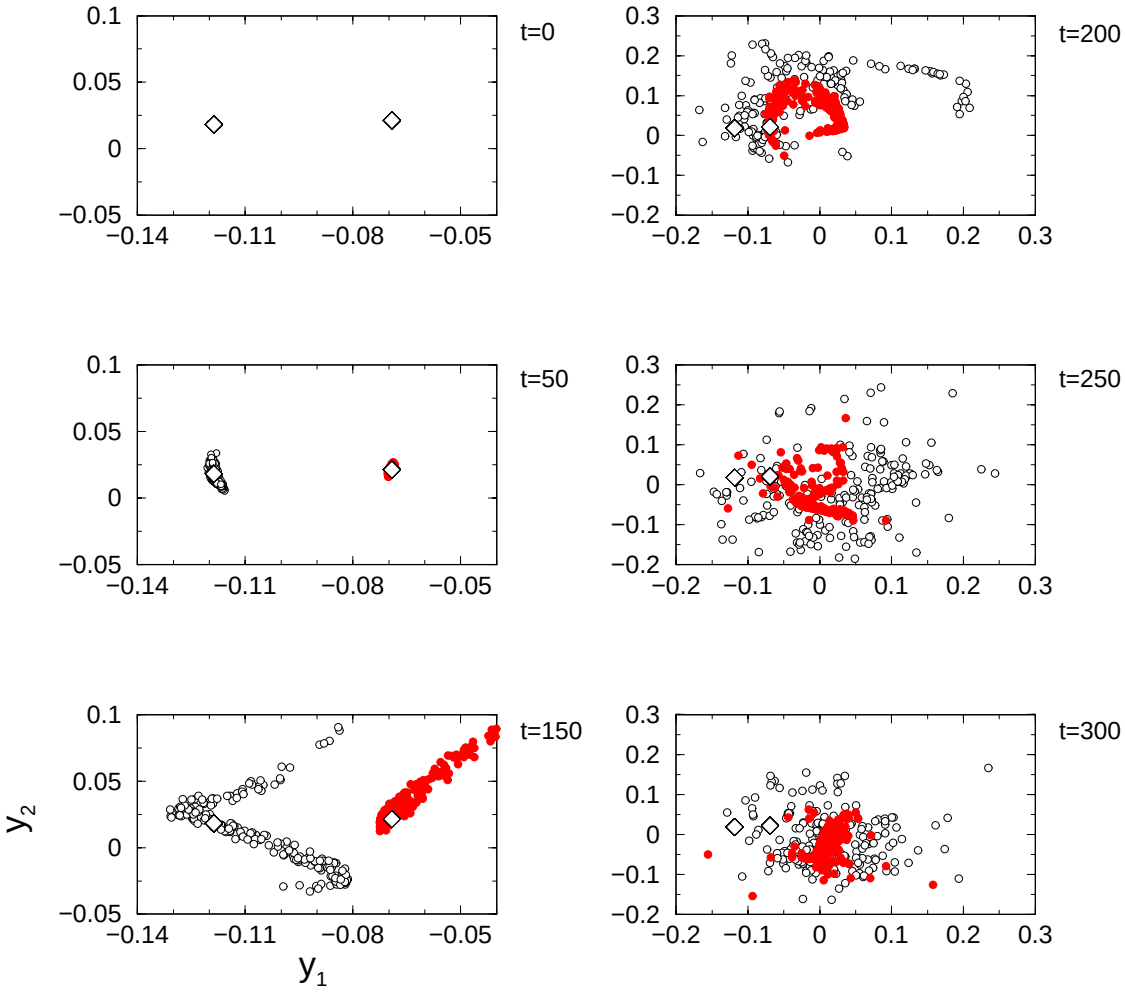

Figure 7.8: Evolution of 400 initial conditions starting near the first 2 stationary states ($\diamond$) at $\mathrm{Re} = 1000$. Open symbols correspond to the ensemble starting near the state of the lower branch. Closed symbols correspond to the ensemble starting at the state of the upper branch. The additional stationary states are not shown. They lie at regions with $y_1 < -0.4$.

any stationary state bifurcates. Therefore, these orbits are studied and their influence on the transition to turbulence will be discussed.

7.4.1 Poincaré section

Since the 9-model is an autonomous system there is no obvious choice for the periodicity of the periodic orbits. The evolution of the components y_i at $\mathrm{Re} = 300$ shows, that the first component y_1 dominates the dynamics (Fig 7.9). It has the largest timescale and contributes mainly to the energy of the system. Therefore a Poincaré section is applied at $y_1 = -0.7$. Every pass from lower to higher values corresponds to the 8 dimensional discrete map

$$\tilde{\mathbf{y}}_{n+1} = \mathbf{f}(\tilde{\mathbf{y}}_\mathbf{n})\,. \tag{7.16}$$

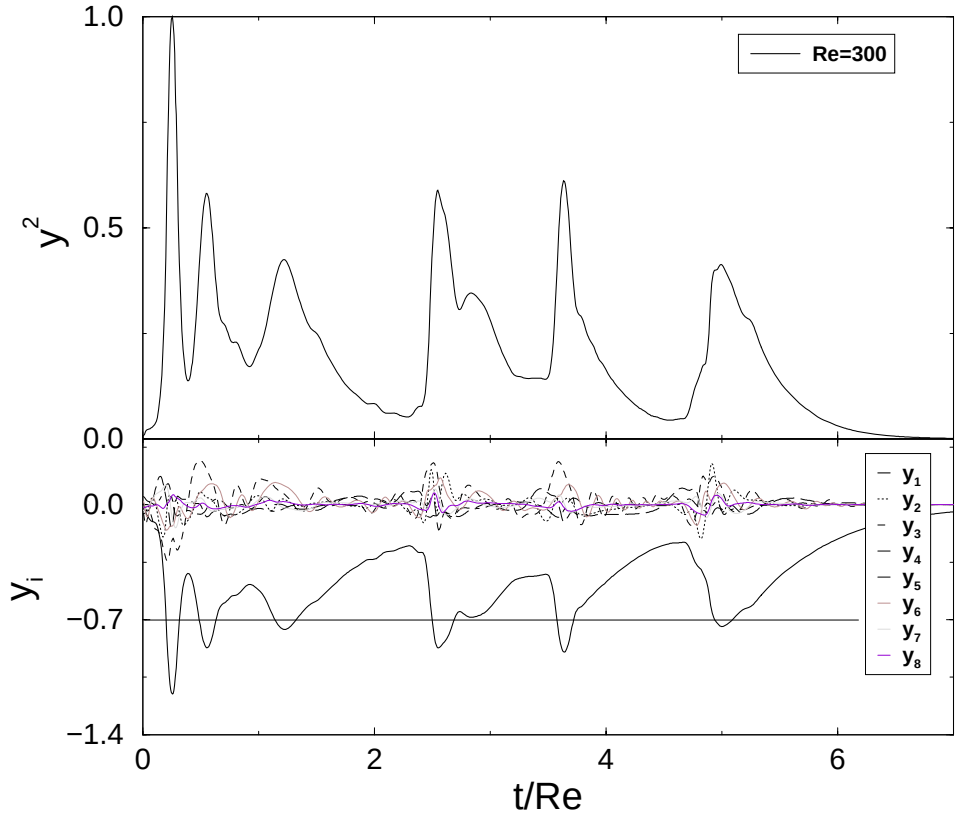

Figure 7.9: Time evolution of a random initial condition at a Reynolds number of 300. The upper panel shows the inner product of the state vector $\mathbf{y}^2$, the lower panel the value of the first 8 components.

A Newton-Raphson method [83] is used to search stationary solutions of the Poincaré map (7.16). The initial values are taken from the chaotic time signal. In order to follow the solution branch initial guesses for the Newton-Raphson method are calculated at different Reynolds numbers using the implicit function theorem .

7.4.2 Bifurcation of periodic orbits

Period-1 orbits

A first pair of unstable periodic orbits originates at $\mathrm{Re} = 133.08$. These orbits move very fast in phase space if the Reynolds number varies and the Poincaré section has to be modified for different values of the Reynolds number. They are born in a saddle node bifurcation. The upper branch moves to lower energies and makes no further bifurcation until $\mathrm{Re} = 300$. The lower branch moves to higher energies. The energy defined by $E_\mathrm{P} := \tilde{\mathbf{y}}^2 + y_1^2$ with $y_1 = -0.455$ for the lower branch is shown in figure 7.10. Between $\mathrm{Re} = 155.15$ and $\mathrm{Re} = 171.6$ and between $\mathrm{Re} = 181.2$ and $\mathrm{Re} = 204$ four orbits exist. They are connected with the branch of the first orbit via backward and forward saddle node bifurcations. This

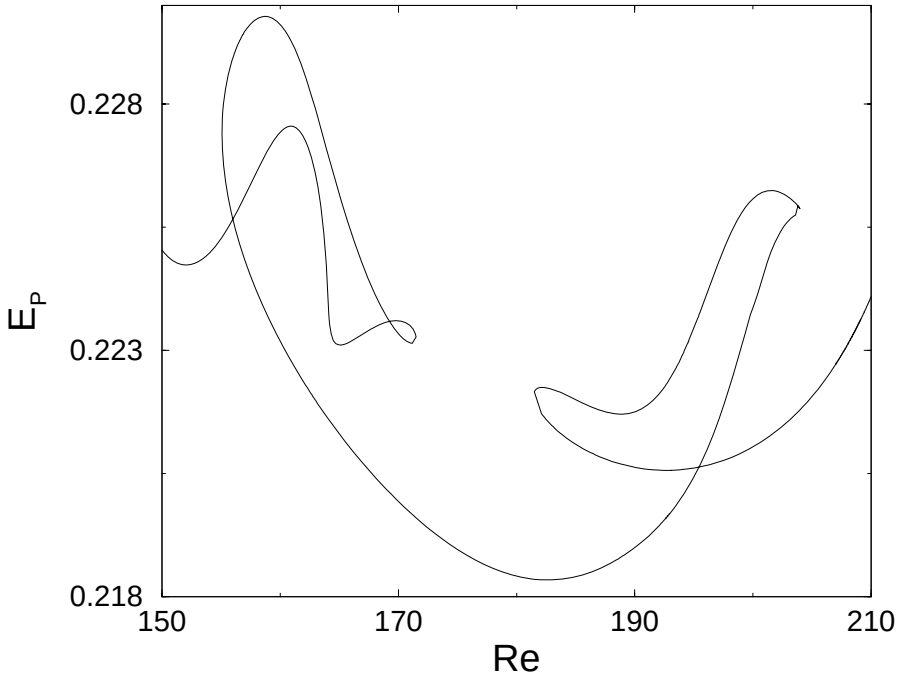

Figure 7.10: $E_p := \tilde{\mathbf{y}}^2 + y_i^2$ of the first periodic orbit at $\mathrm{Re} = 150, ..., 210$. These orbits are connected with an additional orbit not displayed here. The Poincaré section equals $y_1 = -0.455$. These four orbits form a small repellor, which is responsible for the first transient states between $\mathrm{Re} = 150$ and $\mathrm{Re} = 200$ shown in figure 7.1.

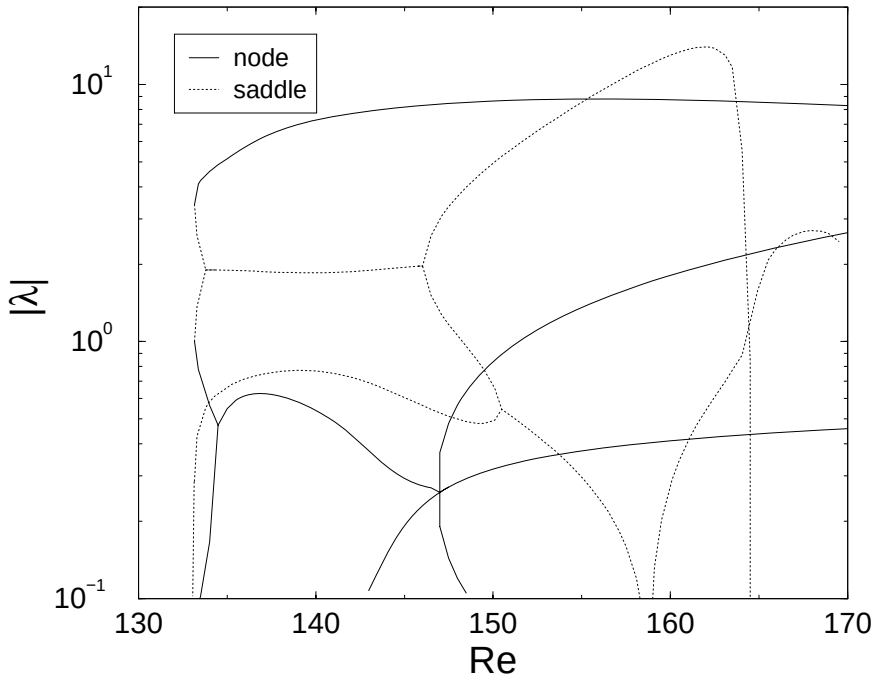

Figure 7.11: Magnitude of the eigenvalues of the Monodromie matrix of the first pair of periodic orbits.

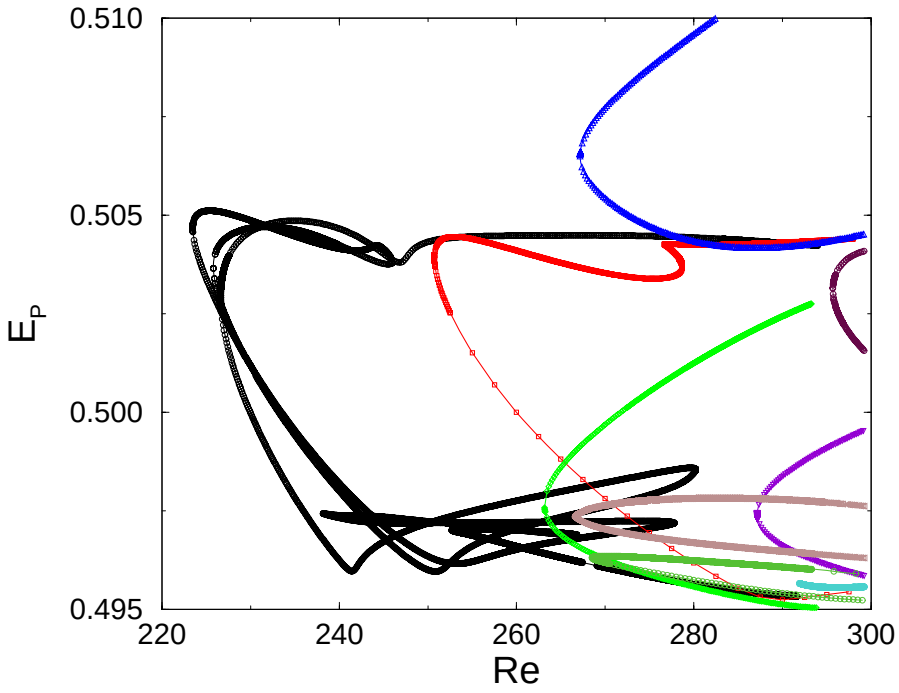

Figure 7.12: $E_p := \tilde{\mathbf{y}}^2 + y_i^2$ of the period-1 orbits at the Poincaré section at $\mathrm{Re} = 220, ..., 300$. The Poincaré section lies at $y_1 = -0.7$.

range of values corresponds to the range of Reynolds numbers where first long living states have been observed (Fig.7.2).

All these periodic orbits are linearly unstable. The absolute values of leading the eigenvalue of their Monodromie matrices are of order 10, except for the surviving lower branch at higher Reynolds numbers (Fig. 7.11). Its absolute value is of order 1000 and grows rapidly. The absolute values of the other eigenvalues are very small.

However, these first orbits are not responsible for the formation of the repellor at higher Reynolds numbers. They do not touch the Poincaré section suggested by the turbulent time signal (Fig. 7.9). Even at higher Reynolds number both orbits lie in a region of the phase space where the turbulent dynamics do not take place. Since they have no neighbors in phase space they are only able to built up a repellor when four orbits exits. These first periodic orbits generate a first repellor, which is not connected to the second one, build up for Reynolds numbers above 220, which dominates the dynamics at higher Reynolds numbers.

At $\mathrm{Re} = 223.4$ two new orbits bifurcate (Fig. 7.12) crossing the Poincaré section at a value of $y_1 = -0.7$. Additional orbits bifurcate at $\mathrm{Re} = 225.6$ and $\mathrm{Re} = 226.6$. They are connected with these first orbits by saddle node bifurcations at $\mathrm{Re} = 245.8$ and $\mathrm{Re} = 277.6$. These orbits undergo additional backward and forward bifurcations and generate up to 8 different orbits. Most of these states vanish at $\mathrm{Re} = 280$ and only two survive.

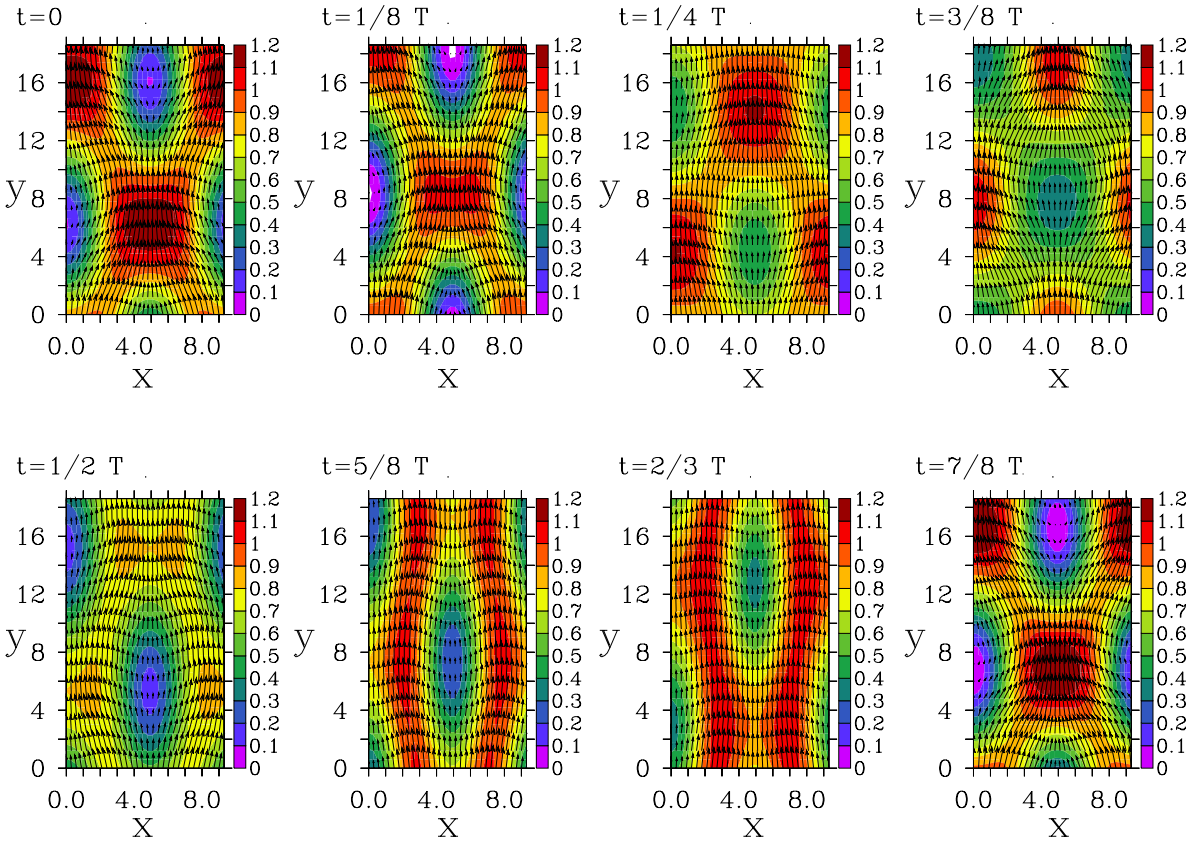

Figure 7.13: Streamwise velocity of the period-1 orbit at $\mathrm{Re} = 133$ at $z = 0$. The time t is measured in units of the periodic length divided by the number of frames $T = 62$.

At $\mathrm{Re} = 250$ two new orbits bifurcate followed by new orbits at $\mathrm{Re} = 263$, 266.6, 267, 268.4, 287, 291.6 and 295.4. They lie in the area where the turbulent motion takes place.

The observed periodic orbits are images of the self sustaining process supposed by Waleffe et al. [42, 105, 106]. Figure 7.13 shows the flow field of an orbit from the lower branch of the first period-1 orbit at a Reynolds number of $\mathrm{Re} = 133$ with period $T = 62$. The series show the streamwise velocity at $z = \pi/4$ and the flow within this plane. There is a localized region with high streamwise velocity that moves along the streamwise direction. This streak starts to vanish at $t = \frac{1}{4}T$ and regenerates till $t = \frac{5}{8}T$, where two elongates streaks are formed. These streaks split into two localized streaks and close the cycle.

Period-2 orbits

The first period-2 orbits have been observed at Reynolds numbers above 248 (Fig. 7.14). At $\mathrm{Re} = 248.1$ the first pair of period-2 orbits arise through a saddle node bifurcation. An additional pair of orbits bifurcates at $\mathrm{Re} = 257.84$. This pair is connected by a period doubling bifurcation of the first pair at $\mathrm{Re} = 274.34$. Two pairs, which are not connected to

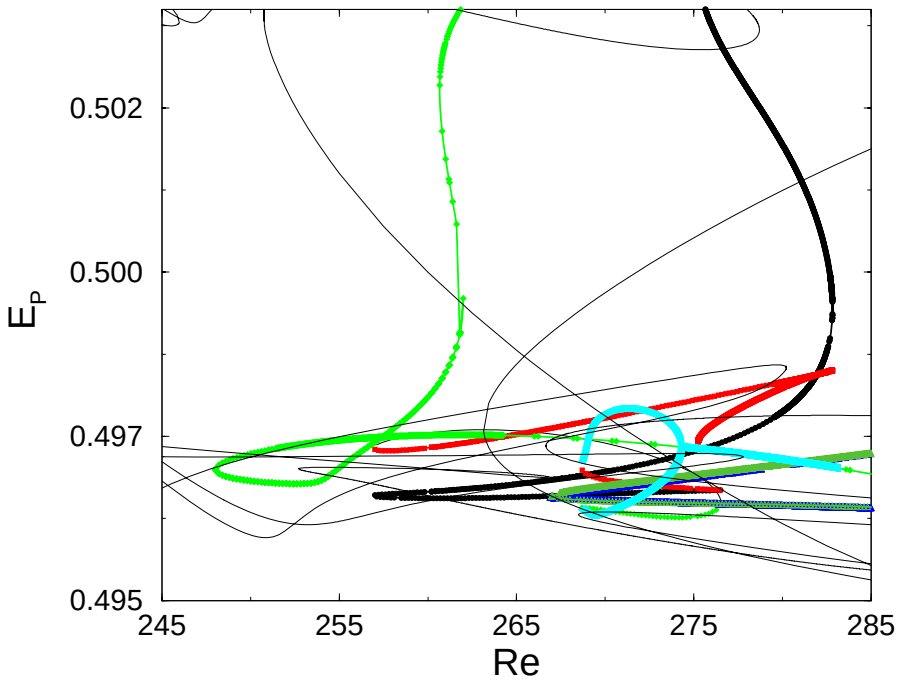

Figure 7.14: $E_P = \tilde{\mathbf{y}}^2 + y_1^2$ of period-2 orbit for different Reynolds number. The thin lines corresponds to the period-1 orbits shown in figure 7.12.

these orbits, bifurcate at $\mathrm{Re} = 266.92$ and $\mathrm{Re} = 266.96$.

There are two different types of period-2 orbits: The first type corresponds to a period-1 orbit with two components oscillating with a different frequency in a way that both compensate each other. Therefore, the time trace of $\mathbf{y}^2$ suggests only a period-1 behavior. The first pair of orbits and the two pairs bifurcating at $\mathrm{Re} = 266.92$ and $\mathrm{Re} = 266.96$ are of this type.

The second type corresponds to an oscillation with two different frequencies. This type bifurcates through a period doubling bifurcation of the first pair at $\mathrm{Re} = 274.34$.

7.5 Approximative global averaging – application of the periodic orbit theory

Since the bifurcation of the periodic orbits coincides with the birth of the turbulent state they are supposed to form the skeleton of this turbulent state. The properties of the chaotic motion can be approximately determined by investigating the properties of these unstable periodic orbits. Time averages can be replaced by global averages which can be expressed in terms of weighted sums over the periodic orbits of the system [29, 30, 39]. After a short introduction to this procedure, I focus on the escape rate and the leading Lyapunov exponent of this repellor.

7.5.1 Averaging using periodic orbits

The propagation of a distribution $\rho(t, \mathbf{x})$ starting with an initial distribution $\rho(t_0, \mathbf{y})$ can be calculated by the Frobenius-Peron operator:

$$\rho(t, \mathbf{x}) = \int_V \mathrm{d}\mathbf{y}\, \delta\left(\mathbf{x} - \mathbf{f}^t(\mathbf{y})\right) \rho(t_0, \mathbf{y})\,, \tag{7.17}$$

where $\mathbf{f}^t(\mathbf{y})$ is the flow of the investigated system and $\mathcal{L}^t = \delta\left(\mathbf{x} - \mathbf{f}^t(\mathbf{y})\right)$ is the Kernel of the evolution operator. In case of a chaotic repellor, where the normalized density ρ is not conserved, the fraction $\Gamma(t)$ which did not leave at a given time t equals

$$\Gamma(t) = \int_V \mathrm{d}\mathbf{x} \int_V \mathrm{d}\mathbf{y}\, \delta\left(\mathbf{x} - \mathbf{f}^t(\mathbf{y})\right) \rho(t_0, \mathbf{y})\,. \tag{7.18}$$

The leading eigenvalue of $\mathcal{L}^t$ dominates the time evolution of Γ. By evaluating its trace

$$\mathrm{tr}\mathcal{L}^t = \int_V \mathrm{d}\mathbf{x} \delta\left(\mathbf{x} - \mathbf{f}^t(\mathbf{x})\right)\,, \tag{7.19}$$

it is possible to calculate these eigenvalues. To calculate the contribution of a periodic orbit with a period n and a periodic time T_p on this trace, $\mathrm{tr}\mathcal{L}_p^{n\,T_p}$, one chooses a coordinate system where $x_\parallel$ refers to the direction parallel to the trajectory of the periodic orbit at a specific time and $\mathbf{x}_\perp$ refers to the plane perpendicular to $x_\parallel$ [49].

$$\mathrm{tr}\mathcal{L}_p^{n\,T_p} = \int \mathrm{d}\mathbf{x}_\perp \mathrm{d}x_\parallel \delta_\parallel \left(\mathbf{x} - \mathbf{f}^{n\,T_p}(\mathbf{x})\right) \delta_\perp \left(\mathbf{x} - \mathbf{f}^{n\,T_p}(\mathbf{x})\right)\,.$$

$\delta_\parallel$ and $\delta_\perp$ are delta functions on $x_\parallel$, $\mathbf{x}_\perp$ subspaces. The evaluation of the perpendicular part gives

$$\int \mathrm{d}\mathbf{x}_\perp \delta_\perp \left(\mathbf{x} - \mathbf{f}^{n\,T_p}(\mathbf{x})\right) = \frac{1}{\left|\det(\mathbf{1} - \mathbf{J}_p^n)\right|}\,, \tag{7.20}$$

where $\mathbf{1}$ is the unity and $\mathbf{J}_p^n$ the Monodromie matrix of the period n-orbit.

To evaluate the parallel part, one changes the variable of integration to $x_\parallel = \mid \mathbf{f}(\mathbf{x}) \mid t'$ and gets

$$\int \delta_\parallel \left(\mathbf{x} - \mathbf{f}^{n\,T_p}(\mathbf{x})\right) \mathrm{d}x_\parallel \rho_p(n\,T, x) = T_p \sum_{n=1}^{\infty} \delta(t - n\,T_p)\,. \tag{7.21}$$

For the trace $\mathrm{tr}\mathcal{L}_p^{n\,T_p}$ one yields

$$\mathrm{tr}\mathcal{L}_p^{n\,T_p} = \sum_{r=1}^{\infty} \frac{\delta(t - r\,T_p) T_p}{\left|\det(\mathbf{1} - \mathbf{J}_p^r)\right|}\,.$$

r is the repetition of this specific orbit. In general one has to sum over all orbits. In such cases the trace equals

$$\mathrm{tr}\mathcal{L}^t = \sum_p \sum_{r=1}^{\infty} \frac{\delta(t - r\,T_p)T_p}{\left|\det(\mathbf{1} - \mathbf{J}_p^r)\right|}\,. \tag{7.22}$$

To calculate the average of an observable Θ eq. (7.22) is multiplied with $e^{\beta\Theta^t}$ and a Laplace transformation of $\mathrm{tr}\mathcal{L}$ is performed to replace the time dependence of this property,

$$\begin{aligned}
\mathrm{tr}\mathcal{L}(s) &= \int_0^{\infty} \mathrm{d}s\, e^{s\,t}\mathrm{tr}\mathcal{L}^t e^{\beta\Theta_p} \\
&= \int_0^{\infty} \mathrm{d}s\, e^{s\,t} \sum_p \sum_{r=1}^{R} \frac{\delta(t - r\,T_p)T_p}{\left|\det(\mathbf{1} - \mathbf{J}_p^r)\right|} e^{\beta\Theta_p} \qquad (7.23)\\
&= \sum_p \sum_{r=1}^{R} \frac{\delta(t - r\,T_p)T_p}{\left|\det(\mathbf{1} - \mathbf{J}_p^r)\right|} e^{\beta\Theta_p - s\,r\,T_p} \\
&=: \frac{\mathrm{d}}{\mathrm{d}\,s} F(s,\beta)\,, \qquad (7.24)
\end{aligned}$$

where $F(s,\beta)$ is the Fredholm determinant:

$$F\left(\beta, s\right) = \exp\left(-\sum_p \sum_{r=1}^{\infty} \frac{e^{r(\beta\Theta_p - sT_p)}}{r\left|\det\left(\mathbf{1} - \mathbf{J}_p^r\right)\right|}\right)\,. \tag{7.25}$$

The average of Θ can be calculated by

$$\langle\Theta\rangle = -\frac{\frac{\mathrm{d}}{\mathrm{d}\,\beta} F}{\frac{\mathrm{d}}{\mathrm{d}\,s} F}\,|_{\beta=0, s=s_0}\,, \tag{7.26}$$

where s_0 equals the first zero of $F(s,\beta)$, which corresponds to the leading eigenvalue of $\mathcal{L}^t$.

Expanding $F(s,\beta)$ up to terms of second order in z yields:

$$\begin{aligned} F(s,\beta) &= \exp\left(-\sum_p \sum_{r=1}^{\infty} \frac{e^{r(\beta\Theta_p - sT_p)}}{r|\det\left(\mathbf{1}-\mathbf{J}_p^r\right)|}\right) \\ &= 1 - \left(\sum_{\substack{p \\ \text{period 1}}} \frac{e^{(\beta\Theta_p - sT_p)}}{|\det\left(\mathbf{1}-\mathbf{J}_p\right)|}\right) + \frac{1}{2}\left(\sum_{\substack{p \\ \text{period 1}}} \frac{e^{(\beta\Theta_p - sT_p)}}{|\det\left(\mathbf{1}-\mathbf{J}_p\right)|}\right)^2 \\ &\quad + \left(-\sum_{\substack{p \\ \text{period 2}}} 2\frac{e^{(\beta\Theta_p - sT_p)}}{|\det\left(\mathbf{1}-\mathbf{J}_p\right)|} + \sum_{\substack{p \\ \text{period 1}}} \frac{e^{2(\beta\Theta_p - sT_p)}}{2|\det\left(\mathbf{1}-\mathbf{J}_p^2\right)|}\right) + \mathcal{O}(3)\,. \end{aligned} \tag{7.27}$$

The terms of second order in z consist of the weighted sum over all period-2 orbits and period 2 repetitions of the period-1 orbits and the square of the sum over all period-1 orbits. Cutting this expansion and disregarding orbits of higher order implies that the weighted sum of the period orbits of higher order are compensated by the powers of the period-2 and period-1 orbits. In the next chapter the above expansion will be used to calculate some properties of the repellor.

7.5.2 Escape rate and the leading Lyapunov exponent

The escape rate of the chaotic repellor ϵ corresponds to the negative value of the leading eigenvalue of the evolution operator $\mathcal{L}^t$ which equals to the first zero of $F(s_0,\beta)$. Since there are two different repellors one would expect a change in the escape rate at $\mathrm{Re} \approx 220$. Since the first repellor lies in areas of the phase space far away from the dynamical observed region the escape rate is supposed to be significantly larger than at $\mathrm{Re} > 220$. Fig. 7.15 shows the calculated escape rate ϵ and the escape rate for an approximation of eq. (7.26) of first order, ϵ_1. These calculation show that there are still quantitative changes in the escape rate but the qualitative results correspond to the lifetime measurements and the investigations of the period-1 orbits. The expected singularities caused by the bifurcation of new periodic orbits are not visible, since they are strongly localized (see for example Fig. 7.11) and lie between the calculated values of Re.

After a sudden decrease from $\mathrm{Re} = 130$ up to 145 the escape rate increases. Between 180 and 220 the escape rate is rather large which is in accordance to the lifetime measurements.

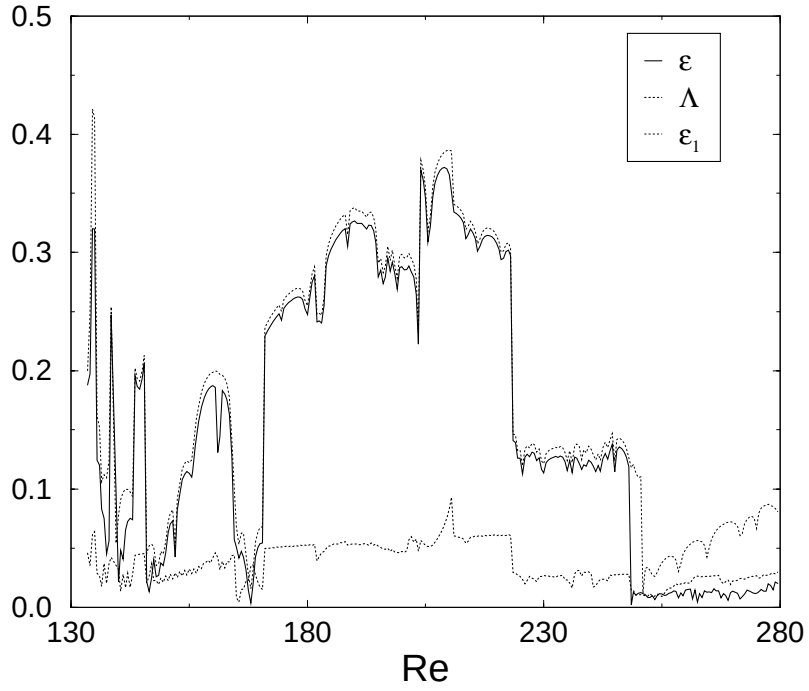

Figure 7.15: Escape rate ϵ and leading Lyapunov exponent Λ of the 9-model. These values have been approximated by the weight sum of the unstable periodic orbits. The expected singularities caused by the bifurcation of new periodic orbits are not visible, since they are strongly localized and lie between the calculated values of Re.

At these Reynolds numbers the first period-1 orbit performs additional saddle node bifurcations but these new periodic orbits increase the escape rate. The bifurcation of the additional periodic orbit at $Re = 220$ decreases the escape rate again but the additional orbits bifurcating from this orbit do not change the escape rate any further. It is the first period-2 orbit at $\mathrm{Re} = 248.1$ which reduces the escape rate drastically.

The leading Lyapunov exponent is a global measure for the divergence of trajectories. It also entered Fig. 7.15. Above $\mathrm{Re} = 150$ it shows a slight increase and a sudden decrease at $\mathrm{Re} = 220$. Above 230 the leading Lyapunov exponent is larger than the escape rate and increases for larger Reynolds numbers. Hence, an ensemble of perturbations spreads faster than it leaves the repellor.

7.6 Conclusions

The 9-model reduced model shows a transition to turbulence which is caused by the formation of a chaotic repellor. This repellor is not formed by stationary states and heteroclinic connections or homoclinic orbits between them. The stationary states bifurcate at Reynolds numbers where the repellor is already established. Contrary to the plane Couette flow it is

formed by periodic orbits.

There are two different repellors: one dominating the flow at Reynolds numbers between 133 and 200 and a second one at Reynolds numbers above 226. The first one consists of a saddle node pair of period-1 orbits. The saddle of this pair undergoes additional saddle node bifurcations at $\mathrm{Re} = 155.1, 171.6, 181.2$, and 204 and allows a nonlinear transient dynamics at very low Reynolds numbers. However, this dynamics takes place in regions of the phase space where no chaotic dynamics is observed at higher Reynolds numbers.

The origin in the difference between the transition to turbulence in plane Couette flow and the transition in this model, presumably, have their origin in the different boundary conditions. The 9-model has stress-free boundary conditions, while the plane Couette flow has no-slip boundary conditions. However, it is not clear how this difference changes the mechanism of the formation of the repellor.

8 Conclusions

Und wenn auch durch den Nebel
nicht viel zu erkennen ist,
hat man doch irgendwie das Gefühl,
in die richtige Richtung zu blicken.

Vladimir Nabokov

The transition to turbulence in plane Couette flow comes along with the formation of a new structure in phase space. Finite perturbations which do not show a linear transient behavior relax to this structure independent of their nature. Their dynamics on this structure is chaotic and their lifetimes depend very sensitively on the shape of the perturbation, its amplitude and the Reynolds number. Therefore, no distinct border between decaying and transitional perturbations exists and the transitional Reynolds number should be defined in a statistical sense. One can define it as the Reynolds number where more than half of the imposed perturbations live longer than the observation time. For an oberservation time of about 3000 time units the resulting transitional Reynolds number is 315 ± 10. However, by performing annealing experiments, where the Reynolds number is slowly decreased, one can follow turbulent states down to an annealing Reynolds number of about $\mathrm{Re}_{\mathrm{anneal}} \approx 240$.

The origin of this phase space structure are presumably heteroclinic connecting flows between the stationary states, which are born in saddle-node and pitchfork bifurcations at Reynolds numbers above $\mathrm{Re} = 125$. These stationary states consist of streamwise streaks and streamwise vortices. One can distinguish these stationary states by their streak topology. The basic topologies are the S- and the I-streaks. The S-streaks consist of long streaks and show a wavy modulation along the streamwise direction while the I-streaks show only a slight streamwise modulation. I-streaks are always staggered and localized along the spanwise direction. Additional streak topologies are possible: the streaks can split into two streaks and unify again. Such streaks are referred to ϕ-streaks; a pair of two streaks can also unify and split again forming an H-streak.

The node of the first pair of stationary states found by Nagata [68, 69] and Busse and Clever [27], the α-branch, undergoes a stable Hopf bifurcation at $\mathrm{Re} = 128$. This bifurcation generates a stable limit cycle in the vicinity of the α-node for Reynolds numbers between

$\mathrm{Re} = 128$ and 181. Additional stable Hopf bifurcations at $\mathrm{Re} = 181$ and $\mathrm{Re} = 199$ destabilize this limit cycle and support the formation of an unstable torus. Perturbations starting in the vicinity of the α-node approaching this torus show long transient lifetimes. The statistical properties of these long living states are different from the properties of turbulent states. Furthermore, the basin of attraction of this torus is rather small.

The α-node is not responsible for the transition to turbulence of finite perturbations which are not starting in the vicinity of the α-node. It seems to be the growing network of heteroclinic connections and homocline orbits of additional, linearly unstable stationary states. At a Reynolds number of about $\mathrm{Re} = 200$ a couple of heteroclinic connecting flows between these states exist. But these connecting flows are not able to generate a closed flow between different states. At $\mathrm{Re} = 240$ connecting flows from different states to states showing homocline flows are observed. Hence, long living states are possible, which follows the network of heteroclinic connecting flows to end up at an unstable homoclinic orbit. From this orbit the perturbations falls off and decays on the laminar state. This network of heteroclinic connecting and homoclinic flows grows for increasing Reynolds numbers. It starts to form at $\mathrm{Re} = 157$ where a first pitchfork bifurcation occurs.

Investigation of a low dimensional model of a linearly stable shear flow shows, that stationary states and their heteroclinic connecting flows are not the only phase space structures which support the buildup of a turbulent state. In this model unstable periodic orbits are the responsible phase space structures. These orbits are born in saddle-node bifurcations and form a chaotic repellor, which is responsible for the transition to turbulence in this model.

These two different examples for the transition to turbulence in a linearly stable shear flow show that it is connected with a global change in the phase space. This change can have its origin in the formation of stationary states or periodic orbits or both. Their heteroclinic connecting flow build up the turbulent state. So far, there is no theory which is able to predict whether unstable periodic orbits or stationary states are the responsible phase space structures. And it is an open question if the observed chaotic repellor becomes an attractor or not.

Former investigations on the transition to turbulence focused on a local investigation of the phase space. By studying the stability of the laminar profile one neglects the global changes of the phase space. Investigation of the non normal amplification of disturbances already suggests that a linear stability analysis might not be sufficient to predict the transition to turbulence. The results of this work show that an evaluation of the phase space structure holds the key for the transition to turbulence. Unfortunately, the investigation of the structure of the phase space is a very difficult task. Its like studying the exposition displayed on the title of this work. It is not clear which exhibits are valuable, which are of historical interests,

and which are totally useless.

But these investigations leads to new questions: For example, it is known that in Blasius boundary layer or plane Poiseuille flow two kinds of transition occur. The bypass transition, which is similar to the transition to turbulence in the plane Couette flow, and the transition via Tollmien-Schlichting waves, i.e. growing eigensolutions of the Orr-Sommerfeld equation [35, 61, 73]. The turbulent flows generated by these two different mechanisms differ. While streamwise streaks and vortices can be observed in bypass transition, lambda vortices dominate the turbulent state. In these flow geometries two different attracting strange sets occupy the phase space. It is an open question whether these two sets combine or not.

Little is known about the formation of the turbulent state in other flow systems. So far one is not able to identify the responsible phase space structure by investigation of the laminar flow and the boundary conditions. However, if one is able to characterize these responsible structures new methods for flow control are possible. Methods which are more sophisticated because they do not only focus on the damping of amplifying structures but also on cutting the *routes to turbulence*. Therefore, further investigations on the formation of the turbulent states in different flow geometries seem to be of great practical interest.

Appendix A Numerical methods

Wenn das einzige Werkzeug,
das du hast ein Hammer ist,
dann neigst du dazu,
jeden Problem als Nagel anzusehen.

Abraham Maslow

The presented results were based on numerical investigations of the Navier-Stokes equation. Since I did not use a standard method, I will introduce the basic concept of the applied numerical method. I will compare this method with other ones and will give some examples of its usefulness.

A.1 Imposing constraints in spectral methods

Consider a one dimensional time dependent partial differential equation

$$\frac{\partial}{\partial t} f(x,t) = \mathcal{F}(f(x,t)) \ , \tag{A.1}$$

with a flow $\mathcal{F}$ acting on a real valued function $f(x,t)$ which is an element of some Hilbert space $\mathcal{H}$ and preserves some additional constraints $\mathcal{G}(f(x,t))$. Assume that these constraints are homogenous and time independent. They can be described in the following form:

$$\forall i,t : \mathcal{G}_i(f(x,t)) = 0 \ . \tag{A.2}$$

This can be a spatial localized restriction like the Dirichlet or Neumann boundary conditions, where $\mathcal{G}_{1,2}(f)$ equals the value of the function f or its derivative at the boundary, or a delocalize restriction (See section A.2.3).

Taking a complete set of orthonormal functions $\{\phi_i(x)\}$ equations (A.1) and (A.2) can be expressed in terms of $\phi_i(x)$,

$$f(x,t) = \sum_{i=1}^{\infty} \langle \phi_i(x) \mid f(x,t) \rangle \phi_i(x) \ , \tag{A.3}$$

where $\langle \cdot \mid \cdot \rangle$ being the inner product of the set of orthonormal functions with a weight function $w(x)$:

$$\langle f \mid g \rangle = \int \mathrm{d}x \, f(x) g(x) w(x) \, . \tag{A.4}$$

This results into an infinite system of ordinary differential equations for the spectral coefficients $c_i(t) := \langle \phi_i(x) \mid f(x,t) \rangle$:

$$\forall i : \frac{\partial}{\partial t} c_i(t) = \sum_{j=1}^{\infty} \langle \phi_j(x) \mid \mathcal{F}(f(x,t)) \rangle \, . \tag{A.5}$$

If the basis satisfy all constraints, i.e.

$$\forall j, i : \mathcal{G}_i(\phi_j(x)) = 0 \tag{A.6}$$

this method is called *Galerkin*-method [19, 45, 52, 75, 77].

If $\{\phi_i(x)\}$ violates the boundary condition problems arise. A couple of techniques have been established to deal with these problems. One famous example is the spectral τ-method [19, 45, 75–79], where the finite basis is expanded to D additional functions one for each constraint:

$$f(x,t) = \sum_{i=1}^{N} c_i(t) \, \phi_i(x) + \sum_{j=1}^{D} \tau_j(t) \, \phi_{N+j}(x) \, . \tag{A.7}$$

In section A.1.1 and section A.2 this technique is introduced and compared with the Lagrangian formalism of the first and second kind.

Other methods solve the boundary conditions at distinct points in physical space [18, 19, 45, 82]. They are only able to handle geometric constraints, to solve other types like incompressibility one has to use different methods.

A.1.1 Solving constraints

Expanding f in $\{\phi\}$ gives an infinite system of ordinary differential equations for the spectral coefficients $\mathbf{c} = \{c_1, c_2, ...\}$ (A.5). One also obtains a spectral formulation of the restrictions (A.2) on c_i,

$$\forall i : G_i(\mathbf{c}(t)) = 0 \, . \tag{A.8}$$

In a finite expansion of order N these equations can be interpreted in the following way: Without equation (A.8), equation (A.5) describes the evolution of a vector $\mathbf{c}(t)$ being element of $\mathcal{M}^N$. $\mathcal{M}$ may be the real- or complex-space and N denotes the number of applied base

functions. For simplicity $\mathcal{M}$ refers to the real space. If there are D constraints the allowed space is a sub manifold of $\mathcal{M}^N$ of dimension $N - D$.

There are two obvious ways to solve (A.8) and (A.5) simultaneously if $\phi_i(x)$ violates the constraints. One can either apply an additional force acting on the right hand side of (A.5) and force it to solve the constraints or map the whole system of equations onto the sub manifold $\mathcal{M}^{N-D}$. The latter corresponds to the Lagrange formalism of the 2^{nd} kind, but there is no obvious way to obtain the mapping between $\mathcal{M}^N$ and $\mathcal{M}^{N-D}$ from (A.5).

If one is able to formulate the problem applying additional forces, which corresponds to the Lagrange formalism of the 1^{st} kind, one has the advantage to obtain this mapping. In the following, I first introduce this method, and show how to make the step from Lagrange formalism of the 1^{st} to the 2^{nd} kind.

Application of the Lagrange formalism of the 1^{st} kind

Equation (A.8) describes a hyper surface. For each i the N-dimensional gradient

$$\left(\text{grad}\, G_i\left(\mathbf{c}(t)\right)\right)_j = \frac{\partial}{\partial c_j} G_i\left(\mathbf{c}(t)\right) \tag{A.9}$$

of this equation is a vector perpendicular to each curve solving equation (A.5) and to each allowed time derivative $\frac{\partial}{\partial t}\mathbf{c}(t)$. This gradient plays the role of a boundary force. These boundary forces act on the time derivative and modify the evolution equation (A.5) by D additional terms:

$$\forall i : \frac{\partial}{\partial t} c_i(t) = \tilde{\mathcal{F}}(\mathbf{c}(t)) + \sum_{k=1}^{D} \lambda_k \left(\text{grad}\, G_k\left(\mathbf{c}(t)\right)\right) . \tag{A.10}$$

The yet unknown coefficients λ_i, the *Lagrangian parameters*, are calculated by multiplying (A.10) with each grad $G_j\left(\mathbf{c}(t)\right)$. This yields

$$\begin{aligned} \sum_{i=1}^{N} \left(\text{grad}\, G_j\left(\mathbf{c}(t)\right)\right)_i \frac{\partial}{\partial t} c_i(t) \;&=\; \sum_{i=1}^{N} \left(\text{grad}\, G_j\left(\mathbf{c}(t)\right)\right)_i \left(\tilde{\mathcal{F}}(\mathbf{c}(t))\right)_i \\ &\quad + \sum_{i=1}^{N}\sum_{k=1}^{D} \lambda_k \left(\text{grad}\, G_j\left(\mathbf{c}(t)\right)\right)_i \left(\text{grad}\, G_k\left(\mathbf{c}(t)\right)\right)_i , \end{aligned} \tag{A.11}$$

which is a system of equations linear in λ. After solving equation (A.11) one obtains the desired values of λ_k and is able to apply the needed corrections to $\tilde{\mathcal{F}}(\mathbf{c}(t))$.

The Lagrange formalism of the first kind simulates the influence of the physical constraints which leads to the mathematical formulation of the evolution equation. Its application is rather simple: One has to project the equations of motion and the boundary conditions down

to some finite set of basis functions, calculate the boundary forces and extend the evolution equation. However, since the application of boundary forces reduces the degrees of freedom the Jacobian of the resulting equation of motion is singular. Applying the Lagrange formalism of the 2^{nd} kind avoids this problem.

Application of the Lagrange formalism of the 2^{nd} kind

The boundary forces derived via the Lagrange formalism of the 1^{st} kind act like a projector $\mathcal{P}_{1st}$ on the state and the equations of motion. By applying the projector $\mathcal{P}_{1st}$ on an arbitrary state $\mathbf{c}$ the resulting state $\mathbf{c}_p$ fulfills the boundary conditions. $\mathcal{P}_{1^{\text{st}}}$ looks like

$$\mathcal{P}_{1st} = \mathbf{1} + \sum_{i=1}^{D} F^{-1}_{j,i} \left(\text{grad}\, G_i\left(\mathbf{c}(t)\right)\right) \left(\text{grad}\, G_i\left(\mathbf{c}(t)\right)\right)^T \ , \tag{A.12}$$

where $\mathbf{1}$ is the identity, $\left(\text{grad}\, G_i\left(\mathbf{c}(t)\right)\right)^T$ the transposed vector of the i^{th} boundary force and $F_{j,i}$ is the metric of the boundary forces, i.e.

$$F_{j,i} = \sum_{k=1}^{N} \left(\text{grad}\, G_j\left(\mathbf{c}(t)\right)\right)^T_k \left(\text{grad}\, G_i\left(\mathbf{c}(t)\right)\right)_k \ . \tag{A.13}$$

$\mathbf{c}_p(t)$ is an element of the span of all states solving the constraints. On elements of this span $\mathcal{P}_{1^{\text{st}}}$ acts like an identity operator. On the span of all states violating the constraints the projector acts like the null operator. One can calculate a base of the span of all allowed states by calculating the eigenvectors of $\mathcal{P}_{1^{\text{st}}}$. $\mathcal{P}_{1^{\text{st}}}$ has the eigenvalues 0 and 1, the corresponding eigenvectors of the latter are the desired vectors. Instead of solving the eigenvector problem, I use the singular value decomposition which splits $\mathcal{P}_{1^{\text{st}}}$ into its nullity and identity [83].

After calculating the span of all allowed states one is able to formulate the whole dynamics on this reduced sub manifold. This procedure is known as the Lagrangian formalism of the 2^{nd} kind and it corresponds to a Galerkin approach. The Jacobian of the equations of motion is no longer singular and the derivation is quite simple: one applies the Lagrange formalism of the 1^{st} kind, calculates the projector $\mathcal{P}_{1^{\text{st}}}$, and then applies the singular value decomposition calculating the nullity and the identity of this projector.

τ-method

The τ-method is another method to solve the constraints. In this method the finite N dimensional approximation $\mathbf{c}(t)$ gets D additional coefficients, the so-called τ-modes (A.7) [19, 45, 76, 78, 79]. The values of the τ-modes are set by the D equations describing the boundary conditions. This technique is only suitable if there are linear constraints, because

there is no unique solution for setting the τ-modes in the nonlinear case. If $\mathbf{g}_{j,i}$ equals the j^{th} component of the i^{th} solution vector of the boundary condition, the τ-projector $\mathcal{P}_\tau$ equals

$$\mathcal{P}_\tau = \begin{pmatrix} 1 & & & & \\ & \cdot & & & \\ & & \cdot & & \\ & & & \cdot & \\ & & & & 1 \\ \mathbf{g}_{1,i} & \cdot & \cdot & \cdot & \mathbf{g}_{N,i,\tau} \\ \cdot & \cdot & \cdot & \cdot & \cdot \\ \mathbf{g}_{1,D} & \cdot & \cdot & \cdot & \mathbf{g}_{N,D,\tau} \end{pmatrix}. \tag{A.14}$$

By calculating the identity of $\mathcal{P}_\tau$ one can generate a Galerkin-τ-method in the same way as it was introduced in case of $\mathcal{P}_{1^{\text{st}}}$.

In practice, one does not need to apply the projector $\mathcal{P}_\tau$ on the state. One can also solve the linear systems of equation resulting from setting the expansion of $f(t)$ (A.7) into the spectral formulation of the constraints (A.6).

The formulation of the τ-method is simple. After formulating the boundary conditions one solves the linear system of equations. These τ-modes apply the necessary modifications. Unfortunately, this method gives less accurate solutions than the Lagrange methods. This will be shown in the following.

A.1.2 Convergence of the Lagrangian formalism of the 1^{st} kind in respect to τ-methods

So far, the set of base functions $\{\phi_i(x)\}$ has not been specified. Solutions of the singular Sturm-Liouville problem are the preferred type, namely Legendre- and Chebyshev-polynomials [19, 45]. If the approximated function is sufficiently smooth both series expansions converge faster than algebraically[45].

This convergence refers to the accuracy of approximating a smooth function without any constraints. To solve the constraints τ-methods and the boundary forces changes the spectral coefficients. Assuming that the boundary forces are orthonormal, one gets upper bounds for the amplitude of this correction, with $\mathcal{G}$ and $\mathcal{H}$ being the projection operator for τ- and

Lagrange method:

$$\begin{aligned}
\sqrt{\langle \sum_{j=1}^{D} \tau_j(t)\,\phi_{N+j}(x) \mid \sum_{i=1}^{D} \tau_i(t)\,\phi_{N+i}(x)\rangle} &= \sqrt{\sum_{j=1}^{D} \tau_j^2} \\
&= \sqrt{(\tau \mid \tau)} = \|\tau\| = \|\mathcal{G}\mathbf{c}\| \\
&\leq \|\mathcal{G}\|\,\|\mathbf{c}\| \\
&\leq \sqrt{N \cdot D}\max_{i,j} \mathcal{G}_{i,j}\|\mathbf{c}\| \qquad \text{(A.15)}
\end{aligned}$$

and

$$\begin{aligned}
\sqrt{\langle \sum_{i=1}^{D} \lambda_i \text{grad}\, G_i(\mathbf{c}(t)) \mid \sum_{i=1}^{D} \lambda_i \text{grad}\, G_i(\mathbf{c}(t))\rangle} &= \sqrt{\sum_{i=1}^{D} \lambda_i^2} \\
&= \sqrt{(\lambda \mid \lambda)} = \|\lambda\| \\
&= \|\sum_{i=1}^{D} \text{grad}\, G_i \mathbf{c}(t)\| \\
&= \|\mathcal{H}\mathbf{c}(t)\| \leq \|\mathcal{H}\|\,\|\mathbf{c}(t)\| \\
&\leq \|\mathcal{H}\|\,\|\mathbf{c}(t)\| \\
&\leq \sqrt{N \cdot D}\max_{i,j} \mathcal{H}_{i,j}\|\mathbf{c}\|\,, \qquad \text{(A.16)}
\end{aligned}$$

with $\|x\| = \sum_{i=1}^{D} x_i^2$. The boundary forces are normalized, hence $\max_{i,j} \mathcal{H}_{i,j} < 1$. This is not the case for $\max_{i,j} \mathcal{G}_{i,j}$. The corrections of the τ-method are higher than the one obtained by applying the Lagrangian method of the first kind. This can cause problems especially if $\max_{i,j} \mathcal{G}_{i,j}$ grows with the number of applied polynomials which is the case for Neumann boundary conditions.

A.1.3 Conservation laws and boundary forces

The application of the Lagrangian method is straight forward: After selecting a set of base functions $\{\phi_i(x)\}$ one calculates the evolution equation for the dynamics of the spectral coefficients $c_i(t)$ and calculates the boundary forces. In this procedure two different kinds of inner products have been used: The inner weighted product of the $\{\phi_i(x)\}$, $\langle \cdot \mid \cdot \rangle$, and the Euclidean inner product $(\cdot \mid \cdot)$.

One would prefer to have a method which does not affect the existing conservation laws of the equation of motions and which conserves the symmetric properties. It is important that the application of projections does not affect the energy balance of the approximation since this causes an instability due to time integration. The term *energy* does not necessarily refers

to the energy in the physical sense. It refers to a quadratic inner product of the state namely

$$E(t) = \int f^n(x,t)\, f^{n^*}(x,t)\, \mathrm{d}x =: \{f^n(x,t) \mid f^n(x,t)\}\ , \tag{A.17}$$

with an arbitrary real number n. For $n = 1$, the energy in the physical sense, the time derivative of E equals

$$\frac{\mathrm{d}}{\mathrm{d}\,t} E(t) = 2\left\{ f(x,t) \mid \frac{\mathrm{d}}{\mathrm{d}\,t} f(x,t)(t) \right\}\ . \tag{A.18}$$

Applying the Lagrangian formalism of the first kind one can split this inner product into two terms:

$$\begin{aligned} \frac{\mathrm{d}}{\mathrm{d}\,t} E(t) &= 2\left\{ f(x,t) \mid \frac{\mathrm{d}}{\mathrm{d}\,t} f(x,t)(t) \right\} \\ &= \frac{1}{2}\left\{ f(x,t) \mid \frac{\mathrm{d}}{\mathrm{d}\,t} \tilde{f}(x,t)(t) \right\} + 2\left\{ f(x,t) \mid \sum_{i=1}^{D} \lambda_i \operatorname{grad} \mathcal{G}_i(x) \right\}\ . \end{aligned}$$

The first term equals the change in energy balance of the reduced system. The second term equals the change of the energy due to the applied forces. In case of an infinite set of base-functions the supposed error in the energy balance vanishes. In case of a finite set the projection of the applied forces onto the state with respect to $\{\cdot \mid \cdot\}$ corresponds to the change in energy. If the forces are orthogonal due to this inner product even the finite set conserves the energy hence the only error applied is an error due to the finite resolution. This is only the case if the inner products $\{\cdot \mid \cdot\}$ and $\langle \cdot \mid \cdot \rangle$ are equal. Disregarding this effect may produce wrong solutions, although the solutions fulfill the boundary conditions.

A.2 Examples

In order to illustrate the Lagrangian formalism of the first kind and compare it to τ-methods some simple examples are given. Some of the above problems are illustrated and investigated.

A.2.1 The heat transfer equation

Consider the heat transfer equation

$$\frac{\partial}{\partial\, t} f(x,t) = \nu \frac{\partial^2}{\partial x^2} f(x,t)\ , \tag{A.19}$$

with Dirichlet boundary conditions:

$$f(x = \pm 1, t) = 0\,. \tag{A.20}$$

Expanding $f(x,t)$ with normalized Chebyshev- or Legendre-polynomials and disregarding the boundary conditions one gets the following two evolution equations for the spectral-modes $c_i(t)$

$$\text{Chebyshev: } \frac{\partial}{\partial t} c_i(t) = \frac{\nu}{\theta_i T_i(1)} \sum_{\substack{j=i+2 \\ i+j \text{ odd}}}^{N} j\left(j^2 - i^2\right) T_j(1)\, c_j \tag{A.21}$$

$$\text{Legendre: } \frac{\partial}{\partial t} c_i(t) = \nu \frac{\left(i+\frac{1}{2}\right)}{L_i(1)} \sum_{\substack{j=i+2 \\ i+j \text{ even}}}^{N} \left(j\,(j+1) - i\,(i+1)\right) T_j(1)\, c_j\,, \tag{A.22}$$

with $\theta_0 = 2$ and $\theta_{n>0} = 1$.

The spectral formulation of the boundary conditions equals

$$0 = \sum_{i=1}^{N} (-1)^{(i-1)} c_i\, T_i(1) \frac{1}{\theta_{i-1}}$$

for Chebyshev polynomials and

$$0 = \sum_{i=1}^{N} (-1)^{(i-1)} c_i\, L_i(1)$$

for normalized Legendre polynomials. The solution of this problem via the τ-method is shown in [19, 23, 45, 82]. Here, I focus on the application of the Lagrange formalism of the first kind:

In both cases the boundary forces are

$$\mathbf{F}_i^1 = \begin{cases} 0 & i \text{ odd} \\ \frac{T_i(1)}{\theta_{i-1}} \text{ or } L_i(1) & i \text{ even} \end{cases}$$
$$\mathbf{F}_i^2 = \begin{cases} \frac{T_i(1)}{\theta_{i-1}} \text{ or } L_i(1) & i \text{ odd} \\ 0 & i \text{ even} \end{cases} \tag{A.23}$$

$\mathbf{F}^{1,2}$ are orthogonal, one just has to normalize these two forces.

The eigenvalues of this operator are given by $\lambda_i = \frac{i^2\pi^2}{4}$. Table A.1 shows the absolute error of the first seven eigenvalues for different kinds of spectral methods. τ-method and Chebyshev-Lagrange show less accurate results than the Legendre-Lagrange formalism since the first two methods violate the energy conservation. The error of Chebyshev-Lagrange is up to 5

λ	Chebyshev Lagrange	Legendre Lagrange	Chebyshev-τ	Legendre-τ
$\frac{\pi^2}{4}$	$.14\,10^{-12}$	$.53\,10^{-13}$	$.14\,10^{-10}$	$.14\,10^{-10}$
π^2	$.87\,10^{-11}$	$.13\,10^{-13}$	$.36\,10^{-7}$	$.26\,10^{-7}$
$\frac{9\,\pi^2}{4}$	$.77\,10^{-7}$	$.27\,10^{-11}$	$.11\,10^{-3}$	$.84\,10^{-4}$
$4\,\pi^2$	$.13\,10^{-5}$	$.66\,10^{-9}$	$.13\,10^{-2}$	$.11\,10^{-2}$
$\frac{25\,\pi^2}{4}$	$.24\,10^{-3}$	$.93\,10^{-5}$	$.10$	$.82\,10^{-1}$
$9\,\pi^2$	$.12\,10^{-2}$	$.12\,10^{-3}$	$.33$	$.27$
$\frac{49\,\pi^2}{4}$	$.99\,10^{-1}$	$.50\,10^{-1}$	5.82	2.84

Table A.1: Absolute error of the numerical solution of the heat-transfer equation (A.19) with Dirichlet boundary conditions. These calculations were done with Maple using 16 polynomial and an accuracy of 16 digits.

orders higher than the error done by Legendre-Lagrange even though both polynomials have the same good rate of convergence.

A.2.2 The vorticity equation

Another example is the vorticity equation:

$$\frac{\partial^2 \partial}{\partial x^2 \partial t} f\,(x,t) = \nu \frac{\partial^4}{\partial x^4} f\,(x,t)\ , \tag{A.24}$$

where f solves Dirichlet and Neumann boundary conditions:

$$f\,(x=\pm 1,t) = \frac{\partial}{\partial\, x} f\,(x=\pm 1,t) = 0 \tag{A.25}$$

There are two additional forces beside the two boundary forces from the former study (A.23):

$$\text{Legendre}: \ \mathbf{F}_i^{3,4} = \sum_{q=1}^{N} (2\,(q-1)+1) \sum_{\substack{p=q+1 \\ p+q \text{ odd}}}^{N} L_p(\pm 1)\,\delta_{i,p} \tag{A.26}$$

$$\text{Chebyshev}: \ \mathbf{F}_i^{3,4} = \sum_{q=1}^{N} \frac{2}{\theta_{q-1}} \sum_{\substack{p=q+1 \\ p+q \text{ odd}}}^{N} p T_p(\pm 1)\delta_{i,p}\ . \tag{A.27}$$

$F^{3,4}$ refers to the left and the right boundary condition and $\delta_{i,j}$ is the Kronecker delta.

The eigenvalue spectrum of the τ-approximation has positive eigenvalues which makes this representation numerically unstable for time integration [45]. This is also the case if one

λ	Legendre Lagrange	Chebyshev Lagrange
π^2	$.15^{-8}$	$.44^{-8}$
$4\,\pi^2$	$.98^{-10}$	$.24^{-9}$
$9\,\pi^2$	$.16^{-10}$	$.33^{-8}$
$16\,\pi^2$	$.12^{-5}$	$.52^{-5}$
$25\,\pi^2$	$.39^{-2}$	$.10^{-2}$
$36\,\pi^2$	$.86$	1.46

Table A.2: Absolute error of the numerical solution of the vorticity-equation equation (A.24). These calculations were done with Maple using 16 polynomials and an accuracy of 16 digits. Positive eigenvalues exists in the case of Chebyshev-Lagrange. This make the time integration of these approximations unstable.

applies Chebyshev-Lagrange. Application of the Legendre-Lagrange-procedure yield a numerical stable solution. If one is only interested in the eigenvalue spectrum, both methods can be applied. Since the boundary conditions imply a high velocity gradient near the boundary Chebyshev polynomials show a better convergence this effect compensates the error done by the violation of energy conservation.

A.2.3 Linearized Navier-Stokes equation in the case of shear flow geometry

Linear stability analysis of a plane shear flow $\mathbf{U}_0$ base on the investigation of the linearized Navier-Stokes-equation

$$\frac{\partial}{\partial\, t}\mathbf{u} \;=\; -\left(\mathbf{U}_0\cdot\text{grad}\,\right)\,\mathbf{u} - \left(\mathbf{u}\cdot\text{grad}\,\right)\,\mathbf{U}_0 - \text{grad}\;p + \text{Re}^{-1}\Delta\mathbf{u}\,, \tag{A.28}$$

where $\mathbf{u}$ is an infinitesimal disturbance of the laminar shear flow [20, 35, 61]. I investigate the simple case of an incompressible shear flow between two infinite plates with periodic boundary conditions in span- and streamwise direction and no-slip boundary condition in the wall normal direction, i.e.:

$$\mathbf{u}_{z=\pm 1} = 0 \tag{A.29}$$

and

$$\text{div}\;\mathbf{u} = 0\,. \tag{A.30}$$

The no-slip boundary condition and its corresponding forces are the same as in A.2.1. $\mathbf{u}$ is expanded in streamwise and spanwise direction by one Fourier mode with the wave vector

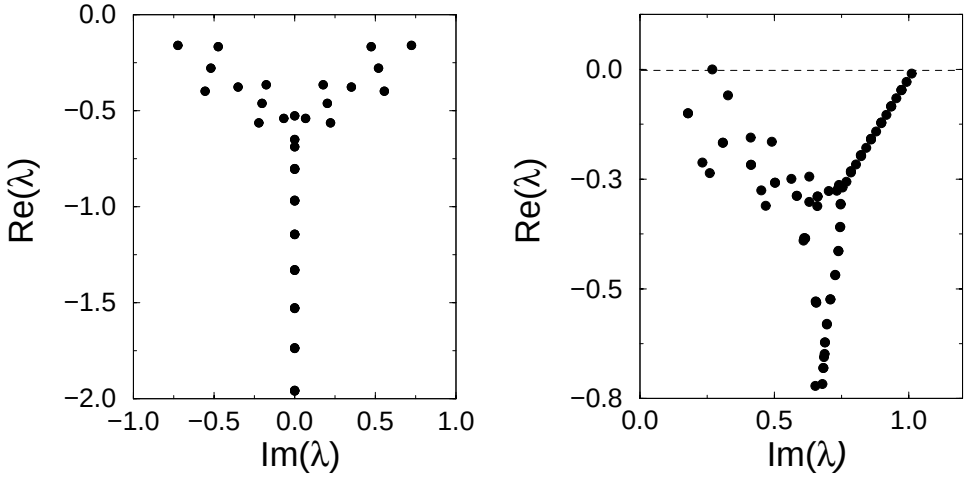

Figure A.1: Spectra of the eigenvalues of the linear operator $\mathcal{L}$ in the case of plane Couette flow (left) at $\mathrm{Re} = 400$ and plane Poiseuille flow (right) at $\mathrm{Re} = 5773$. The former has no eigenvalue with positive real part, the latter has one, bifurcating at $\mathrm{Re} = 5772.4$.

α in streamwise and β in spanwise direction. For Legendre-Lagrange the boundary force for N polynomials applying equation (A.30) are:

$$F_p^n = \begin{cases} i\,\alpha & ,p \leq N \\ i\,\beta & ,N < p \leq 2\,N \\ (2(n-1)+1)\,\frac{L_p(1)}{L_n(1)} & ,2N < p \leq 3\,N \end{cases} . \tag{A.31}$$

F_p^n is the p^{th}-component of the n^{th} boundary force.

The right hand side of equation (A.28) is a linear operator. The analysis of its eigenspectrum gives information on the stability of the investigated flow. Two examples are the plane Poiseuille flow, with $\mathbf{U_0} = (1 - z^2)\mathbf{e}_x$, and the plane Couette flow, with $\mathbf{U_0} = z\mathbf{e}_x$. The former flow becomes linear unstable at $\mathrm{Re} = 5772.4$ [35, 61], while the latter is stable for all Reynolds numbers [93]. Note that in the case of plane Poiseuille flow, the Reynolds number is based on the full gap width and the full speed, hence the Reynolds number is four times larger than the Reynolds number used in plane Couette flow.

In figure A.1 the spectra of eigenvalues for both systems are shown. The instability of the plane Poiseuille flow and the stability of the plane Couette flow can be proven. Both spectra have been calculated with 32 Legendre polynomials.

A.3 Conclusions

In this appendix the application of Lagrangian method of the 1^{st} and 2^{nd} for solving partial differential equations with constraints have been introduced. This method is rather simple

and the results are even better than the τ-method. Combining the Lagrangian method with an Legendre expansion gives an energy conserving spectral approximation of the equations of motion with an high rate of convergence. Due to the simple application of these approximation, Lagrangian method of the 1^{st} kind should be the first attempt to formulate a spectral representation of a boundary value problem if a suitable Galerkin approach is not obvious.

Appendix B Spectral representation of the investigated symmetries

The investigation of stationary states in plane Couette flow (chapter 5) focused on members of the two symmetry group `NBC` and `I`. The reduction of the equations of motion to members of these group leads to relationships between the spectral coefficients. In this chapter, these relationships are given.

The spectral representation of the flow field and the application of the boundary condition has been shown in chapter A.2.3. In this chapter, I use an extended version of the form

$$u^{x,y,z}(\mathbf{x}) = \sum_{\mathbf{n},p} \left(\tilde{a}^{x,y,z} + i\,\tilde{b}^{x,y,z} \right)_{\mathbf{n},p} e^{2\pi\, i \left(\frac{n_x}{L_x} x + \frac{n_y}{L_y} y \right)} L_p(z)\,.$$

Here, $\left(\tilde{a}^j + i\,\tilde{b}^j \right)$ equals the complex spectral coefficient $\tilde{u}^j$, $j = x, y, z$. Note that the reality of u gives an additional constraint: $\left(\tilde{a}^{x,y,z} + i\,\tilde{b}^{x,y,z} \right)_{\mathbf{n},p} = \left(\tilde{a}^{x,y,z} - i\,\tilde{b}^{x,y,z} \right)_{-\mathbf{n},p}$.

B.1 $\mathcal{P}$ symmetry

$$\mathcal{R} : \begin{pmatrix} u \\ v \\ w \end{pmatrix} (x,y,z) = \begin{pmatrix} -u \\ -v \\ -w \end{pmatrix} (-x,-y,-z)$$

$$\begin{aligned} a^i_{\mathbf{k},p} &= 0 \quad p\,\text{even} \\ b^i_{\mathbf{k},p} &= 0 \quad p\,\text{odd} \end{aligned}$$

B.2 $\tilde{\mathcal{R}}$ symmetry

$$\tilde{\mathcal{R}} \begin{pmatrix} u \\ v \\ w \end{pmatrix} (x, y + L_y/2, z) = \begin{pmatrix} u \\ -v \\ w \end{pmatrix} (x, -y - L_y/2, z)$$

$$\begin{aligned}
a^{x,z}_{n_x,n_y,p} &= (-1)^{n_y}\, a^{x,z}_{n_x,-n_y,p} \\
b^{x,z}_{n_x,n_y,p} &= (-1)^{n_y}\, a^{x,z}_{n_x,-n_y,p} \\
a^{y}_{n_x,n_y,p} &= (-1)^{n_y+1}\, a^{y}_{n_x,-n_y,p} \\
b^{y}_{n_x,n_y,p} &= (-1)^{n_y+1}\, b^{y}_{n_x,-n_y,p}
\end{aligned}$$

B.3 $\mathcal{W}$ symmetry

$$\mathcal{W} : \begin{pmatrix} u \\ v \\ w \end{pmatrix} (x, y, z) = \begin{pmatrix} u \\ -v \\ w \end{pmatrix} (x + L_x/2, -y, z)$$

$$\begin{aligned}
a^{x,z}_{n_x,n_y,p} &= (-1)^{n_x}\, a^{x,z}_{-n_x,n_y,p} \\
b^{x,z}_{n_x,n_y,p} &= (-1)^{n_x+1}\, b^{x,z}_{-n_x,n_y,p} \\
a^{y}_{n_x,n_y,p} &= (-1)^{n_x+1}\, a^{y}_{-n_x,n_y,p} \\
b^{y}_{n_x,n_y,p} &= (-1)^{n_x}\, b^{y}_{-n_x,n_y,p}
\end{aligned}$$

B.4 $\mathcal{V}$ symmetry

$$\mathcal{V} : \begin{pmatrix} u \\ v \\ w \end{pmatrix} (x, y, z) = \begin{pmatrix} -u \\ v \\ -w \end{pmatrix} (-x, y + L_y/2, -z)$$

$$\begin{aligned}
a^{x,z}_{n_x,n_y,p} &= (-1)^{n_y+1+p}\, a^{x,z}_{-n_x,n_y,p} \\
b^{x,z}_{n_x,n_y,p} &= (-1)^{n_y+1+p}\, b^{x,z}_{-n_x,n_y,p} \\
a^{y}_{n_x,n_y,p} &= (-1)^{n_y+p}\, a^{y}_{-n_x,n_y,p} \\
b^{y}_{n_x,n_y,p} &= (-1)^{n_y+p}\, b^{y}_{-n_x,n_y,p}
\end{aligned}$$

Appendix C General equations of motion for the $9d$-model

The following substitutions are being used:

$$\begin{aligned} S_1 &= \sqrt{\frac{L^2+1}{L^2}} \\ S_2 &= \sqrt{1+\alpha^2} \\ S_3 &= \sqrt{\frac{L^2+4}{L^2}} \\ L &= \sqrt{\alpha^2+\beta^2} \end{aligned}$$

The parameters α and β determ the box lengths in spanwise (α) and streamwise (β) directions.

$$\begin{aligned} \frac{\mathrm{d}}{\mathrm{d}\,t}\,x_1 &= 4\,\frac{\alpha\,x_5x_3}{S_1\,L} - 2\,\frac{\alpha\,x_7x_4}{S_2} + \left(-4\,\frac{\alpha\,x_9}{S_1\,L} - 12\,\frac{\beta\,x_8}{L^2S_3\,S_1}\right)x_5 \\ &\quad -4\,\frac{\alpha\,x_8x_6}{S_3\,L} - \nu\,x_1 \\ \frac{\mathrm{d}}{\mathrm{d}\,t}\,x_2 &= -9\,\nu\,x_2 - 6\,\frac{\alpha\,x_7x_4}{S_2} + \left(12\,\frac{\beta\,x_8}{L^2S_3\,S_1} + 12\,\frac{\alpha\,x_9}{S_1\,L}\right)x_5 - 12\,\frac{\alpha\,x_8x_6}{S_3\,L} \\ \frac{\mathrm{d}}{\mathrm{d}\,t}\,x_3 &= \left(\left(-2\,\frac{\beta^2\alpha}{(L^2)^{3/2}\,S_1} - 2\,\frac{\alpha^3}{(L^2)^{3/2}\,S_1}\right)x_5 + \left(-2\,\frac{\beta\,\alpha^2}{L^2} - 2\,\frac{\beta^3}{L^2}\right)x_6\right)x_1 \\ &\quad + \left(\left(6\,\frac{\beta^2\alpha}{(L^2)^{3/2}\,S_1} - 2\,\frac{\alpha^3}{(L^2)^{3/2}\,S_1}\right)x_5 + \left(-2\,\frac{\beta^3}{L^2} + 6\,\frac{\beta\,\alpha^2}{L^2}\right)x_6\right)x_4 \\ &\quad + \left(-16\,\frac{\alpha^3}{\pi^2\,(L^2)^{3/2}\,S_1} - 16\,\frac{\beta^2\alpha}{\pi^2\,(L^2)^{3/2}\,S_1}\right)x_5 + \left(-16\,\frac{\beta\,\alpha^2}{\pi^2L^2} - 16\,\frac{\beta^3}{\pi^2L^2}\right)x_6 \\ &\quad + \left(\left(-12\,\frac{\beta\,\alpha^2}{S_2\,(L^2)^{3/2}\,S_3} + 4\,\frac{\beta^3}{S_2\,(L^2)^{3/2}\,S_3}\right)x_8 + \left(-2\,\frac{\alpha^3}{S_2\,L^2} + 6\,\frac{\beta^2\alpha}{S_2\,L^2}\right)x_9\right)x_7 \\ &\quad -\nu\,L^2x_3 \end{aligned}$$

$$
\begin{aligned}
\frac{\mathrm{d}}{\mathrm{d}\,t}\,x_4 &= \frac{\alpha\,x_7x_1}{S_2} + 3\,\frac{\alpha\,x_2x_7}{S_2} + \left(4\,\frac{\alpha^3}{(L^2)^{3/2}\,S_1} - 2\,\frac{\alpha}{S_1\,L} + 4\,\frac{\beta^2\alpha}{(L^2)^{3/2}\,S_1}\right)x_5x_3 \\
&+ \left(6\,\frac{\beta\,x_8}{L^2S_3\,S_1} + \left(2\,\frac{\alpha}{S_1\,L} + 4\,\frac{\beta^2\alpha}{(L^2)^{3/2}\,S_1} + 4\,\frac{\alpha^3}{(L^2)^{3/2}\,S_1}\right)x_9\right)x_5 \\
&+ \left(-8\,\frac{\alpha^3}{(L^2)^{3/2}\,S_3} + 2\,\frac{\alpha}{S_3\,L} - 8\,\frac{\beta^2\alpha}{(L^2)^{3/2}\,S_3}\right)x_8x_6 + 8\,\frac{\alpha\,x_7}{\pi^2S_2} - \nu\,\left(4\,\alpha^2+1\right)x_4 \\
\frac{\mathrm{d}}{\mathrm{d}\,t}\,x_5 &= \left(-\frac{\beta}{L^2S_3\,S_1} + \frac{\beta}{S_3\,S_1} + 4\,\frac{\alpha^2\beta}{L^4S_3\,S_1} + 4\,\frac{\beta^3}{L^4S_3\,S_1}\right)x_8x_1 \\
&+ \left(-\frac{\beta}{S_3\,S_1} + 4\,\frac{\alpha^2\beta}{L^4S_3\,S_1} + 4\,\frac{\beta^3}{L^4S_3\,S_1} + \frac{\beta}{L^2S_3\,S_1}\right)x_8x_2 - 4\,\frac{\beta^2\alpha\,x_3x_4}{(L^2)^{3/2}\,S_1} \\
&+ \left(\left(\frac{\beta}{L^2S_3\,S_1} + 4\,\frac{\alpha^2\beta}{L^4S_3\,S_1} - \frac{\beta}{S_3\,S_1} - 4\,\frac{\beta^3}{L^4S_3\,S_1}\right)x_8 - 4\,\frac{\beta^2\alpha\,x_9}{(L^2)^{3/2}\,S_1}\right)x_4 \\
&+ \left(\left(\frac{\alpha^3}{L^2\,(L^2+1)\,S_2} - \frac{L^2\alpha}{(L^2+1)\,S_2} - \frac{\alpha}{(L^2+1)\,S_2} - \frac{\beta^2\alpha}{(L^2+1)\,S_2}\right.\right. \\
&\left.\left. + \frac{\alpha^3}{(L^2+1)\,S_2} - \frac{\beta^2\alpha}{L^2\,(L^2+1)\,S_2}\right)x_7 - \nu\,\left(L^2+1\right)\right)x_5 \\
&+ \left(-2\,\frac{\beta\,\alpha^2}{LS_2\,S_1} - 2\,\frac{\beta\,\alpha^2}{(L^2)^{3/2}\,S_2\,S_1}\right)x_7x_6 \\
&+ \left(32\,\frac{\beta\,\alpha^2}{\pi^2L^4S_3\,S_1} - 8\,\frac{\beta}{\pi^2L^2S_3\,S_1} + 8\,\frac{\beta}{\pi^2S_3\,S_1} + 32\,\frac{\beta^3}{\pi^2L^4S_3\,S_1}\right)x_8 \\
\frac{\mathrm{d}}{\mathrm{d}\,t}\,x_6 &= \left(\left(\frac{\beta\,\alpha^2}{L^2} + \frac{\beta^3}{L^2}\right)x_3 + \left(2\,\frac{\beta^2\alpha}{(L^2)^{3/2}\,S_3} - \frac{\alpha}{S_3\,L} + 2\,\frac{\alpha^3}{(L^2)^{3/2}\,S_3}\right)x_8\right. \\
&\left. + \left(\frac{\beta\,\alpha^2}{L^2} + \frac{\beta^3}{L^2}\right)x_9\right)x_1 + \left(\left(2\,\frac{\beta^2\alpha}{(L^2)^{3/2}\,S_3} + 2\,\frac{\alpha^3}{(L^2)^{3/2}\,S_3} + \frac{\alpha}{S_3\,L}\right)x_8\right. \\
&\left. + \left(\frac{\beta\,\alpha^2}{L^2} + \frac{\beta^3}{L^2}\right)x_9\right)x_2 + \left(\left(\frac{\beta^3}{L^2} - 3\,\frac{\alpha^2\beta}{L^2}\right)x_4 + 8\,\frac{\alpha^2\beta}{\pi^2L^2} + 8\,\frac{\beta^3}{\pi^2L^2}\right)x_3 \\
&+ \left(\left(-6\,\frac{\beta^2\alpha}{(L^2)^{3/2}\,S_3} + 2\,\frac{\alpha^3}{(L^2)^{3/2}\,S_3} + \frac{\alpha}{S_3\,L}\right)x_8 + \left(\frac{\beta^3}{L^2} - 3\,\frac{\alpha^2\beta}{L^2}\right)x_9\right)x_4 \\
&+ \left(\frac{\beta}{LS_2\,S_1} - \frac{\alpha^2\beta}{(L^2)^{3/2}\,S_2\,S_1} + \frac{\beta^3}{(L^2)^{3/2}\,S_2\,S_1}\right)x_7x_5 \\
&+ \left(-8\,\frac{\alpha}{\pi^2S_3\,L} + 16\,\frac{\beta^2\alpha}{\pi^2\,(L^2)^{3/2}\,S_3} + 16\,\frac{\alpha^3}{\pi^2\,(L^2)^{3/2}\,S_3}\right)x_8 \\
&+ \left(8\,\frac{\alpha^2\beta}{\pi^2L^2} + 8\,\frac{\beta^3}{\pi^2L^2}\right)x_9 \\
&+ \left(-\nu\,\left(L^2+1\right) + 2\,\frac{\beta^2\alpha\,x_7}{S_2\,L^2}\right)x_6
\end{aligned}
$$

$$
\begin{aligned}
\frac{\mathrm{d}}{\mathrm{d}\,t}x_7 &= \left(\left(4\,\frac{\beta\,\alpha^2}{L S_3\,S_2}-4\,\frac{\beta}{L S_3\,S_2}+16\,\frac{\beta\,\alpha^2}{S_2\,\left(L^2\right)^{3/2}\,S_3}\right)x_8-8\,\frac{\alpha\,\beta^2 x_9}{S_2\,L^2}\right)x_3\\
&+\left(-4\,\frac{\alpha^3}{\left(L^2+1\right)S_2}+4\,\frac{L^2\alpha}{\left(L^2+1\right)S_2}-4\,\frac{\alpha^3}{L^2\left(L^2+1\right)S_2}+4\,\frac{\alpha}{\left(L^2+1\right)S_2}\right){x_5}^2\\
&+\left(4\,\frac{\beta\,\alpha^2}{L S_2\,S_1}+8\,\frac{\beta\,\alpha^2}{\left(L^2\right)^{3/2}\,S_2\,S_1}-4\,\frac{\beta}{L S_2\,S_1}\right)x_6x_5-4\,\frac{\beta^2\alpha\,{x_6}^2}{S_2\,L^2}\\
&-\nu\,\left(4\,\alpha^2+4\right)x_7\\
\frac{\mathrm{d}}{\mathrm{d}\,t}x_8 &= \left(4\,\frac{\beta}{L^2S_3\,S_1}-4\,\frac{\beta\,\alpha^2}{L^4S_3\,S_1}-\frac{\beta}{S_3\,S_1}-4\,\frac{\beta^3}{L^4S_3\,S_1}\right)x_5x_1\\
&+\left(-4\,\frac{\beta\,\alpha^2}{L^4S_3\,S_1}-4\,\frac{\beta}{L^2S_3\,S_1}-4\,\frac{\beta^3}{L^4S_3\,S_1}+\frac{\beta}{S_3\,S_1}\right)x_5x_2\\
&-2\,\frac{\beta\,\alpha^2x_3x_7}{L S_3\,S_2}+\left(\left(-4\,\frac{\beta\,\alpha^2}{L^4S_3\,S_1}-4\,\frac{\beta}{L^2S_3\,S_1}+\frac{\beta}{S_3\,S_1}+4\,\frac{\beta^3}{L^4S_3\,S_1}\right)x_5\right.\\
&+\left(-8\,\frac{\beta}{\pi^2S_3\,S_1}+32\,\frac{\beta}{\pi^2L^2S_3\,S_1}-32\,\frac{\beta^3}{\pi^2L^4S_3\,S_1}-32\,\frac{\alpha^2\beta}{\pi^2L^4S_3\,S_1}\right)x_5\\
&\left.+8\,\frac{\beta^2\alpha\,x_6}{\left(L^2\right)^{3/2}\,S_3}\right)x_4-\nu\,\left(L^2+4\right)x_8\\
\frac{\mathrm{d}}{\mathrm{d}\,t}x_9 &= \left(\left(2\,\frac{\alpha}{S_1\,L}-\frac{\beta^2\alpha}{\left(L^2\right)^{3/2}\,S_1}-\frac{\alpha^3}{\left(L^2\right)^{3/2}\,S_1}\right)x_5+\left(-\frac{\beta^3}{L^2}-\frac{\alpha^2\beta}{L^2}\right)x_6\right)x_1\\
&+\left(\left(-\frac{\beta^2\alpha}{\left(L^2\right)^{3/2}\,S_1}-2\,\frac{\alpha}{S_1\,L}-\frac{\alpha^3}{\left(L^2\right)^{3/2}\,S_1}\right)x_5+\left(-\frac{\beta^3}{L^2}-\frac{\alpha^2\beta}{L^2}\right)x_6\right)x_2\\
&+\left(\left(-2\,\frac{\alpha}{S_1\,L}-\frac{\alpha^3}{\left(L^2\right)^{3/2}\,S_1}+3\,\frac{\beta^2\alpha}{\left(L^2\right)^{3/2}\,S_1}\right)x_5+\left(-\frac{\beta^3}{L^2}+3\,\frac{\alpha^2\beta}{L^2}\right)x_6\right)x_4\\
&+\left(-8\,\frac{\beta^2\alpha}{\pi^2\,\left(L^2\right)^{3/2}\,S_1}+16\,\frac{\alpha}{\pi^2S_1\,L}-8\,\frac{\alpha^3}{\pi^2\,\left(L^2\right)^{3/2}\,S_1}\right)x_5\\
&+\left(-8\,\frac{\beta^3}{\pi^2L^2}-8\,\frac{\alpha^2\beta}{\pi^2L^2}\right)x_6+\left(\frac{\beta^2\alpha}{S_2\,L^2}+\frac{\alpha^3}{S_2\,L^2}\right)x_7x_3-\nu\,\left(L^2+4\right)x_9
\end{aligned}
$$

Appendix C General equations of motion for the $9d$-model

The following substitutions are being used:

$$\begin{aligned} S_1 &= \sqrt{\frac{L^2+1}{L^2}} \\ S_2 &= \sqrt{1+\alpha^2} \\ S_3 &= \sqrt{\frac{L^2+4}{L^2}} \\ L &= \sqrt{\alpha^2+\beta^2} \end{aligned}$$

The parameters α and β determ the box lengths in spanwise (α) and streamwise (β) directions.

$$\begin{aligned} \frac{\mathrm{d}}{\mathrm{d}\,t}\,x_1 &= 4\,\frac{\alpha\,x_5x_3}{S_1\,L} - 2\,\frac{\alpha\,x_7x_4}{S_2} + \left(-4\,\frac{\alpha\,x_9}{S_1\,L} - 12\,\frac{\beta\,x_8}{L^2S_3\,S_1}\right)x_5 \\ &\quad -4\,\frac{\alpha\,x_8x_6}{S_3\,L} - \nu\,x_1 \\ \frac{\mathrm{d}}{\mathrm{d}\,t}\,x_2 &= -9\,\nu\,x_2 - 6\,\frac{\alpha\,x_7x_4}{S_2} + \left(12\,\frac{\beta\,x_8}{L^2S_3\,S_1} + 12\,\frac{\alpha\,x_9}{S_1\,L}\right)x_5 - 12\,\frac{\alpha\,x_8x_6}{S_3\,L} \\ \frac{\mathrm{d}}{\mathrm{d}\,t}\,x_3 &= \left(\left(-2\,\frac{\beta^2\alpha}{(L^2)^{3/2}\,S_1} - 2\,\frac{\alpha^3}{(L^2)^{3/2}\,S_1}\right)x_5 + \left(-2\,\frac{\beta\,\alpha^2}{L^2} - 2\,\frac{\beta^3}{L^2}\right)x_6\right)x_1 \\ &\quad + \left(\left(6\,\frac{\beta^2\alpha}{(L^2)^{3/2}\,S_1} - 2\,\frac{\alpha^3}{(L^2)^{3/2}\,S_1}\right)x_5 + \left(-2\,\frac{\beta^3}{L^2} + 6\,\frac{\beta\,\alpha^2}{L^2}\right)x_6\right)x_4 \\ &\quad + \left(-16\,\frac{\alpha^3}{\pi^2\,(L^2)^{3/2}\,S_1} - 16\,\frac{\beta^2\alpha}{\pi^2\,(L^2)^{3/2}\,S_1}\right)x_5 + \left(-16\,\frac{\beta\,\alpha^2}{\pi^2L^2} - 16\,\frac{\beta^3}{\pi^2L^2}\right)x_6 \\ &\quad + \left(\left(-12\,\frac{\beta\,\alpha^2}{S_2\,(L^2)^{3/2}\,S_3} + 4\,\frac{\beta^3}{S_2\,(L^2)^{3/2}\,S_3}\right)x_8 + \left(-2\,\frac{\alpha^3}{S_2\,L^2} + 6\,\frac{\beta^2\alpha}{S_2\,L^2}\right)x_9\right)x_7 \\ &\quad -\nu\,L^2x_3 \end{aligned}$$

$$
\begin{aligned}
\frac{\mathrm{d}}{\mathrm{d}\,t}\,x_4 &= \frac{\alpha\,x_7x_1}{S_2} + 3\,\frac{\alpha\,x_2x_7}{S_2} + \left(4\,\frac{\alpha^3}{(L^2)^{3/2}\,S_1} - 2\,\frac{\alpha}{S_1\,L} + 4\,\frac{\beta^2\alpha}{(L^2)^{3/2}\,S_1}\right)x_5x_3 \\
&+ \left(6\,\frac{\beta\,x_8}{L^2S_3\,S_1} + \left(2\,\frac{\alpha}{S_1\,L} + 4\,\frac{\beta^2\alpha}{(L^2)^{3/2}\,S_1} + 4\,\frac{\alpha^3}{(L^2)^{3/2}\,S_1}\right)x_9\right)x_5 \\
&+ \left(-8\,\frac{\alpha^3}{(L^2)^{3/2}\,S_3} + 2\,\frac{\alpha}{S_3\,L} - 8\,\frac{\beta^2\alpha}{(L^2)^{3/2}\,S_3}\right)x_8x_6 + 8\,\frac{\alpha\,x_7}{\pi^2S_2} - \nu\,\left(4\,\alpha^2+1\right)x_4 \\
\frac{\mathrm{d}}{\mathrm{d}\,t}\,x_5 &= \left(-\frac{\beta}{L^2S_3\,S_1} + \frac{\beta}{S_3\,S_1} + 4\,\frac{\alpha^2\beta}{L^4S_3\,S_1} + 4\,\frac{\beta^3}{L^4S_3\,S_1}\right)x_8x_1 \\
&+ \left(-\frac{\beta}{S_3\,S_1} + 4\,\frac{\alpha^2\beta}{L^4S_3\,S_1} + 4\,\frac{\beta^3}{L^4S_3\,S_1} + \frac{\beta}{L^2S_3\,S_1}\right)x_8x_2 - 4\,\frac{\beta^2\alpha\,x_3x_4}{(L^2)^{3/2}\,S_1} \\
&+ \left(\left(\frac{\beta}{L^2S_3\,S_1} + 4\,\frac{\alpha^2\beta}{L^4S_3\,S_1} - \frac{\beta}{S_3\,S_1} - 4\,\frac{\beta^3}{L^4S_3\,S_1}\right)x_8 - 4\,\frac{\beta^2\alpha\,x_9}{(L^2)^{3/2}\,S_1}\right)x_4 \\
&+ \left(\left(\frac{\alpha^3}{L^2\,(L^2+1)\,S_2} - \frac{L^2\alpha}{(L^2+1)\,S_2} - \frac{\alpha}{(L^2+1)\,S_2} - \frac{\beta^2\alpha}{(L^2+1)\,S_2}\right.\right. \\
&\left.\left. + \frac{\alpha^3}{(L^2+1)\,S_2} - \frac{\beta^2\alpha}{L^2\,(L^2+1)\,S_2}\right)x_7 - \nu\,\left(L^2+1\right)\right)x_5 \\
&+ \left(-2\,\frac{\beta\,\alpha^2}{LS_2\,S_1} - 2\,\frac{\beta\,\alpha^2}{(L^2)^{3/2}\,S_2\,S_1}\right)x_7x_6 \\
&+ \left(32\,\frac{\beta\,\alpha^2}{\pi^2L^4S_3\,S_1} - 8\,\frac{\beta}{\pi^2L^2S_3\,S_1} + 8\,\frac{\beta}{\pi^2S_3\,S_1} + 32\,\frac{\beta^3}{\pi^2L^4S_3\,S_1}\right)x_8 \\
\frac{\mathrm{d}}{\mathrm{d}\,t}\,x_6 &= \left(\left(\frac{\beta\,\alpha^2}{L^2} + \frac{\beta^3}{L^2}\right)x_3 + \left(2\,\frac{\beta^2\alpha}{(L^2)^{3/2}\,S_3} - \frac{\alpha}{S_3\,L} + 2\,\frac{\alpha^3}{(L^2)^{3/2}\,S_3}\right)x_8\right. \\
&\left. + \left(\frac{\beta\,\alpha^2}{L^2} + \frac{\beta^3}{L^2}\right)x_9\right)x_1 + \left(\left(2\,\frac{\beta^2\alpha}{(L^2)^{3/2}\,S_3} + 2\,\frac{\alpha^3}{(L^2)^{3/2}\,S_3} + \frac{\alpha}{S_3\,L}\right)x_8\right. \\
&\left. + \left(\frac{\beta\,\alpha^2}{L^2} + \frac{\beta^3}{L^2}\right)x_9\right)x_2 + \left(\left(\frac{\beta^3}{L^2} - 3\,\frac{\alpha^2\beta}{L^2}\right)x_4 + 8\,\frac{\alpha^2\beta}{\pi^2L^2} + 8\,\frac{\beta^3}{\pi^2L^2}\right)x_3 \\
&+ \left(\left(-6\,\frac{\beta^2\alpha}{(L^2)^{3/2}\,S_3} + 2\,\frac{\alpha^3}{(L^2)^{3/2}\,S_3} + \frac{\alpha}{S_3\,L}\right)x_8 + \left(\frac{\beta^3}{L^2} - 3\,\frac{\alpha^2\beta}{L^2}\right)x_9\right)x_4 \\
&+ \left(\frac{\beta}{LS_2\,S_1} - \frac{\alpha^2\beta}{(L^2)^{3/2}\,S_2\,S_1} + \frac{\beta^3}{(L^2)^{3/2}\,S_2\,S_1}\right)x_7x_5 \\
&+ \left(-8\,\frac{\alpha}{\pi^2S_3\,L} + 16\,\frac{\beta^2\alpha}{\pi^2\,(L^2)^{3/2}\,S_3} + 16\,\frac{\alpha^3}{\pi^2\,(L^2)^{3/2}\,S_3}\right)x_8 \\
&+ \left(8\,\frac{\alpha^2\beta}{\pi^2L^2} + 8\,\frac{\beta^3}{\pi^2L^2}\right)x_9 \\
&+ \left(-\nu\,\left(L^2+1\right) + 2\,\frac{\beta^2\alpha\,x_7}{S_2\,L^2}\right)x_6
\end{aligned}
$$

$$
\begin{aligned}
\frac{\mathrm{d}}{\mathrm{d}\,t}x_7 &= \left(\left(4\,\frac{\beta\,\alpha^2}{L S_3\,S_2}-4\,\frac{\beta}{L S_3\,S_2}+16\,\frac{\beta\,\alpha^2}{S_2\,\left(L^2\right)^{3/2}\,S_3}\right)x_8-8\,\frac{\alpha\,\beta^2 x_9}{S_2\,L^2}\right)x_3\\
&+\left(-4\,\frac{\alpha^3}{\left(L^2+1\right)S_2}+4\,\frac{L^2\alpha}{\left(L^2+1\right)S_2}-4\,\frac{\alpha^3}{L^2\left(L^2+1\right)S_2}+4\,\frac{\alpha}{\left(L^2+1\right)S_2}\right){x_5}^2\\
&+\left(4\,\frac{\beta\,\alpha^2}{L S_2\,S_1}+8\,\frac{\beta\,\alpha^2}{\left(L^2\right)^{3/2}\,S_2\,S_1}-4\,\frac{\beta}{L S_2\,S_1}\right)x_6x_5-4\,\frac{\beta^2\alpha\,{x_6}^2}{S_2\,L^2}\\
&-\nu\,\left(4\,\alpha^2+4\right)x_7\\
\frac{\mathrm{d}}{\mathrm{d}\,t}x_8 &= \left(4\,\frac{\beta}{L^2S_3\,S_1}-4\,\frac{\beta\,\alpha^2}{L^4S_3\,S_1}-\frac{\beta}{S_3\,S_1}-4\,\frac{\beta^3}{L^4S_3\,S_1}\right)x_5x_1\\
&+\left(-4\,\frac{\beta\,\alpha^2}{L^4S_3\,S_1}-4\,\frac{\beta}{L^2S_3\,S_1}-4\,\frac{\beta^3}{L^4S_3\,S_1}+\frac{\beta}{S_3\,S_1}\right)x_5x_2\\
&-2\,\frac{\beta\,\alpha^2x_3x_7}{L S_3\,S_2}+\left(\left(-4\,\frac{\beta\,\alpha^2}{L^4S_3\,S_1}-4\,\frac{\beta}{L^2S_3\,S_1}+\frac{\beta}{S_3\,S_1}+4\,\frac{\beta^3}{L^4S_3\,S_1}\right)x_5\right.\\
&+\left(-8\,\frac{\beta}{\pi^2S_3\,S_1}+32\,\frac{\beta}{\pi^2L^2S_3\,S_1}-32\,\frac{\beta^3}{\pi^2L^4S_3\,S_1}-32\,\frac{\alpha^2\beta}{\pi^2L^4S_3\,S_1}\right)x_5\\
&\left.+8\,\frac{\beta^2\alpha\,x_6}{\left(L^2\right)^{3/2}\,S_3}\right)x_4-\nu\,\left(L^2+4\right)x_8\\
\frac{\mathrm{d}}{\mathrm{d}\,t}x_9 &= \left(\left(2\,\frac{\alpha}{S_1\,L}-\frac{\beta^2\alpha}{\left(L^2\right)^{3/2}\,S_1}-\frac{\alpha^3}{\left(L^2\right)^{3/2}\,S_1}\right)x_5+\left(-\frac{\beta^3}{L^2}-\frac{\alpha^2\beta}{L^2}\right)x_6\right)x_1\\
&+\left(\left(-\frac{\beta^2\alpha}{\left(L^2\right)^{3/2}\,S_1}-2\,\frac{\alpha}{S_1\,L}-\frac{\alpha^3}{\left(L^2\right)^{3/2}\,S_1}\right)x_5+\left(-\frac{\beta^3}{L^2}-\frac{\alpha^2\beta}{L^2}\right)x_6\right)x_2\\
&+\left(\left(-2\,\frac{\alpha}{S_1\,L}-\frac{\alpha^3}{\left(L^2\right)^{3/2}\,S_1}+3\,\frac{\beta^2\alpha}{\left(L^2\right)^{3/2}\,S_1}\right)x_5+\left(-\frac{\beta^3}{L^2}+3\,\frac{\alpha^2\beta}{L^2}\right)x_6\right)x_4\\
&+\left(-8\,\frac{\beta^2\alpha}{\pi^2\,\left(L^2\right)^{3/2}\,S_1}+16\,\frac{\alpha}{\pi^2S_1\,L}-8\,\frac{\alpha^3}{\pi^2\,\left(L^2\right)^{3/2}\,S_1}\right)x_5\\
&+\left(-8\,\frac{\beta^3}{\pi^2L^2}-8\,\frac{\alpha^2\beta}{\pi^2L^2}\right)x_6+\left(\frac{\beta^2\alpha}{S_2\,L^2}+\frac{\alpha^3}{S_2\,L^2}\right)x_7x_3-\nu\,\left(L^2+4\right)x_9
\end{aligned}
$$

Appendix D Bifurcation of stationary states in plane Couette flow

In this appendix the solution branches of the observed stationary states of the NBC and the I symmetry group are displayed for Reynolds number between 100 and 400. Each symbol corresponds to a found solution. These symbols are connected to sketch the solution branch. E is the energy density of the perturbation, expressed in terms of the energy of the laminar flow field E_0

$$E = \frac{1}{2V E_0} \int \mathbf{u} \cdot \mathbf{u}^* \, \mathrm{d}V \,. \tag{D.1}$$

S the shear rate of the full flow field $\mathbf{u} + \mathbf{U}_0$

$$S = \frac{1}{A} \int \frac{\partial}{\partial z} (u + z) \,|_{z=1} \, \mathrm{d}A \,. \tag{D.2}$$

D.1 Stationary states in the NBC group

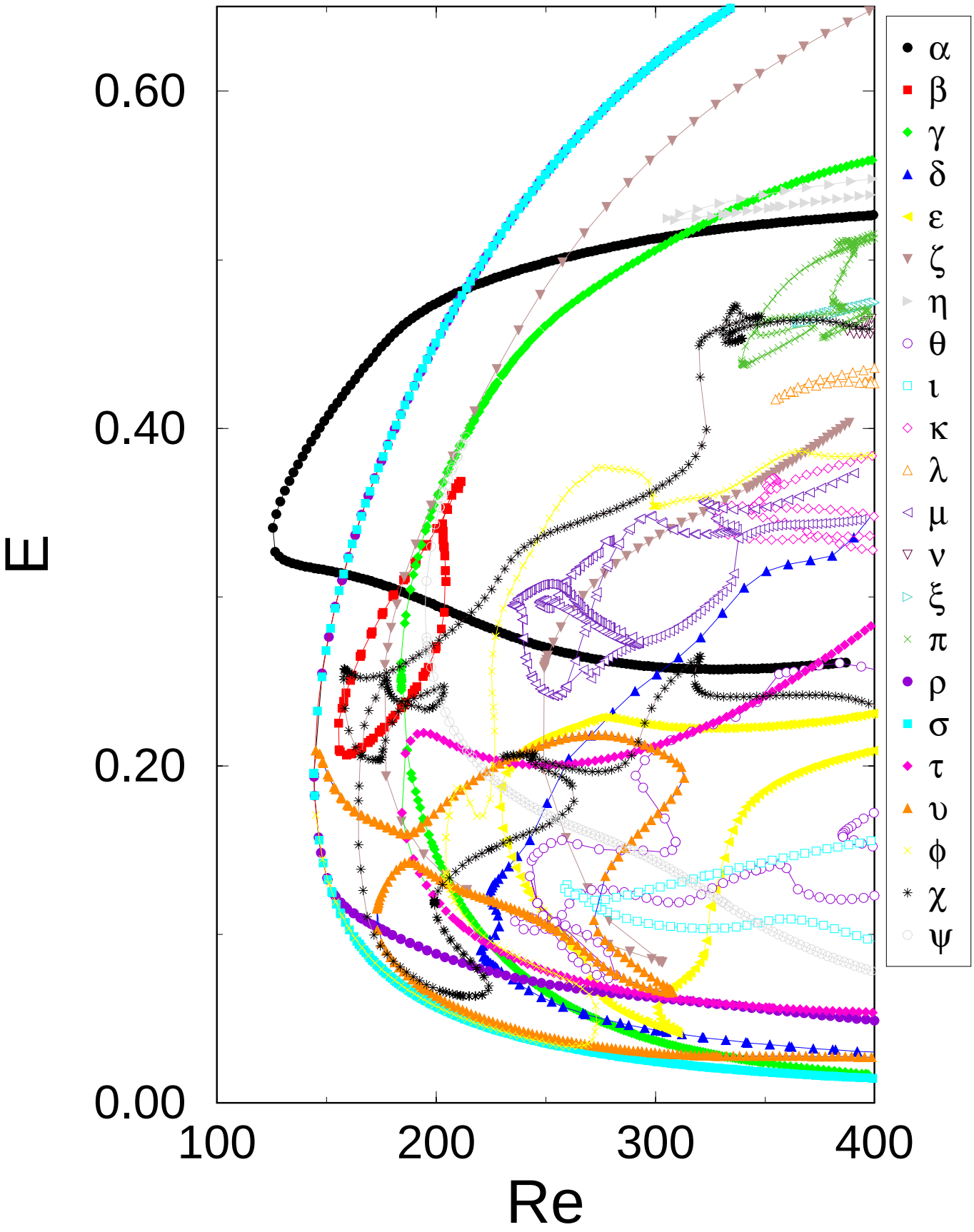

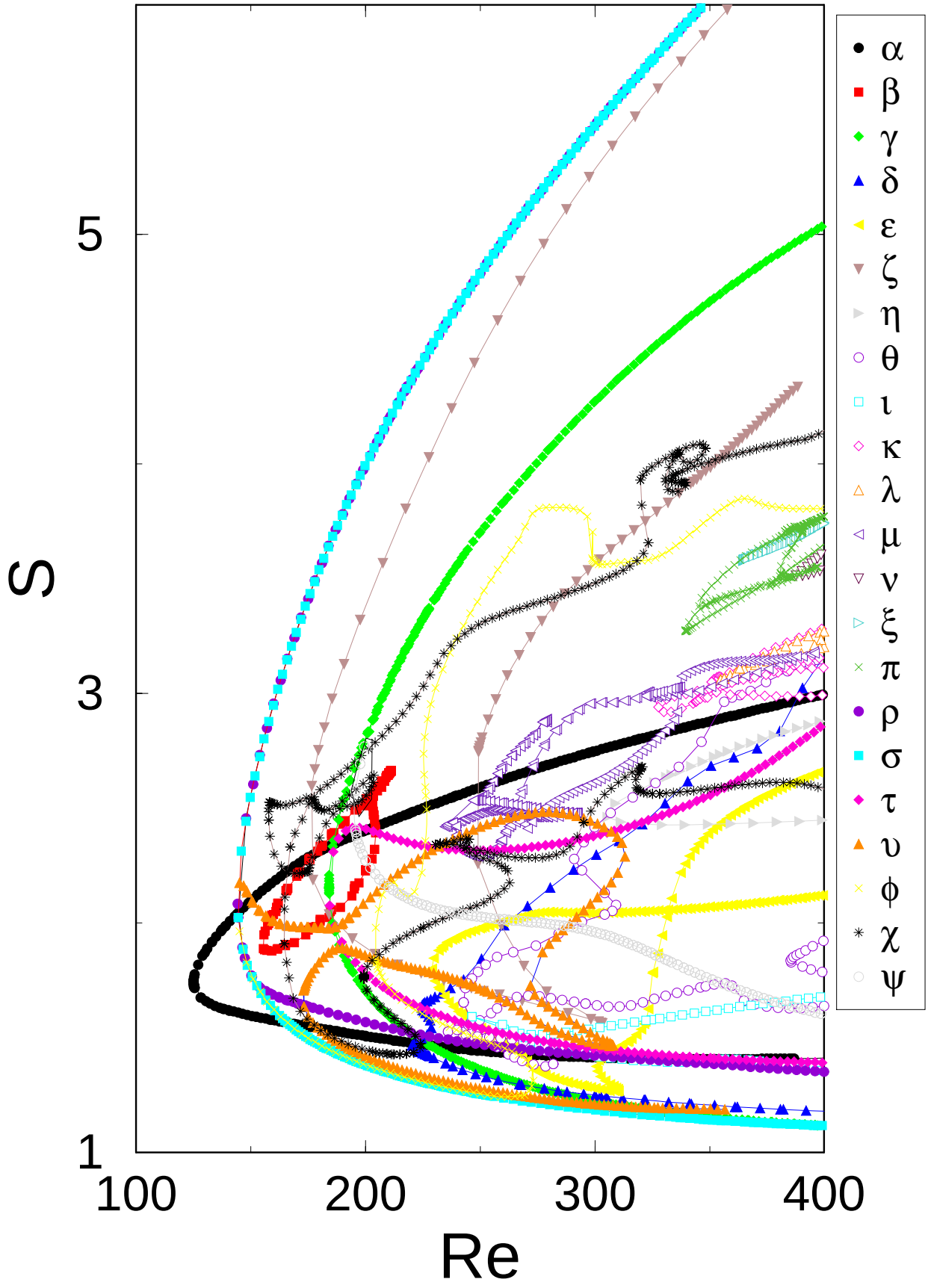
S
5
3
1
100
200
300
400
Re
α
β
γ
δ
ε
ζ
η
θ
ι
κ
λ
μ
ν
ξ
π
ρ
σ
τ
υ
ϕ
χ
ψ

D.2 Stationary states in the I group

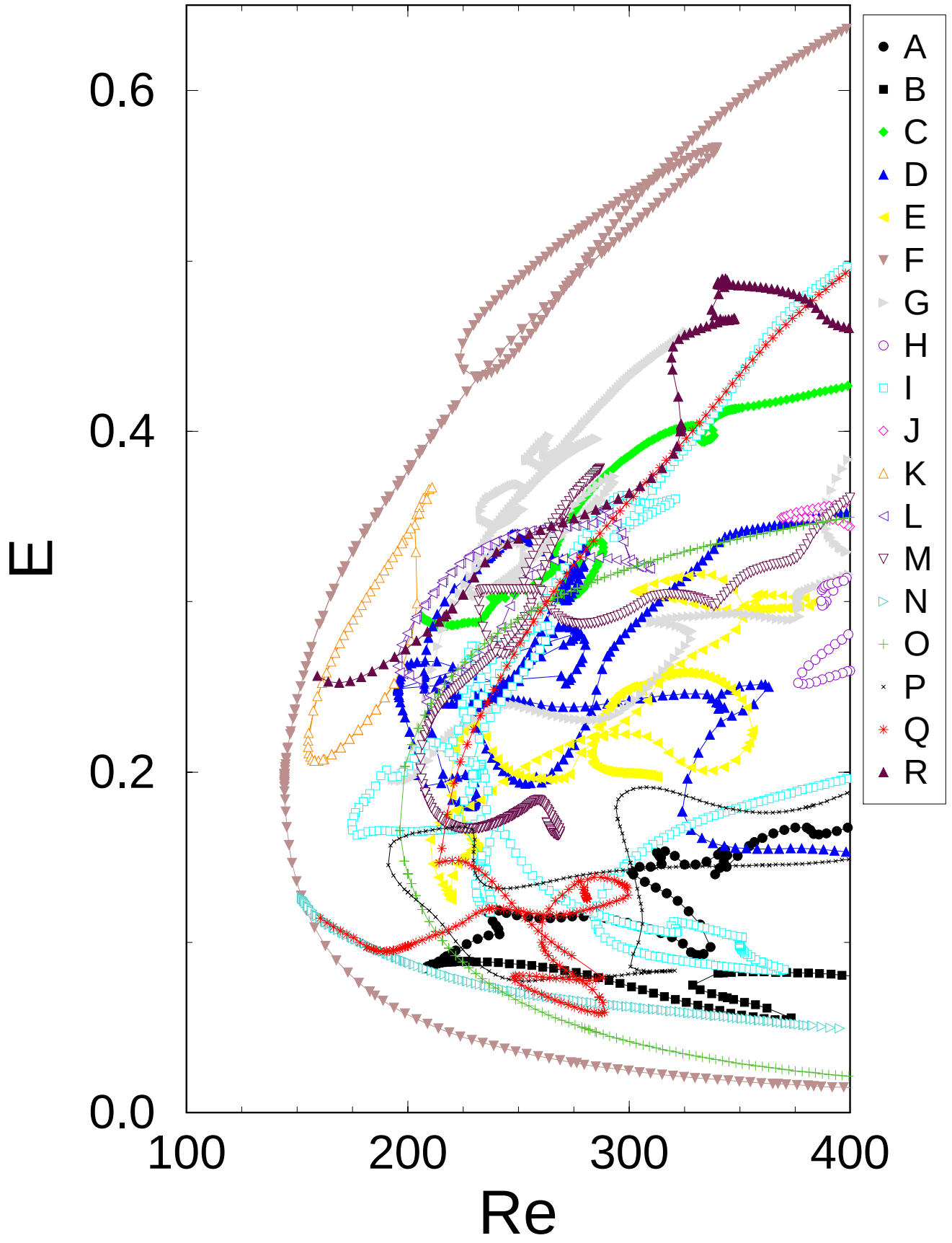

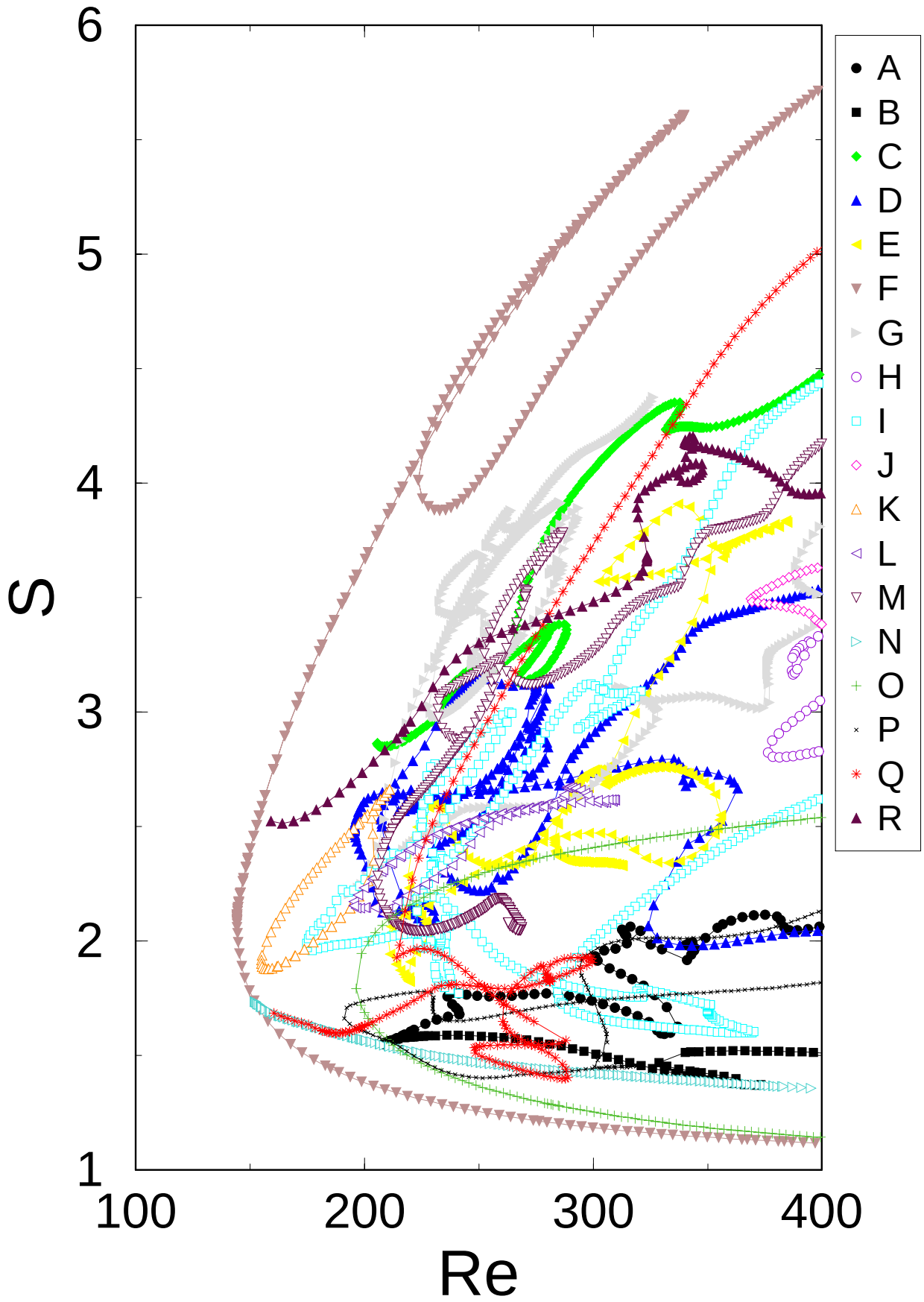
6
5
4
3
2
1
S
100
200
300
400
Re
A
B
C
D
E
F
G
H
I
J
K
L
M
N
O
P
Q
R

Appendix E Stationary states in plane Couette flow

In this appendix the stationary states are classified by the symmetries of u_+, Ω and $\langle u \rangle$. The group $\mathcal{A}, \mathcal{B}, \mathcal{C}, \mathcal{D}$ consists of members of the $\mathcal{NBC}$ symmetry group. The $\mathcal{E}, \mathcal{F}, \mathcal{G}$ of the member of the $\mathcal{I}$ group. The investigated symmetries are the translation of the streaks along the streamwise and/or the spanwise direction and the reflection along the x or z axis.

$$\mathcal{T}_{\Delta x, \Delta y} : \begin{pmatrix} u \\ v \end{pmatrix}(x, y) = \begin{pmatrix} u \\ v \end{pmatrix}(x + \Delta x, y + \Delta y) \tag{E.1}$$

$$\mathcal{R}_y : \begin{pmatrix} u \\ v \end{pmatrix}(x, y) = \begin{pmatrix} u \\ -v \end{pmatrix}(x, -y) \tag{E.2}$$

$$\mathcal{R}_z : \begin{pmatrix} u \\ v \\ w \end{pmatrix}(x, y) = \begin{pmatrix} u \\ v \\ -w \end{pmatrix}(x, y, -z) \tag{E.3}$$

The number of streaks and streak layers gives an additional characteristic:

$$\begin{pmatrix} m : \text{number of streaks} \\ n : \text{number of streak layers} \end{pmatrix} \tag{E.4}$$

E.1 NBC group

E.1.1 $\mathcal{A}$

$$\mathcal{A}_1 : \begin{pmatrix} 1 \\ 1 \end{pmatrix} \mathrm{Re}_{\mathrm{cr}} = 125$$

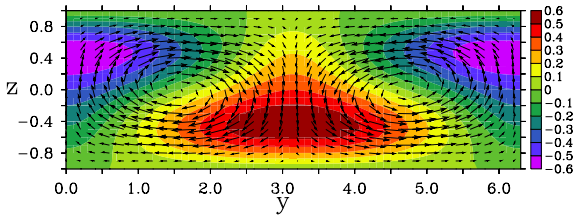

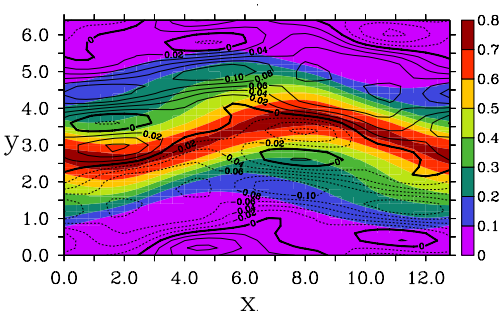

α-branch

$$\mathcal{A}_2 : \begin{pmatrix} 1 \\ 1 \end{pmatrix} \mathrm{Re}_{\mathrm{cr}} = 280$$

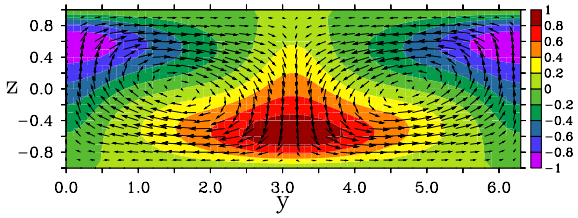

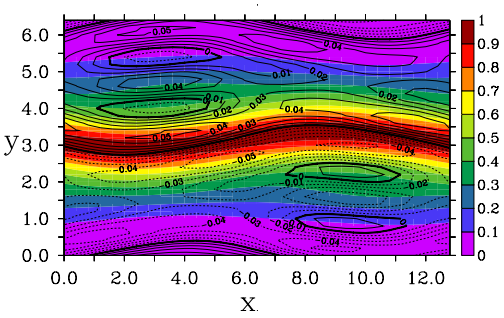

η-branch

$$\mathcal{A}_3 : \mathcal{T}_{L_x/3}, \mathcal{T}_{L_y/3} \begin{pmatrix} 3 \\ 1 \end{pmatrix} \mathrm{Re}_{\mathrm{cr}} = 256$$

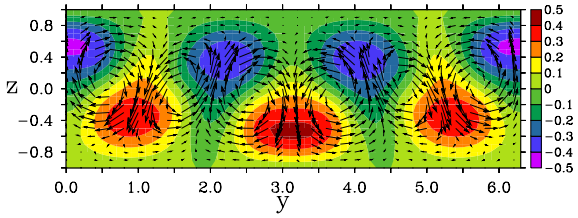

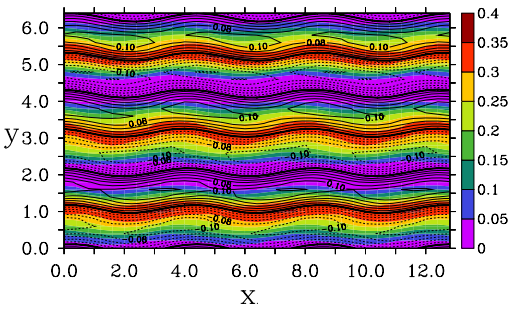

ι-branch

E.1.2 $\mathcal{B}$

$$\mathcal{B}_1 : \mathcal{T}_{L_x/2,L_y/4},\ \mathcal{R}_z \begin{pmatrix} 4 \\ 2 \end{pmatrix} \mathrm{Re}_{\mathrm{cr}} = 183$$

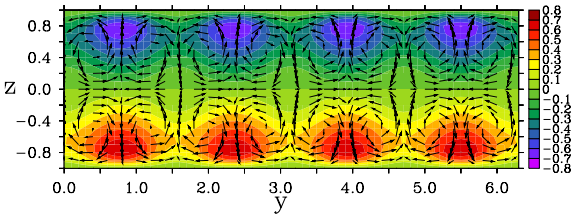

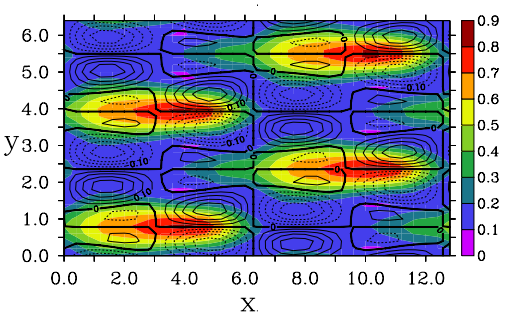

γ-branch

$$\mathcal{B}_2 : \mathcal{T}_{L_x/2,L_y/4},\ \mathcal{R}_z \begin{pmatrix} 4 \\ 2 \end{pmatrix} \mathrm{Re}_{\mathrm{cr}} = 223$$

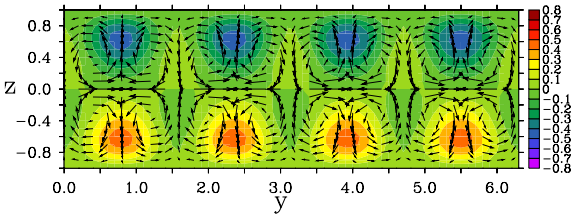

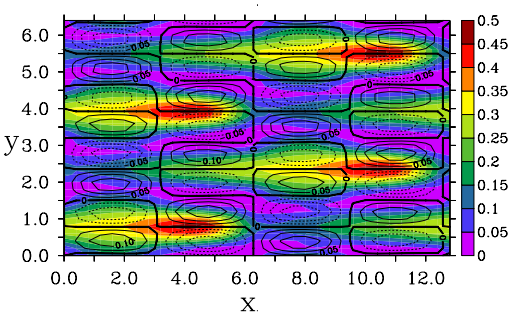

ψ-branch

$$\mathcal{B}_2' : \begin{pmatrix} 4 \\ 2 \end{pmatrix} \mathrm{Re}_{\mathrm{cr}} = 235$$

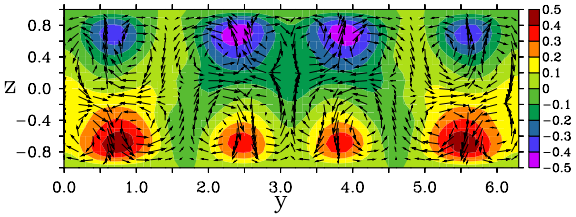

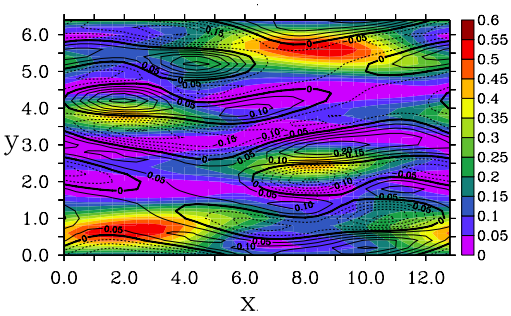

θ-branch

$$\mathcal{B}_2'' : \mathcal{R}_z \begin{pmatrix} 4 \\ 2 \end{pmatrix} \mathrm{Re}_{\mathrm{cr}} = 229$$

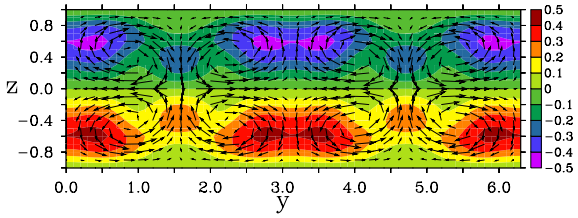

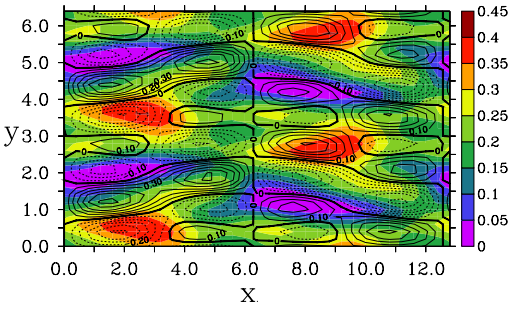

ϵ-branch

$$\mathcal{B}_3 : \begin{pmatrix} 6 \\ 2 \end{pmatrix} \mathrm{Re}_{\mathrm{cr}} = 220$$

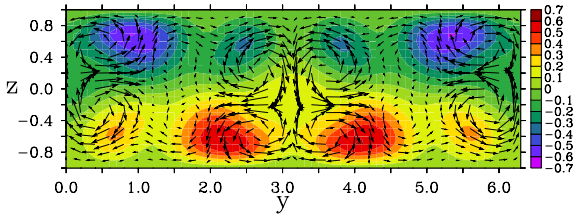

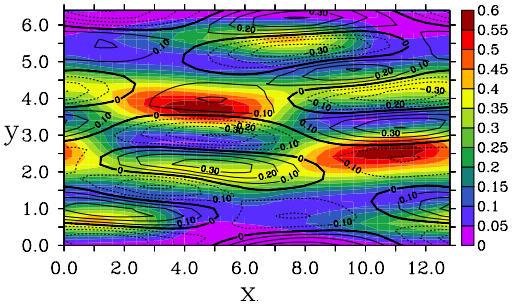

δ-branch

$$\mathcal{B}_4 : \mathcal{T}_{L_x/4,L_y/4},\ \mathcal{R}_z,\ \mathcal{R}_y, \begin{pmatrix} 8 \\ 2 \end{pmatrix} \mathrm{Re}_{\mathrm{cr}} = 235$$

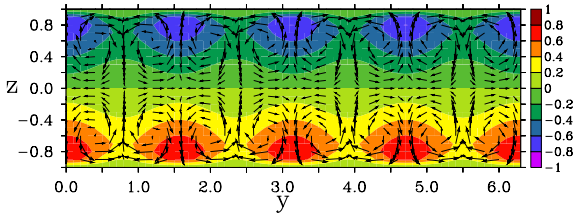

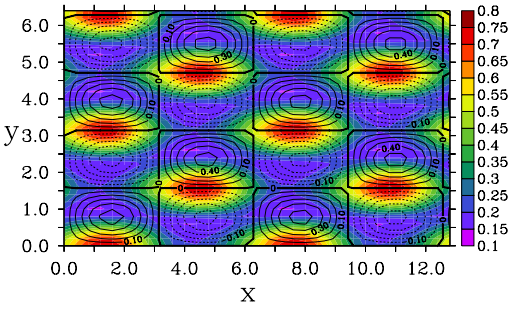

σ-branch

$$\mathcal{B}_4' : \mathcal{R}_z \begin{pmatrix} 8 \\ 2 \end{pmatrix} \mathrm{Re}_{\mathrm{cr}} = 154$$

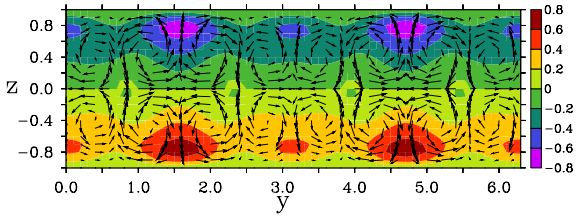

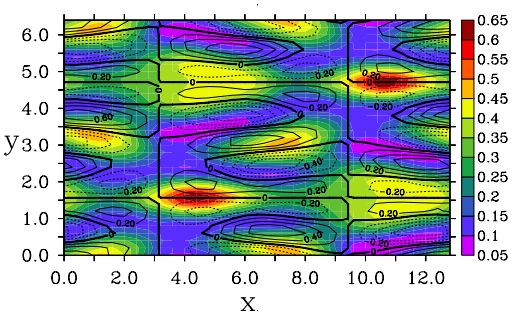

χ-branch

$$\mathcal{B}_5 \mathcal{T}_{L_x/2, L_y/2}, \mathcal{R}_z \begin{pmatrix} 12 \\ 4 \end{pmatrix} \mathrm{Re}_{\mathrm{cr}} = 172$$

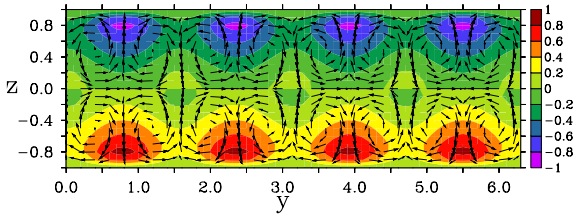

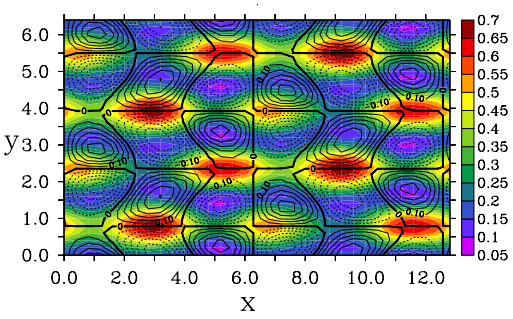

ζ-branch

$$\mathcal{B}_6 : \mathcal{T}_{L_x/2, L_y/2}, \mathcal{R}_y, \mathcal{R}_z \begin{pmatrix} 16 \\ 4 \end{pmatrix} \mathrm{Re}_{\mathrm{cr}} = 387$$

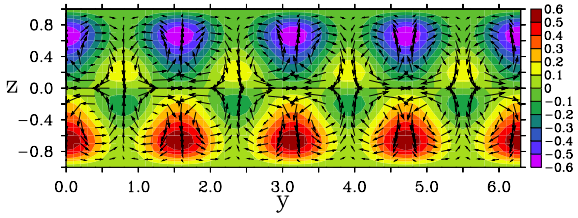

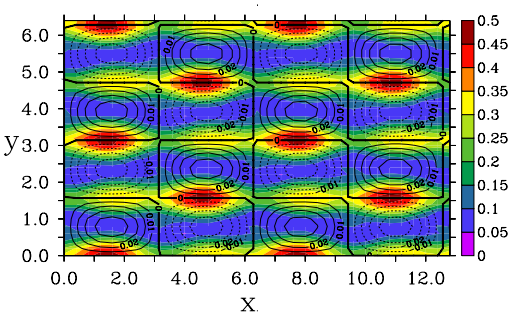

τ-branch

E.1.3 $\mathcal{C}$

$$\mathcal{C}_1 : \mathcal{T}_{L_x/2},\, \mathcal{T}_{L_y/2},\, \mathcal{R}_y \begin{pmatrix} 8 \\ 2 \end{pmatrix} \mathrm{Re}_{\mathrm{cr}} = 153$$

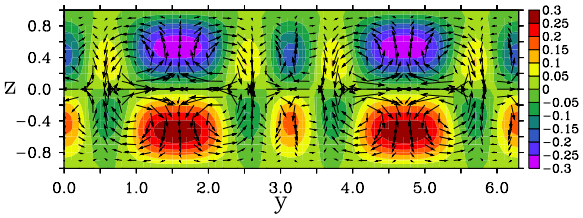

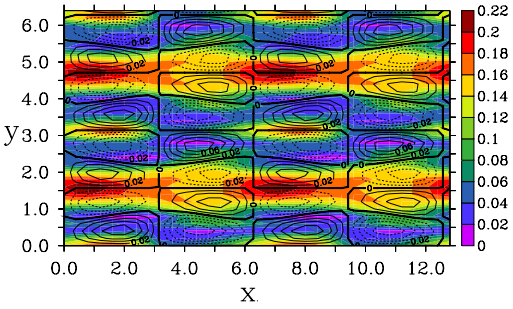

ρ-branch

$$\mathcal{C}_2 : \begin{pmatrix} 8 \\ 2 \end{pmatrix} \mathrm{Re}_{\mathrm{cr}} = 258$$

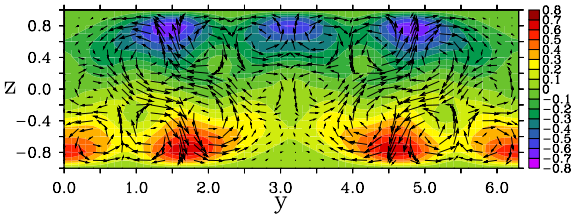

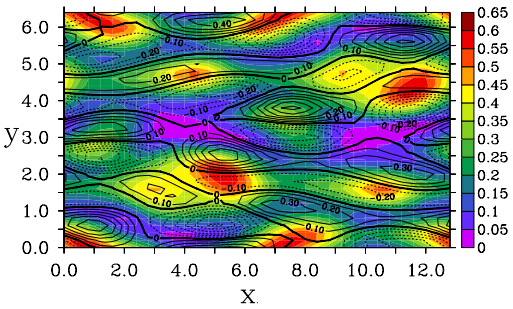

ϕ-branch

$$\mathcal{C}_3 : \mathcal{R}_y \begin{pmatrix} 8 \\ 2 \end{pmatrix} \mathrm{Re}_{\mathrm{cr}} = 153$$

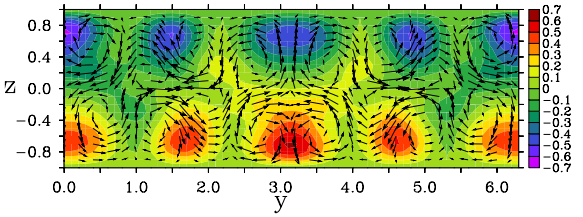

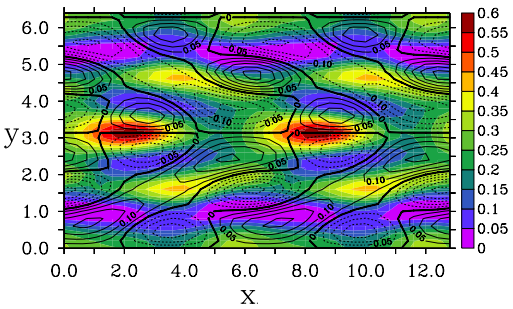

υ-branch

E.1.4 $\mathcal{D}$

$$\mathcal{D}_1 : \mathcal{T}_{L_x/2,L_y/2},\ \mathcal{R}_y,\ \mathcal{R}_z \begin{pmatrix} 4 \\ 2 \end{pmatrix} \mathrm{Re}_{\mathrm{cr}} = 153$$

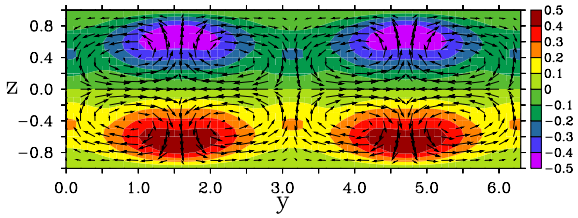

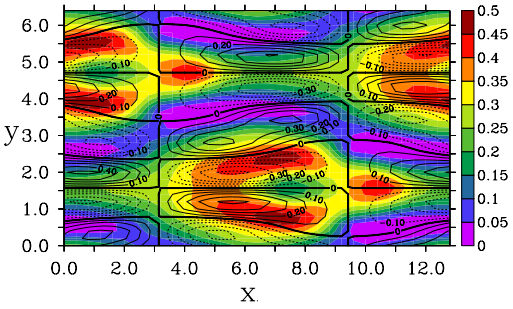

β-branch

$$\mathcal{D}_1' : \begin{pmatrix} 4 \\ 2 \end{pmatrix} \mathrm{Re}_{\mathrm{cr}} = 364$$

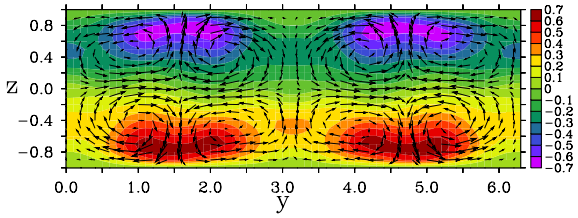

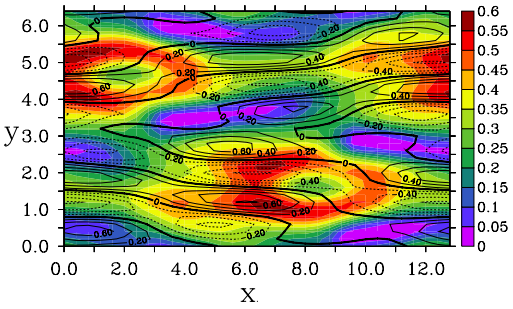

ξ-branch

$$\mathcal{D}_2 : \begin{pmatrix} 4 \\ 2 \end{pmatrix} \mathrm{Re}_{\mathrm{cr}} = 353$$

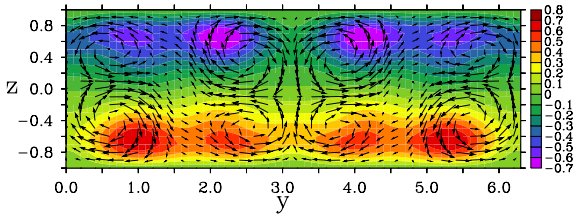

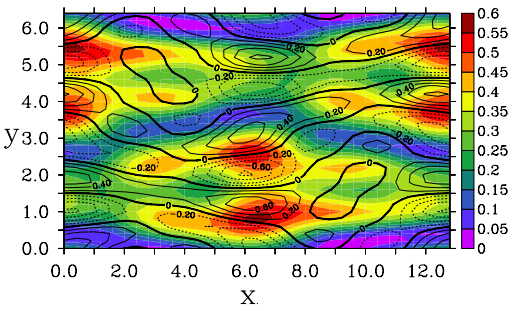

λ-branch

$\mathcal{D}_3 : \begin{pmatrix} 4 \\ 2 \end{pmatrix}$ $\mathrm{Re}_{\mathrm{cr}} = 339$

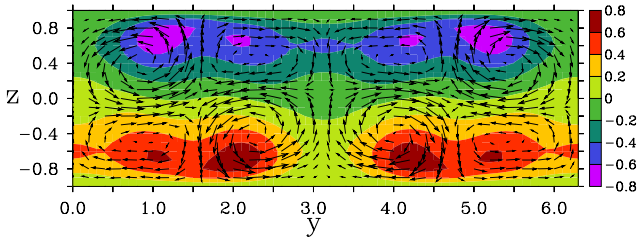

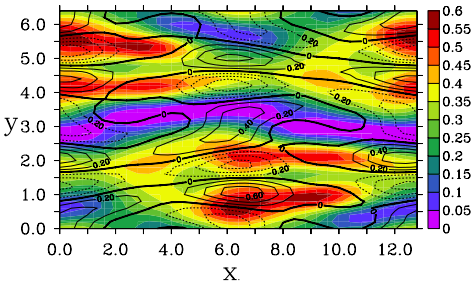

π-branch

$\mathcal{D}_4 : \begin{pmatrix} 8 \\ 2 \end{pmatrix}$ $\mathrm{Re}_{\mathrm{cr}} = 144$

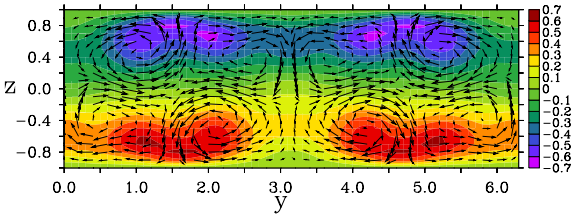

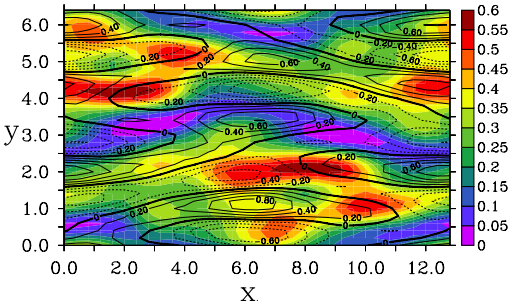

ν-branch

$\mathcal{D}_5 : \begin{pmatrix} 8 \\ 2 \end{pmatrix}$ $\mathrm{Re}_{\mathrm{cr}} = 144$

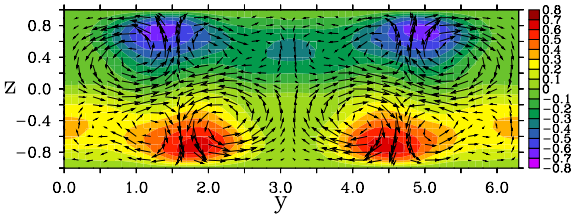

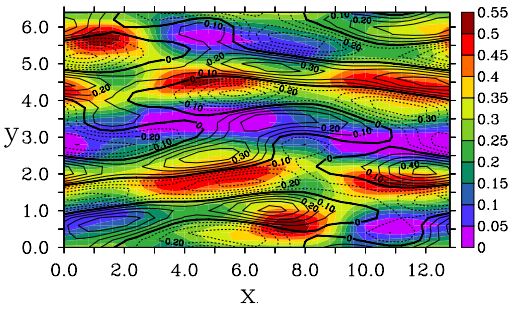

μ-branch

$$\mathcal{D}_6 : \begin{pmatrix} 8 \\ 2 \end{pmatrix} \mathrm{Re}_{\mathrm{cr}} = 144$$

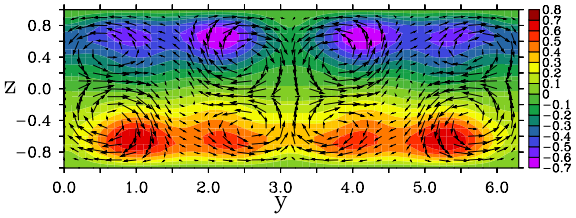

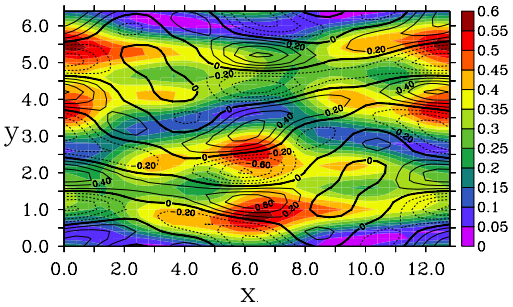

κ-branch

E.2 $\mathcal{I}$-group

E.2.1 E

$$\mathcal{E}_1 : \begin{pmatrix} 6 \\ 2 \end{pmatrix} \mathrm{Re}_{\mathrm{cr}} = 208$$

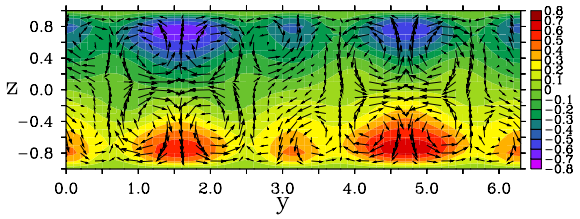

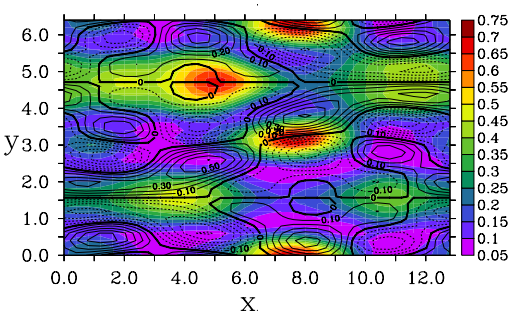

M-branch

$$\mathcal{E}_1' : \mathcal{R}_y \begin{pmatrix} 6 \\ 2 \end{pmatrix} \mathrm{Re}_{\mathrm{cr}} = 169$$

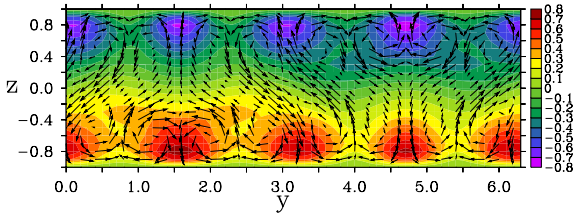

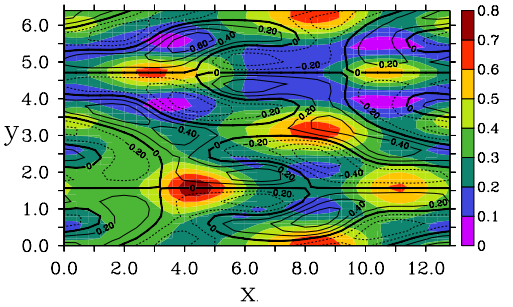

I-branch

$$\mathcal{E}_2 : \mathcal{T}_{L_x/2,L_y/2},\ \mathcal{R}_y,\ \mathcal{R}_z \begin{pmatrix} 8 \\ 2 \end{pmatrix} \mathrm{Re}_{\mathrm{cr}} = 144$$

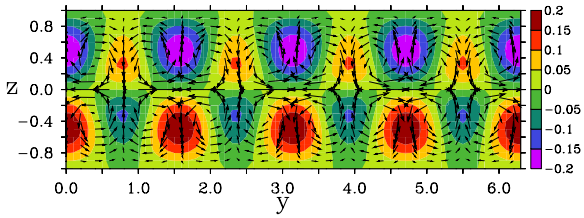

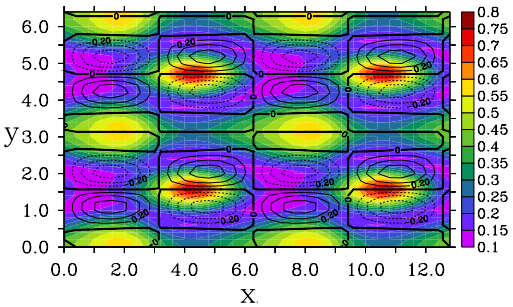

F-branch

$$\mathcal{E}_2' : \begin{pmatrix} 8 \\ 2 \end{pmatrix} \mathrm{Re}_{\mathrm{cr}} = 208$$

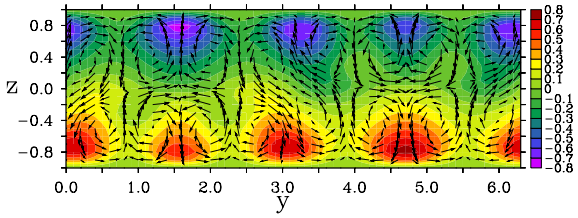

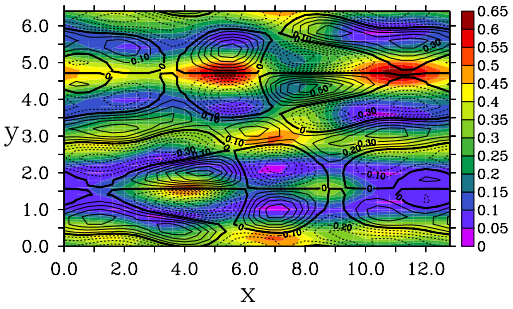

C-branch

$$\mathcal{E}_3 : \mathcal{T}_{L_y/2}\,\mathcal{R}_y,\, \mathcal{R}_z \begin{pmatrix} 8 \\ 2 \end{pmatrix} \mathrm{Re}_{\mathrm{cr}} = 191$$

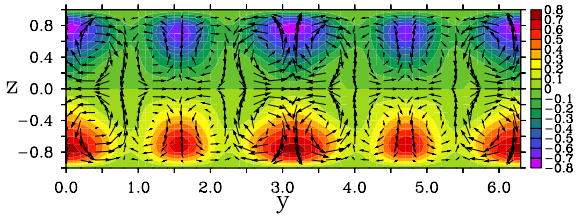

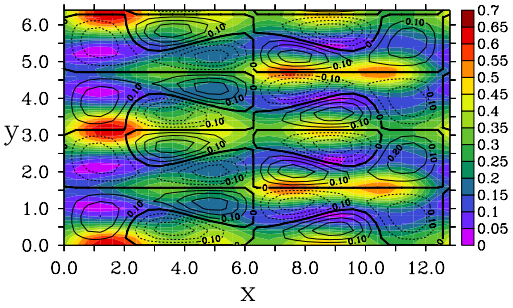

Q-branch

$$\mathcal{E}_4 : \mathcal{T}_{L_x/2} \begin{pmatrix} 8 \\ 2 \end{pmatrix} \mathrm{Re}_{\mathrm{cr}} = 210$$

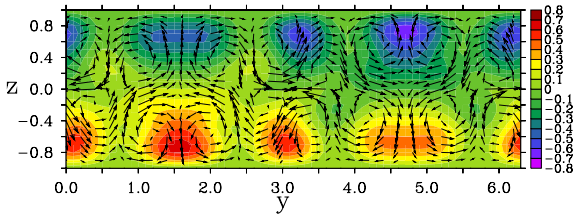

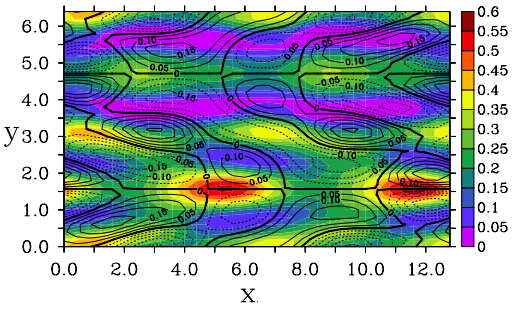

E-branch

$$\mathcal{E}_5 : \mathcal{T}_{L_y/2} \begin{pmatrix} 8 \\ 2 \end{pmatrix} \mathrm{Re}_{\mathrm{cr}} = 197$$

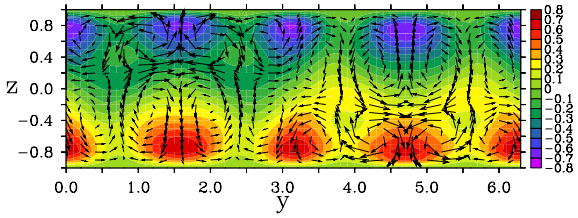

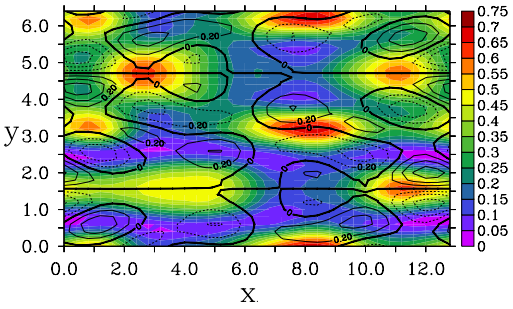

G-branch

$$\mathcal{E}_6 : \begin{pmatrix} 8 \\ 2 \end{pmatrix} \mathrm{Re}_{\mathrm{cr}} = 375$$

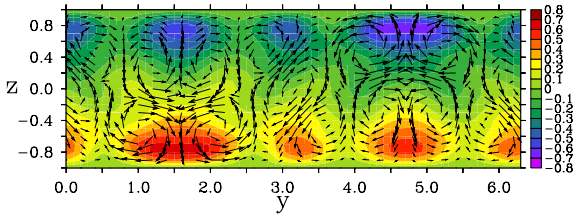

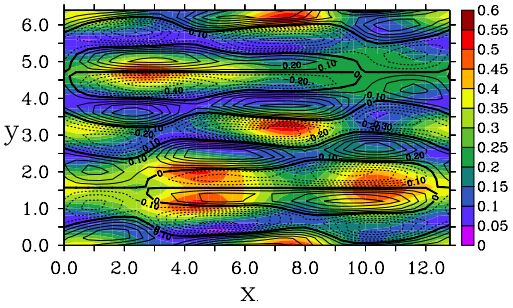

H-branch

$$\mathcal{E}_7 : \mathcal{T}_{L_x/2, L_y/2} \begin{pmatrix} 6 \\ 2 \end{pmatrix} \mathrm{Re}_{\mathrm{cr}} = 220$$

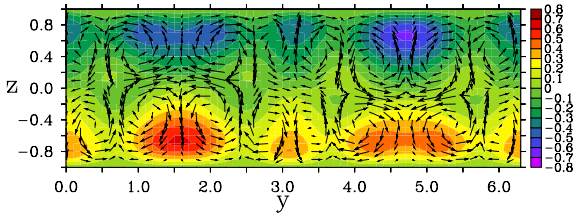

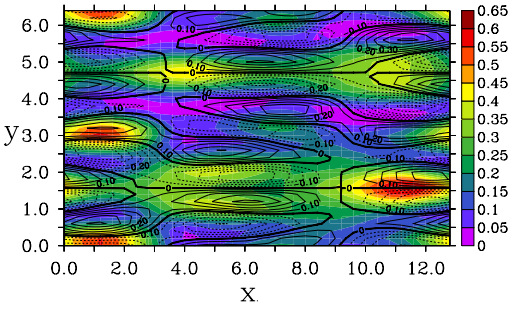

D-branch

$$\mathcal{E}_7 : \mathcal{T}_{L_x/4,L_y/4} \begin{pmatrix} 6 \\ 2 \end{pmatrix} \mathrm{Re}_{\mathrm{cr}} = 220$$

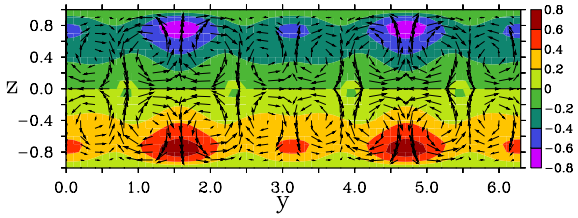

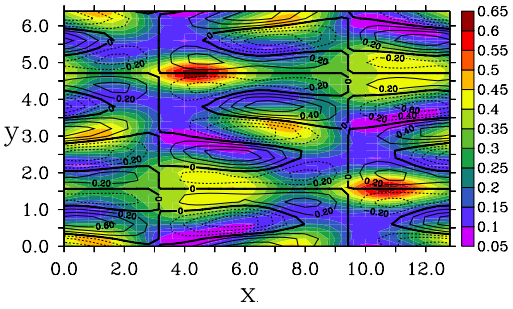

R-branch

E.2.2 $\mathcal{F}$

$$\mathcal{F}_1 : \mathcal{T}_{L_x/2,L_y/2},\ \mathcal{R}_z \begin{pmatrix} 8 \\ 2 \end{pmatrix} \mathrm{Re}_{\mathrm{cr}} = 151$$

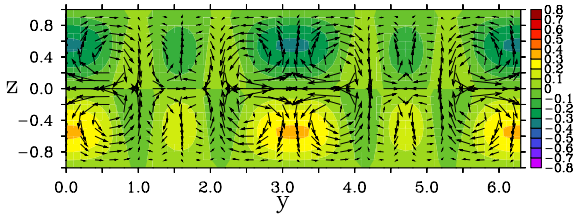

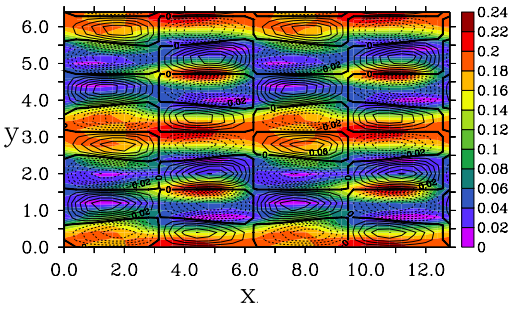

N-branch

$$\mathcal{F}_1' : \mathcal{T}_{L_x/2,L_y/2},\ \mathcal{R}_z \begin{pmatrix} 8 \\ 2 \end{pmatrix} \mathrm{Re}_{\mathrm{cr}} = 206$$

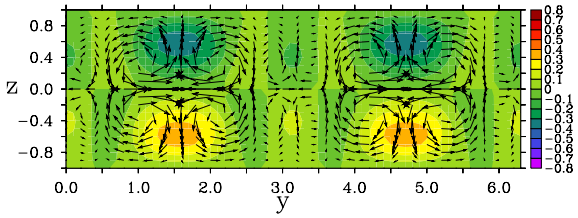

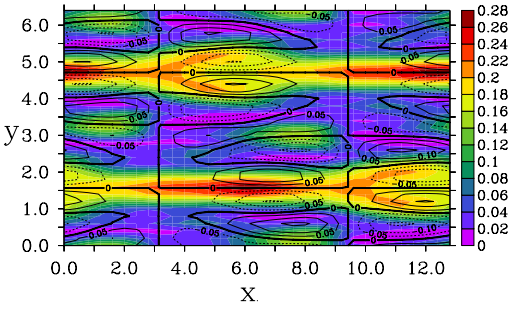

B-branch

$$\mathcal{F}_1'' : \begin{pmatrix} 8 \\ 2 \end{pmatrix} \mathrm{Re}_{\mathrm{cr}} = 208$$

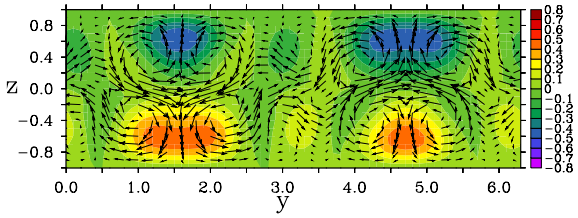

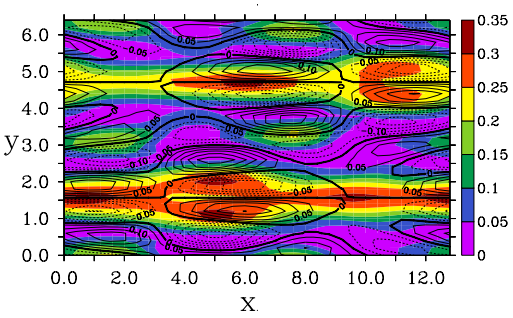

A-branch

E.2.3 $\mathcal{G}$

$$\mathcal{G}_1 : \begin{pmatrix} 5 \\ 2 \end{pmatrix} \mathrm{Re}_{\mathrm{cr}} = 186$$

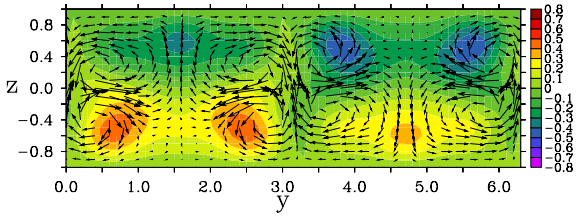

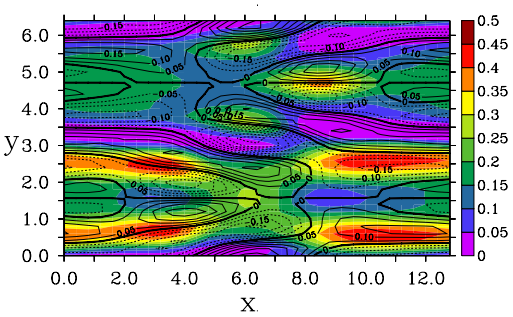

P-branch

$$\mathcal{G}_2 : \begin{pmatrix} 6 \\ 2 \end{pmatrix} \mathrm{Re}_{\mathrm{cr}} = 194$$

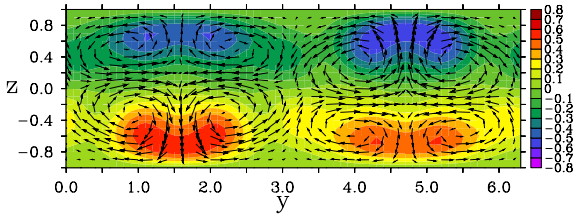

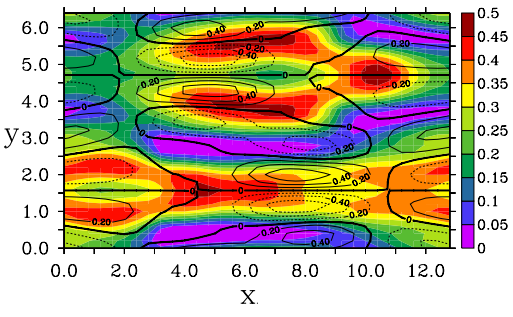

L-branch

$$\mathcal{G}_3 : \begin{pmatrix} 8 \\ 2 \end{pmatrix} \mathrm{Re}_{\mathrm{cr}} = 368$$

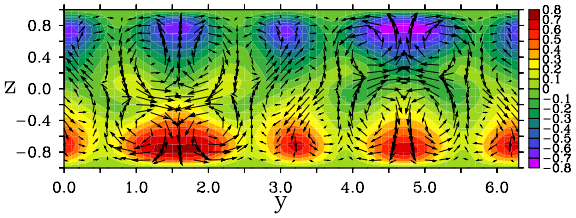

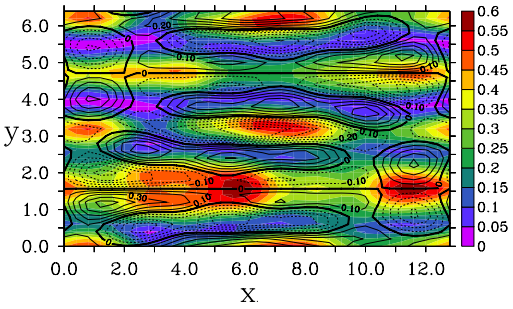

J-branch

$$\mathcal{G}_4 : \mathcal{T}_{L_x/4,L_y/2},\ \mathcal{R}_x,\ \mathcal{R}_y,\ \mathcal{R}_z \begin{pmatrix} 6 \\ 2 \end{pmatrix} \mathrm{Re}_{\mathrm{cr}} = 195$$

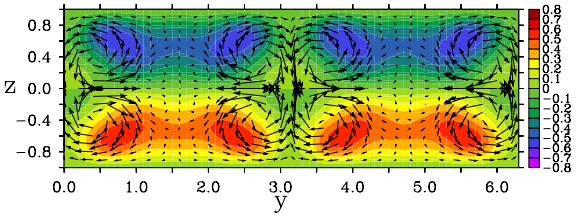

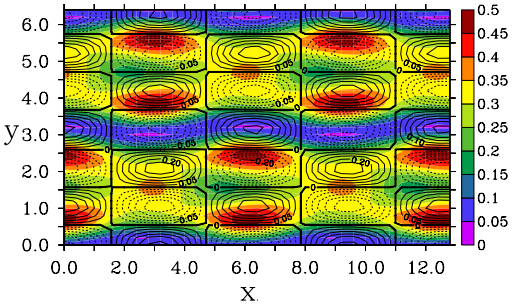

O-branch

Danksagung

Man entdeckt keine neuen Erdteile,
ohne den Mut zu haben,
alte Küsten aus den Augen zu verlieren.

André Gide

Innerhalb der drei Jahre, die diese Arbeit zum Wachsen und Gedeihen benötigte, haben sich eine Vielzahl von Menschen um die Fertigstellung dieser Arbeit verdient gemacht. In erster Linie ist hier mein Doktorvater Prof. Dr. Bruno Eckhardt zu nennen. Ihm danke ich für die Bereitstellung der notwendigen Ressourcen und die Möglichkeit, diese Arbeit vollenden zu können. Sehr schätze ich unseren wissenschaftlichen Diskurs, der mit viel Leidenschaft betrieben wurde. Wenn auch das Rasiermesser manchmal schmerzte, so war man am Ende doch stets der Erkenntnis ein wenig näher gekommen. Prof. em. Dr. Siegfried Großmann danke ich für eine Unzahl von Denkanstößen, die mir ein Dasein als Brownsches Teilchen garantierten. Es war jener Vortrag, den er anlässlich der Verleihung der Max-Planck-Medaille in Berlin hielt, mit dem alles seinen Anfang nahm. Prof. Dr. Florian Gebhard danke ich für die spontane Bereitschaft zur Begutachtung dieser 180 Seiten Hydrodynamik.

Die ehemaligen Mitglieder der AG Statistische Physik verdienen einen besonderen Platz in dieser Aufzählung. Als unsere Arbeitsgruppe Komplexe Systeme noch ganz klein war, waren es diese Mitglieder, die beim Aufbau der neuen Gruppe halfen. Insbesondere möchte ich mich bei Dr. Klaus Drese und Dr. habil. Gerald Ristow bedanken, die dafür sorgten, daß ich in Marburg sehr schnell eine liebgewonnene Heimat gefunden habe. Mit ihnen war der private und der physikalische Diskurs stets eine Freude. Dr. habil. PD. Martin Holthaus machte sich durch die Bereitstellung unvergesslicher Limericks und einiger programmatischer Fingerzeige, die mich manchmal in die rechte Richtung wiesen, sehr verdient.

Doch irgendwann wuchs auch die AG Komplexe Systeme heran, und so kamen neue Mitmenschen hinzu, mit denen das gemeinsame Jobshearing mit Sysiphus betrieben wurde. Insbesondere mein Lieblings-Post-Doc Dr. Jörg Schumacher ist zu nennen, der mittlerweile die

Ebene Couette-Strömung sehr gut kennt, und mit dem ich viele interessante Diskussionen über die Entstehung der Turbulenz führte. Sein Kaffee und seine Musik werden mir stets im Gedächtnis bleiben. Holger Faisst verdanke ich wichtige Diskussionen über die Numerik, die stationären Zustände und ihre Bedeutung für den Turbulenzübergang. Beiden sei zudem gedankt, daß sie es auf sich genommen haben, das Manuskript Korrektur zu lesen. Matthias Lange war eine tatkräftige Unterstützung beim Aufbau und der Betreuung des PC-Netzwerkes, und Wolfgang Braun, der Matthias Erbe angetreten hat trug einen großen Teil der Last, die mit diesem Netzwerk verbunden ist. Peter Pollner danke ich für viele Anregungen zur Fredholm-Determinante.

Der wichtigsten Person gilt es am Schluß zu danken: Meiner Frau Karin. Sie verstand es, die blank liegenden Nerven abzudecken, zerteilte meine Sorgen und stützte mich. So blieb mir Tantalus stets ein wenig fremd.

All diesen und dem ganzen Rest sei gedankt. Die Früchte ihrer Taten liegen in diesen Seiten.

List of Figures

List of Tables

Bibliography

[1] AHYDIN, M. ; LEUTHEUSSER, H. J.: Novel experimental facility for the study of plane Couette flow. In: *Rev. Sci. Instrum.* **50** (1979), S. 1362–1366

[2] ANDERSSON, P. ; BERGGREN, M. ; HENNINGSON, D.S.: Optimal disturbances and bypass transition in boundary layers. In: *Phys. Fluids* **11** (1999), S. 134–150

[3] ARGYRIS, J. ; FAUST, G. ; HAASE, M.: *Die Erforschung des Chaos*. Wiesbaden : Vieweg, 1995

[4] BAGGETT, J.S. ; DRISCOLL, T. A. ; TREFETHEN, L.N.: A mostly linear model of transition to turbulence. In: *Phys. Fluids* **7** (1995), S. 833–838

[5] BALAKUMAR, P.: Finite-amplitude equilibrium solutions for plane Poiseuille-Couette flow. In: *Theoret. Comput. Fluid Dynamics* **9** (1997), S. 103–119

[6] BARKLEY, D. ; TUCKERMAN, L.S.: Stability analysis of perturbed plane Couette flow. In: *Phys. Fluids* **11** (1999), S. 1187–1195

[7] BECH, K.H. ; TILLMARK, N. ; ALFREDSSON, P.H. ; ANDERSSON, H.I.: An investigation of turbulent plane Couette flow at low Reynolds numbers. In: *J. Fluid Mech.* **286** (1995), S. 291–325

[8] BEYN, W.-J.: Global bifurcations and their numerical computation. In: ROOSE, D. (Hrsg.) ; DE DIER, B. (Hrsg.) ; SPENCE, A. (Hrsg.): *Continuation and Bifurcations: Numerical techniques and applications*. Kluwer Academic Publishers, 1990, S. 169–181

[9] BOBERG, L. ; BROSA, U.: Onset of turbulence in a pipe. In: *Z. Naturforsch.* **43a** (1988), S. 697–726

[10] BOIKO, A.V. Flat plate boundary layer response to controlled free-stream axial vortices. 11th Interantional Couette-Taylow workshop. 1999

[11] BOTTIN, S. ; CHATÉ, H.: Statistical analysis of the transition to turbulence in plane Couette flow. In: *Eur. Phys. J. B* **6** (1998), S. 143–155

[12] BOTTIN, S. ; DAUCHOT, O. ; DAVIAUD, F. ; MANNEVILLE, P.: Experimental evidence of streamwise vortices as finite amplitude solutions in transitional plane Couette flow. In: *Phys. Fluids* **10** (1998), S. 2597–2607

[13] BOTTIN, S. ; DAVIAUD, F. ; MANNEVILLE, P. ; DAUCHOT, O.: Discontinuous transition to spatiotemporal intermittency in plane Couette flow. In: *Europhys. Lett.* **43** (1998), S. 171–176

[14] BROSA, U.: Linear analysis of the currents in a pipe. In: *Z. Naturforsch.* **41 a** (1986), S. 1141–1153

[15] BROSA, U.: Turbulence without strange attractor. In: *J. Stat. Phys.* **55** (1989), S. 1303–1312

[16] BROSA, U. ; GROSSMANN, S.: Minimum Description of the onset of pipe turbulence. In: *Eur. Phys. Journal* **43a** (1999), S. 697–726

[17] BUTLER, K. M. ; FARRELL, B. F.: Three-dimensional optimal perturbation in viscous shear flow. In: *Phys. Fluids A* **4** (1992), S. 1637–1650

[18] CANUTO, C.: Boundary conditions in Chebyshev and Legendre methods. In: *SIAM J. Numer. Anal.* **23** (1986), S. 815–831

[19] CANUTO, C. ; HUSSAINI, M. Y. ; QUARTERONI, A. ; ZANG, T. A.: *Spectral Methods in Fluid Dynamics*. New York : Springer, 1987

[20] CHANDRASEKHAR, S.: *Hydrodynamic and hydromagnetic stability*. New York : Dover Publication, (1961)

[21] CHERHABILI, A. ; EHRENSTEIN, U.: Spatially localized two-dimensional finite-amplitude states in plane Couette flow. In: *Eur. J. Mech. B/Fluids* **14** (1995), S. 677–696

[22] CHERHABILI, A. ; EHRENSTEIN, U.: Finite-amplitude equilibrium states in plane Couette flow. In: *J. Fluid Mech.* **342** (1997), S. 159–177

[23] CHOW, C.-Y.: *An Introduction to Computational Fluid Mechanics*. New York : John Wiley & Sons, 1979

[24] CHRISTIANSEN, F. ; CVITANOVIĆ, P. ; PUTKARADZE, V.: Hopf's last hope: spatiotemporal chaos in therms of unstable recurrent patterns. In: *Nonlinearity* **10** (1997), S. 55–70

[25] CLEVER, R.M. ; BUSSE, F.H.: Three-dimensional convection in a horizontal fluid layer subjected to a constand shear. In: *J. Fluid Mech.* **234** (1992), S. 511–527

[26] CLEVER, R.M. ; BUSSE, F.H.: Bifurcation sequences in problems of thermal convection and of plane Couette flow. In: GRUE, J. (Hrsg.): *Waves and nonlinear processes in hydrodynamics*. Kluwer Academic Publishers, 1996, S. 209–226

[27] CLEVER, R.M. ; BUSSE, F.H.: Tertiary and quarternary solutions in plane Couette flow. In: *J. Fluid Mech.* **344** (1997), S. 137–153

[28] CRUTCHFIELD, J. P. ; KANEKO, K.: Are attractors relevant to turbulence? In: *Phys. Rev. Lett.* **60** (1988), S. 2715–2718

[29] CVITANOVIĆ, P.: Dynamical averaging in terms of periodic orbits. In: *Physica D* **83** (1995), S. 109–131

[30] CVITANOVIĆ, P. ; ECKHARDT, B.: Periodic orbit expansions for classical smooth flows. In: *J. Phys. A* **24** (1991), S. L237–L241

[31] DARBYSHIRE, A.G. ; MULLIN, T.: Transition to turbulence in constant-mass-flux pipe flow. In: *J. Fluid Mech.* **289** (1995), S. 83–114

[32] DAUCHOT, O. ; DAVIAUD, F.: Finite-Amplitude perturbation in plane Couette flow. In: *Europhysics Letters* **28** (1994), S. 225–230

[33] DAUCHOT, O. ; DAVIAUD, F.: Streamwise vortices in plane Couette flow. In: *Phys. Fluids* **7** (1995), S. 901–903

[34] DAVIAUD, F. ; J. HEGSETH, P. B.: Subcritical transition to turbulence in plane Couette flow. In: *Phys. Rev. Lett.* **69** (1992), S. 2511–2514

[35] DRAZIN AND W. H. REID, P. G.: *Hydrodynamic stability*. Cambridge : Cambridge University Press, (1981)

[36] ECKHARDT, B.: Chaotische Transienten. In: *Phys. Bl.* **47** (1991), Nr. 11

[37] ECKHARDT, B. ; MARZINZIK, K. ; SCHMIEGEL, A.: Transition to turbulence in shear flows. In: PARISI, J. (Hrsg.) ; MÜLLER, S.C. (Hrsg.) ; ZIMMERMANN, W. (Hrsg.): *A perspective look at nonlinear media in physics, chemistry and biology*. Springer, Berlin, 1998, S. 327–338

[38] ECKHARDT, B. ; MERSMANN, A.: Transition to turbulence in a shear flows. In: *Phys. Rev. E* **60** (1999), S. 509–517

[39] ECKHARDT, B. ; OTT, G.: Periodic orbit analysis of the Lorenz attractor. In: *Z. Phys. B* **95** (1994), S. 259–266

[40] ELLINGSEN, T. ; GJEVIK, B. ; PALM, E.: On the non-linear stability of plane Couette flow. In: *J. Fluid Mech.* **40** (1970), S. 97–112

[41] F.WALEFFE ; KIM, J.: How streamwise rolls and streaks self-sustain in a shear flow. In: PANTON, R. (Hrsg.): *Self-sustaining mechanisms of wall-bounded turbulence*. Computational mechanics publications, 1997

[42] F.WALEFFE ; KIM, J. ; HAMILTON, M.: On the origin of streaks in tubulent shear flows. In: DURST, F. (Hrsg.) ; FRIEDRICH, R. (Hrsg.) ; LAUNDER, B.E. (Hrsg.) ; SCHMIDT, F.W. (Hrsg.) ; SCHUMANN, U. (Hrsg.) ; WHITELAW, J.H. (Hrsg.): *Turbulent shear flows 8: selected papers from the eighth International Symposium on turbulent shear flows, Munich, Germany, Sep. 9-11, 1991*. Springer-Verlag, Berlin, 1993, S. 37–49

[43] GEBHARDT, T. ; GROSSMANN, S.: Chaos transition despite linear stability. In: *Phys. Rev. E* **50** (1994), S. 3705–3711

[44] GOLDSTEIN, H.: *Classical Mechanics*. London : Addison-Wesley, 1980

[45] GOTTLIEB, D. ; ORZAG, S. A.: *Numerical Analysis of Spectral Methods: Theory and Applications*. Philadelphia : Society for Industrial and Applied Mathematics, 1977

[46] GROSSMANN, S.: Wie entsteht eigentlich Turbulenz. In: *Phys. Bl.* **51** (1995), S. 641–646

[47] GROSSMANN, S.: The onset of shear flow turbulence. In: *to appear in Rev. of modern phys.* (1999)

[48] GUCKENHEIMER, J. ; HOLMES, P.: *Nonlinear Oscillations, dynamical systems and bifurcations of vector fields*. New York : Springer, 1983

[49] GUTZWILLER, M.C.: *Chaos in Classical and Quantum Mechanics*. New York : Springer, 1990

[50] HAMILTON, J. M. ; KIM, J. ; WALEFFE, F.: Regeneration mechanisms of near-wall turbulence structures. In: *J. Fluid Mech.* **287** (1995), S. 317–348

[51] HENNINGSON, D.S. ; LUNDBLADH, A. ; JOHANSSON, A.V.: A mechanism for bypass transition from localized disturbances in wall boundard shear flows. In: *J. Fluid Mech.* **250** (1993), S. 169

[52] HIGGINS, R. W.: From the equations of motion to spectral models. In: SHIRER, H.N. (Hrsg.): *Nonlinear hydrodynamic modelling: a mathematical introduction*. Springer-Verlag, 1987

[53] JIMÉNEZ, J.: On the structure and control of near wall turbulence. In: *Phys. Fluids* **6** (1994), S. 944–953

[54] KANTZ, H. ; GRASSBERGER, P.: Repellers, semi-attractors and log-lived chaotic transients. In: *Physica D* **17** (1985), S. 75–86

[55] KOMMINAHO, J. ; LUNDBLADH, A. ; JOHANSSON, A. V.: Very large structures in plane turbulent Couette flow. In: *J. Fluid Mech.* **320** (1996), S. 259–285

[56] KOSCHMIEDER, E.L.: *Bénard cells and Taylor vortices*. Cambridge : Cambridge University Press, (1993)

[57] KOZLOV, V.V.: Methods of control for laminar-turbulent transition research and control. In: *Proceedings of the 19th International Congress of Theoretical and Applied Mechanics, Kyoto, Japan* Bd. 25-31

[58] LEUTHEUSSER, H. J. ; CHU, V. H.: In: *J. Hydr. Div., ASCE* **HY9** (1971), S. 1269

[59] LEVEN, R. ; KOCH, B.-P. ; POMPE, B.: *Chaos in dissipativen Systemen*. Berlin : Akademie Verlag, 1994

[60] LICHTENBERG, G. C.: *Schriften und Briefe – Sudelbücher, Fragmente, Fabeln, Verse*. Insel Verlag, 1983

[61] LIN, C. C.: *The theory of hydrodynamic stability*. Cambridge : Cambridge University Press, (1955)

[62] LUNDBLADH, A. ; JOHANSSON, A. V.: Direct simulation of turbulent spots in plane Couette flow. In: *J. Fluid Mech.* **229** (1991), S. 499–516

[63] MALERUD, S. ; MÂLØY, K. J. ; GOLDBURG, W. I.: Measurements of turbulent velocity fluctuations in a planar Couette cell. In: *Phys. Fluids* **7** (1995), S. 1949–1955

[64] MARSDEN, J.E. ; MCCRACKEN, M.: *The hopf bifurcation and its applications*. New York : Springer, 1976

[65] MOORE, D.W.: The interaction of a diffusing line vortex and an aligned shear flow. In: *Proc. R. Soc. Lond. A* **399** (1985), S. 367–375

[66] MORGENDSTERN, C.: *Gedicht, Verse, Sprüche*. Limassol : Lechner Verlag, 1993

[67] MORKOVIN, M.V.: Bypass transition to turbulence and research desiderata. In: *NASA Conf. Publ.* **2386** (1984), S. 161

[68] NAGATA, M.: Three-dimensional finite-amplitude solutions in plane Couette flow: bifurcation from infinity. In: *J. Fluid Mech.* **217** (1990), S. 519–527

[69] NAGATA, M.: Nonlinear solutions of modified plane Couette flow in the presence of a transverse magnetic field. In: *J. Fluid. Mech.* **307** (1996), S. 231–243

[70] NAGATA, M.: Three-dimensional traveling-wave solutions in plane Couette flow. In: *Phys. Rev. E* **55** (1997), S. 2023–2025

[71] NAGATA, M.: Tertiary solutions and their stability in rotating plane Couette flow. In: *J. Fluid. Mech* **358** (1998), S. 357–378

[72] NISHIOKA, M. ; IIDA, S. ; ICHIKAWA, Y.: An experimental investigation of the stability of plane Poiseuille flow. In: *J. Fluid Mech.* **72** (1975), S. 731–751

[73] OERTEL, J. DELFS, H.: *Strömungsmenchanische Instabilitäten*. Berlin : Springer, (1996)

[74] ORSZAG, S. A.: Accurate solution of the Orr-Sommerfeld stability equation. In: *J. Fluid Mech.* **50** (1971), S. 689–703

[75] ORSZAG, S. A.: Galerkin Approximations to Flows within Slabs, Spheres and Cylinders. In: *Phys. Rev. Lett.* **26** (1971), S. 1100–1103

[76] ORSZAG, S. A.: Numerical simulation of incompressible flows within simple boundaries: accuracy. In: *J. Fluid Mech.* **49** (1971), S. 75–112

[77] ORSZAG, S. A.: Numerical Simulation of incompressible flows within simple boundaries. Galerkin (spectral) Representations. In: *Stud. App. Math.* **L** (1971), S. 293–327

[78] ORSZAG, S. A.: Numerical simulation of incompressible flows within simple boundaries: galerkin (spectral) representations. In: *Studies in Applied Mathematics* **I** (1971), S. 293–327

[79] ORSZAG, S. A.: Spectral Methods for Problems in Complex Geometries. In: *J. Comp. Phys.* **37** (1980), S. 70–92

[80] ORSZAG, S.A. ; KELLS, L.C.: Transition to turbulence in plane Poiseuille and plane Couette flow. In: *J. Fluid Mech.* **96** (1980), S. 159–205

[81] PEARSON, C.F. ; ABERNATHY, F.H.: EWvolution of the flow field associated with a streamwise diffusing vortex. In: *J. Fluid Mech.* **146** (1984), S. 271–283

[82] PEYNET, R. ; TAYLOR, T. D.: *Computational methods for fluid flow*. Berlin : Springer, 1983

[83] PRESS, W. H. ; TEUKOLSKY, S. A. ; VETTERLING, W. T. ; FLANNERY, B. P.: *Numerical Recipes in C. The art of scientific computing*. Cambridge : Cambridge university press, 1992

[84] REDDY, S.: Energy transfer analysis of transition initiated by streamwise vortices in plane channel flow. In: *submitted* (1999)

[85] REDDY, S. C. ; HENNIGSON, D. S.: Energy growth in viscous channel flows. In: *J. Fluid. Mech.* **252** (1993), S. 209–238

[86] REICHARDT, H.: In: *ZAMM (Sonderheft)* **S26** (1956)

[87] REICHARDT, H.: In: *Mitteilungen AVA Goetingen* **22** (1959)

[88] RHEINBOLDT, W.: Solution Field of Nonlinear Equations and Continuation Methods. In: *SIAM Journal of Numerical Analysis* **17** (1980), S. 221–237

[89] RHEINBOLDT, W.: *Numerical Analysis of Parametrized Nonlinear Equations*. New York : John Wiley & Sons, 1986

[90] RILEY, J. J. ; GAD-EL-HAK, M.: The dynamics of turbulent spots. In: S. H. DAVIS, J. L. L. (Hrsg.): *Frontiers in Fluid Mechanics*. Springer, 1985, S. 123–155

[91] ROBERTSON, J. M.: In: *Proc. VIth Annual Conf. Fl. Mech., Univ. of Texas* **169** (1959)

[92] ROBERTSON, J. M. ; JOHONSON, H. F.: In: *J. Engr. Mech. Div., ASCE* **1171** (1970)

[93] ROMANOV, V. A.: Stability of plane Couette flow. In: *Funkt. Anal. Appl.* **7** (1973), S. 137

[94] SAFFMAN, P.G.: *Vortex dynbamics*. Cambridge : Cambridge University Press, 1995

[95] SCHMIEGEL, A.: *Turbulenzübergang in der Ebenen Couette-Strömung*, Carl von Ossietzky-Universität, Oldenburg, Diplomarbeit, 1996

[96] SCHMIEGEL, A. ; ECKHARDT, B.: Fractal stability border in plane Couette flow. In: *Phys. Rev. Lett.* **79** (1997), S. 5250–5253

[97] SCHMIEGEL, A. ; ECKHARDT, B.: Dynamics of perturbations in plane Couette flow. In: *submitted* (1999)

[98] TÉL, T.: Controlling transient chaos. In: *J. Phys. A* 24 (1991), S. 1359–1368

[99] TÉL, T.: Transient chaos. In: BAI-LIN, H. (Hrsg.): *Direction in chaos* Bd. 3. Singapore : World scientific, 1991, S. 149–211

[100] TILLMARK, N.: On the spreading mechanisms of a turbulent spot in plane Couette flow. In: *Europhys. Lett.* **37** (1995), S. 481–485

[101] TILLMARK, N. ; ALFREDSSON, P. H.: Experiments on transition in plane Couette flow. In: *J. Fluid Mech.* **235** (1992), S. 89–102

[102] TREFETHEN, A.E. ; TREFETHEN, L.N. ; SCHMID, P.J.: Spectra and pseudospectra for pipe poiseuille flow. In: *Comp. Meth. Appl. Mech. Engr., to appear)* (1999)

[103] TREFETHEN, L.N. ; TREFETHEN, A. E. ; REDDY, S. C. ; DRISCOLL, T.A.: Hydrodynamic stability without eigenvalues. In: *Science* **261** (1993), S. 578–584

[104] U. EHRENSTEIN, W. K.: Three-dimensional wave-like equilibrium states in plane Poiseuille flow. In: *J. Fluid Mech.* **228** (1991), S. 111–148

[105] WALEFFE, F.: Hydrodynamic stability and turbulence: beyond transients to a self-sustaining process. In: *Stud. App. Math.* **95** (1995), S. 319–343

[106] WALEFFE, F.: Transition in shear flows. Nonlinear normality versus non-normal linearity. In: *Phys. Fluids* **7** (1995), S. 3060–3066

[107] WALEFFE, F.: On a self-sustaining process in shear flows. In: *Phys. Fluids* **9** (1997), S. 883–900

[108] WATSON, J.: On the non-linear mechanics of wave disturbances in stable and unstable parallel flows, Part 2. The development of a solution for plane Poiseuille flow and for plane Couette flow. In: *J. Fluid. Mech.* **9** (1960), S. 371–389

[109] WIGGINS, S.: *Introduction to applied nonlinear dynamical systems and chaos*. New York : Springer, 1990

[110] ZIKANOV, O.Y.: On the instability of pipe Poiseuille flow. In: *Phys. Fluids* **8** (1996), S. 2923–2932